LASER SURFACE CLADDING/PARTICLE INJECTION OF WEAR RESISTANT ALLOYS AND COMPOSITES

By

GHAZANFAR ABBAS

A Thesis Submitted for the Degree of
Doctor of Philosophy of the
University of London

1990

Department of Materials, Royal School of Mines
Imperial College of Science, Technology and Medicine
London

Dedicated to
Imam Ali Ibn Abu Talib (A.S)
"Babul Ilm"

ABSTRACT

High power lasers have been clearly recognized in the past two decades as reliable heat sources for the deposition of hard and wear resistant layers, e.g. of cobalt-base alloys, on relatively soft metal surfaces. This project reports work carried out to produce alloy and composite clad deposits on an En 3b mild steel substrate for enhanced hardness and wear properties. A series of experiments was done to form single and overlapping clad tracks by either injecting SiC particles or blowing a mixture of powders of SiC with Stellite alloy 6, a low alloy steel (Alloy 4815) and an austenitic stainless steel respectively.

A 2 kW CW CO_2 laser was used to generate a melt pool on the substrate. The powder mixtures were blown into the melt pool using a pneumatic powder delivery system. The clads were produced using various combinations of processing parameters to study their effect on the clad quality and also to obtain optimum conditions for a good clad. The parameters varied during this study include, substrate traverse speed, powder feed rate, powder mixture composition, and laser power density.

The powder particle velocity was found to influence the powder intake into the melt pool. Higher particle velocities resulted in more powder loss. An acoustic emission technique was used to determine the effect of various parameters, related to the powder feed system, such as carrier gas flow rate, powder density and feed tube length , on the particle velocity.

Clad samples were subjected to various metallurgical and mechanical tests to observe the effect of different processing parameters. Microstructural studies were done by using various electron microscopy techniques including SEM and TEM. Samples were chemically analysed using electron probe micro analysis to determine the dilution level of the clads. X-ray diffraction was used to examine different phases.

Overlapping clad samples were subjected to two types of abrasive wear tests, namely, two- and three-body wear test. The wear testing equipment was designed to provide severe wear conditions simulating those encountered in service.

The comparative studies of the various alloys and composites produced showed that the composite clads were far better than the alloy clads in hardness and wear resistance. The increase in the hardness and wear resistance of the composite clad matrices was attributed mainly to the dissolution of SiC; resulting in the enrichment of the matrix regions in carbon and consequent formation of fine carbides. Composites of relatively inexpensive low alloy steel (Alloy 4815) and SiC particles showed high wear resistance comparable with that shown by expensive Stellite alloy and SiC composite.

ACKNOWLEDGMENTS

(In the name of God, the Merciful, the Compassionate)

I am extremely grateful to my project supervisor, Prof. D.R.F. West, for his continuous guidance and encouragement during the research work. His valuable suggestions and discussion, constructive criticism and also untiring reading and correction of the manuscript, have made it possible to bring the thesis in the present shape. I equally owe to Prof. W.M. Steen, University of Liverpool (then at Imperial College), for suggesting the present area of research and also for his help in the early stages of the work.

I would like to express my gratitude to Dr. R.D. Rawlings and Dr. V.M. Weerasinghe, for their cooperation in applying the acoustic emission technique for powder flow monitoring.

Many thanks are also due to my sister Dr. Rayhana Firdous for her ever polite advice and well wishes.

I am indebted to all my colleagues of the past and the present laser group, especially Dr. Rehan Akhtar and Mr. M.J. Kadhim, for their help and also for giving me a good time during my stay.

Miss Norma Hikel has been very kind and helpful. I am very much grateful for her cooperation during my stay at the department, especially for allowing me to use her office as waiting room during the times whenever Prof. West was busy with other visitors.

I would also like to acknowledge the help and assistance of the following staff of the department,

Mr. Alec Neve, chief technician

Mr. R. Baxter and other staff of the workshop

Mr. G. Briers, Mr. Nulin and Mr. J. Wood of electron microscopy group

Mr. R. Sweeney of x-diffraction group

Mr. Phil and Miss. R. Driscoll of photography group

Acknowledgements are also due to BP Research Centre Sunbury-on-Thames, for providing financial assistance, materials and access to equipment. In particular my thanks go to Dr. Nigel Gibbs and Mr. John Clark for their help in using the wear testing equipment, and also to Dr. M.J. Tricker and Mrs. Collins of University Liaison.

The financial support of the Government of Pakistan, Ministry of Science and Technology, by awarding a scholarship, is highly appreciated.

My special thanks are also due to all my colleagues in the Corps of EME for their encouragements, especially the past (Maj. Gen. (Retd.) Qazi Abid Hussain) and the present (Maj. Gen. Javed Anwar Hashmi) Directors of the EME Corps, whose sincere efforts made it possible for me to avail this opportunity of research. I am also obliged to Brig. Saeed Ismat, Defence and Army Attache, High Commission for Pakistan in London, for his help during my stay in London.

And last, but surely not least, I am greatly thankful to all my family members in Pakistan, who have been waiting for such a long time for my return. I always missed them - may be they missed my company too! In particular, I would like to express my extreme gratitude to my loving mother Mrs. Ansar Zahra and devoted father Mr. A.F Abbas for their kind help, constant encouragement and continuous guidance, at every stage of my life, in every possible way.

CONTENTS

List of Figures

List of Tables

CHAPTER 1

INTRODUCTION

1.1 GENERAL INTRODUCTION

This project is mainly concerned with the improvement of the surface properties of relatively cheap mild steel substrate by cladding with hard and wear resistant alloy and composite layers using a high power laser as a heat generating source.

Wear is considered to be an unavoidable process which occurs in a variety of forms in both industrial and "everyday" use machinery. In many service applications, for example; oilwell drilling and automobile engines, wear of certain operating parts is a major factor in determining the overall life and performance of machine components. The untimely replacement of worn parts and subsequent losses due to process shut down, can lead an industry to high annual expenses. In general engineering use, various parts of a component are subjected to different wear conditions. It is , therefore, desirable to improve the wear resistance of the surface which faces a "harsh" environment while the rest of the component will keep its bulk properties.

One process for improving the wear resistance of specific surface is known as hardfacing. In this process a hard and wear resistant material is "welded" onto a surface to increase its service life at a relatively low expense. There are numerous conventional hardfacing techniques, including TIG welding and oxyacetylene torch welding, which have been widely used for overlaying the hard and wear resistant layers onto inexpensive material substrates.

Cobalt-base alloys have been extensively used in wear related engineering applications for more than half a century because of their good mechanical properties e.g. high

strength and hardness even at elevated temperatures, and also good corrosion resistance. The cobalt-base commercial alloys include the Stellites, which cover a range of compositions. Their relatively high cost has led to interest in processes for improving the surface properties of cheaper substrates rather than using special alloys for manufacturing the bulk component.

The process of hardfacing was further developed when high power lasers were introduced in this field in 1970's. Lasers can truly be considered as one of the most important discoveries of this century for their economical impact and variety of applications. The use of high power lasers in materials processing applications has been a subject of interest for many researchers during the last two decades. Lasers have been applied for a range of processes such as cutting, welding, transformation hardening, surface melting, alloying and cladding of many materials.

Some significant advantages of lasers which favour their application in material processing include high productivity, high flexibility and easy automation. These advantages come from the following intrinsic characteristics of the laser beam as a working tool (1).

1. Transfers energy fluxes of extremely high intensity.
2. Localized rapid heating upto temperatures of 2×10^4 K possible.
3. Applies its energy to any surface which is optically reachable.
4. Saves processing energy.
5. Reduces/eliminates post processing finishing operations.
6. Performs in a clean manner.
7. Quick response to commands, e.g. intensity and position of the beam.
8. Performs as a self restoring tool.

1.2 LASER CLADDING/PARTICLE INJECTION

Laser surface cladding is a process which usually involves the deposition of a metallic layer onto another metallic substrate for producing hard and wear/corrosion resistant layers wherein the laser beam acts as a heat generating source to melt both the substrate and the cladding material, commonly in powder form. There are a number of methods for applying the cladding powder, for example; preplacing powder on the substrate, or blowing the powder into the melt pool. In the present studies, a pneumatic powder blowing technique was used. Laser cladding using blown powder has the main advantages of being capable of producing fusion bonded clad layers having very low dilution from the substrate. It is also potentially capable of automation. These advantages make the process an interesting competitor in the fast growing market for hardfacing. The laser hardfacing process was first used in 1981 on an industrial basis.

In a later study (2), a laser injection process was developed whereby hard and wear resistant surfaces were produced by injection carbide particles (e.g. TiC and WC) into various substrates (e.g. Ti-6Al-4V and Inconel).

1.3 MAIN OBJECTIVES OF PRESENT WORK

One important example of wear conditions is that of drilling bits in various cutting and drilling processes, especially oilwell drilling operations; where, wear is an important factor in determining the shut down periods of the process. Frequent replacements of the drilling bits may increase the operational cost to a high level.

The main objective of the present study was, therefore, to investigate suitable alloy compositions which can be applied as coatings to drilling bits and other similar type of applications using a high power laser as a heat producing source. The present work was divided into two parts. In the first part, laser was used to inject SiC particles into a mild steel substrate and also to produce overlapping clads of various alloys, e.g. Stellite alloy

6, an austenitic stainless steel and a low alloy steel (Alloy 4815) and their composites with SiC by including SiC particles in the cladding powders. In the second part, comparative wear studies of various alloy and composite deposits were carried out. This task was, therefore, started in the following sequence to achieve the set goals.

1. An indepth review of the previous literature on the subject was carried out.
2. Laser processing conditions were established by producing various single track clads using different processing parameters e.g. laser beam diameter, substrate traverse speed and powder feed rate.
3. Preliminary microstructural studies and hardness measurements were carried out to find out some suitable composite compositions for better wear properties by changing the proportion of SiC in the cladding powder.
4. Wear studies were made of various alloy and composite overlapping clad deposits to establish their ranking in the wear resistance. Relationships between the wear behaviour and their structural properties were also determined.

The present work of cladding and particle injection differs from previous studies in two ways. Firstly in the present work on particle injection, relatively cheaper carbide particles (SiC) were used for injecting into a mild steel substrate. In all the previously reported work on particle injection, the carbide particles used were relatively expensive TiC and WC particles. Secondly, in most of the previous studies, the hard and wear resistant surfaces were produced by either injecting the hard carbide particles (e.g TiC and WC) into various substrates (e.g. Ti-6Al-4V and Inconel) or by cladding some suitable hardfacing alloys (e.g. Stellite or stainless steel). However, in the present studies, composite clads were produced by blowing mixtures of hardfacing alloy powders (Stellite and stainless steel) and carbide particles (SiC) into the laser generated melt pool in various proportions and feed rates to study the effect of incorporated SiC particles on the wear properties of the clads. By using this combination, it was aimed to superimpose the advantageous properties of both the components with the hard carbide component

providing hardness and wear resistance and the relatively ductile binder (Stellite or stainless steel) contributing towards the toughness.

Wear is a complex phenomenon and usually occurs in more than one form depending on the service conditions. However, about 50% of the total wear loss results from the abrasive type of wear; for that reasons present studies were confined to abrasive wear testing only. The alloy and composite clad samples were subjected to both type of abrasive wear, namely, two-body and three-body abrasive wear. In the preliminary studies, a qualitative two-body abrasive test was carried out on a variable composition (constant Stellite and variable SiC) Stellite + SiC composite clad to find out the effect of SiC feed rate on the wear properties of the composite. On the basis of these preliminary studies, overlapping track clad samples were produced for quantitative wear testing. In the first series of tests, the samples were tested for two-body wear under a high stress, severe wear conditions; the effect of various process parameters, e.g. sliding distance and applied pressure, on the wear loss was studied. The three-body wear set-up used was, in fact, a simulation of drilling process in the sea water. These tests were carried to calculate the wear loss of various laser produced composites to find out their feasibility to apply as coatings on the oilwell drilling bits.

CHAPTER 2

LITERATURE SURVEY

2.1 INTRODUCTION

The chapter on the literature survey includes the following two sections.

1. Lasers and their interactions with materials
2. Laser cladding

The first section gives an outline of the history of lasers and a brief description of the physics of CO_2 lasers and their interactions with materials. In the second section an indepth review of previous work on laser cladding/injection of various alloys and carbide particles is presented.

2.2. LASERS AND THEIR INTERACTIONS WITH MATERIALS

2.2.1. Short History of Lasers

The process of laser invention was, in fact, first started in 1917, when Albert Einstein showed that the process of simulated emission must exist which would allow light to be amplified. The experience gained in the development of radar during world war 2 helped and led scientists to explore the conditions necessary for laser action to be achieved. In the early 1950's a group at Columbia University (USA) headed by C.H. Townes operated a microwave device that amplified radiations by the stimulated emission process (3). The device was termed as 'MASER', an acronym for Microwave Amplification by Stimulated Emission of radiation. The maser principle was employed in

many materials until 1958, when Schawlow and Townes published an important paper (4) in which they discussed its extension to the optical region of the electromagnetic spectrum. After that a new area of research was opened to investigate the systems that might serve as the basis for an optical maser or laser. T.H. Maiman (3), in 1960, was the first to achieve the lasing action at optical frequencies. His laser consisted of a pink ruby rod with silvered ends to act as mirrors inserted in the helical coil of a photographic flash lamp. A major advance occurred when in 1964, C.N. Patel (5) developed a CO_2 laser. Although the laser developed by Patel was of low power, it led to the development of high power CO_2 lasers.

2.2.2 Physics of CO_2 Lasers

CO_2 lasers fall in the category of molecular laser systems where the active media are molecules. This laser is considered to be the most efficient and powerful continuously operating gas laser. The maximum efficiency of a conventional CW CO_2 laser discharge has been reported as upto 30% at low laser output (5-6). In CO_2 lasers the lasing action occurs by the emission of photons from the excited CO_2 molecules. Nitrogen is used as an efficient excitation mechanism for CO_2 molecules. The emission of photons can occur in the following two ways as shown in Fig. 2.1.

1. By the atom changing to the lower state at random. This is called spontaneous emission.
2. By a photon having energy equal to the energy difference between the two levels interacting with the atoms in the upper state and causing the atom to change to the lower state with the creation of a second photon. This process is, in fact, the converse of absorption and is known as stimulated emission.

It is thus apparent that in a system containing a very large number of atoms (or molecules) the dominating process will depend on the relative numbers of atoms in the upper and lower states. A large number of atoms (also called population) in the upper

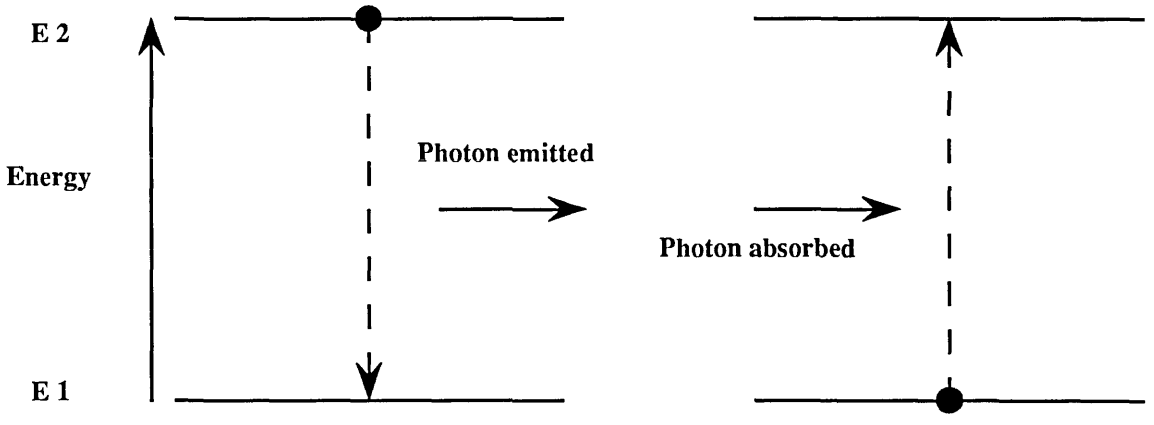

(a) Spontaneous emission and absorption

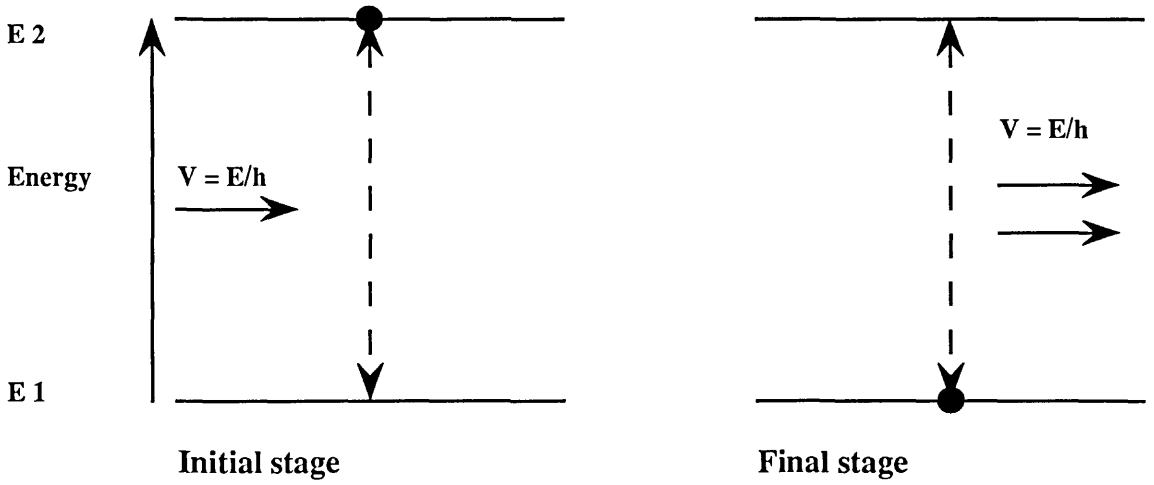

(b) Stimulated emission

Fig. 2.1 Spontaneous and stimulated emission of photons.

level will result in stimulated emission dominating, while if there are more atoms in the lower level, there will be more absorption than stimulated emission. For stimulated emission to dominate, it is necessary to increase the population of the upper energy level so that it is greater than that of the lower level. This situation is known as population inversion.

The carbon dioxide molecules, composed of two oxygen atoms and a carbon atom between them, undergoes three types of oscillation as shown in Fig. 2.2.

These three fundamental vibrational configurations are called vibrational modes. According to the quantum theory, the energy of oscillation of a molecule in any one mode can have only discrete values. These discrete values are all integers multiple of some fundamental value. At any one time, a CO_2 molecule can be vibrating in a linear combination of the three fundamental modes. The energy state of the molecule can then be represented by three numbers (ijk). These numbers represent the amount of energy, or the number of energy quanta, associated with each mode. For example the number (002) next to the highest energy level shown in Fig. 2.3 means that a molecule in this energy state is in the pure asymmetric stretch mode with two units of energy i.e. with no unit of energy associated with the symmetric stretch or bending mode. In addition to the vibrational states, rotational states, associated with the rotation of the molecule about the centre of mass, are also possible. The energies associated with the rotational states are generally small compared to those of the vibrational state and are observed as splittings of the vibrational level into a number of much finer sub-levels.

The various low-lying energy levels of the CO_2 molecule that are responsible for the laser transition are shown in Fig. 2.3. Each group of lines represent a different vibrational energy level and each individual line represents a different rotational energy level. In the 'CO_2 laser', the molecules are pumped from the ground state to higher energy states from which they trickle back by radiative and non-radiative process to state (001) which is metastable. With sufficient pumping a population inversion is produced between the (001) state and the (100) and (020) states. If the losses in the laser cavity are

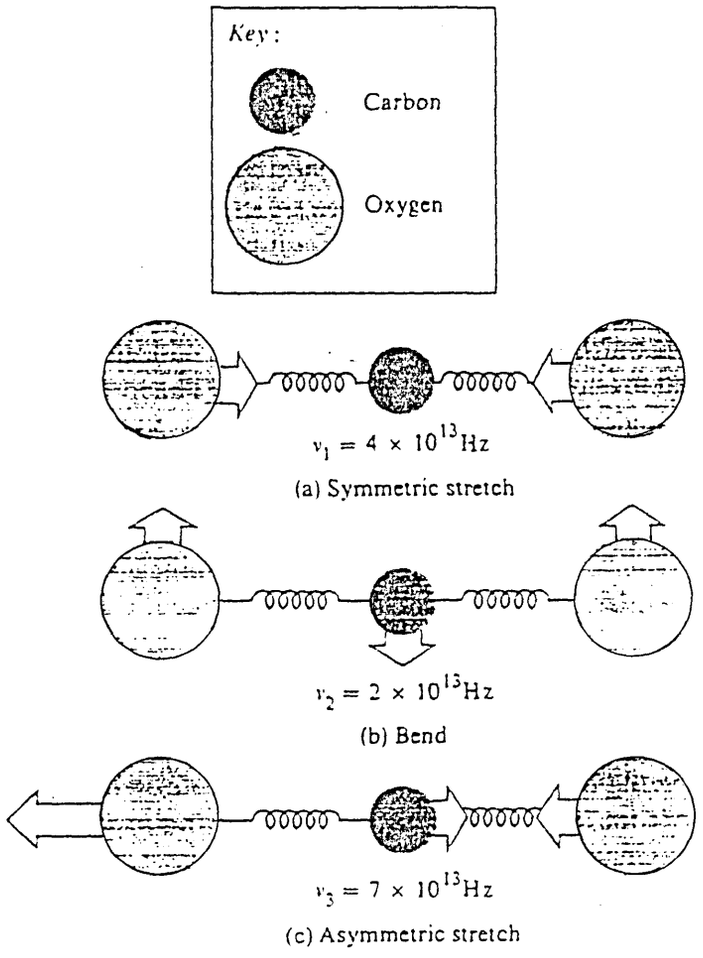

Fig. 2.2 Different ways of CO_2 molecule oscillation (Ref. 3).

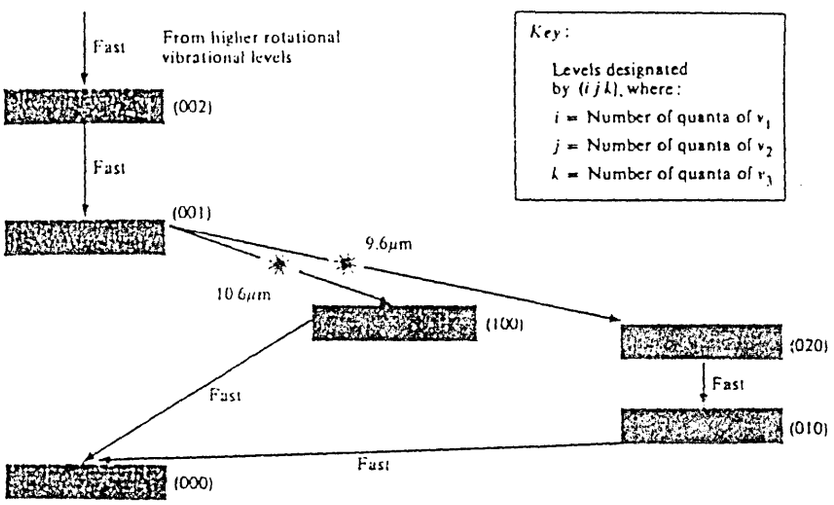

Fig. 2.3 Energy level diagram for CO_2 laser (Ref. 3).

sufficiently low, laser oscillation begins. The strongest line of the CO_2 laser is at a wavelength of 10.6 μm in the infrared region. For improving the laser output, nitrogen and helium are added to the gas mixture. The excited nitrogen molecules transfer energy to the CO_2 molecules by resonant collisions, whereas helium increases the laser efficiency by speeding up the transition from the (100) energy level to the ground level maintaining a large population inversion.

2.2.3 Types of CO_2 Lasers

A large number of CO_2 lasers are available today, varying in structure, method of excitation and capacity. The following types of lasers have been reported by Duley (5) based on excitation method, gas flow pressure and direction relative to optical axis. The reader is advised to consult reference (5) for a detailed study of these lasers.

1. Slow axial flow system
2. Fast axial flow system.
3. Fast gas transported system.
4. Waveguide lasers.

2.2.4 Fundamentals of Laser-Materials Interaction

In order to produce good quality clads, with a CO_2 laser, by exercising control over different processing parameters, it is helpful to understand the fundamentals of laser beam interaction with materials. The first question that arises is what happens when a solid surface is irradiated by a laser beam ? When a laser beam falls on an opaque metal surface, heat is transferred to the metal by the interaction of the photons with free and bound electrons (7). Electrons absorb the quanta of light energy and are raised to higher energy states. The electrons very rapidly give up their energy via collision processes in a time of the order of 10^{-12} seconds or less (8). The absorbed energy is

thus transferred very rapidly into lattice vibrations i.e. heat. The temperature of the metal is raised due to heat absorption. The increase in temperature depends on laser power, interaction time, absorption coefficient, specific heat and thermal diffusivity (8-9).

The following three types of laser-metal interaction have been reported by Ready (10) depending upon the heat absorption.

1. Heating without phase change.
2. Heating with a solid-liquid phase change.
3. Melting with a solid-liquid phase change combined with plasma formation.

This list omits the important use of heating with a solid state change as is important e.g. in steels. The physics of laser interaction is different for each type. The first two types are related to only the surface heat treatment whereas the third type provides a melt pool for powder injection for cladding.

The efficiency of laser process depends on the absorption of light energy by the substrate. Thus, the reflectivity of metals is an important factor affecting the coupling of laser energy to the substrate. The reflectivity of all metals is high in the long infrared wavelength. Almost all metals have a reflectivity greater than 90% for wavelengths greater than 5 μm (11). The machined surfaces show a reflectivity of about 80-95% at the 10.6 μm wavelength of CO_2 (12-13). At wavelengths greater than 5 μm, the reflectivity is dependent on electrical conductivity. Metals with high electrical conductivity have the highest values of infrared reflectivity. When the laser beam falls on a metal substrate, only a portion of the incident laser energy is absorbed by the metal within its electromagnetic skin depth typically 10-100 nm (14-15). However, it has been reported by Oakley and Engel (16-17) that the infrared radiation absorptivity of metal increases very rapidly when their melting points are reached. For example, the absorptivity of Al increases from less than 10% at room temperature to 40-50% at its melting point and to as high as 90% at its vaporization point. This means that small variations in solid reflectivity will have a lesser effect if the laser is incident upon a pool of molten material at the surface. Therefore, surface reflectivity variations will be more

critical during laser heat treatment, when no surface melting occurs, than during laser welding, cladding or alloying (18). Reflectivity also changes as the angle between the laser beam and the surface changes, making it difficult to get heat into surfaces that are not close to normal to the beam (19).

Roessler (20) has described the laser-material interaction in termsof another parameter called coupling coefficient. If a small portion (H) of the incident laser energy (H_o) is absorbed by the metal surface, then the fraction H/H_o can be defined as the coupling coefficient, γ. For smooth and solid surfaces that are sufficiently thick and absorbing so that the incident light is not transmitted completely through them, the coupling coefficient γ would be equal to 1-R, where R is the reflectivity of the metal. Since the reflectivity varies with the wavelength of laser emission and the temperature of the metal, γ will change accordingly. The reflectivity of some materials at room temperature as a function of incident light wavelength is shown in Fig. 2.4. This figure shows that NaCl is transparent throughout the visible range of the spectrum and much of the near ultraviolet and near infrared. This means that for cutting such material we require a laser operating in the far ultraviolet or far infrared wavelength ranges. The absorptivity of iron, however, decreases as we go far away from the ultraviolet region. The reflectivity of aluminium is so high at wavelengths higher than 1 μm that the coupling coefficient is only a few percent. On the other hand, at wavelengths lower than 1 μm only a small decrease in the reflectance of aluminium and iron would result in a large increase in coupling coefficient γ. As the temperature of the surface increases, the reflectivity of almost all metals decreases, making better coupling of the laser beam. However, Roessler (20) has reported that the reflectivity of silicon sharply increases throughout the visible and near infrared region when it melts. The effect of temperature on the coupling coefficient of steel is shown in Fig. 2. 5. At the beginning of the heating, the reflectivity decreases slowly leading to a corresponding increase in γ. But once the melting is stated, the coupling coefficient γ is rapidly increased due to the differences in the optical properties of the liquid and solid phases and also due to non specular reflections by the molten

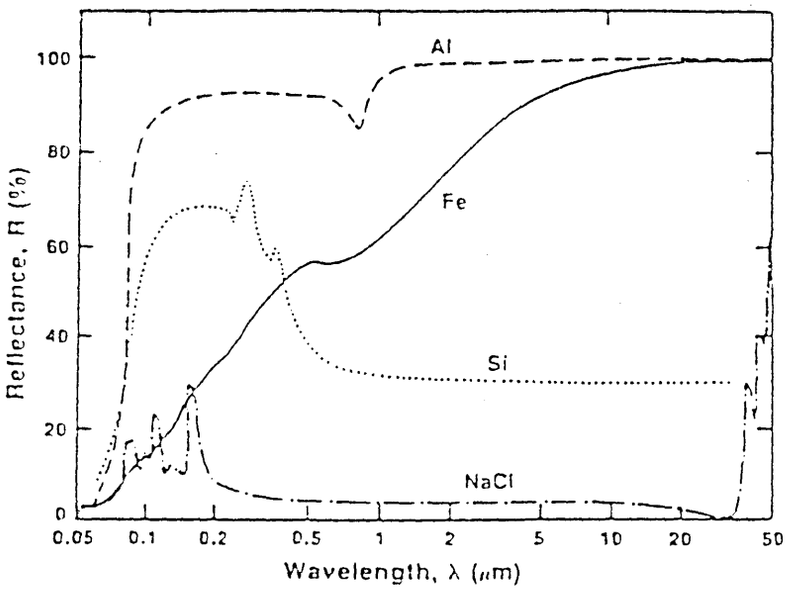

Fig. 2.4 Relationship between reflectivity of various materials and wavelength of laser (Ref. 20).

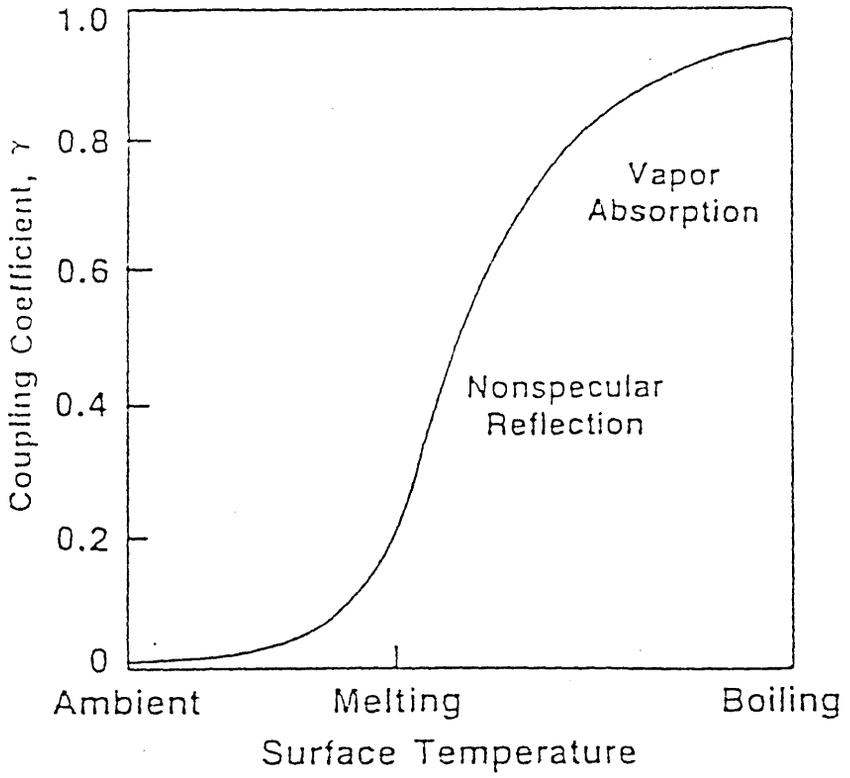

Fig. 2.5 Effect of surface temperature on the coupling coefficient of steel (Ref. 20).

surface. If the heating is continued, vaporization will occur and the absorption by the vaporized material or plasma formed above the surface may sometimes lead to decoupling of the laser beam.

2.2.4.1 Coatings for Decreasing Reflectivity

As earlier mentioned, the reflectivity is not very critical in cladding or alloying where a molten pool is formed soon after the beam is interacted with the metal surface. Sand blasting of the substrate prior to cladding will serve to provide sufficient coupling of the laser beam. However, for the processes that do not involve surface melting, it is advisable to apply some absorptive coating to the surface of the metal to increase laser coupling. Surface coatings provide a uniform and high absorptivity of the far infrared laser energy up to the melting point of the metal irrespective of the surface finish. Engel (17) has reported some of the criteria to consider in selecting the proper coatings which are as follows,

1. Coatings should be absorptive in the far infrared portion of the electromagnetic spectrum. Crystalline materials such as oxides, phosphates and fine ground metal and carbon powders suspended in a binder are good choices.
2. Coatings should have high melting points.
3. Should be good thermal conductors to conduct the heat into the metals.
4. Should be compatible with the base metal having good adherence with the metal surface.
5. Should be easily applicable and controllable in thickness.
6. Coatings should be economical.

Some of the most commonly used absorbant coatings are colloidal graphite, manganese phosphate, zinc phosphate, and black paint. A mixture of sodium and potassium silicate is also known to produce very high absorptivity (21). All these coatings have been found to show a laser beam absorptivity of about 60-90%.

2.3 LASER SURFACE CLADDING

Conventional surface cladding or hardfacing is a process which involves the application of a hard and wear resistant material to the surface of a component by welding, spraying or allied welding processes in order to reduce wear loss of material by abrasion, impact, erosion, galling and cavitation (22). Duley (23) and Belforte (24) have defined laser cladding as a process involving the bonding of an alloy material layer to a metal substrate surface, producing a hard and wear resistant surface by using the scanned laser beam as a heat source. The advantages of laser cladding over the conventional processes, such as fusion welding, have been a subject of debate since it was first applied in 1976. Monson (25) has carried out a comparative study of laser and conventional cladding processes. He has shown the superiority of laser clad deposits in many aspects, e.g. hardness, microstructure and wear. The conventional cladding or hardfacing processes used by Monson (25) are listed below,

1. Tungsten Inert Gas (TIG) welding.
2. Oxyacetylene welding.
3. Plasma Transferred Arc (PTA).
4. Spray Welding (oxyacetylene torch fused).
5. Spray Welding (vacuum furnace fused).
6. Fusion Welding.

The process of laser cladding is the same as that of alloying except that in alloying substantial dilution of the applied material by the melted substrate is necessary while in cladding a minimum dilution is required because it degrades the properties of the clad layer. The laser cladding process can be carried out by using the clad material either as a metal powder, or as a wire, sheet or rod. Nurminen et. al. (26) have reported that cladding using metal powder is especially suitable for many of the brittle cobalt-base hardfacing alloys which are not available in wire or rod form. Although many of the cobalt base alloys are also available these days in the form of wire, rod and electrode

(36), laser cladding using alloy powders is still preferred due to many advantages as reported at the end of this section. Matthews (27) reports that the first patent entitled 'cladding' describes the use of direct wire feed under a scanning beam of a laser. However, the latter researches (27) showed that the shadowing effect of the solid wire does not seem to couple the laser energy as effectively as powder and hence the powder would be the preferred consumable for hardfacing.

Several different methods have been explored for applying the powder to the substrate surface. The most simple and straight forward method was that reported by Steen and Courtney (28). They passed a defocused laser beam of 2 mm diameter over a uniform layer of powder (1-2 mm thick) resting on the surface to be clad. Another method of laser cladding is by placing the powder as a paste on the substrate using some organic binders. However, this method often results in increased porosity or surface roughness due to the ejection of vapours from the binder. Eihalzer et al (29) have reported some of the advantages of the pre-placed powder cladding which include,

1. Reduced distortion.
2. Reduced machining.
3. Reduced alloy material loss.
4. Minimum clad dilution.
5. Production of novel alloys.
6. Adaptability of process to automated techniques.

However, despite these advantages of pre-placed powder cladding method, it is difficult to use this technique for irregularly shaped substrates because of the difficulty of maintaining a uniform layer at the desired position (30).

Rolls Royce Ltd. adapted a blown powder technique for cladding part of high pressure turbine blades of aero engines owing to the difficulty in pre-placing powder on the small pad area (31). Weerasinghe and Steen (32) developed another powder delivery system, where the powder clad material was directly delivered into the laser-substrate interaction

region. Steen (7,12) has reported some of the characteristics of the laser cladding by blown powder method which are listed below;

1. Controlled levels of dilution.
2. Localized heating which reduces the thermal distortion.
3. Controlled shape of clad within certain limits.
4. Thickness between 0.3 and 3.0 mm in one pass.
5. Smooth surface finish (25 μm).
6. Good fusion bonding.
7. Fine quenched microstructures.
8. Non-contact method of application.
9. Easily automated.

Powell and Steen (33) suggested another powder delivery system for cladding where the powder was blown with a spray gun. The powder flow rate was governed by the argon gas flow.

2.3.1 Laser Cladding with Stellite

Before proceeding to a detailed review of the work carried out to date on the cladding with Stellite, a brief introduction will be given to the history and physical, chemical and mechanical properties of Stellite.

Stellite is a trade name of cobalt-base hardfacing alloys produced by Cabot Corporation, Kohomo, Indiana USA. Stellite alloys were first developed in 1900 by Elwood Haynes and are the first cobalt-base alloys of commercial use. The initial Stellite alloys, so called because of their star like lustre, were simple binary cobalt-chromium alloys which were subsequently modified and improved by the addition of tungsten, nickel, molybdenum or both (34). Deloro Stellite (UK) Ltd. also produces cobalt-base Stellite and nickel-base Deloro alloys under their own trade name. More than 20 types of

Stellite alloys are commercially available today. The chemical composition of some of these alloys is given in Table 2.1.

Table 2.1

Nominal Composition of some Stellite Alloys

Alloy	Wt.% Co	Wt.% Cr	Wt.% W	Wt.% C	Wt.% Mo	Wt.% Fe	Wt.% Ni	Wt.% others
Stellite alloy 1	bal.	30	12	2.5	-	-	-	-
Stellite alloy 6*	bal	28	4	1.1	-	-	2.0	-
Stellite alloy S6	bal	28	4	1.1	-	3	2.5	-
Stellite SF6	bal	19	8	0.7	-	-	13	Si=3,B =1.7
Stellite SF20	bal	19	15	1.5	-	-	13	Si=3,B =3
Deloro alloy C	-	17	5	0.1	17	6	bal	-

* Used in present work.

These alloys are essentially based on Co-Cr-C system with high Cr content up to ~ 30 wt.% and with carbon content up to ~ 2.5 wt.%; other carbide forming elements , such as W, are also present. References (34-36) present a complete range of nickel and cobalt-base hardfacing alloys. Stellite and Deloro alloys are available as castings, rods, wires, electrodes and fine powders. Stellite alloys are extensively used in wear related engineering applications for their high strength, wear resistance, corrosion resistance, and high hardness even at elevated temperatures. Some physical and mechanical

properties of some Stellite alloys are listed in Table 2.2; also high temperature hardness data are given Table 2.3.

A number of experiments were carried by Matthews (27) using various cobalt and nickel base Stellite alloys for laser cladding on to a steel substrate. The powder pastes were prepared by mixing the powders with organic binders and water and then spread on to the substrate to a thickness of 1.1 mm. He studied the effect of laser beam frequency and traverse speed on the surface roughness and microstructure of the clads using a 1.2 kW pulsed CO_2 laser at frequencies of 10, 50, and 100 Hz and traverse speeds of 1.7, 3.4, and 5.0 mm/s. A combined effect of fastest traverse speed (5.0 mm/s) and slowest oscillation frequency (10 Hz) resulted in the roughest clad surface.

On the other hand, the smoothest clad surfaces were obtained by fusing the alloys at the slowest speed (1.7 mm/s) with the highest frequency (100 Hz). Also, fine dendritic structures were obtained in alloys fused at relatively higher traverse speeds. Since a pulsed laser was used for these experiments, the frequency of oscillation together with the beam diameter and traverse speed also determine the depth of melting and cooling rate. Matthews (27) has reported a relationship to correlate these parameters as follows,

$$N = 120\, fd/t$$

where,

N = number of times the beam passes through a given point along the centre line on the substrate.

d = beam diameter in inches

f = oscillation frequency Hz

t = traverse speed inches/minute

The optimum parameters found for a smooth surface and fine dendritic structures were, a laser frequency of 75 Hz, traverse speed of 2.5 mm/s and N equals to 30. Although the pre-placed powder clad samples were dried at 150 °C for two hours before laser fusing, a considerable amount of porosity was found in almost all clads.

Table 2.2

Physical and mechanical properties of some Stellite alloys

Alloy	Melting point, °C	Density, g/cm^3	Hardness, Hv	Tensile strength, MN/m^2
Stellite 1	1255-1290	8.69	550-685	618
Stellite 6	1285-1395	8.46	380-425	896
Stellite 12	1280-1315	8.56	480-550	834
Stellite SF6	1085-1150	8.32	425-460	633
Stellite SF20	1010-1215	8.39	740-900	-

Table 2.3

High temperature hardness data of some Stellite alloys

Alloy	Test co -ndition	Hv at 20 °C	Hv at 100 °C	Hv at 200 °C	Hv at 300 °C	Hv at 400 °C	Hv at 500 °C
Stellite 1	As cast	606	573	540	508	485	453
Stellite 6	As cast	410	390	356	345	334	301
Stellite12	As cast	546	456	418	390	380	371
Stellite SF6	Deposit	450	450	439	418	396	365
Stellite SF20	Deposit	850	830	790	738	670	590

Nurminen and Smith (26) studied the effect of physical nature (i.e. loose powder, sintered powder, or fused preform) of pre-placed S 156 Stellite alloy on the laser beam coupling. A series of clad runs was conducted with various combinations of materials condition, laser power and substrate traverse speed. At constant laser power, the absorption efficiency of the powder was found to vary from 80% for loose powder to 57% for sintered powder and 20% for fused preforms. It was also observed that the laser melting efficiency, for loose and sintered powder, was increased with increasing traverse speed. This may be attributed to less heating of the substrate by conduction at higher traverse speeds. These results showed that the maximum energy efficiency for laser hardfacing of Stellite alloy, S 156, would be attained by using loose powder with a combination of high power density and high traverse speed. Argon shielding was preferred over helium for the parameters studied since its density is greater than air, thus giving effective shielding to prevent excessive oxidation. However, for processes which require power densities in excess of 10^8 W/cm^2, helium is found suitable because argon becomes subject to ionization which generates an opaque plasma that absorbs the incident laser radiation and prevents the laser energy from reaching the work piece.

Surface cladding of various Stellite alloys on a mild steel substrate was reported by Metzbower and co-workers (37) using a pneumatic powder feeding system. They used a CW CO_2 laser at a power of 9 kW which was found to provide 10% less power at the interaction point than the recorded power at the calorimeter. Single and triple clad tracks were produced using a 10 mm beam at a constant traverse speed of 8.5 mm/s and powder feed rate of 1.1, 1.7, and 2.5 kg/h. The triple clad track was produced by depositing two passes separately parallel to each other at a distance of 4 mm. The third pass was deposited between the first two. The dilution of single tracks in both single and triple passes was found to be within the range of 1.6-16.4%. However, the dilution for the third pass in the triple pass was reported to be higher (8.4-25.2%) than the other two passes. The higher dilution level in the third pass is contradictory to the previous studies by Weerasinghe (38) which showed a lesser dilution in subsequent passes in the case of

multiple track cladding. The reason for this, as reported by Metzbower, could be the errors in measuring the penetration of the melt into the substrate. The hardness tests showed a maximum of 600 Hv in the centre of the single track with a decreasing tendency towards the heat affected zone. Addition of 25% stainless steel powder to Stellite alloy 158 was found to reduce the hardness of the clad deposit but did not affect the metallurgical bonding.

Giordano and Ramous (39) observed the effect of laser power density and interaction time on the microstructure and hardness of Stellite alloy F and SF6 deposited on an AISI 304 stainless steel substrate. It was claimed that 2-3 mm thick clad deposit can be obtained with a laser having a power density of 0.12 kW/mm^2, a coverage rate of 8.3 mm^2/s with a rectangular beam of 10 x 10 mm. The short laser interaction time of 0.1-1 second for the parameters studied resulted in cooling rates of the order of 50-5000 K/s as compared with 10 K/s for TIG deposited coatings. Consequently, a fine dendritic structure was formed with an average primary and secondary dendrite arm spacing of 70 and 8 μm respectively. The dendrite size of the laser melted coatings has been reported to be increased with increasing energy supplied during melting (36). Higher hardness values were observed in those clads formed at low interaction times resulting in high cooling rates and hence fine dendritic structure as shown in Fig. 2.6.

Li and Mazumder (30) studied the mechanism of pre-placed and pneumatically delivered powder cladding on mild steel and stainless steel plates using Stellite alloy 6 and a nickle-base alloy containing 80% Ni, 12% Cr, 6% Al and 2% Hf. Stellite alloy powder was levelled on a 9 mm thick mild steel and 6 mm thick stainless steel plate before cladding in the 0.5, 1.0, and 1.5 mm thickness layers. The nickel-base alloy was pneumatically delivered from a screw powder dispenser at a rate of 7.8 g/min. A 10 kW CW CO_2 laser was used with a 6 x 6 mm spot size beam at different power densities. The main emphasis in this work was given to the specific energy requirements for producing good clads and its effect on the microstructure and dimensions of the clad formed. Some interesting conclusions made in this study are summarized below.

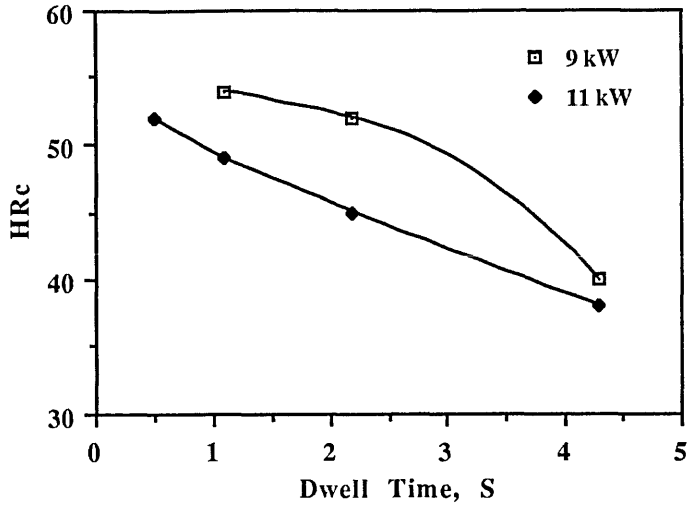

Fig. 2.6 Surface hardness of Stellite coatings formed at different specific energies (Ref. 36).

1. The mechanism of the laser cladding process of pre-placed powder is different from that of pneumatically delivered powder; the powder layer is first melted and then the substrate heated through the melted powder layer whereas in the latter case the substrate and powder are melted almost simultaneously.
2. If the powder layer is relatively thin, the specific energy needed for powder melting is negligible and the heat conduction of the process can be treated as laser beam incident on the substrate surface with an absorptivity of the melted powder layer.
3. The absorptivity of melted Stellite layers to the laser beam was found to be 37%.
4. Powder thickness does not have much influence on the minimum specific energy of the laser cladding process within the experimental parameter range studied, so the calculation for this powder layer can be used to estimate the minimum specific energy for thicker powder layers.

5. In order to obtain higher energy efficiency, a small beam diameter, a substrate with low thermal conductivity, density and specific heat, and a high traverse speed are needed.
6. The cross sectional area of a laser clad bead is equal to that of the melted powder, but its width depends on how wide a region of the substrate is wetted. The higher the laser power and specific energy, the wider and shorter the bead.
7. In order to obtain a fine grain size structure in the clad layer, the specific energy should not be much higher than the minimum required to obtain wetting of the substrate and achieving a bond.

A comparative study of conventional and laser hardfacing process has been reported by Monson and Steen (40) for cladding of Stellite alloy 6 on a mild steel substrate. The process parameters used include a laser beam power of 1.8 kW with 5 mm beam diameter, 12 g/min Stellite feed rate and a substrate traverse speed of 8.33 mm/s. The deposits formed by laser cladding were found superior to those formed by conventional methods when subjected to hardness and abrasive wear tests. The results showed that the clad deposit hardness was inversely related to the mean secondary dendrite arm spacing, as shown in Table 2.4.

Table 2.4

Effect of dendrite arm spacing on the hardness of deposits produced by various techniques (Ref. 40).

Hardfacing process	Mean secondary dendrite arm spacing, μm	Hv, kg/mm^2
Oxyacetylene	15	467
TIG	10	475
PTA	8	475
Laser	3.5	565

Macintyre (31) has discussed some economic aspects of laser processing work carried out at Rolls Royce Ltd. for cladding of cobalt-base hardfacing alloy on Ni-base gas turbine blades for aero engine use. The blades had been hardfaced previously using a manual TIG welding process. The TIG process is reported to utilize high heat input, producing deposits high in dilution by Ni from the substrate, and extended heat affected zones initiating cracking in the blade material. The laser cladding process was found to eliminate these problems by producing deposits free from porosity, fully fused to the blade material, and with a Ni content of only 1-2% higher than the cobalt-base alloy. Macintyre claimed that despite the higher operating cost of the laser, the cost for the laser cladding process was reduced due to reduction in process time from 14 minutes (required for the TIG welding process) to only 75 seconds for laser processing. The consumption of expensive cobalt-base alloy was also estimated to be cut by 50%.

Steen and Courtney (28) used Stellite alloy 12 powder for cladding on to a thin sheet (1.1 mm) of Nimonic 75 (Ni-20Cr-0.4Ti-5Fe) substrate using a 2 kW CO_2 laser at various beam powers. The powder was simply placed on the substrate by levelling off a pile of powder between two metal shim plates. Different thicknesses were obtained without packing down the powder layer so formed. Although, this method of applying powder for cladding can no longer be recommended for industrial use due to the disadvantages described earlier in this section, this work still explains some basic process parameters affecting the quality of clad. It was found that to achieve wetting of the Nimonic 75 substrate by Stellite alloy 12, the average energy per unit area must exceed about 23 J/mm^2 for 0.5 mm initial powder thickness and 27 J/mm^2 for 1.0 mm powder thickness.

Liu et. al. (41) produced overlapping clads of Stellite alloy 6 on types 304 and 410 stainless steel substrates by pre-placing the alloy powder in layers of different thicknesses (0.9 and 1.65 mm). The experiments were done on an AVCO HPL 15 kW laser with a square beam of 12.7 x 12.7 mm. The substrates covered with Stellite alloy powder were scanned under the laser beam of powers 6 kW and 7 kW at speeds of 5.0 mm/s and 4.2

mm/s respectively. The calculations of energy requirements of this process showed that for a specific coating material and thickness a certain level of energy is required to form a coating. For example, for a layer of Stellite alloy 6 powder 0.9 mm thick at a relatively low energy level of 38 J/mm^2, melting of the powder and agglomeration into large molten beads occurred. The energy was not sufficient to cause the molten alloy to flow and wet the substrate. A higher energy level of 52 J/mm^2 was found sufficient for melting the powder and wetting the substrate, but no molten pool flow was occurred; hence rough coated surfaces resulted. However, a smooth coating was formed at an energy level of 64 J/mm^2 when melting, wetting and flow of the molten pool were achieved.The microstructures showed relatively much longer dendrites for thick coatings. This was a result of higher laser energy required for thick coatings inducing more heat in the specimen and hence resulting in comparatively lower solidification rate. The dilution level of the clads was found to be in the range of 6-27% depending on the power density level. However, the dilution level of the second pass in the overlapping clads was reduced to 14%, as compared with 22% of the first pass, due to partial melting of the first. The hardness was found to be inversely related to the dilution level for the parameters studied.

Thermal stress induced cracking and deposit porosity are some of the drawbacks of laser cladding which have not been overcome completely so far. The porosity is however much reduced in comparison with other methods, but is still considered as a problem particularly when the deposit thickness exceeds 1 mm. Powell and Steen (33) have reported a reduction in both porosity and cracking to a lower level by using in-process ultrasonic vibrations of the substrate during laser cladding. The ultrasonic vibrators used for this purpose were standard powerful cleaning transducers (Lead-zirconium-titanate piezo- electric crystals with a frequency of 25 kHz). The experiments were carried out by blowing a nickel-base Deloro Stellite alloy, SF40, into the molten pool produced on a mild steel substrate. The experimental arrangements were the same as for the ordinary cladding process except that the substrate was spring clamped to an aluminium plate

attached to the transducer for vibration. The amplitude of the vibration of the substrate was of the order of 20 μm. They claimed that by using the 'vibro-cladding' technique, the extent of crack and porosity formation was reduced to an average of about 64%.

2.3.2 Laser Cladding/Alloying with Stainless Steel

Stainless steel surface coatings have been successfully produced on mild steel substrates for improved mechanical properties by either alloying or cladding processes. In alloying the elements are added in various proportions to mix with molten substrate to form stainless steel surface of the desired composition, whereas in cladding, stainless steel powder of a selected grade is melted on the mild steel substrate to produce a clad having good fusion bond and low dilution from the substrate. The work on alloying ferrous and non ferrous substrate materials has been reviewed by Draper (14-15,42). A brief review of stainless steel surface formation on mild steel substrate by alloying or cladding is given below; however, the reader can find more information in reference (43).

The work carried out by Weerasinghe and Steen (32, 44) involved the investigation of the effects of various process parameters on the quality of clad layers of 316 L stainless steel on a mild steel substrate using a pneumatic powder delivery system. The clad features investigated include, microstructure, compositional homogeneity, degree of dilution, corrosion resistance, porosity and cracking. The laser used was a 2 kW CW CO_2 machine with the following main processing parameters.

Laser power	= 1.8 kW
Beam diameter	= 2-5 mm
Powder feed rate	= 0.16-0.22 g/s
Substrate traverse speed	= 7-40 mm/s

The conclusions of this study are summarized below.

1. For a given traverse speed and powder flow rate, there is an optimum spot diameter for maximising the clad rate.
2. For a given specific energy, the injected powder mass flow controls the level of dilution.
3. Porosity in clad layers may be caused by one or a combination of the cavities between the tracks, solidification cavities, and gas evolution.
4. Cracking occurs due to tensile solidification stresses which result from differential expansion in the steep thermal gradient associated with laser processing.
5. Very small amounts of dilution (0-5%) were found in the clads together with little macro segregation.
6. Thermal penetration of the order of 1-2 mm was found with a low substrate distortion.
7. The melting efficiency of the process was improved from 6% to around 15% by using a hemispherical laser radiation reflecting device.
8. The corrosion rate (using boiling magnesium chloride solution) of the clads was found to be greater than that of the wrought 316L stainless steel, but a relatively small number of pits were observed on the laser clad layers.

Takeda et. al. (45-46) investigated the in-situ alloy formation of Fe-Cr-Ni steel using three elemental powders either premixed or fed through separate feeders into a common delivery pipe. The experimental results showed that significant lack of homogeneity in composition occurred when the traverse speed was greater than 7.0 mm/s for a 1.7 kw beam power, 7.9 mm beam diameter and 0.293 g/s powder feed rate. However, below 7.0 mm/s traverse speed, the composition was approximately uniform. The compositional inhomogeneity occurred preferentially at the edges of the deposits or at the clad-substrate interface and in deposits formed when the powder was injected at a point late in the melting process. These observations indicate that the time for which the material is molten is probably the most important factor in establishing the level of inhomogeneity. Takeda claimed that at the regions where inhomogeneities were found,

there is likely to be less convective stirring and therefore the mixing mechanism would be confined principally to diffusion processes. For the short melt times encountered in the process (of the order of 0.3 s) the expected diffusion distance would be of the order of a few microns. Therefore without significant convective stirring inhomogeneities would be expected. A comparison of hardness values in the literature and those observed by Takeda for different compositions is given in Table 2.5.

Table 2.5

Comparison of experimental hardness values with those reported in the literature.

Stainless steel Cr : Ni	Structure	Hv observed
13:6	Martensitic	330-380
18:9	austenitic/martensitic /ferritic	322-386
25:20	martensitic/ferritic	158-183

A great deal of work has been carried out by Mazumder and Singh (47-49) and Eiholzer et. al. (29) to develop a cobalt free Fe-Cr-Mn-C alloy for cladding which exhibits superior wear properties as compared with cobalt base alloys such as Stellite alloy 6. The cladding (48) was done on an AISI 1016 steel substrate by blowing a mixture of Cr, Mn, and C powders in the ratio of 10:1:1 through a pneumatically operated powder dispenser. An AVCO HPL 10 kW CW CO_2 laser was used for the cladding with the following process parameters; laser power = 3-5 kW, beam diameter = 2 mm, substrate traverse speed = 6-50 mm/s. A variation in hardness was observed across the laser clad region and substrate. The scattering and fluctuations in hardness were reported to be due to the presence of fine and uniform distributions of the second

phase in the matrix. The degree of uniformity and fine structure depended on the laser processing conditions. The microstructure also was found to influence the wear and friction properties. The best friction and wear properties were achieved at lower laser power and high traverse speed.

Liu and Humphries (50) examined the significance of various parameters (including laser power density, scan speed, beam optics, slurry binder and addition of boron) on the properties of laser cladding of pre-placed 310 stainless steel powder on 310 stainless steel substrate. The powder was applied as slurry using accetate/acetone as binder. The results showed that a laser power level of 4.5 kW with a scanning speed of 1.9 mm/s would provide adequate energy to form a coating. Increasing power levels caused an increase in melt depth. However, the melt depth was found independent of the scan speed except at very low speeds ($\leq$ 2.0 mm/s at 12 kW laser power) where excessive melting of the substrate could occur. A boron addition to 310 stainless steel powder results in a lower melting temperature, enhanced fluidity and wettability of the melt. The process with 310 stainless steel powder showed an average energy loss of 12% and 68.4% with integrated and oscillated laser beams respectively. This energy loss was reduced to only 2.6% and 7.6% for integrated and oscillated laser beams with addition of boron to the stainless powder.

Marsden et. al. (51) have reported an increase in the hardness of 420 stainless steel (12% Cr, 0.15% C) by carbon alloying using graphite coatings. Studies were carried out by using various coating thicknesses, traverse speed and laser power. The trend observed was to increasing microstructural refinement with increasing traverse speed and hence increasing the cooling rate from liquid state. For example, the secondary dendrite arm spacing was found to vary from about 1.8 μm (for tracks produced at 10 mm/s traverse speed indicating a cooling rate of the order of 5×10^3 K/s) to about 0.6 μm (for the traverse speed of 200 mm/s indicating a cooling rate of the order of 6×10^4 K). The maximum hardness values achieved were 600 Hv and 1500 Hv in hypoeutectic and hypereutectic structures.

Chand at. al. (52) used an AISI 1016 steel substrate for the alloying of Ni and Cr. A mixture of 50 wt.% of Ni and Cr was blown into the laser generated molten pool by using a pneumatic powder delivery system. A 10 kW CW CO_2 laser was used at power densities upto 2 x 10^5 W/mm^2 at traverse speeds upto 30 mm/s. Their observations were that stainless steel alloys of uniform chemical composition could possibly be produced this way with very smooth top surfaces (with an average surface roughness, Ra, of 29.3 μm). Surface roughness decreased with increase in substrate speed and beam diameter. An increase in speed from 25 to 50 mm/s decreased the surface roughness average (Ra) by 14.8 μm, while increasing beam diameter from 0.8 to 1.28 mm decreased Ra values by 11.8 μm on the average.

The surface properties of a free machining stainless steel (19 at.% Cr, 1.3 at.% Mo) substrate have been reported (53) to be improved by alloying with Mo and B. The alloying powder was applied as a paint containing about one ml of glue, 2-3 g of powder and diluted with some solvent for easy painting on the substrate. A low power (100-150 W) CW CO_2 laser with a defocused beam of 150-450 μm diameter was used to provide power densities in the range of 1-5 x 10^3 W/mm^2. These power densities were found sufficient for alloying when scanning the substrate at speeds 10-100 mm/s. Microstructural studies showed that the average grain size was related to the interaction time. EDAX analysis showed that the initial laser alloying process resulted in a fairly inhomogeneous structure. However, remelting the alloy region, under the same processing conditions except for high traverse speeds, resulted in structural homogeneity. A maximum hardness of 800 Hv of stainless steel substrate was reported on alloying with 10.2% molybdenum and 9.2% boron.

A different method of applying Ni and Cr powders has been reported by Weston and Wright (54) to produce stainless steel surfaces on an alloy steel substrate. The alloying elements were electroplated on the substrate in various ratios before melting by scanning under a CW CO_2 laser beam. This procedure provided a clean surface coating with uniform thickness. However, the deposit thickness was restricted to only a few microns

with a total melt depth in the range of 30-130 μm. Surfaces produced with melt depths in excess of 100 μm were reported to be very rough. The microstructural analysis showed that the surfaces containing more than 20 wt.% of alloying elements (Cr or Cr/Ni) were not free from cracks. Crack formation was reduced by placing the samples in stainless steel holders which were preheated to 450 °C prior to laser alloying. Preheating at high temperature , however, resulted in low surface quench rates promoting coarse microstructures. Chemically homogeneous surfaces were produced by 60% overlapping laser tracks which ensured double melting and adequate element mixing in the melt pool.

2.3.3 Laser Surface Treatments with other Fe-base Alloys

Laser cladding of low alloy steel powders on a mild steel substrate has not so far been reported in the literature. The reason is that it does not seem advantageous to clad steel powders on steel substrates while the same surface properties could be achieved by other methods (e.g. alloying, melting and transformation hardening), at comparatively low cost. However, low alloy steel powders may be used with other alloying elements or ceramic particles as a carrier powder. The author's present work also includes cladding of an iron-base alloy 4815 with SiC particles to produce a composite on a mild steel substrate for enhanced wear resistance. A brief review of some work done on laser treatments of low alloy steel is included here for comparative study with the author's cladding work on the same type of material.

The most simple method of improving the surface properties of an En8 mild steel substrate reported by Oakley (55) is transformation hardening using a 2 kW CW CO_2 laser. The sample was scanned under laser beams of wide diameter (7.1, 10, 14.1 and 20 mm) at high speeds (upto 200 mm/s). The high cooling rate resulted in martensitic transformation increasing the hardness from 230 Hv of the substrate to 880-1000 Hv for the hardened zones.

The surface properties of some cast irons and pure iron substrates have been reported (56-60) to be improved by either melting or alloying with other alloying elements. All these studies showed that the hardness of the processed layer is increased due to the refinement of the microstructure and to the formation of hard phases (martensite and carbides), which is attributed to high cooling rates and short interaction times associated with laser processing.

2.3.4 Laser Surface Injection of Carbide Particles

Hard and wear resistant surface layers can be produced by injecting carbide particles into laser generated melt pools on different metal substrates, and thus making them an integral part of the coatings. The process of particle injection was first developed in 1979 by Scheafer et. al. (61) where TiC and WC were injected into Ti-6Al-4V and Inconel X-750 substrates using a pneumatic powder delivery system. The laser particle injection process consists of first producing a melt pool on the substrate surface and then injecting the carbide particles so that they do not come in contact with the laser beam before entering the melt pool. The processing conditions are chosen such that the injected particles dissolve as little as possible before the substrate solidifies. This makes the process different from laser cladding in which the clad layer produced is of the same composition as the powder applied and also different from the laser alloying where the added material is deliberately dissolved into the melt. The processing parameters selected by Scheafer et.al. (61) for their study included a laser beam power of 3-10 kW, 3 mm beam diameter and 50-150 mm/s of scan speed. About 100-700 μm thick layers were produced by this method. The volume fraction of the carbide in the layers was found to be upto approximately 50%. The surfaces produced were rough because of partially embedded particles projecting above the matrix material.

This work was extended by Ayers and co-workers (2, 62-63) and several investigations were made injecting WC and TiC particles successfully into other metallic

substrates including 5052 Al, Al-bronze and 304 stainless steel substrates. The experiments were carried out using a CW CO_2 laser at power levels of 3-16 kW and beam diameters of 1.5-3.5 mm. The processing was done in an evacuated chamber at a pressure of about 100 Pa. The samples were translated under the laser beam at speeds ranging from about 25 to 150 mm/s. The carbide powder was injected into the melt pool at feed rates ranging from 0.1-1.0 cm^3/s. The preliminary studies of particle injection showed that above the laser power necessary to achieve surface melting, the actual volume of carbide incorporated into a melt pass is nearly independent of laser power. However, at a given feed rate, the volume fraction of carbide in a melt pass decreases with increasing laser power. A maximum volume fraction of about 45% has been reported when injecting TiC particles into 304 stainless steel at 6 kW laser power. The hardness of the matrix on the upper surface of the clad was found to be increased with increased carbide particle dissolution.

The solubility of carbide varies from metal to metal; thus, for example, no solution of TiC was found to occur in a 5052 Al alloy with, therefore, no hardening of the matrix. On the other hand, extensive dissolution of TiC occurs in titanium and iron-base alloys hence increasing the matrix hardness as given in Table 2.6.

Table 2.6

Hardness of various TiC injected matrices.

Alloy	Hv, as received	Hv, HAZ	Hv, carbide injected
Ti-6Al-4V	345	405	460
304 Stainless steel	152	196	219
4340 Tool steel	430	950	1061
5052 Al	78	70	71
Al-bronze	225	239	287

The composite layers formed showed the presence of porosity and cracking of the carbide particles. The porosity was attributed to the entrapment of the carrier gas in the melt and was controlled by minimizing the impingement of carrier gas on the surface. Individual carbide particles can be cracked by thermal stressing which is reduced by screening out the large particles.

Montez et. al. (64) have reported improvement in surface properties of 42CD4 steel (0.42% C, 1.0% Cr-Mo) by injecting WC particles. Their study showed that the coatings with large proportions of carbide particles had more cracks and porosity. The surface hardness of the WC injected composite matrix was increased to 800-1000 Hv as compared with 300 Hv for the substrate. The microstructure showed fine dendrites with large proportions of undissolved carbides near the upper surface of the processed zone, with a cellular structure at the bottom of the zone. They have also reported that at higher velocities the entire matrix showed a cellular microstructure and a smaller amount of undissolved carbides, showing that the cooling rate decreases with an increase in the scanning velocity. However, their statement is contradictory to all the previous work including the author's work on the subject which showed lower cooling rates and higher particle dissolutions at lower scanning speed.

Lewis et. al. (65) used arc melted buttons of Fe-37 vol.% TiC composite for laser glazing using a 3 kW CW CO_2 laser. A slow homogenization pass was first made to dissolve large carbide particles in the as-cast buttons. This treatment was followed by a pass at a very high scan speed of 500 mm/s which generated a shallow melt zone of 130 μm depth. The microstructure obtained was an equiaxed cellular matrix with embedded fine TiC particles. The dissolution of carbide particles was low due to limited solubility of Ti/TiC in iron ($\leq$ 0.5%). The hardness was increased from 550 KHN of the as-received buttons to 1100-1300 KHN for the matrix of the processed surface.

Ayers et. al. (66) studied the effect of TiC particle injection, into Ti-6Al-4V substrate, on the coefficient of friction of the composite surface formed. The samples were produced by overlapping 10 melt passes of about 2 mm width advancing about 1.2 mm

after each melt pass. Sliding wear tests on TiC-6Al-4V substrate and carbide particle injected Ti-6Al-4V/TiC composite showed a decrease in the coefficient of friction from 0.4 for the former to 0.16-0.29 for the latter.

Tucker and co-workers (67) used mixtures of carbide/silicide (TiC, WC, $MoSi_2$) and Stellite alloy 6 for cladding on AISI 1018 steel substrate to improve wear properties. The conditions leading to the best clad properties include laser power 2-3 kW, powder feed rate 50-100 mm^3/s, sample traverse speed 20-40 mm/s, laser beam diameter 2.3 mm and helium shield-carrier gas 1.5 m^3/h. The tendency for dissolution of the carbide particles in the melt layer was higher with WC than with TiC. Furthermore, the dissolved WC did not reprecipitate on cooling as did the TiC. As a result the dissolved W and C components remained in solid solution reducing the ductility of the binder phase and hence increasing cracking tendency. The embrittlement of the matrix was reduced by replacing Stellite with pure cobalt but it generated significant internal porosity. Cladding with 50 vol.% mixture of $MoSi_2$ and Stellite alloy 6 showed complete $MoSi_2$ particle dissolution in the laser generated melt pool. This dissolution produced a highly alloyed melt which formed a brittle structure on cooling. The clad layer was severely cracked and unsuitable for wear evaluation. Injection of $MoSi_2$ particles into a 304 stainless steel substrate also showed the same type of behaviour on solidification due to complete dissolution of $MoSi_2$ in the steel matrix.

Cooper and Ayers (68) studied the effect of different parameters, including melt width and powder feed rate, on the cracking tendency of the composites produced by injecting TiC and WC into laser melted Inconel 650 substrate. The results obtained were similar to previous studies (62-64) with other substrates, e.g. Inconel X 750, AISI 1018 steel, except for a few new observations about the effect of particle size. The results showed that for the medium (45-75 μm) and coarse (75-150 μm) WC, the crack density diminishes with increasing powder feed rate. For the medium (45-75 μm) TiC particles, the crack density increases initially with increasing feed rates followed by a slight decrease at higher powder feed rates. At medium to high powder feed rates (20-50

mm^3/s) a substantially larger degree of cracking occurs in layers treated with fine WC and medium TiC, compared with those treated with medium and coarse WC particles.

Following the first development of the laser particle injection process in 1979 (61), most of the work has dealt with the injection of TiC and WC into various substrates. Although hard and wear resistant composite surfaces can be produced by the injection of SiC particles at relatively low cost and comparable properties with those of TiC and WC injected composites, unfortunately there are few publications on this subject except for those reported in this thesis and in conference proceedings (69-72). The work on laser injection of SiC particle was started by the author of the thesis in 1986 producing composites by either injecting SiC into mild steel or cladding a mixture of SiC with other alloys including Stellite alloy 6, SMO 254 stainless steel, and Alloy 4815 on mild steel substrate. Subsequently Abboud and West (73) studied the feasibility of SiC particle injection into commercial purity titanium and Ti-6Al-4V alloy substrates. Their preliminary studies showed that composites of SiC and titanium alloys can be produced with a low dissolution of SiC particles in the matrix. The microhardness of both composite matrices was increased to 650 Hv as compared with values of 210 Hv and 355 Hv for CP Ti and Ti-6Al-4V respectively, due particularly to the formation of TiC.

2.3.4.1 Properties of SiC

Since the work presented in this thesis is mainly concerned with the formation of composites of SiC with other alloys, it is appropriate to briefly review the physical, chemical, mechanical and thermal properties of SiC.

Silicon carbide is a man-made mineral of high hardness and wear resistance. It is the ideal abrasive for grinding materials of low tensile strength. Its thermal properties along with high hardness make it an excellent medium for use in manufacture of refractory products, turbine blades, ceramic seals etc. (74). Silicon carbide is manufactured by

melting together silica and ground petroleum coke in an electric arc furnace at 2400 °C for 36 hours (75).

Some of the physical, chemical, mechanical and thermal properties of SiC are listed below (76), whereas the Si-C binary phase diagram is shown in Fig. 2.7 (78). The Si-C phase diagram shows that SiC decomposes on heating by a peritectic reaction at ~ 2545 °C: $SiC \rightleftharpoons Liquid + C$.

Colour	: Black
Melting Point	: Decomposes at 2773 K
Density	: 3.2 g/cm^3
Chemical Composition	: 70 wt.% Si and 30 wt.% C
Spectral Emissivity	: 0.77 at 1823 K.
Thermal Conductivity	: 2.1 W/m K at 1273 K.
Thermal Expansion	: 2.17×10^{-8}/K at 297-2773 K.
Hardness	: 3000-3500 Hv.
Structure	: (i) Cubic (β) at low temperature, a = 4.349 Å (ii) hexagonal (α) at high temperature, a = 3.073 Å, c = 15.070 Å.
Bending strength	: 7.7×10^6 kg/m^2 at 1673 and 1.05×10^7 kg/m^2 at 2073 K.
Specific heat	: 1.465 kJ/kg K at 1823 K.

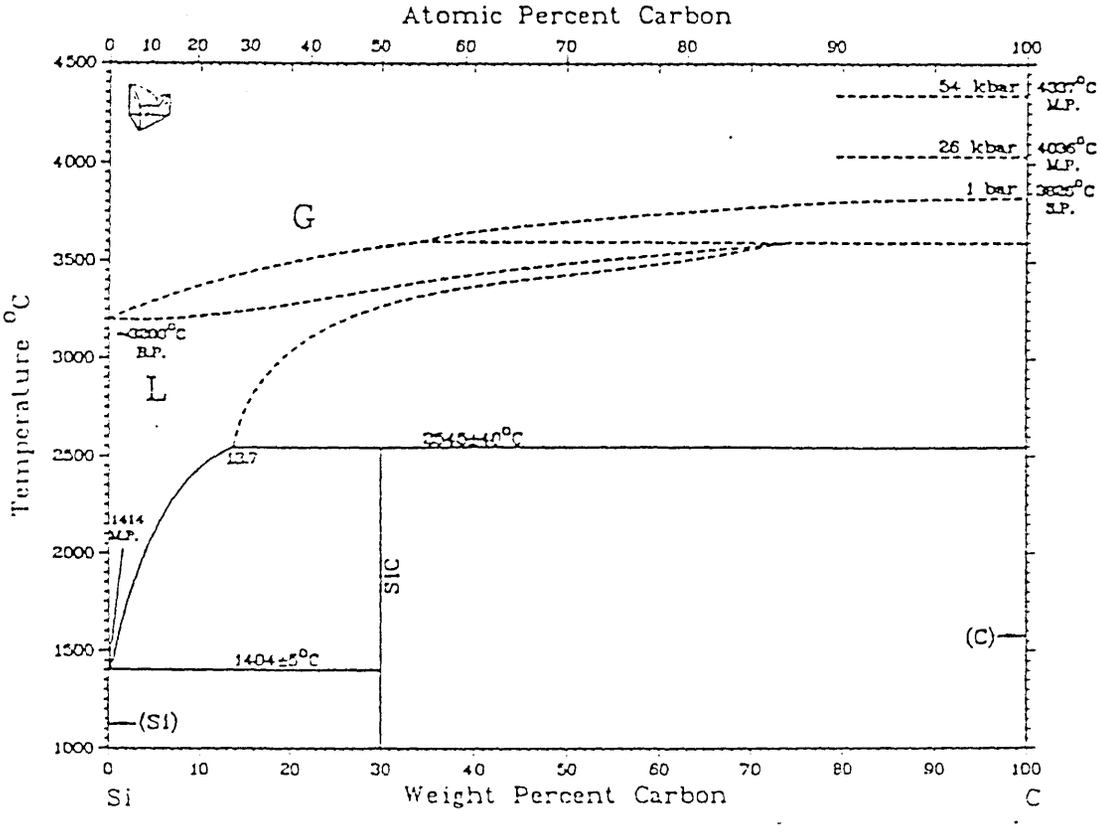

Fig. 2.7 Si-C phase diagram (Ref. 77).

CHAPTER 3

EXPERIMENTAL PROCEDURE

3.1 INTRODUCTION

This chapter describes the materials, apparatus and process involved in the production of high quality clad deposits of different alloys and composites. The experimental procedure will be reported in two parts i.e. as pre- and post-cladding treatments.

3.2 PRE-CLADDING TREATMENTS

3.2.1 Materials Used

The material used for the present work was En 3b mild steel with the following nominal composition (wt.%); C = 0.25, Si = 0.35, Mn = 1.0, Fe = balance.

Four different types of powders were used for producing alloy and composite clads. These powders include SiC, 254 SMO stainless steel, Stellite alloy 6, and an iron base alloy 4815. The SiC powder was of irregular shape containing 70 wt.% Si and 30 wt.% C. Three different size ranges (i.e. 50-150, 250-450, 250-750 μm) of SiC were used whereas for the other powders used throughout this work only one particle size range was used for each type as follows, stainless steel (40-200 μm), Stellite alloy 6 (50-200 μm), alloy 4815 (40-250 μm). The screen analysis of particle size range of SiC is shown in Fig. 3.1 and for the rest of the powders in Fig. 3.2. The nominal composition of Stellite alloy 6, Stainless steel and alloy 4815 is given in Table 3.1.

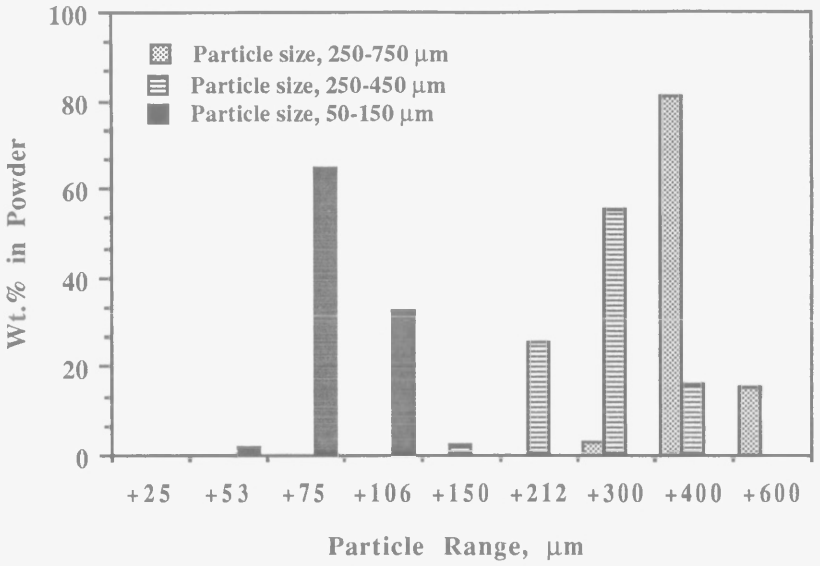

Fig. 3.1 Screen analysis of various SiC powders.

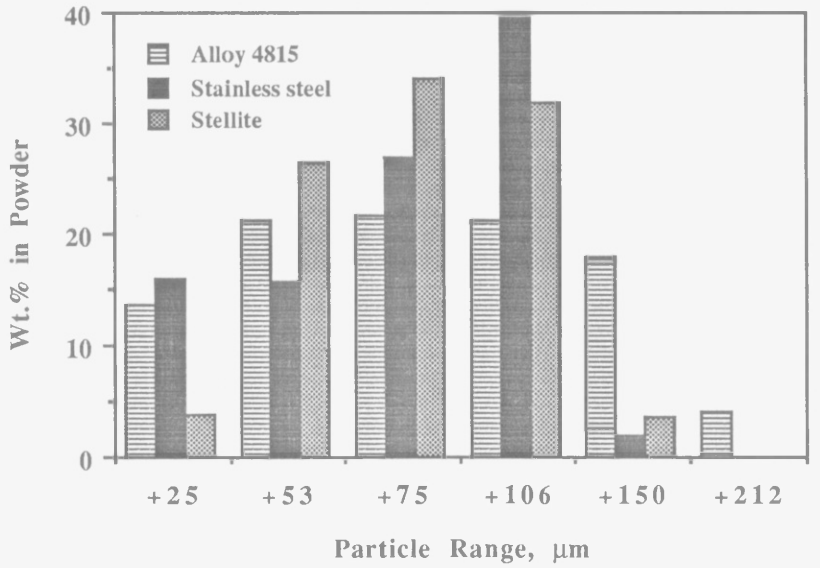

Fig. 3.2 Screen analysis of different powders.

Table 3.1

Nominal composition of alloy powders.

Alloy	Wt.% C	Wt.% Fe	Wt.% Co	Wt.% Cr	Wt.% Mn	Wt.% Si	Wt.% Mo	Wt.% W	Wt.% Ni
Stellite alloy 6	1.1	bal.	60.0	28.0	-	-	-	4.0	2.0
Alloy 4815	0.15	bal.	-	-	0.5	0.27	0.25	-	3.5
Stainle-ss steel	0.02	bal.	-	20.0	-	-	6.2	-	18.0

3.2.2 Laser Used

A 2 kW fast axial flow CW CO_2 laser, developed by Control Laser, was used as a heat source for cladding during the present work. The general lay-out of this laser is shown in Fig. 3.3. The laser assembly can be divided into the following five different parts based on their functions (78);

1. Optical System
2. Power Supply
3. Water Cooling System
4. Gas Flows
5. Laser Beam Manipulations

The machine carries four electric discharge tubes connected optically in series to produce one long tube which is then folded in the middle by means of two mirrors. These discharge tubes are supported on a rigid 4m long laser bench making a total cavity of 8 metres. The four cathodes of the tube are earthed to a central cathode box. This cathode box also acts as gas manifold through which the laser gas from the four tubes can

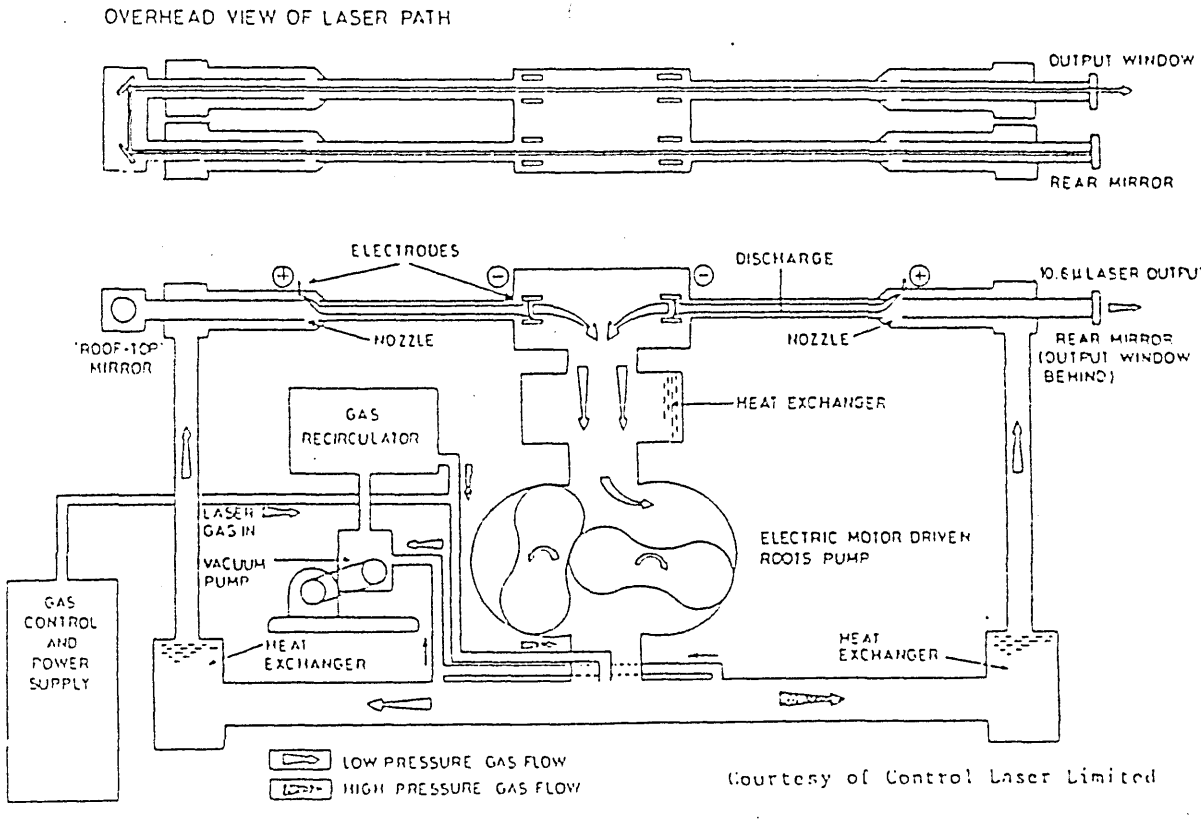

Fig. 3.3 Lay out of a 2 kW CO_2 laser.

be drawn to a heat exchanger provided to extract the heat produced by the discharge current.

A mixture of CO_2, He and N_2 (0.8 : 1 : 7) is introduced into the discharge tubes by means of a blower at a pressure of 30-35 tor (mm Hg). A combination of low current (140 mA maximum) and high voltage (30 kV) electrical discharge results in excitation of the gas mixture through the glass tube to produce a 10.6 μm laser radiation. This radiation is strongly absorbed by many materials; so it is necessary to use specialized unsusceptible material for CO_2. The out put window used in a 2 kW CO_2 Control laser is made of water cooled GaAs which has a reflectivity of 35% at 10.6 μm wavelength.

The laser head consists of a lens assembly. The laser beam passed through the lens assembly is focussed on to the work-piece at a desired distance which depends on the focal length of the lens. A KCl lens of 150 mm focal length was used for this purpose.

3.2.2.1 Laser Power Output Setting

This laser can provide a maximum power of 2 kW. When the laser beam is not in use, it is directed to the cone of a water-cooled calorimeter which acts as an output power measuring device and also power dump. A metered flow of water cools the calorimeter cone and the difference between the water inlet and outlet temperature is measured by different thermocouples whose output is directly displayed on a digital meter as watts of laser power. The laser output power depends on many parameters including gas mixture composition, gas flow rate, discharge current, gas pressure, and tube diameter (5). Since all parameters except discharge current were kept constant, the laser output was found to be a function of discharge current. The discharge current determines the rate at which CO_2 molecules in the laser tube are pumped by direct excitation and by collision with excited N_2 molecules. The output laser power would therefore be expected to be increased by increasing the discharge current. However, a saturation point is reached

where the heating effect at the tube axis becomes substantial so that the gain decreases, resulting in a decrease in power.

3.2.2.2 Laser Beam Alignment

The alignment of the laser beam, emitted from the output window, with the laser head is an important factor for obtaining maximum laser power at the work piece. The misalignment of the beam at any point in the beam path would result in edge truncation, causing a decrease in output power. The clipping of the beam with the nozzle was found to be causing an excessive heat loss and nozzle melting as well.

A visible red colour HeNe laser was used for the alignment of the main laser beam with working laser head to obtain a focussed beam through the nozzle without any clipping. The laser was fired, for a very short time, on a fire brick placed in the beam path, thus making a spot on the brick without entering the laser head. The HeNe laser beam, following the same path as main laser beam, was then aligned with the spot marked on the fire brick by the CO_2 laser. This method was repeated under the laser head to align the beam with the nozzle aperture.

3.2.2.3 Beam Diameter Setting

The laser beam emitted from the output window was about 22 mm in diameter. The beam is focussed on a point at the work piece to achieve maximum heat energy by placing a converging lens in its path. The distance of the focal point depends on the focal length of the lens used.

A focussed beam was obtained just at the bottom of the nozzle by placing the spacers below the lens holder to make the distance between the lens and bottom of nozzle equal to the focal length of the lens. A KCl lens of 150 mm focal length and 38 mm in diameter was used for all experiments reported in this thesis. The focal position was then checked

by changing the distance between the nozzle and the work piece. A range of distance, which is called depth of focus and increases with focal length of the lens, was obtained over which the laser produced a blue flash with argon gas. The centre of this was considered as the focal point.

An overfocussed beam (3-5 mm) was used for cladding, during the present work, to prevent excessive melting of the substrate which results with a focussed beam. The working distances for the beam diameter used were calculated by using the following relationship (79),

Working Distance = (D x F)/22

where, D = Required beam diameter in mm

F = Focal length of the lens

22 = Original beam diameter in mm

The working distance is about 34 mm for a 5 mm beam diameter with a lens of 150 mm focal length. This working distance was used for most of the experiments unless stated otherwise.

3.2.2.4 Beam Mode Structure

The beam mode structure is the most important process parameter in determining the heat distribution of the laser beam output obtained on the work piece. The mode structure depends on the optical cavity design and the lasing medium used. Two types of modes exist in laser cavities. The modes parallel and perpendicular to the optical axis of the laser cavity are called longitudinal and transverse modes respectively. The transverse mode of a laser is more important and determines the beam propagation and pattern marked on the work piece. Transverse modes are denoted by TEM_{mn}, where m and n are integers referring to the number of zeroes of intensity in the x and y directions respectively. Fig. 3.4 shows examples of intensity profiles of some low order modes. The CO_2 lasers generally operate in two modes. The most commonly used mode is the uniphase TEM_{00}

mode. This structure mode produces a Gaussian intensity distribution and hence is generally referred to as a ' Gaussian beam' mode. The Gaussian beams contain more energy which can be focussed to a small size and, therefore, are preferred for cutting and welding applications. The other beam mode is denoted by TEM_{01}* and is referred to as 'doughnut' mode. This beam mode produces more uniformly distributed heat energy and is generally used for surface treatment applications including hardening, alloying and cladding.

The laser used throughout this work produces a mixed Gaussian and doughnut mode. A beam burn print was produced on a piece of perpex before and after the experiments to ensure the stability of the mode structure. A laser beam analyser (LBA) was also used sometimes to assist with in-process monitoring of the mode structure.

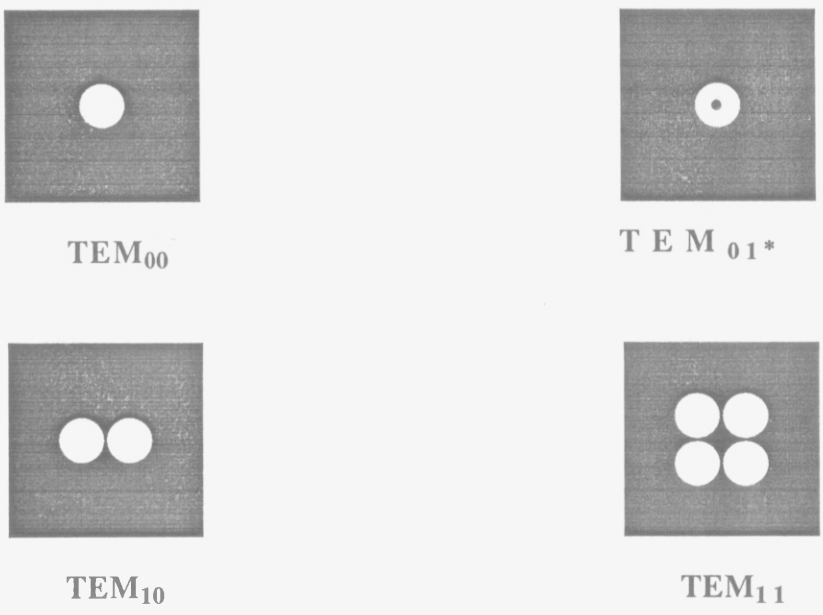

Fig. 3.4 Some examples of low order beam modes

3.2.3 Powder Feeding System

A pneumatic powder delivery system was used for the present work. The design of the powder feeders used was the same as the that developed by Weerasinghe (38). This powder feeder utilizes a standard twist drill as the feeding screw. The rotation of the drill transports the powder away from the shank through flutes. The powder flow increases with screw speed until a point where it becomes non-linear due to many factors as reported by Weerasinghe (38). The screw is driven by coupling it with a variable speed motor having a control for screw rotation speed over a wide range. A smooth and regular flow of powder was achieved by introducing argon as the carrier gas ahead of the powder entry point. The accumulation of the powder in the delivery tube may cause cyclic flow of powder which can be avoided by making all surfaces inclined at some angle.

The argon gas flow was kept to a minimum necessary required for effective conveying of powder. The high gas flow increases the particle velocity which reduces the deposition rate due to many factors including unfavorable particle distribution in the particle jet, increased convective cooling effects, and particle rebounce from the surfaces (25). The minimum effective gas flow used for powders of different compositions and particle sizes is given in Table 3.2.

For the cladding of composites of SiC particles with other alloys, two different powder feeders were used for SiC and other alloys, for providing separate control over the feed rate of both powders. The two powders were conveyed through two separate copper tubes (3 mm internal diameter) to a Y-junction, where they were mixed and blown into the laser generated melt pool. Single alloys and alloy mixtures (pre-mixed with SiC) were blown into the melt pool by using the same type of powder feeder. The powder was directed towards the melt pool using a copper tube positioned at an angle of about 40 degrees and at an approximate distance of 15 mm from the melt pool. The angle and distance of feeding tube was chosen so as to provide a minimum rebound of particles from the surface. The cladding set-up is shown in Fig. 3.5.

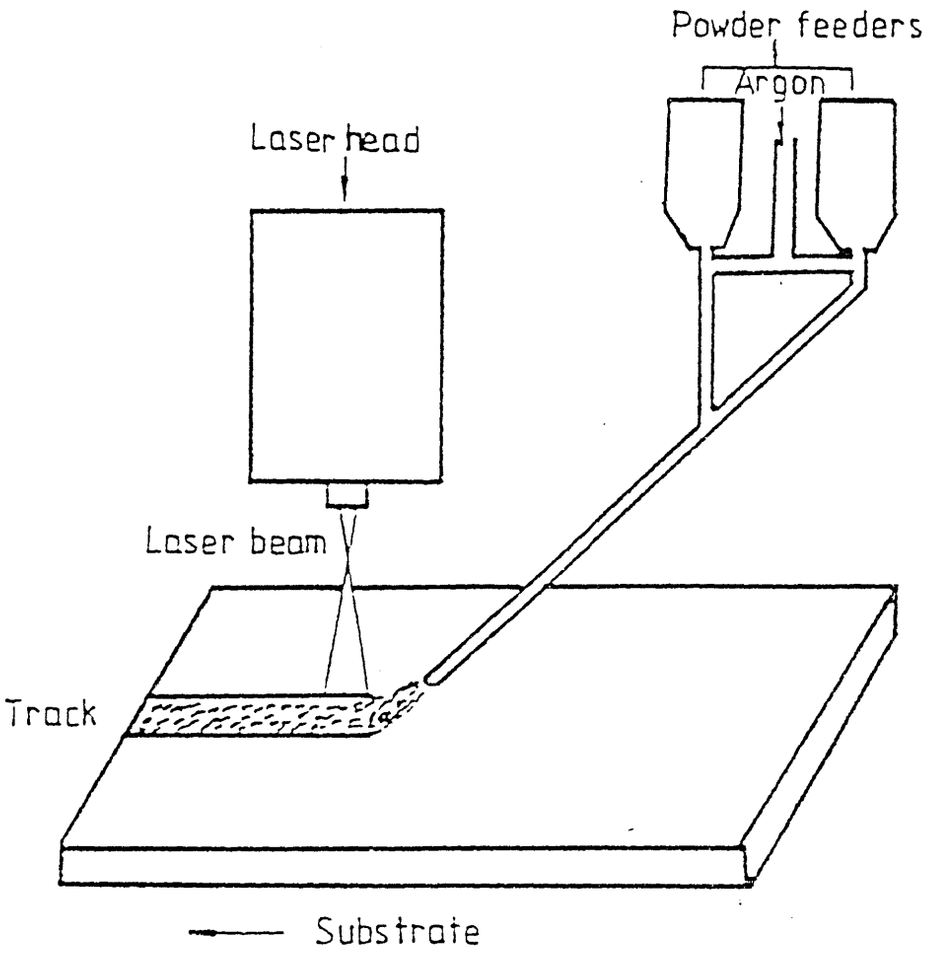

Fig. 3.5 Experimental arrangements for laser cladding.

Table 3.2

Carrier gas (argon) flows used for various powders

Nos.	Powder	Gas flow, lit/min
1.	Stellite	1.7
2.	Stainless steel	1.7
3.	Alloy 4815	1.7
4.	Stellite + SiC	2.5-2.9
5.	Stainless steel + SiC	2.9
6.	Alloy 4815 + SiC	2.5
7.	SiC	2.1-2.9

3.2.4 Sample Preparation

A mild steel substrate in the form of 120 x 60 x 10 mm flat plates was used throughout this work unless stated otherwise. All sample surfaces were sand blasted prior to cladding to minimise the heat loss by reflection of the incident laser beam, and then washed thoroughly with alcohol to remove any dust particles. The samples were first held in position on the working table by using double sided adhesive tape. Samples were then fixed with help of clamps on both ends to resist thermal distortion and keep them flat during cladding.

3.2.5 Laser Working Station

The laser working station is comprised of a laser head and a working table. The standard laser head is shown in Fig. 3.6. It consists of a lens holder assembly and a 15

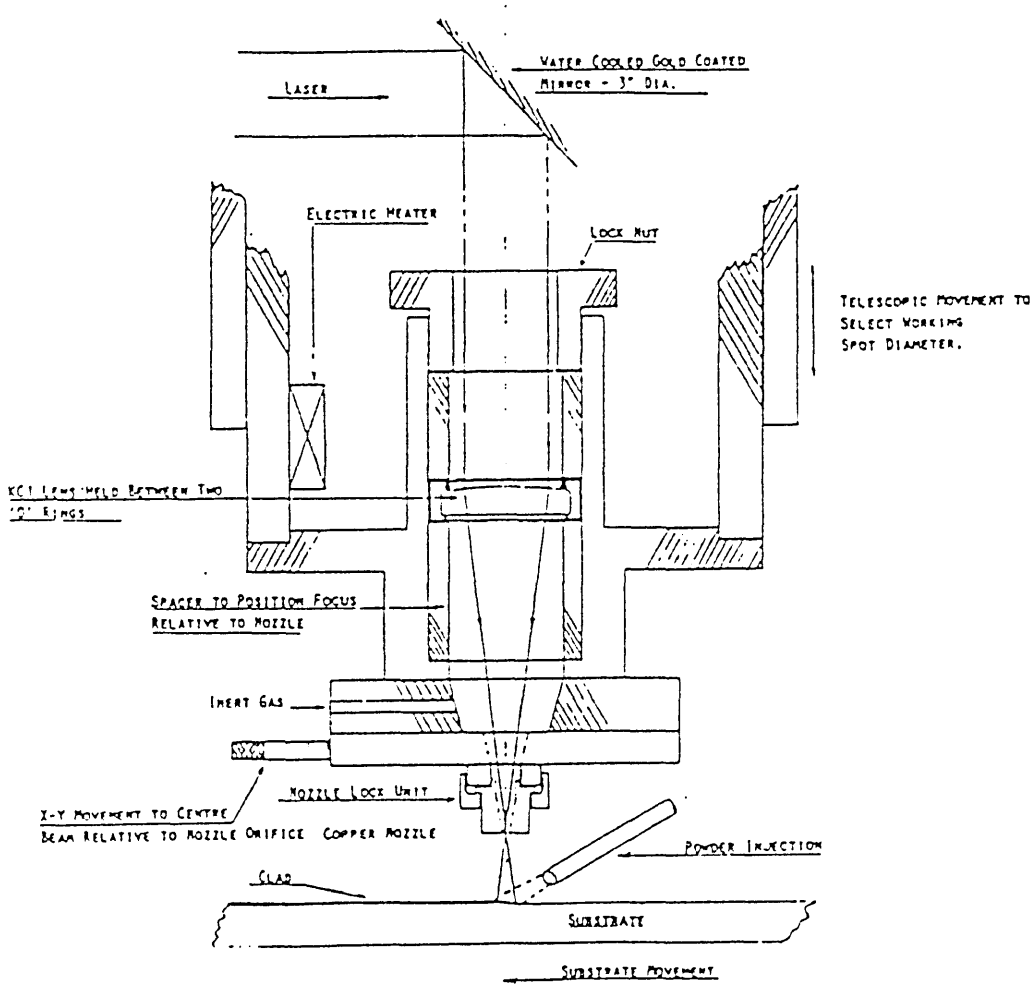

Fig. 3.6 Schematic diagram of laser head (Ref. 38).

mm high copper nozzle with 1.5 mm aperture. Argon was introduced into the nozzle at a flow rate of about 1.2 lit/min to prevent smoke or particle entry into the lens chamber without disturbing the powder flow into the molten pool. The working table is a moveable X-Y table capable of moving hydraulically in the X-direction at a range of speeds and manually in the Y-direction . This table is provided with a digital timer to measure the speed of the working table. The sample is fixed on the table and can be traversed under the laser beam at a range of speeds. The laser was first fired on the substrate to make a spot. The powder was then aligned with the beam print on the substrate by adjusting the position of the powder delivery tube.

3.2.6 Processing Parameters

The various processing parameters which were used, either kept constant or varied, throughout this work are given below,

1. Laser power : 1.85-2.0 kW
2. Beam diameter : 3 - 5 mm
3. Substrate traverse speed : 2.5 - 20.0 mm/s
4. Powder feed rate
   - (i) SiC : 3.5 - 59.4 g/min
   - (ii) Stellite : 11.4 -60.0 g/min
   - (iii) Stainless steel : 11.2 and 37.0 g/min
   - (iv) Alloy 4815 : 13.0 - 27.5 g/min
   - (v) 10% SiC + Stellite : 36.0 g/min (for overlapping clads)
   - (vi) 20% SiC + Stellite : 10.0 g/min (for overlapping clads)
   - (vii) 20% SiC + Stainless steel : 9.0 g/min (for overlapping clads)
   - (viii) 10% SiC + Alloy 4815 : 45.0 g/min (for overlapping clads)
   - (ix) 20% SiC + Alloy 4815 : 13.0 g/min (for overlapping clads)

3.3 POST CLADDING TREATMENTS

Samples covered with single and overlapping clad tracks of different alloys and composites were prepared for different types of tests. These include microstructure, microhardness, compositional analysis, wear resistance tests, x-ray diffraction and surface topography.

3.3.1 Microscopy

The microstructure and compositional analysis of clads produced using different powder flow rates and traverse speeds were studied systematically by optical microscopy, and by scanning and transmission electron microscopy to assess the quality of the clads.

3.3.1.1 Optical microscopy

Low magnification (X 50 -100) optical micrographs were obtained to determine the dimensions of the clads and melted substrate. High magnification optical microscopy was used to observe the distribution of different phases. A Nikon optical microscope was used for this purpose. The samples for optical and scanning electron microscopy were prepared in the following sequence;

1. Small samples were cut from the transverse sections of different clad tracks using a laboratory cut-off wheel.
2. Samples were mounted in cold setting resin making a size 30 mm in height and 30 mm in diameter suitable for loading into the electron microscope.
3. Mechanically ground using SiC abrasive papers starting from 120 and going upto 1200 in steps.
4. Polished in four stages of 14, 6, 3, and 1 μm on a polishing wheel using diamond spray.

5. Etching; all samples were etched firstly with 2% nital for few seconds to reveal the microstructure of the HAZ (heat affected zone) and substrate without affecting the clads. This solution was also found effective for the etching of alloy 4815 and its composite with SiC.
6. Stainless steel and stainless steel + SiC composite clads were etched using Vilella's reagent (picric acid = 1 g, nitric acid = 5.0 ml, methyl alcohol = 100 ml). The normal time required for etching was 0.5-1.0 minute. This solution completely darkened the substrate.
7. Electrolytic etching was used for Stellite and Stellite + SiC clads with a solution containing 6 g of chromic acid, 10 ml of nitric acid and 90 ml of distilled water. The normal etching time taken by this solution was about 10 seconds at 0.6 A current with a Ni cathode. By using this method only the clad microstructure was revealed without any further etching of the HAZ or substrate.

3.3.1.2 Scanning Electron Microscopy

Electron microscopy was used to study the microstructures of the clads at magnifications upto 5000 and for EDAX (energy dispersed analysis of x-rays) and EPMA (electron probe microanalysis) of some selected clads.

Etched samples were first coated with carbon and then covered with silver dag to enhance electrical contact and prevent charging.

Jeol electron microscopes (models T220 and T200) were used for obtaining secondary image micrographs. Quantitative compositional analysis of the clads was done on a JSM 35 electron microscope. Energy dispersive analysis (EDAX) of wide clad areas (150 x 150 μm) and micro probe analysis (EPMA) of some selected spots in the clad area were done on this microscope. The x-ray detector attached to the microscope is fitted with a thin beryllium window to protect it against any foreign particles. X-rays produced by the elements having atomic number less than 9 cannot enter the detector due

to their insufficient energy to penetrate the thin window. The carbon content in the clad could not be analysed due to its low atomic weight. However, the balance to a 100% composition was treated as the amount of carbon present. An experimental error of $\pm$ 1% was taken as acceptable for EDAX analysis.

3.3.1.3 Transmission Electron Microscopy

A few selected clads, from which thin foils could be prepared, were examined under a Phillips 'EM 301' transmission electron microscope (TEM). The microstructure of some slightly thicker samples which could not be seen using 'EM 301' microscopy were examined using a high voltage transmission electron microscope. Thin foils suitable for the examination under these microscopes were prepared in the following sequence;

1. A 10 x 30 x 3 mm slice was cut from each selected overlapping clad track by using a laboratory cut off wheel under a stream of coolant to avoid heating.
2. The specimens were then ground down to 100 μm size on SiC papers from the under side of the clad.
3. These specimens were then used to cut 3 mm diameter discs by using a Metals Research 'Servomet' spark machine.
4. These discs were subjected to electrochemical thinning in a Struers 'Tinupol' machine.

3.3.1.3.1 Electrochemical Thinning

A Struer 'Tinupol' electrochemical thinning machine consists of a twin jet device which is designed to detect the formation of a hole in the disc. The sample holding chamber has a shining light on one side of the disc and a photo-cell on the other dark side of the disc. When the hole is formed, light is passed through it and is fallen on the photo-

cell, a buzzer sounds indicating the initiation of hole. Thinning of all samples was done at potential of 15 V at -20 °C.

3.3.2. Microhardness Testing

Microhardness tests of the clads were performed on the same samples prepared for the optical and electron microscopy. A Leitz miniload 2 diamond pyramid microhardness tester was used for this purpose. Preliminary studies showed that the hardness measured on the matrix region of all the alloy and composite clads varied significantly with load in the range of 50-500 g (Fig. 3.7): a value of 300 g was, therefore, selected for results presented in this thesis to obtain comparative values. Microhardness tests were carried out using a 300 g load. At least three readings on each sample were taken to ensure the reproducibility. The diameter of the indentation produced on the sample was measured and the corresponding hardness value was read from the table available with this instrument. The indentation produced on SiC particles was very small and its corresponding hardness value could not be found in the given table, and was calculated from the following relation (80),

$Hv = (189 \times 10^3) F/d$

where, F = force applied in N, d = diameter of diagonal produced, Hv = Vicker's hardness number

3.3.3. Surface Roughness

Comparative studies of worn samples were made by measuring their surface roughness on a 'Talysurf 10' surface texture measuring instrument. A metered cut off length of .8 mm, with a 2.5 µm radius diamond stylus, was used to generate average surface roughness values (Ra). A mean of the five roughness values measured on the same length was taken as the average roughness value.

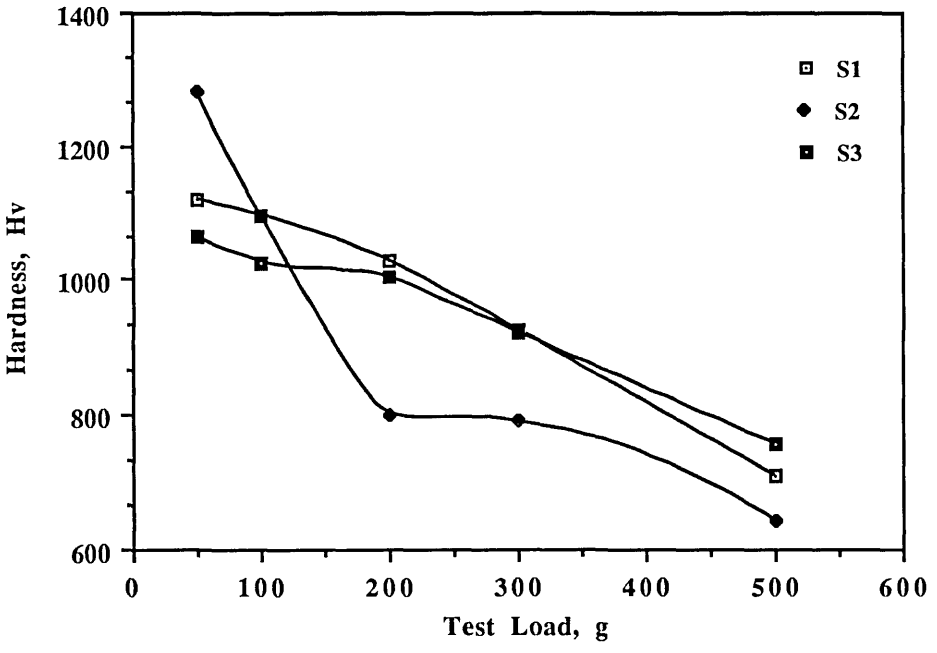

Fig. 3.7 Effect of applied load on the hardness of the matrix region of Stellite + SiC clads, Power = 1.85 kW, Powder feed rate (50 wt.% SiC premixed) = 14 g/min., Traverse speed, mm/s; S1 = 16, S2 = 7.7, S3 = 11.6.

3.3.4. X-Ray Diffraction

Specimens for x-ray diffraction were prepared by cutting overlapping tracks of different clads to a size 15 x 10 x 1 mm. The samples were then ground on emery paper of grade 220 to 600 to make the surfaces flat and smooth. The work was carried out on a Phillips 'PW 1710' diffractometer using copper Kα radiations at 40 kV potential and 38 mA current. The specimens were rotated through angles ranging from 10 to 140 degrees at a constant scanning speed of one degree per minute. The samples were spun during diffractrometery to minimize texture effects. The diffraction patterns obtained were indexed and compared with standard data available (81).

3.4 METHOD ADOPTED FOR PRESENTATION OF RESULTS

The results in this thesis will be reported in four ways; either as photographs, line sketches, tables or plotted as curves. The graphs presented were drawn on a computer using 'Cricket Graph' software. This software, sometimes, draws 'serrated' curves rather than smooth.

CHAPTER 4

PARAMETRIC STUDIES OF LASER CLADDING

4.1 INTRODUCTION

This chapter presents the results of preliminary studies carried out on the laser injection of SiC particles and also cladding of various alloys and composites using different combinations of various processing parameters, including substrate traverse speed, powder feed rate, powder composition, beam diameter, particle size and particle velocity. The clad parameters studied include thickness, buildup, width and also substrate melt depth. Some possible relationships were also established between the laser processing parameters and the clad parameters and also some derived parameters like % area dilution. Fig. 4.1 shows the nomenclature for various regions of clads. For the sake of simplicity, the area dilution of clad was, in fact, calculated as the ratio of substrate melt depth (M) and the clad thickness (T) rather than the ratio of their areas. However, in a study of area dilution measurements on some selected clads, the dilution values obtained using both methods, i.e. by considering the actual clad area or M/T ratio, were found to be in a good agreement ($\pm$ 10%). The alloys and composites studied are listed below.

1. Stellite alloy 6
2. Stellite alloy 6 and SiC (separately fed to obtain variable composition)
3. Stellite alloy 6 and SiC (pre-mixed)
4. Stainless steel and SiC (pre-mixed)
5. Stainless steel and SiC (separately fed to obtain variable composition)
6. Alloy 4815

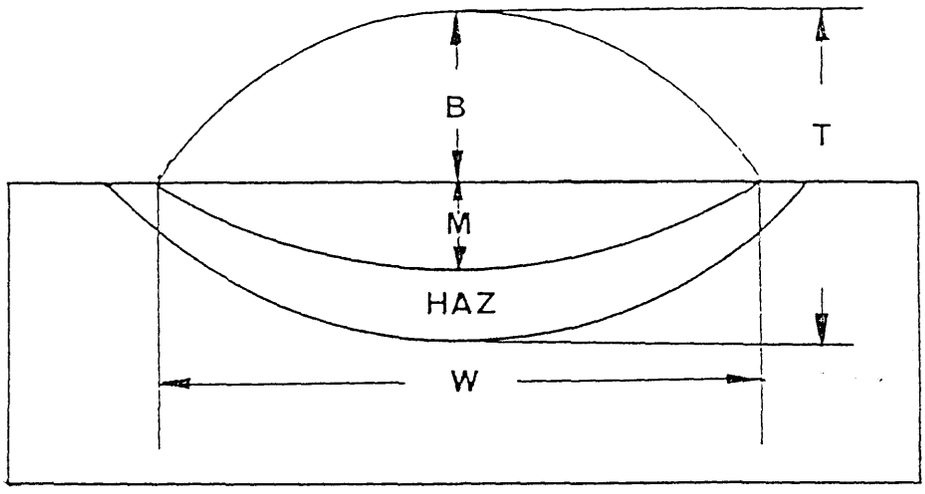

Fig. 4.1 Schematic diagram showing various features of clad deposit, B = clad buildup, M = substrate melt depth, T = clad thickness, W = clad width, HAZ = Heat affected zone.

7. Alloy 4815 and SiC (pre-mixed)

The laser beam power was kept approximately constant during each set of experiments in the range 1.85-2 kW. An experimental error of about ± 15% (of calculated dimensions) was considered to be acceptable during compilation of these results. This error was always expected to occur during laser processing due to either malfunctioning of the equipment or due to its manual handling. The results of these preliminary studies provided a basis for selecting the best combination of parameters for producing good clads with low dilution. This experience was then used to produce overlapping track clads of various alloys and composites for wear resistance studies. The processing parameters used for producing overlapping track clads are reported at the end of this chapter.

4.2 LASER INJECTION OF SIC PARTICLES (Figs. 4.2-4.12)

The laser surface injection of SiC particles was carried out by using three particle sizes, namely fine (50-150 μm), medium (250-450 μm) and coarse (250-750 μm). The surfaces injected with large particles (250-750 μm) showed a substantial amount of porosity due to embedding of large particles into a limited melt depth (≤ 1 mm) produced on the substrate by the parameters used. On the other hand, surfaces produced by injecting fine SiC particles (50-150 μm) showed a complete solution of injected particles with poor fusion bonding. Both of these sets of results have been discarded for parametric studies. The results presented here are those obtained by injecting the medium particle size (250-450 μm) of SiC. The parameters studied are feed rate, traverse speed, and particle velocity.

4.2.1 Effect of Feed Rate on Clad Dimensions

This set of clads was produced using a constant beam power of 2 kW and a beam diameter of 5 mm. The particle feed rate ranged from 9 g/min to 19.2 g/min at a constant substrate speed of 6.5 mm/s. The argon carrier gas flow rate was 2 l/min which provided a particle velocity of about 1.6 m/s. Fig. 4.2 shows the effect of particle feed rate on the clad dimensions. The clad thickness was slightly increased with an increase in the feed rate whereas the substrate melt depth was decreased. A comparatively larger increase was found in the clad buildup with increasing feed rate. However, the clad width was slightly decreased with increasing particle feed rate (Fig. 4.3). Fig. 4.4 shows an interesting plot relating feed rate, hardness and % area dilution. The % area dilution showed an inverse relation with the feed rate at constant values of other parameters whereas no definite trend was found on the hardness of the processed surfaces.

4.2.2 Effect of Traverse Speed and Particle Velocity

Two sets of SiC particle injected clads were produced using a constant laser power and beam diameter of 1.95 kW and 4 mm respectively. The other processing parameters used for these two sets are given in Table 4.1.

Table 4.1

Processing parameters

Set No.	Particle velocity, m/s	Particle feed rate, g/min	Traverse speed, mm/s
1.	4.0	59.4	16.5-22.5
2.	2.5	34.0	16.0-35.0

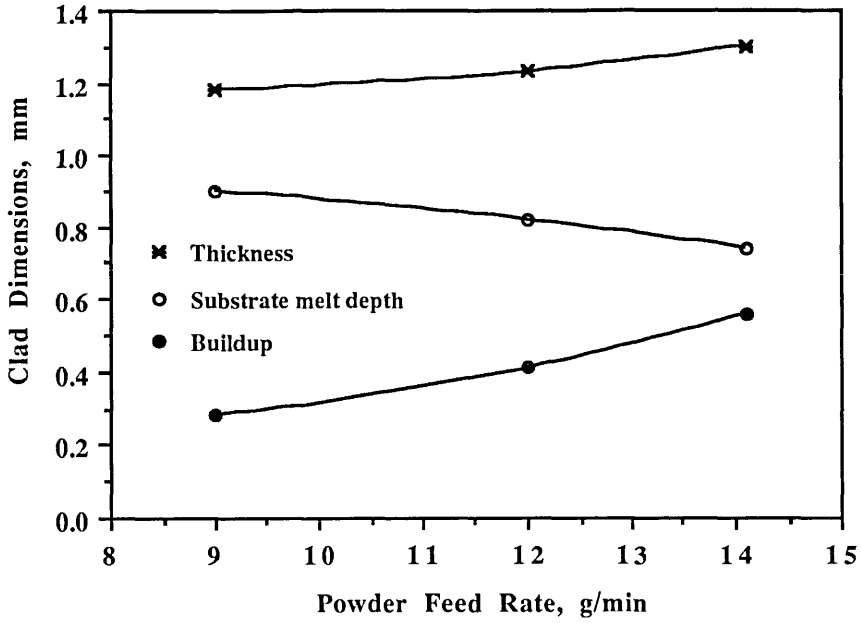

Fig. 4.2 Effect of powder feed rate on clad dimensions.

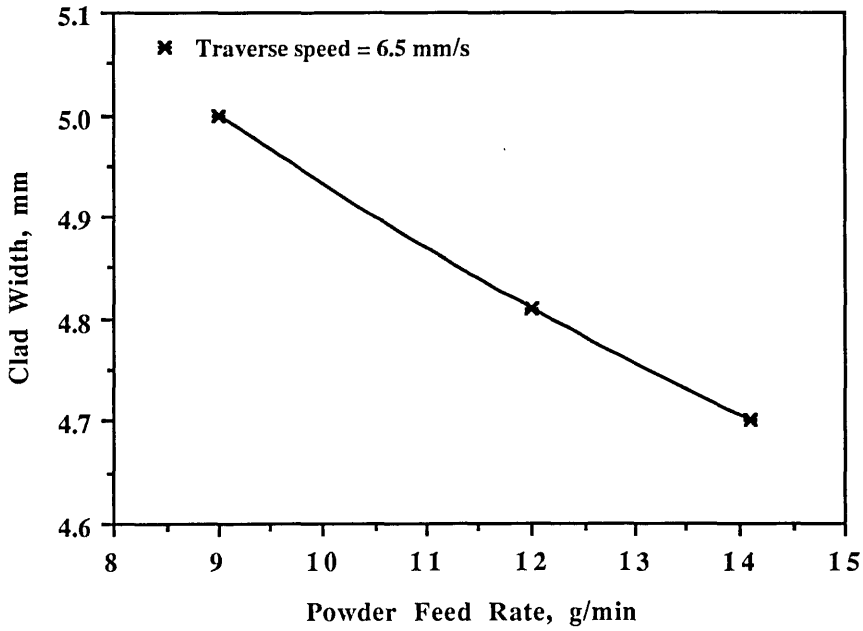

Fig. 4.3 Effect of powder feed rate on clad width.

Figs. 4.5 and 4.6 show the effect of traverse speed on the clad dimensions of set 1 and set 2 respectively. The overall trend observed was the same in both the cases except for the magnitude of the changes in the clad dimensions which is attributed to the difference in the particle velocity. An almost constant clad buildup, together with a comparatively larger decrease in both thickness and substrate melting, was observed with increasing substrate traverse speed. A comparison of the effect of traverse speed on the thickness and width of these two sets produced at different particle velocity and feed rate is shown in Figs. 4.7 and 4.8 respectively.The trend observed was a decrease in both the thickness and the width of clads with increasing traverse speed. The effect of traverse speed on the clad dimensions was found to be more pronounced at lower particle velocity (2.5 m/s) than at higher velocity (4 m/s). An interesting point to be noted in Fig. 4.7 is that at a given substrate speed, the thickness of clad formed is greater at lower particle velocity despite the low feed rate (34 g/min) as compared with that (59.4 g/min) at higher particle velocity (4 m/s). This shows a lower particle deposition rate at higher particle velocity. Both the sets showed a slight decrease in the clad width with increasing the traverse speed up to 25 mm/s. However, a marked decrease in the width of set 2 occurred when the traverse speed was increased beyond 25 mm/s (Fig. 4.8) which is attributed to the low specific energy available for substrate melting at that speed. Although the substrate melt depth was greater in the clads formed at lower particle velocity than those formed at higher particle velocity at a given substrate traverse speed (Fig. 4.9), the corresponding area dilution was lower in the case of the former (Fig. 4.10) which is attributed to the larger clad thickness (Fig. 4.7). Fig. 4.11 shows the effect of traverse speed on the hardness of the matrix regions of both clad sets. In set 1 a slight decrease in hardness was observed at the beginning with an increase in the traverse speed with almost no change with any further increase in the speed. However, the hardness of set 2 was found to be increased, at the beginning, with an increase in the substrate traverse speed, but was decreased sharply with further increase in the speed. The effect of area dilution

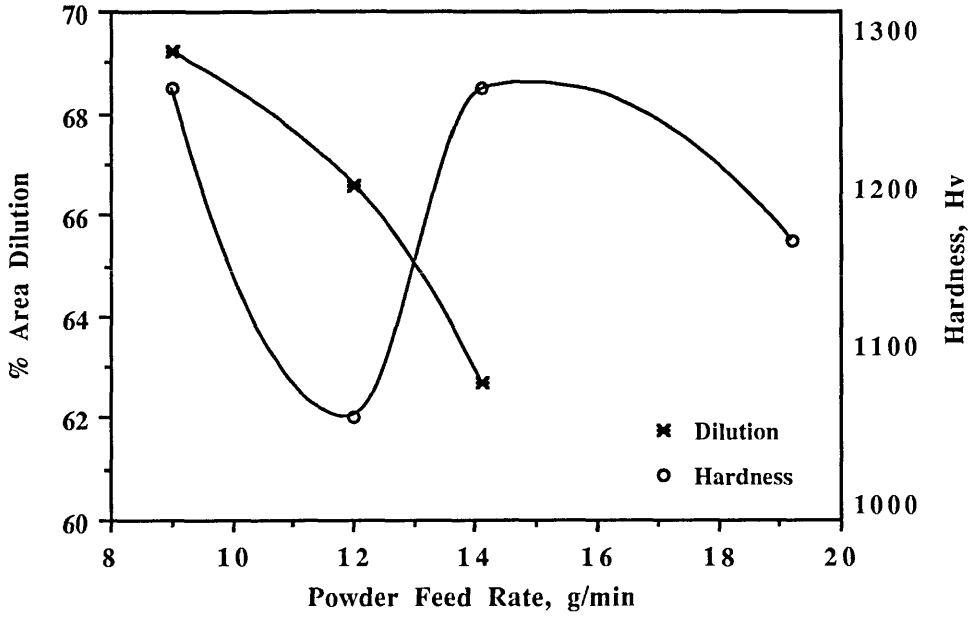

Fig. 4.4 Effect of powder feed rate on dilution and hardness of the matrix region of SiC injected clad.

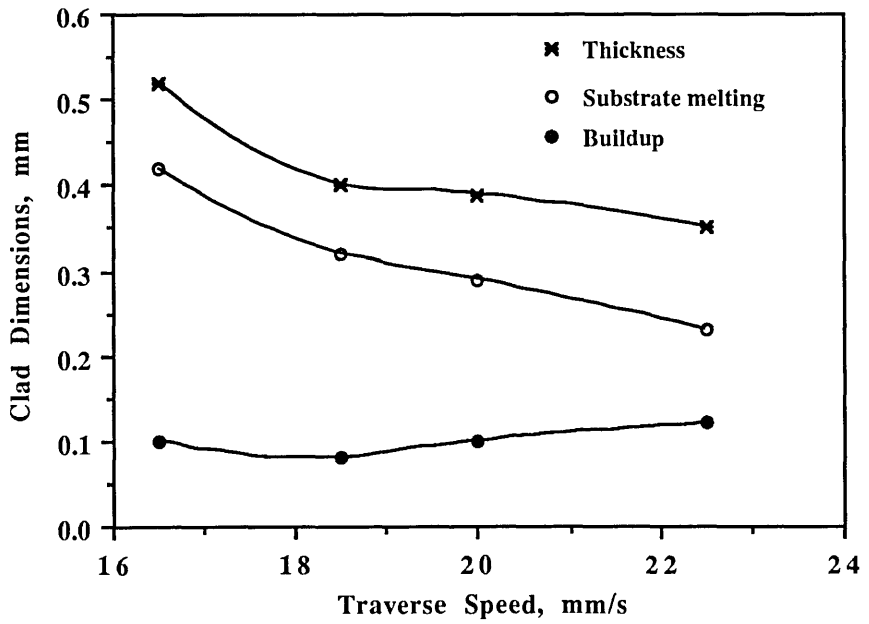

Fig. 4.5 Effect of traverse speed on clad dimensions (particle velocity = 4 m/s).

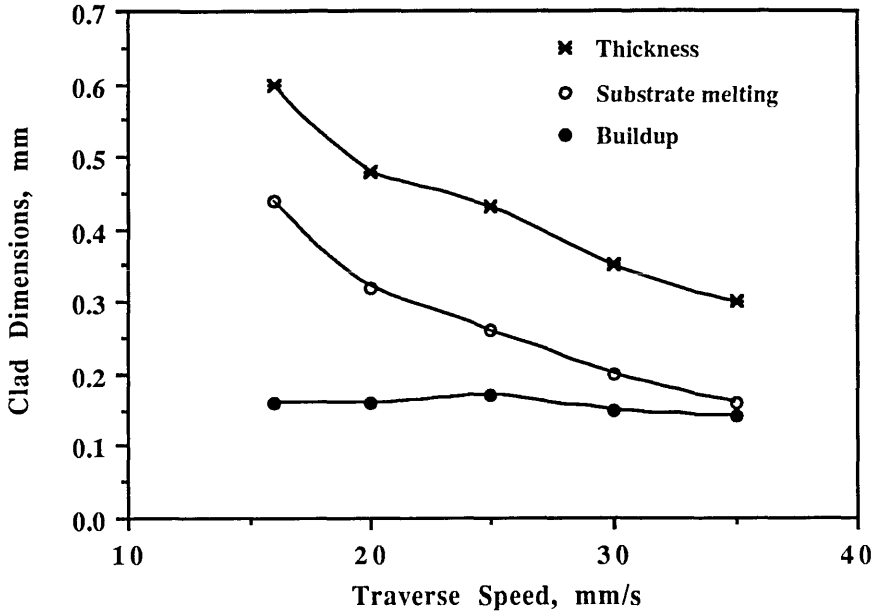

Fig. 4.6 Effect of traverse speed on clad dimensions (particle velocity = 2.5 m/s).

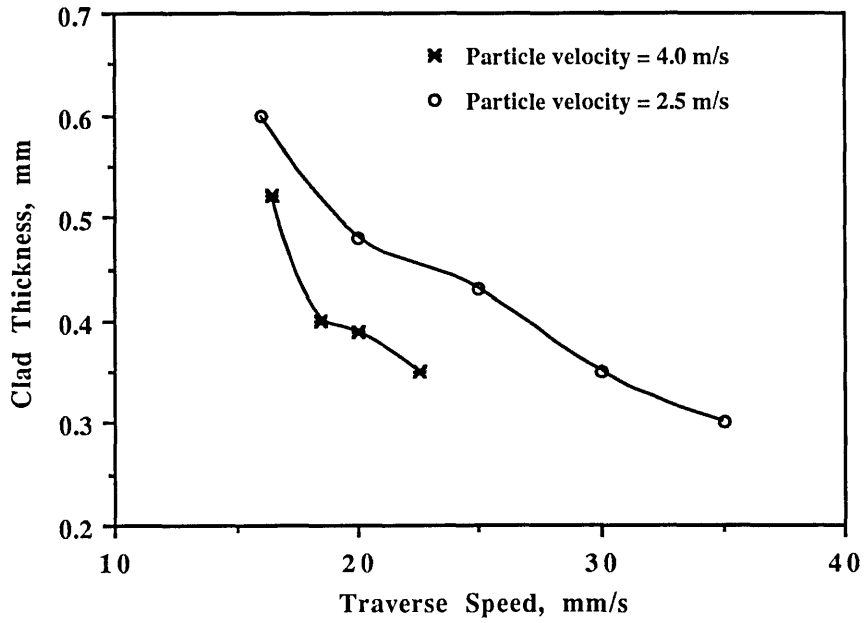

Fig. 4.7 Effect of traverse speed on the thickness of SiC injected clads produced at different particle velocities.

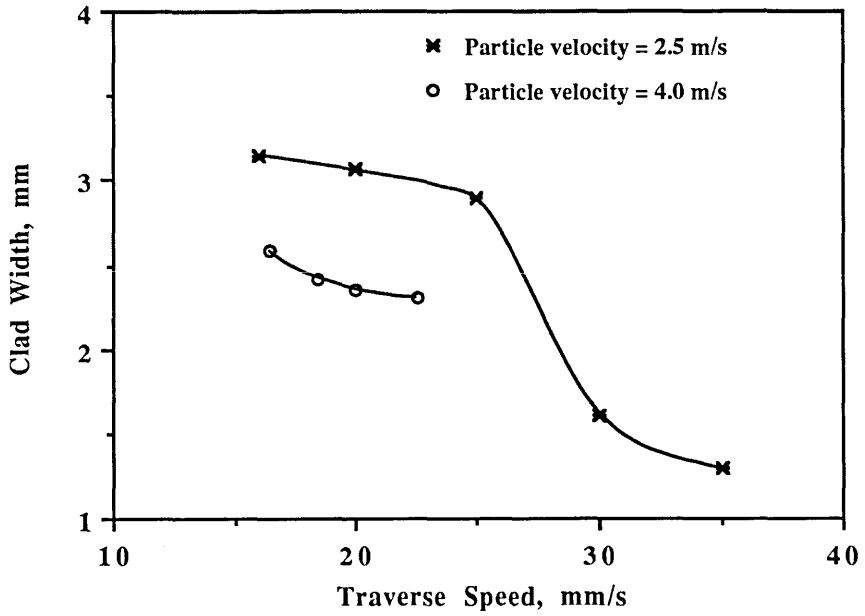

Fig. 4.8 Effect of traverse speed on the width of SiC injected clads produced at different particle velocities.

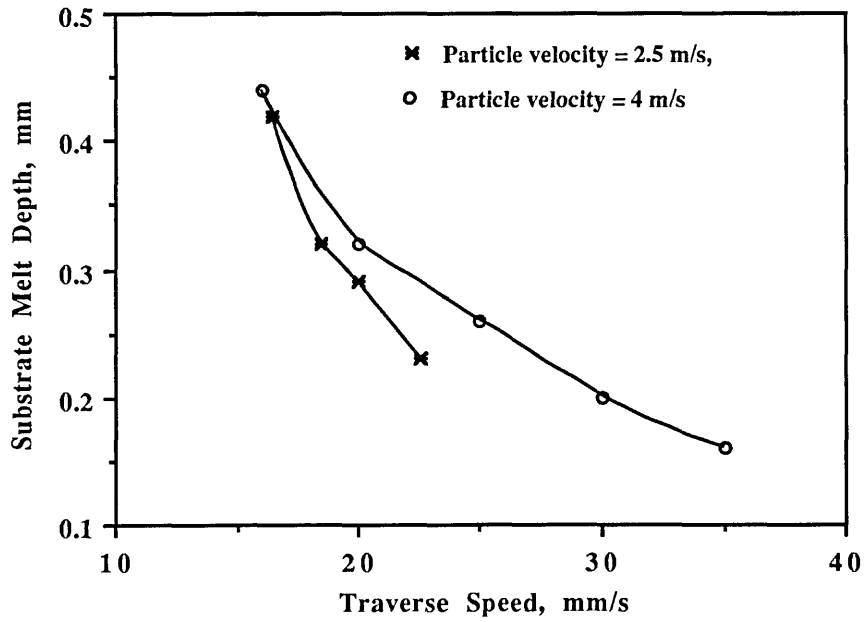

Fig. 4.9 Effect of traverse speed on the substrate melt depth of SiC injected clads produced at different feed rates (34 and 59.4 g/min) and particle velocities.

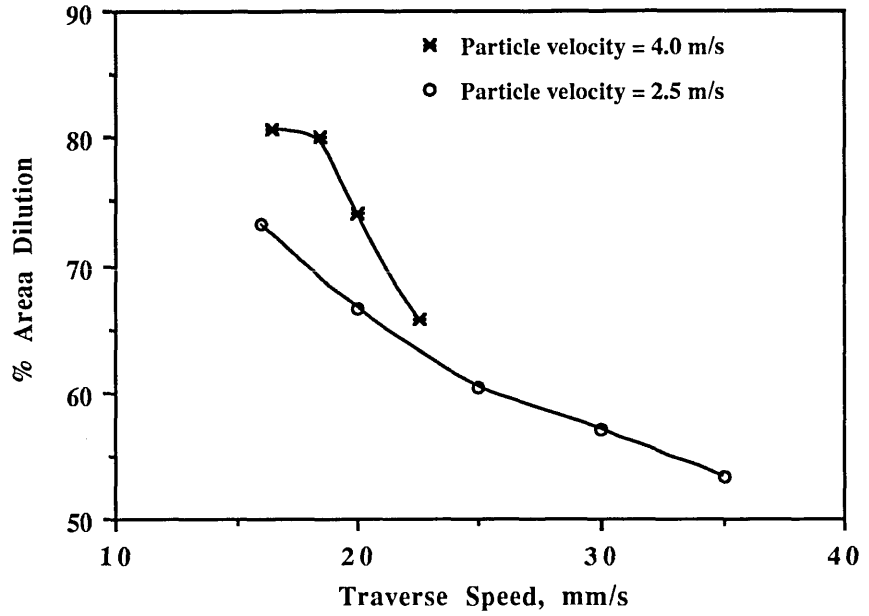

Fig. 4.10 Effect of traverse speed on the dilution of SiC injected clads.

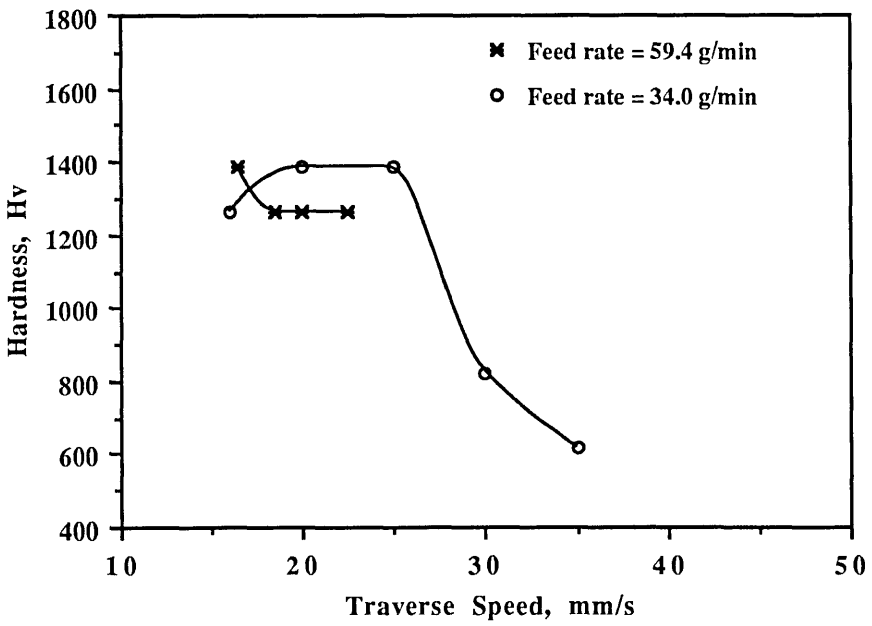

Fig. 4.11 Effect of traverse speed on the hardness of the matrix region of SiC injected clads.

on the clad hardness, in the case of set 1, was found almost negligible except for a slight increase at the dilution level corresponding to a traverse speed of 16.5 mm/s (Fig. 4.12). On the other hand, in case of set 2, the hardness increased with an increase in the area dilution reaching a steady state and then a relatively small decrease with further dilution as shown in Fig. 4.12.

4.3 LASER CLADDING WITH STELLITE (Figs. 4.13-4.19)

Single clad tracks of Stellite alloy were produced in three sets at various substrate traverse speeds and powder feed rates to study their effect on clad dimensions, hardness and dilution. The experiments for all these sets were performed at a constant laser power level of 1.85 kW and beam diameter of 4 mm.

4.3.1 Effect of Powder Feed Rate

Stellite powder was blown at feed rates ranging from 23 g/min to 60 g/min while keeping the traverse speed constant at 5 mm/s. The clad dimensions, both the thickness and width, were found to increase with an increase in the powder feed rate; however, the effect of feed rate was less pronounced on the width as compared with the thickness (Fig. 4.13). The increase in the dimensions of clad with feed rate also affected the quality of the clads formed. The dilution was low ($\leq 7\%$) and by increasing the powder feed, the dilution of the clad matrix by iron from the substrate was reduced as is evident from Fig. 4.14. The dilution plotted in Fig. 4.14 is a compositional dilution and was calculated as the difference in iron content between the the applied Stellite powder and the clad matrix. Fig. 4.15 shows that the hardness of the matrix regions of clads produced at speeds of 5 and 7.5 mm/s is increased with increase in the feed rate; this is attributed to the decrease in dilution at the higher feed rate.

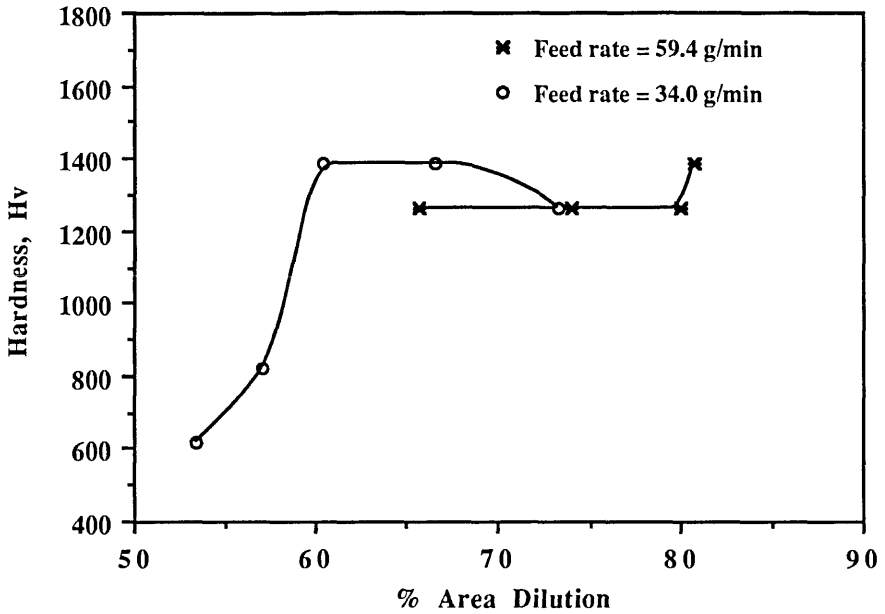

Fig. 4.12 Relationship between dilution and hardness of the matrix region of SiC injected clads.

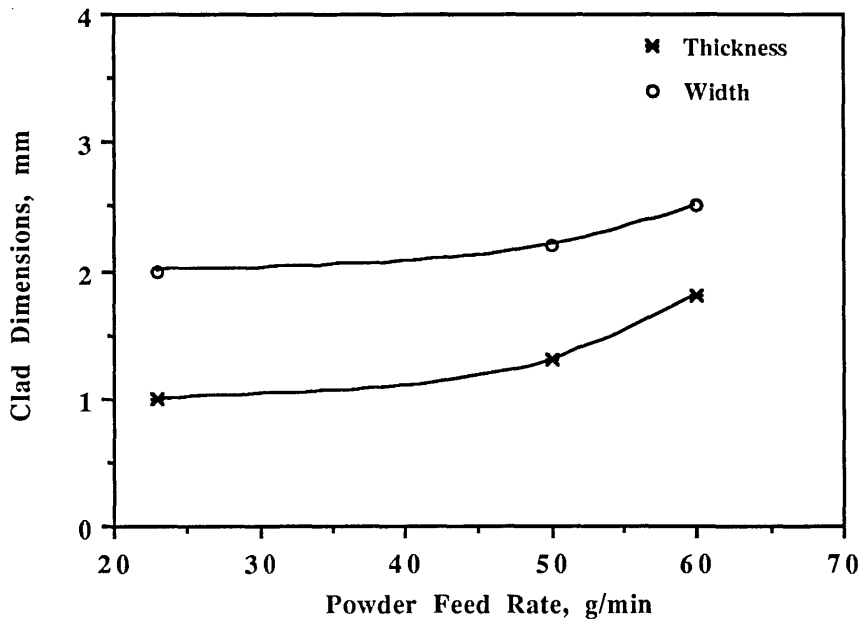

Fig. 4.13 Effect of powder feed rate on the dimensions of Stellite clad, traverse speed = 5 mm/s.

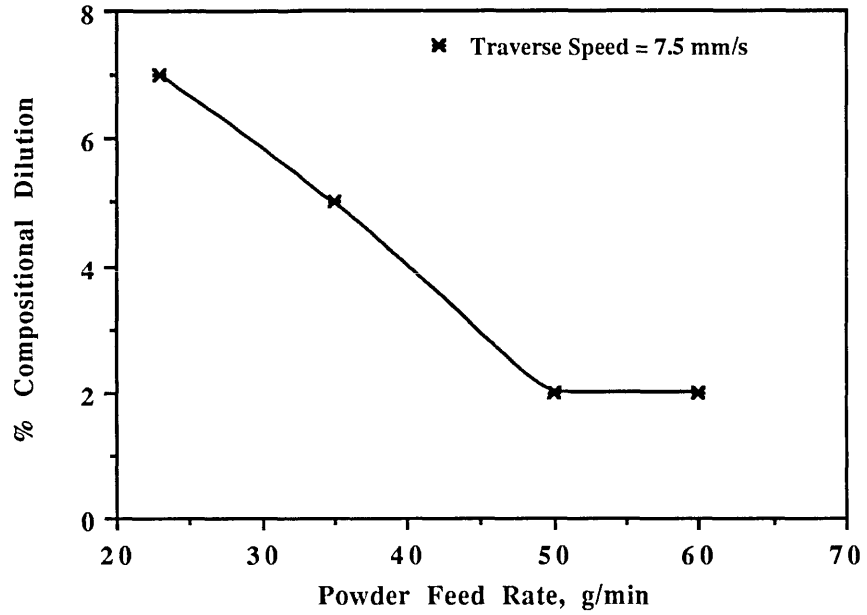

Fig. 4.14 Effect of powder feed rate on the dilution of Stellite clad, traverse speed = 5 mm/s.

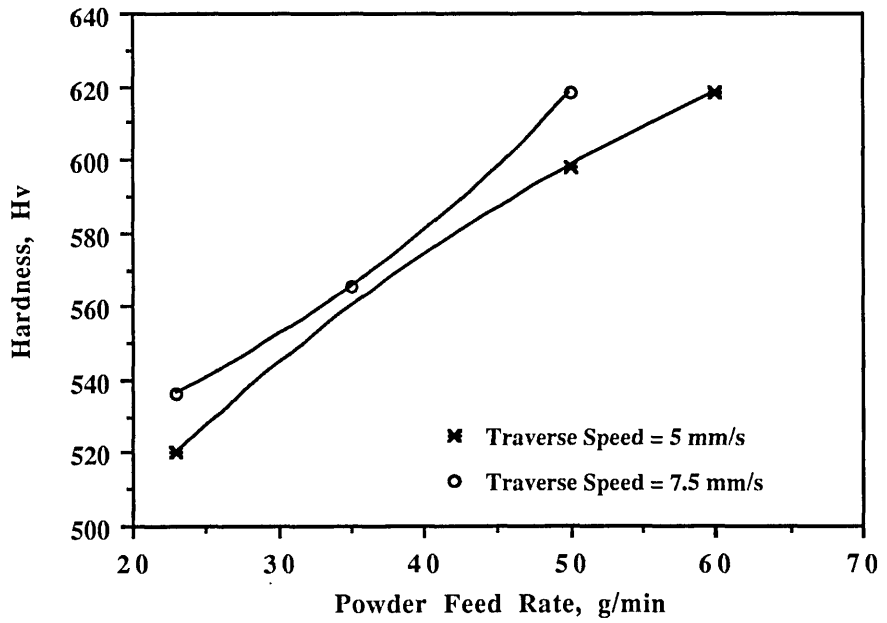

Fig. 4.15 Effect of powder feed rate on the hardness of Stellite clads produced at different traverse speeds.

4.3.2 Effect of Traverse Speed

Two sets of clads were produced using constant feed rates of 50 g/min and 60 g/min at traverse speed ranges of 2.5-7.3 mm/s and 3.5-8.5 mm/s respectively. The thickness and width of both these sets of clads were found to be inversely related to the substrate traverse speed (Figs. 4.16 and 4.17). A substantial increase in the hardness of the clad from 530 to 618 Hv was found when the traverse speed was increased from 2.5 to 7.3 mm/s at a powder feed rate of 50 g/min (Fig. 4.18)

4.3.3 Variation in Hardness with Position in the Clads

These studies were carried out to find out the consistency of the hardness values at various points within the clad track. Three samples produced at different speeds and feed rates were selected from the series described in sections 4.3.1 and 4.3.2. The microhardnesses were measured at four different points, 0.3 mm apart from each other, starting from near the surface of clad down to the clad-substrate interface using a 300 g load. The hardness of all these clads was found to be slightly ($\leq$ 50 Hv) lower near the clad-substrate interface (Fig. 4.19) and this is attributed to the higher dilution near this interface. The hardness values measured at various points on the clads formed at relatively lower traverse speeds were more consistent than for those produced at higher substrate traverse speeds. The reason is lack of homogeneity of structure at the higher speeds due to the shorter mixing times available than at lower traverse speeds.

4.4 LASER CLADDING WITH STELLITE + SIC POWDER MIXTURES (Figs. 4.20-4.31)

Three sets of Stellite and SiC composite clads were produced using various compositions, powder feed rates and substrate scanning speeds. In the first set, pre-

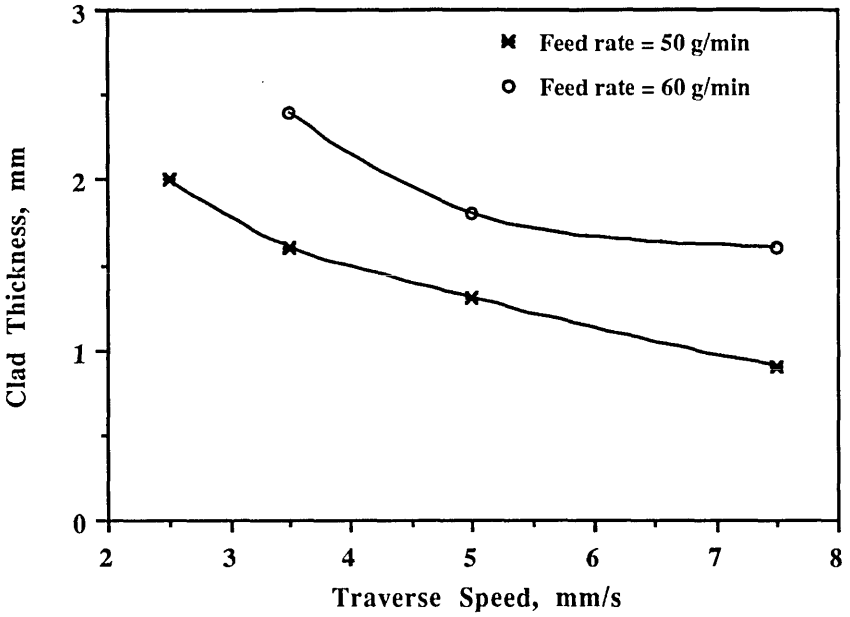

Fig. 4.16 Effect of traverse speed on the thickness of Stellite clads produced at different feed rates.

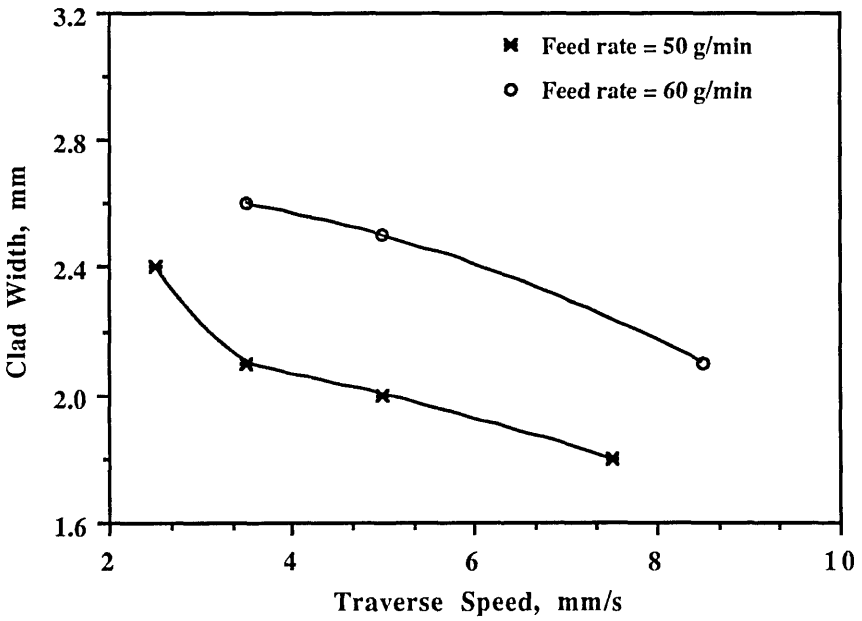

Fig. 4.17 Effect of traverse speed on the width of Stellite clads produced at different feed rates.

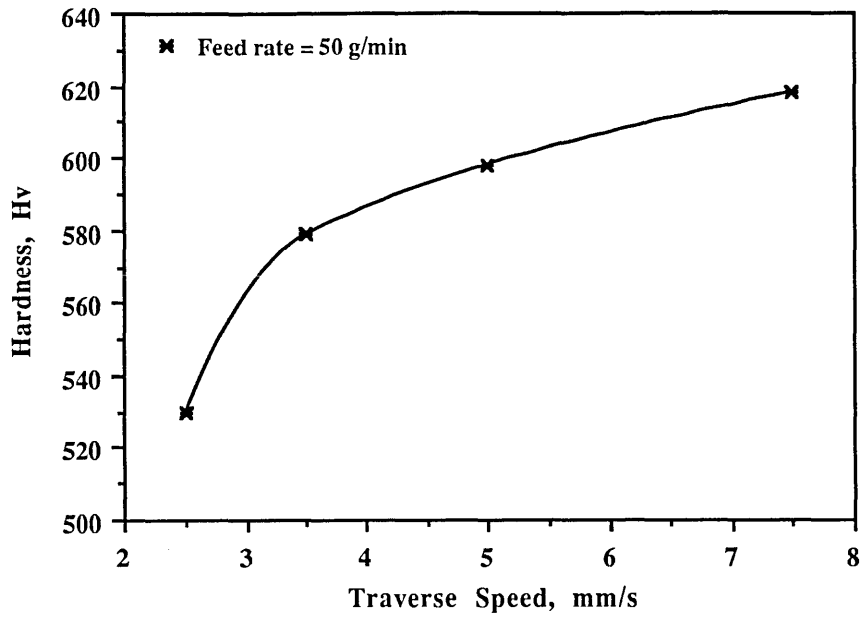

Fig. 4.18 Effect of traverse speed on the hardness of Stellite clad.

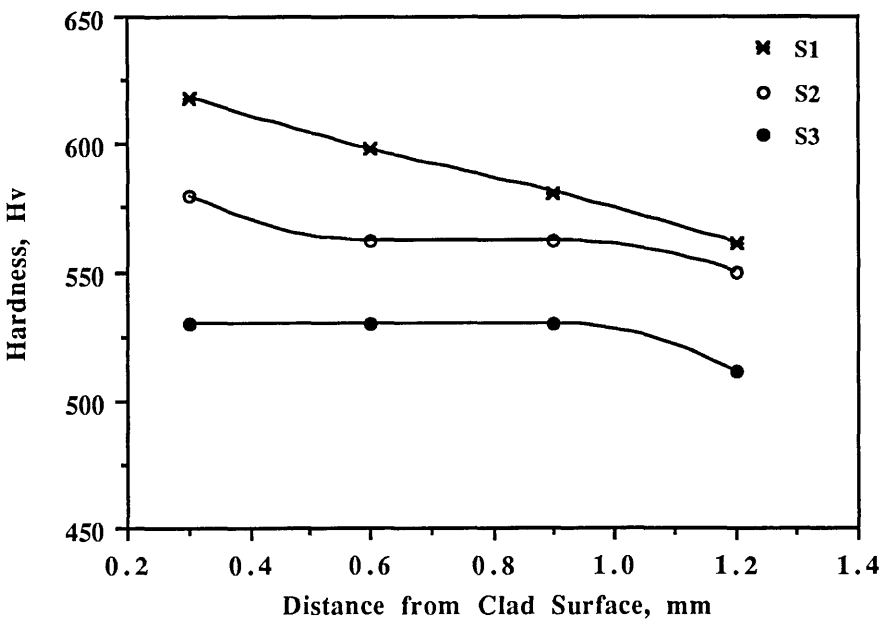

Fig. 4.19 Effect of distance from the clad surface on the hardness of Stellite clads, laser power = 1.85 kW, beam diameter = 4 mm, traverse speed, mm/s; S1 = 5, S2 = 3.5, S3 = 2.5, feed rate g/min; S1 and S2 = 60, S3 = 50.

mixed 50 wt.% SiC (particle size 250-750 μm) and Stellite powder was blown into the laser generated melt pool: in the other two sets, SiC (50-150 μm) and Stellite powders were fed separately at various feed rates to produce clads of various compositions. Neither the fine nor the coarse SiC particle sizes provided fine distributions of particles in the Stellite matrix as a result of complete solution of the fine particles and a large amount of porosity in the case of the coarse particles due to limited clad dimensions (≤ 1 mm) as compared with particle size.

4.4.1 Cladding with Stellite + SiC Pre-mixed Powder

Composite clads were formed at constant powder feed rate of 10 g/min with scanning speeds from 6.2 to 16 mm/s and a constant laser power of 1.85 kW and 4 mm beam diameter. Fig. 4.20 shows the effect of traverse speed on the clad dimensions. A reduction in clad thickness and depth of substrate melting with little effect on buildup was found with increase in traverse speed, associated with a decrease in area dilution (Fig. 4.21). This decrease in area dilution was accompanied by an increase in hardness (Fig. 4.21). The width of the clad also decreased with increase in traverse speed (Fig. 4.22).

4.4.2 Cladding with Separate Feeding of Stellite and SiC Powder

Two sets of composite clads were produced. The powder mixtures were fed at various rates keeping SiC and Stellite feed rate constant in set 1 and set 2 respectively. The laser power, beam spot diameter and substrate traverse speed for both sets were kept constant at 1.85 kW, 4 mm and 7 mm/s respectively whereas the other processing parameters are given in Table 4.2.

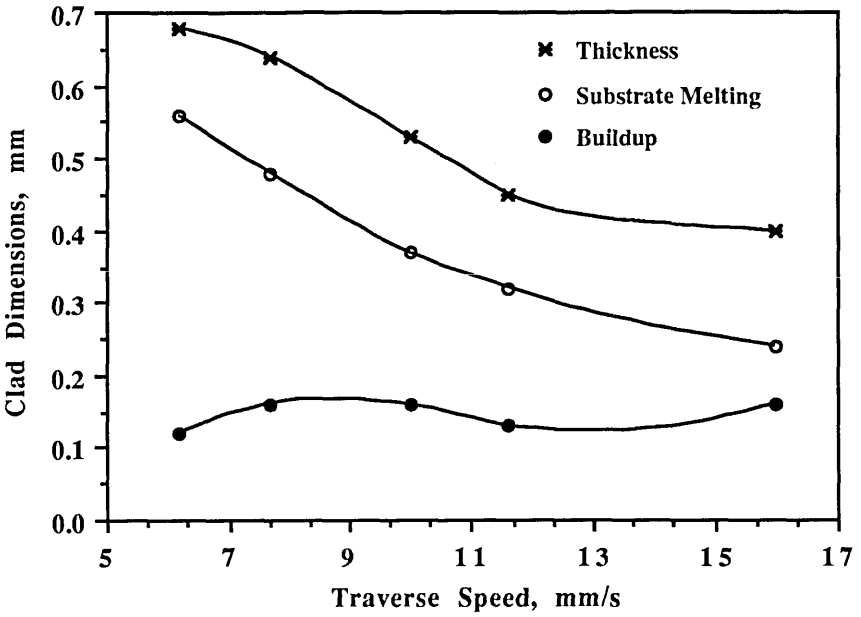

Fig. 4.20 Effect of traverse speed on clad dimensions of Stellite + SiC composite, laser power = 1.85 kW, feed rate (50 wt.% premixed) = 10 g/min.

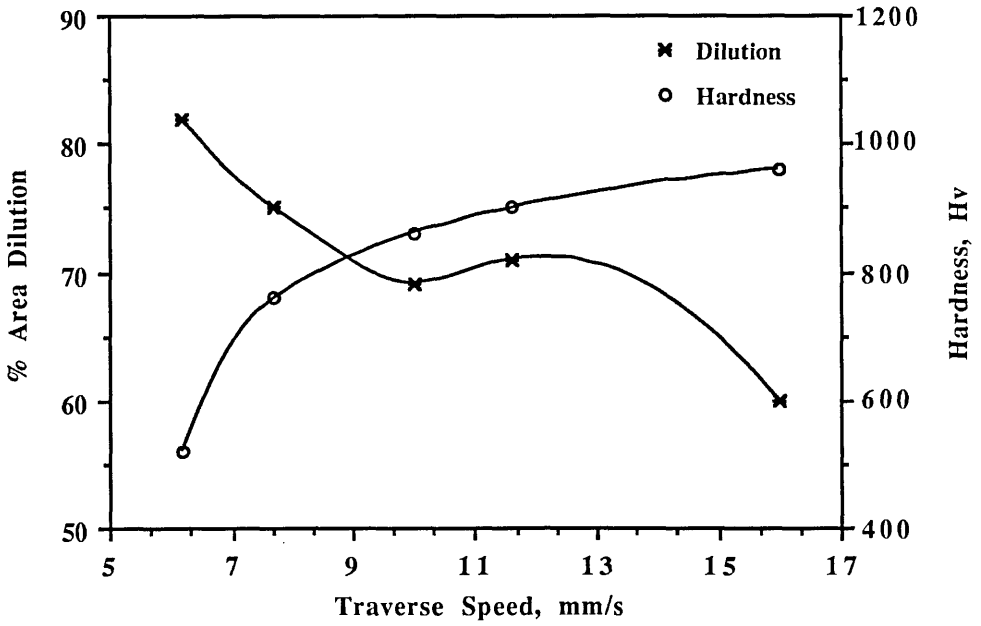

Fig. 4.21 Effect of traverse speed on the dilution and hardness of the matrix region of Stellite + SiC clad.

Table 4.2

Processing parameters for set 1 and set 2

Set No.	SiC feed rate, g/min	Stellite feed rate, g/min	Total feed rate g/min	Wt.% SiC in mixture
1.	7.0	11.4-26.7	18.4-33.7	20.0-38.0
2.	3.5-9.8	35.0	38.5-44.8	9.0-21.8

4.4.2.1 Effect of Various Parameters on Clad Dimensions

The effect of total powder feed rate (Stellite + SiC) on the clad dimensions of set 1 and set 2 is shown in Figs. 4.23 and 4.24 respectively. An increase in the thickness and clad buildup, with little effect on the substrate melt depth, was found in both the sets with increasing powder feed rate. However, at constant Stellite feed rate, a decrease in clad thickness was observed above a value of 41 g/min feed rate (Fig. 4.25). An increase in width occurred with increase in the total feed rate irrespective of the wt.% of SiC in the powder mixture (Fig. 4.26). The width of clads formed at constant Stellite feed rate decreased sharply when the feed rate exceeded 41 g/min.

4.4.2.2 Effect of Various Parameters on Microhardness of Clads

Fig. 4.27 shows the relationship between the % area dilution and the microhardness of the matrix regions of both clad sets. The microhardness decreased markedly as the clad dilution increased. As the dilution of the clad area can be decreased by increasing the powder feed rate, the microhardness of the clad matrices was also dependent on the feed

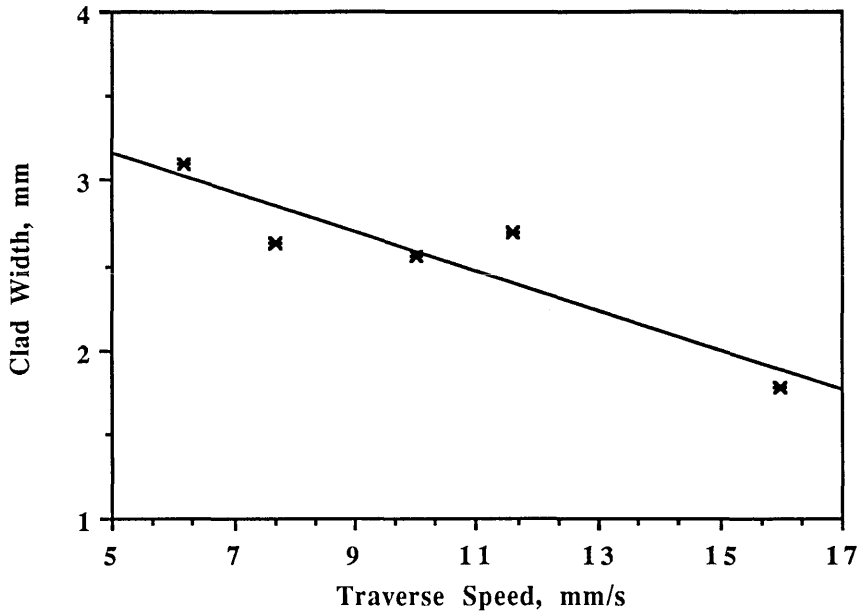

Fig. 4.22 Effect of traverse speed on the width of Stellite + SiC (premixed) clad.

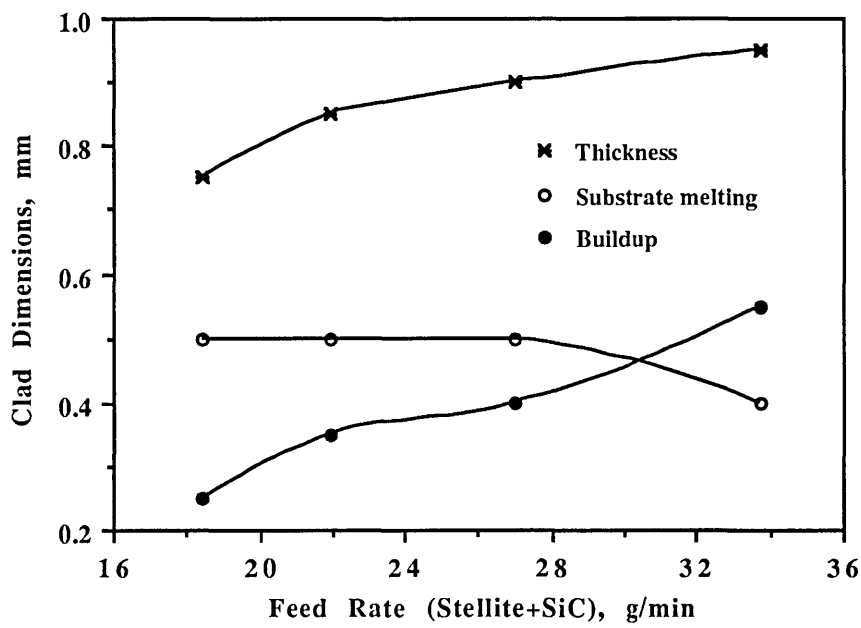

Fig. 4.23 Effect of powder feed rate on the clad dimensions of separately fed Stellite + SiC composite clads (constant SiC).

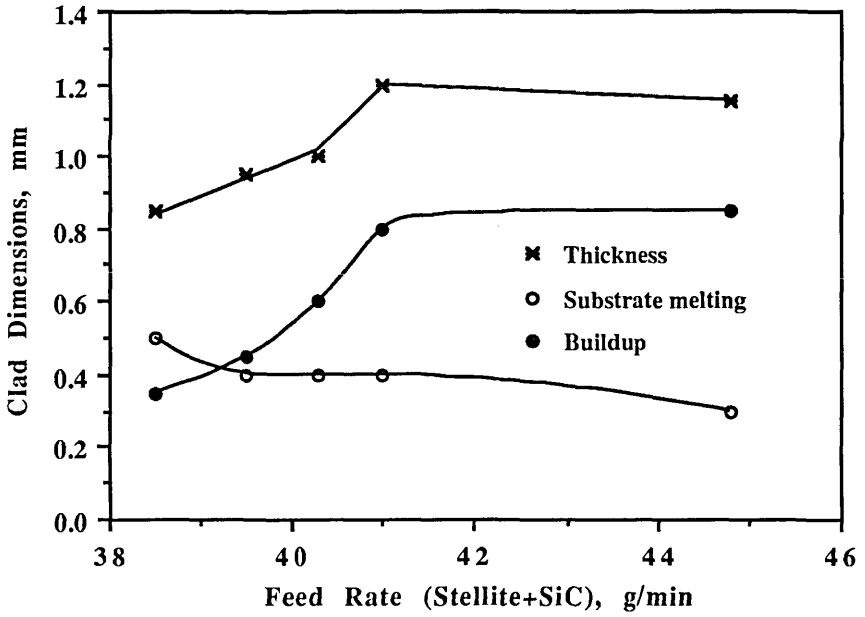

Fig. 4.24 Effect of powder feed rate on the dimensions of separately fed Stellite + SiC clads (constant Stellite).

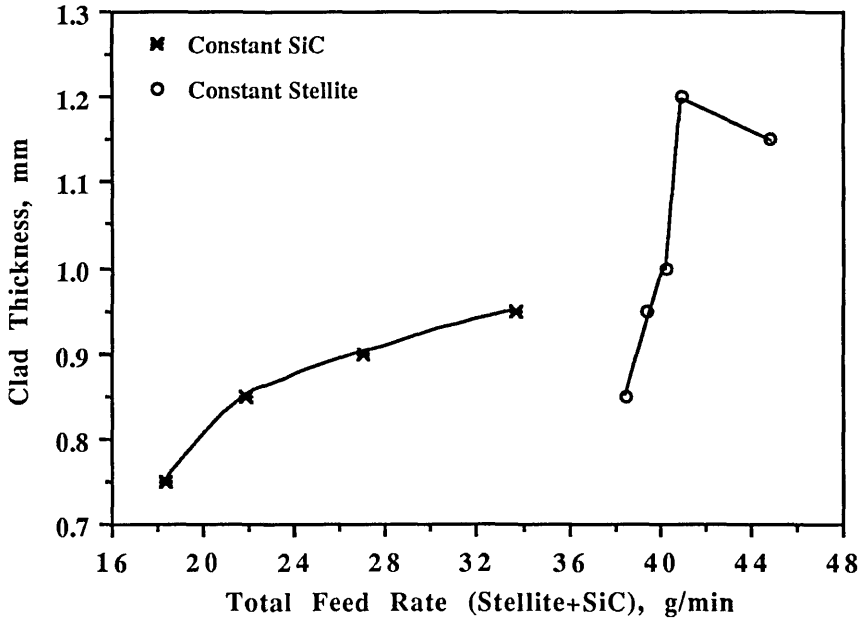

Fig. 4.25 Effect of powder feed rate on the thickness of a set of Stellite + SiC clads produced at constant Stellite and variable SiC feed rates and vice versa, respectively.

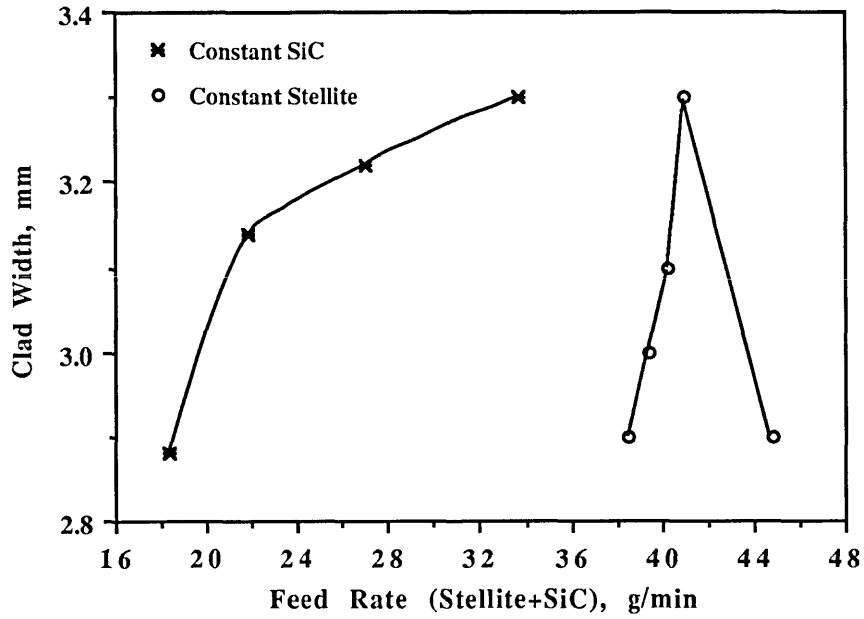

Fig. 4.26 Effect of powder feed rate on the width of a set of Stellite + SiC clads produced at constant Stellite and variable SiC feed rates and vice versa, respectively.

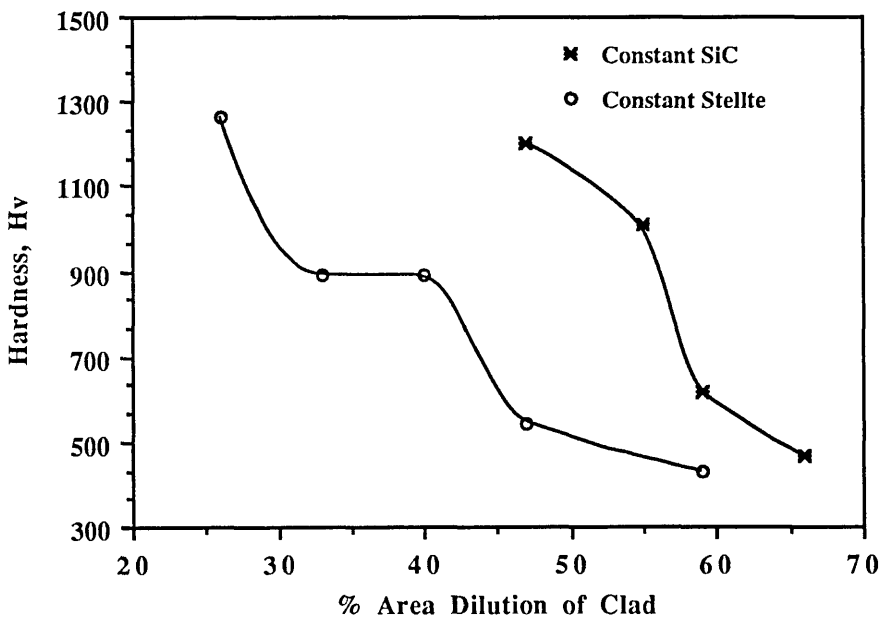

Fig. 4.27 Relationship between the hardness and the dilution of a set of Stellite + SiC clads produced at constant Stellite and variable SiC feed rates and vice versa, respectively.

rate (Fig. 4.28). The trend observed was an increase in the hardness with increasing feed rate. A plot of SiC wt.% in the powder mixture versus microhardness of clads (Fig. 4.29) shows that the hardness of clads formed at constant Stellite feed rate is increased with increasing wt.% of SiC in the powder mixture to a maximum of about 1260 Hv at about 22 wt.% of SiC. On the other hand, the microhardness of the clads formed at constant SiC decreased with increasing the SiC beyond 16.6 wt.% from a maximum of about 1200 Hv.

4.4.2.3 Effect of Various Parameters on Area Dilution of Clads

The area dilution of both sets of clads was found to be inversely related to the powder feed rate. The effect of increasing powder feed rate in decreasing the % area dilution of clads is illustrated in Fig. 4.30. The relative decrease in dilution level is lower at constant SiC feed rate, despite the large change in total feed rates, as compared with the dilution for constant Stellite feed rate. Fig. 4.31 shows that the dilution is substantially decreased with increase in SiC content of the mixture for clads formed at constant Stellite feed rate and is increased with increase in SiC content of the mixture beyond 20 wt.% with constant SiC feed rate. It is of interest to note that at about 20 wt% SiC, the dilution for the constant Stellite feed rate is considerably less than that for the constant SiC case; this arises from the fact that the total feed rate is higher in the former case ($\geq$ 41 g/min) than in the latter ($\leq$ 33.7 g/min).

4.5 LASER CLADDING WITH STAINLESS STEEL AND SIC POWDER MIXTURE (Figs. 4.32-4.34)

Stainless steel powder and coarse SiC particles (250-750 μm) were fed separately at constant feed rates of 37 g/min and 10.5 g/min respectively. The clads formed had large amounts of porosity for the same reason as in the case of Stellite and SiC composites

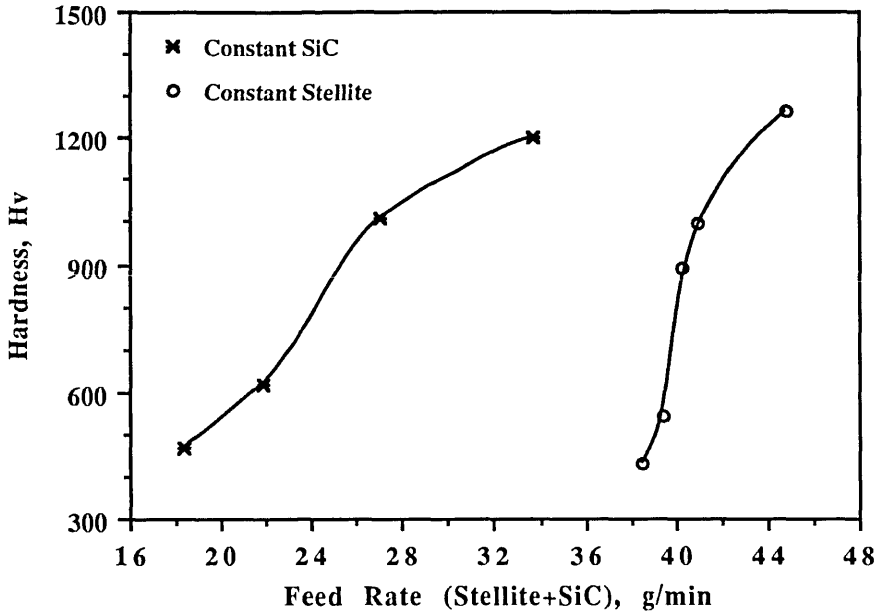

Fig. 4.28 Effect of powder feed rate on the hardness of the matrix regions of a set of separately fed Stellite + SiC clads.

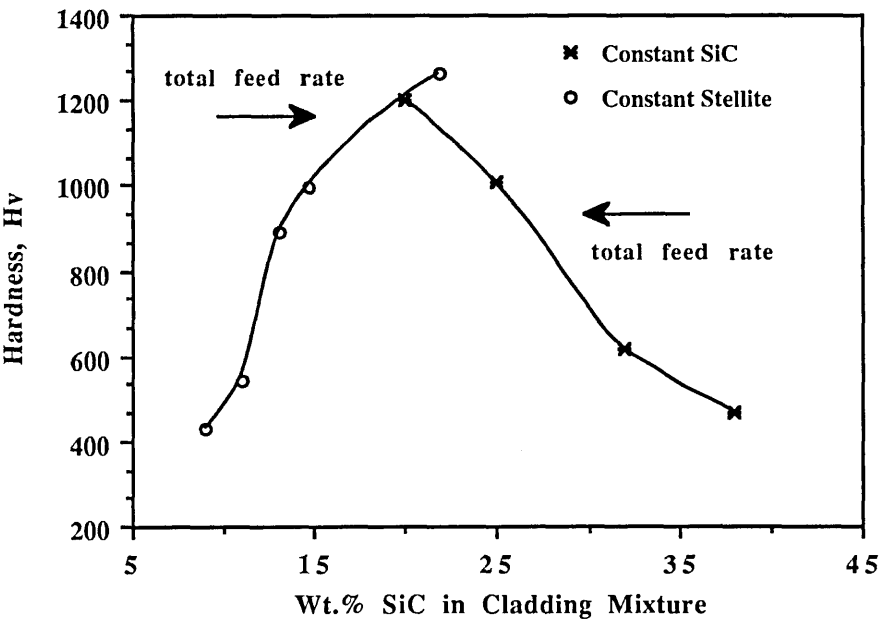

Fig. 4.29 Effect of wt.% SiC in the cladding powder mixture on the hardness of the matrix region of a set of Stellite + SiC clads.

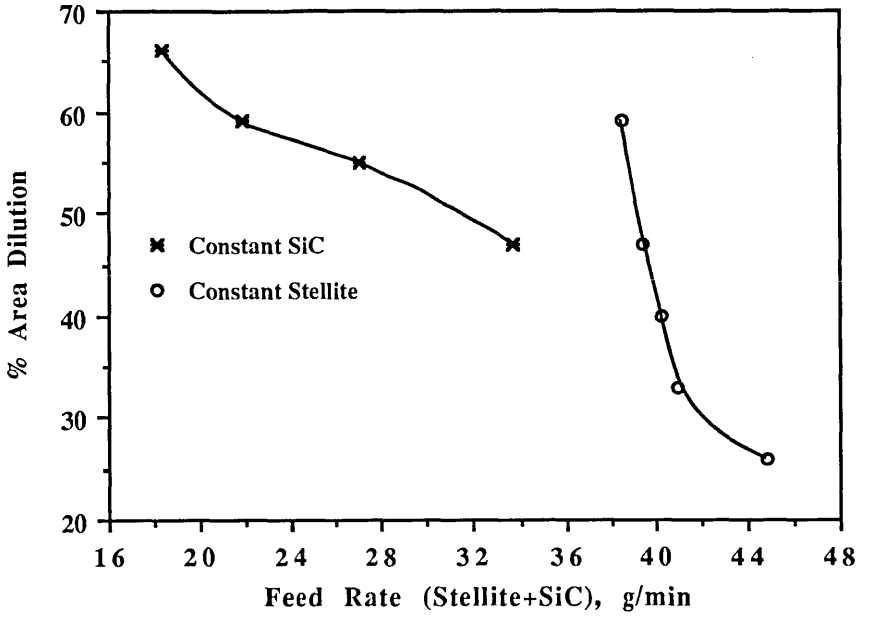

Fig. 4.30 Effect of powder feed rate on the dilution of a set of Stellite + SiC clads.

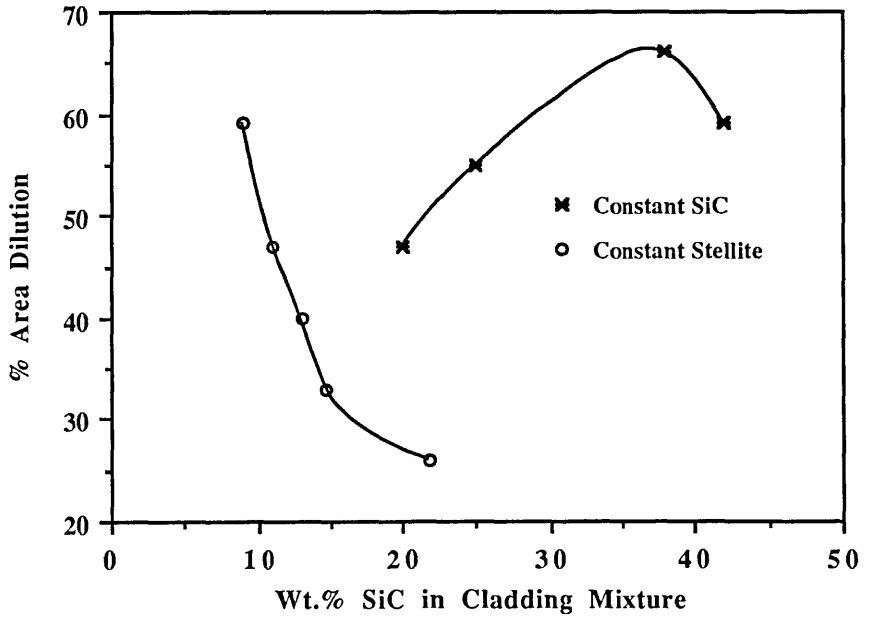

Fig. 4.31 Effect of wt.% SiC in the cladding powder mixture on the dilution of Stellite + SiC clads.

described in section 4.4. A laser power of 2 kW with a beam spot diameter of 3 mm and traverse speed 3 to 10 mm/s were used.

Fig. 4.32 shows the effect of traverse speed on the clad dimensions. The trend observed was a decrease in the clad thickness and substrate melt depth with increase in the traverse speed. However, only a small effect of speed was found on the clad buildup except at very low traverse speed (3 mm/s) where the powder flux was so high that only a small amount of heat reached the substrate resulting in very shallow melting and poor fusion bonding. At higher speeds (8-10 mm/s) a good compromise between substrate melting and clad buildup was achieved. Fig. 4.33 shows the effect of traverse speed on the clad width. The width was found relatively low at low traverse speeds due to excessive feed intake. It increased with speed to a maximum and the decreased with further increase in speed. A trend of decreasing dilution with increasing traverse speed was observed (Fig. 4.34) except at very low speed where poor substrate melting occurred due to excessive powder intake as mentioned earlier.

4.6 LASER CLADDING WITH ALLOY 4815 AND SIC POWDER MIXTURE (Figs. 4.35-4.39)

Two sets of clads were produced at a constant laser beam power of 1.85 kW and beam spot diameters of 3.5 mm and 4 mm respectively. The SiC particles used were of a medium particle size range (250-450 μm). The first set was produced by blowing premixed 5 wt.% SiC and Alloy 4815 powder at a feed rate of 27.5 g/min with traverse speeds from 4 to 12.5 mm/s. The other set was formed using a 10 wt.% SiC and alloy 4815 premixed powder at a constant feed rate of 36 g/min and traverse speeds ranging from 12 to 25 mm/s. The SiC particles, in most cases, completely dissolved possibly due to low weight fractions in the powder feed, except in a few cases where partial solution occurred and particles segregated to upper regions of the clad surface. Drastic change in the hardness of the matrix regions of the clads formed occurred due to the

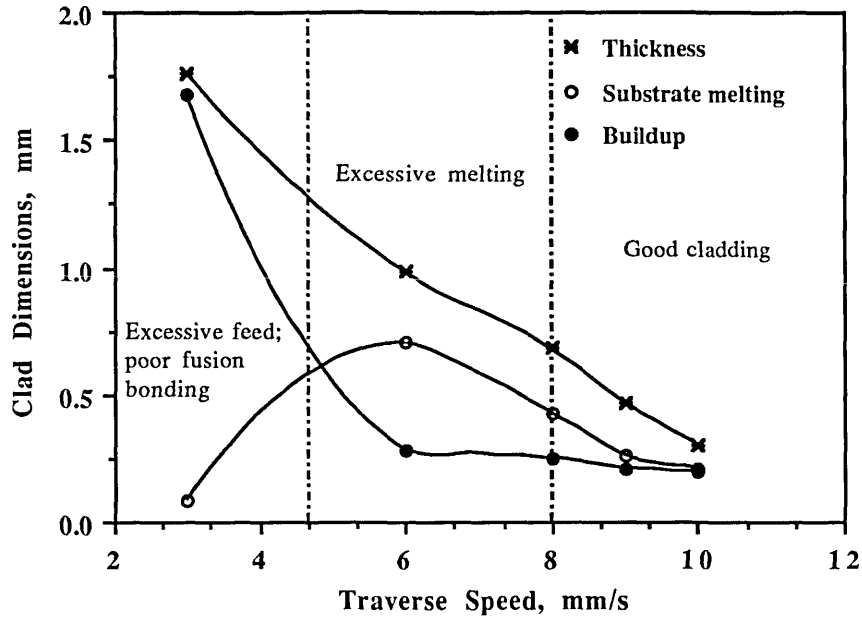

Fig. 4.32 Effect of traverse speed on the dimensions of stainless steel + SiC clads.

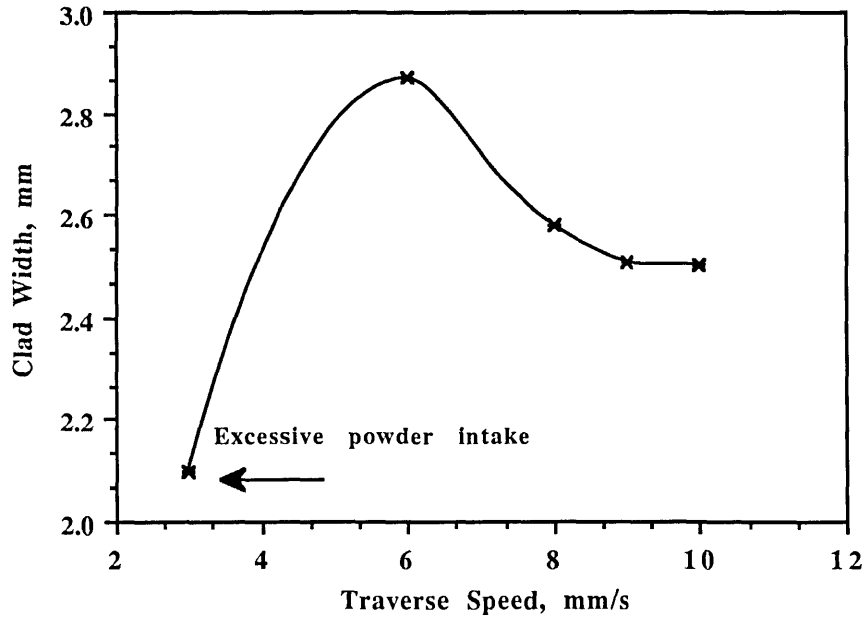

Fig. 4.33 Effect of traverse speed on the width of stainless steel + SiC clads.

solution of SiC particles. The maximum hardness measured was about 950 Hv as compared with that of 211 Hv for alloy 4815 clads.

Figs. 4.35 and 4.36 show the effect of traverse speeds on the dimensions of clads formed at 27.5 and 36 g/min feed rates respectively. The trend observed in the first set was a decrease in the thickness and substrate melt depth, with little effect on buildup, with increase in the speed. However, in the second set the clad thickness and buildup decreased with increasing speed whereas the substrate melt depth was slightly increased at higher speeds. The relationship between the clad width and the traverse speed for both the sets is shown in Fig. 4.37. A marked decrease in the width was found in both cases with increase in the speed. The data in Fig. 4.38 show a decrease in area dilution with increasing traverse speed for 27.5 g/min feed rate. In the case of high feed rate (36 g/min), the trends of dilution are much lower and show a trend to increase with increasing speed. Fig. 4.39 shows a significant effect of feed rate on the hardness of the matrix regions of both clads. For a feed rate of 27.5 g/min, the hardness decreases with increasing traverse speed reaching an approximate constant value at $\geq$ 8 mm/s. For the higher feed rate (36 g/min) a maximum hardness is reached at 20 mm/s traverse speed.

4.7 SELECTION OF PARAMETERS FOR OVERLAPPING TRACK CLADS

The parametric studies on single tracks were used to select optimum cladding conditions for producing overlapping clads with low dilution and good surface features (i.e. buildup, width, and continuity etc.). Initially single tracks were formed using these optimum conditions for different alloys and composites which were subsequently overlapped at different overlapping distances. The parameters for different clads were chosen so as to obtain the same clad buildup suitable for subsequent comparative wear studies. Three sets of overlapping clads were produced at various processing parameters reported in Tables 4.3-4.5.

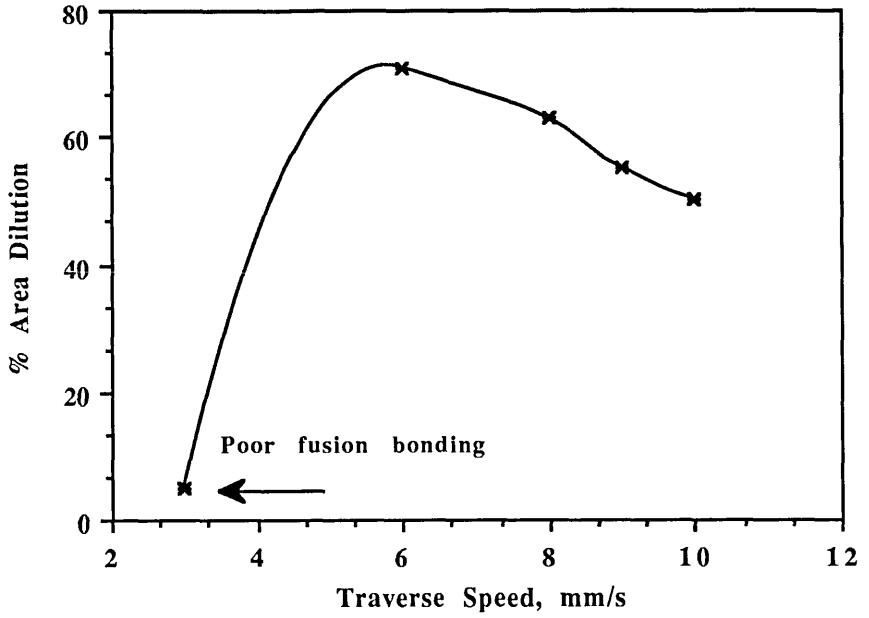

Fig. 4.34 Effect of traverse speed on the dilution of stainless steel + SiC clads.

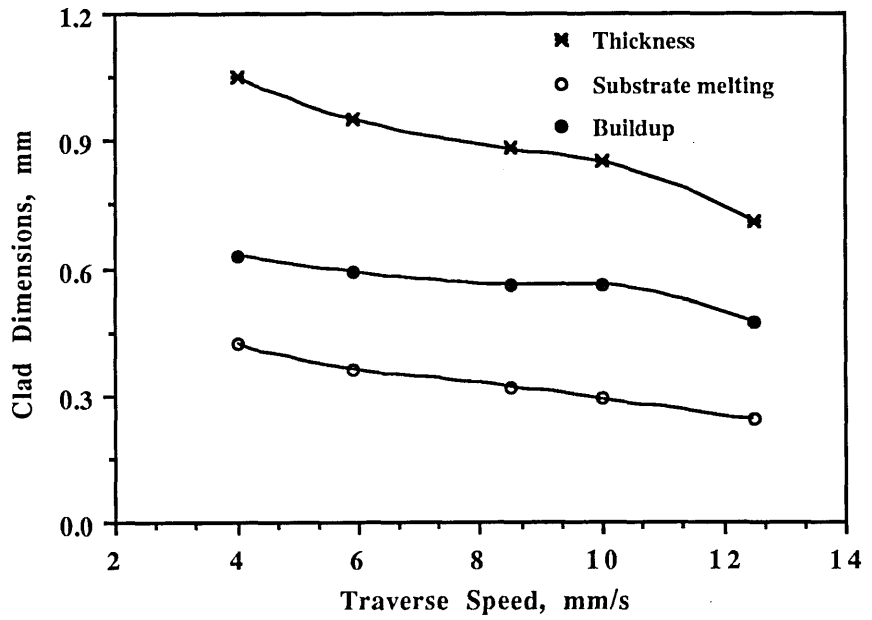

Fig. 4.35 Effect of traverse speed on the dimensions of Alloy 4815 + SiC clads, feed rate (5 wt.% SiC premixed) = 27.5 g/min.

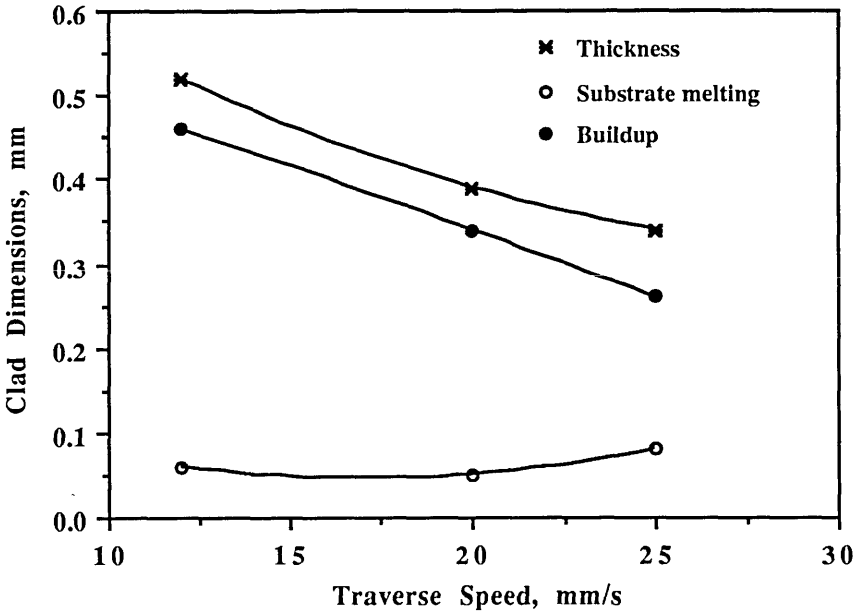

Fig. 4.36 Effect of traverse speed on the dimensions of Alloy 4815 + SiC clads, feed rate (10 wt.% SiC premixed) = 36 g/min.

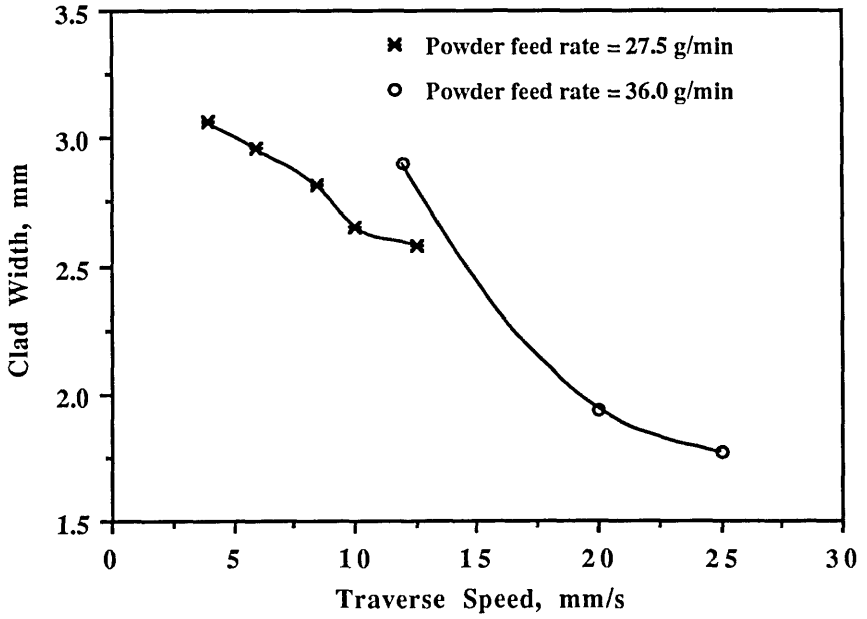

Fig. 4.37 Effect of traverse speed on clad width of a set of Alloy 4815 + SiC clads produced at different feed rates.

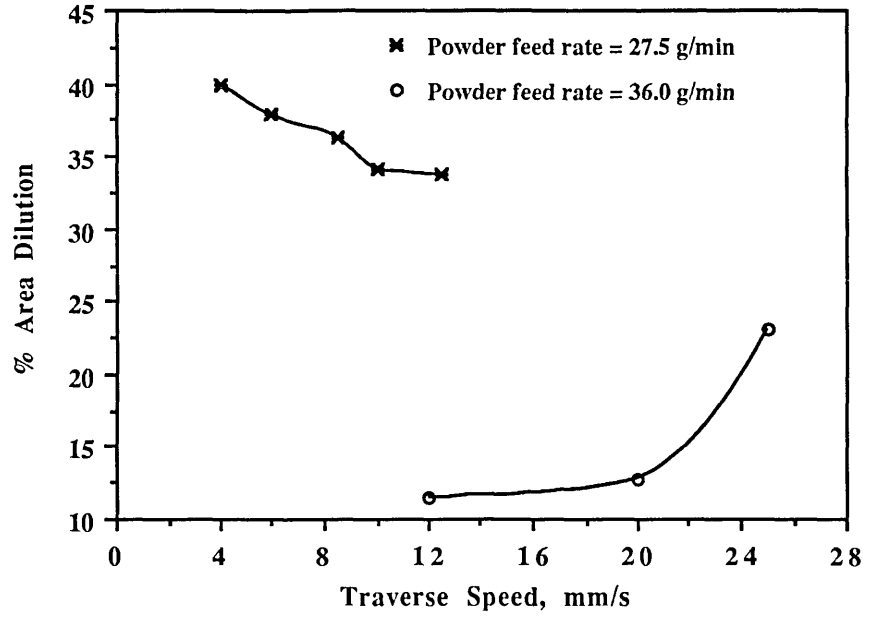

Fig. 4.38 Effect of traverse speed on the dilution of a set of Alloy 4815 + SiC clads produced at different feed rates.

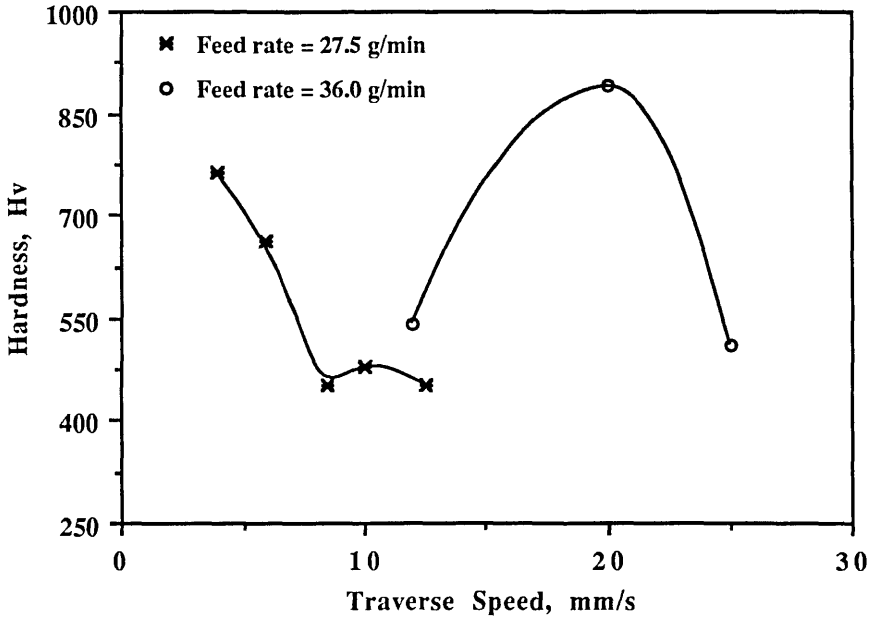

Fig. 4.39 Effect of traverse speed on the hardness of the matrix regions of a set of Alloy 4815 + SiC clads produced at different feed rates.

Table 4.3

Processing parameters and surface features of clads formed

with 5 mm beam diameter and 1.9 kW laser power (series 2 and 4, Ch. 6)

Powder composition	Powder feed rate, g/min	Traverse speed, mm/s	Overlapping distance, mm / % overlap	Clad height, mm	Height at overlap, mm	Substrate melt depth, mm
Stainless steel	11.2	2.5	2.5 / 52	2.6	2.6	Negligible
Stellite	12.4	2.5	2.5 / 52	2.8	2.8	Negligible
Alloy 4815	13.0	2.5	2.5 / 52	3.2	3.2	0.16
20 wt.% SiC + Stellite	10.0	4.5	2.0 / 45	1.0	0.73	0.16
20 wt.% SiC + stainless steel	9.0	4.5	2.0 /45	1.3	1.3	Negligible
20 wt.% SiC + Alloy 4815	10.0	4.5	2.0 / 45	1.0	1.0	0.16

Table 4.4

Processing parameters and surface features of clads formed with 4 mm beam diameter and 1.85 kW laser power (series 3, Ch.6)

Powder composition	Powder feed rate, g/min	Traverse speed, mm/s	Overlapping distance, mm / % overlap	Clad height, mm	Height at overlap, mm	Substrate melt depth, mm
Stellite	22.7	4.8	1.5 / 42	1.2	0.8	Negligible
Alloy 4815	22.7	4.8	1.5 / 42	1.0	1.0	Negligible
10 wt.% SiC + Stellite	36.0	20.0	1.5 /50	0.65	0.32	Negligible
10wt.%SiC +Alloy 4815	45.0	20.0	1.5 / 50	0.65	0.4	Negligible

Table 4.5

Processing parameters and surface features of 10% SiC + Alloy 4815 composite produced at various feed rates and traverse speeds, beam diameter = 4 mm, laser power = 1.85 kW (series 5, Ch. 6)

Sample Nos.	Powder feed rate, g/min	Traverse speed, mm/s	Overlapping distance, mm / % overlap	Clad height, mm	Height at overlap, mm	Substrate melt depth, mm
S1	17.7	12.5	2.0 / 47	0.7	0.7	Negligible
S2	17.7	5.0	2.0 / 44	1.0	1.0	Negligible
S3	21.5	12.5	2.0 / 47	0.8	0.8	Negligible

CHAPTER 5

STRUCTURAL STUDIES OF CLADS

5.1 INTRODUCTION

This chapter comprises three main parts. In the first part, structures as observed by light and scanning electron microscopy are reported. The second part contains the micro-probe analyses of some typical samples from each set of clads. In the third part, x-ray diffraction data of these clads are reported for the identification of various phases present.

5.2 LOW AND HIGH MAGNIFICATION MICROSCOPY

5.2.1 General Features of Overlapping Clads

Figs. 5.1-5.6 show the macrographs of plan views of overlapping track clads of Stellite alloy 6, stainless steel, Alloy 4815 and their composites with SiC. The heights of the alloy clads (Stellite - Fig. 5.1, stainless steel - Fig. 5.3, Alloy 4815 - Fig. 5.5) were about 2 mm whereas the composite clads (Stellite + SiC - Fig. 5.2, stainless steel + SiC - Fig. 5.4, Alloy 4815 + SiC - Fig. 5.6) were around 1-1.5 mm high. Other related data about the dimensions of these overlapping clads are reported in chapter 4. Generally, the alloy clad surfaces were rougher than the composite clad surfaces due to their lower asperity ratios (width/height ratio) but the latter were high in surface porosity which was attributed to the presence of SiC particles in the cladding mixtures. Small in size and round shaped droplets of alloys were found on the surfaces of Stellite (Fig. 5.1) and stainless steel (Fig. 5.3) clads, but the occurrence was less frequent in the case of the latter. A narrow region at the upper surface of Alloy 4815 (Fig. 5.5) clad was found to

A. **Fig. 5.1** Macrograph showing plan view of overlapping track clad of Stellite alloy 6, Laser power, P = 1.9 kW, Beam diameter, D = 5 mm, Powder feed rate, F = 12.4 g/min., Substrate traverse speed, S = 2.5 mm/s, Overlapping distance, d = 2.5 mm, 2.3 X.

B. **Fig. 5.2** Macrograph showing plan view of overlapping track clad of Stellite + SiC composite, P = 1.9 kW, D = 5 mm, F (Stellite + 20 wt.% SiC) = 10 g/min., S = 4.5 mm/s, d = 2 mm, 2.3 X.

C. **Fig. 5.3** Macrograph showing plan view of overlapping track clad of stainless steel, P = 1.9 kW, D = 5 mm, F = 11.2 g/min., S = 2.5 mm/s, d = 2.5 mm, 2.3 X.

D. **Fig. 5.4** Macrograph showing plan view of overlapping track clad of stainless steel + SiC composite, P = 1.9 kW, D = 5 mm, F (stainless steel + 20 wt.% SiC) = 9 g/min., S = 4.5 mm/s, d = 2 mm, 2.3 X.

E. **Fig. 5.5** Macrograph showing plan view of overlapping track clad of Alloy 4815, P = 1.9 kW, D = 5 mm, F = 13 g/min., S = 2.5 mm/s, d = 2 mm, 2.3 X.

F. **Fig. 5.6** Macrograph showing plan view of overlapping track clad of Alloy 4815 + SiC, P = 1.9 kW, D = 5 mm, F (Alloy 4815 + 20 wt.% SiC) = 10 g/min., S = 4.5 mm/s, d = 2 mm, 2.3 X.

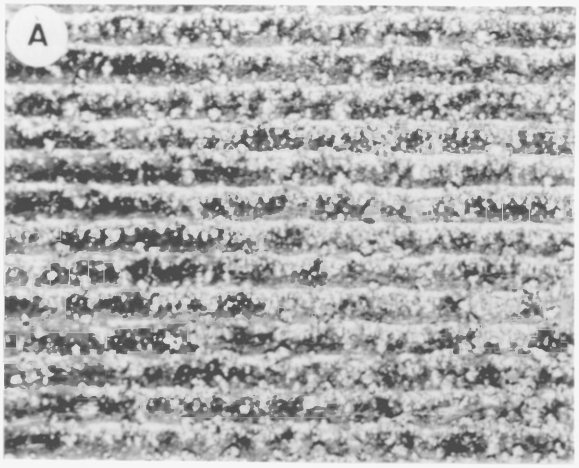
A


B

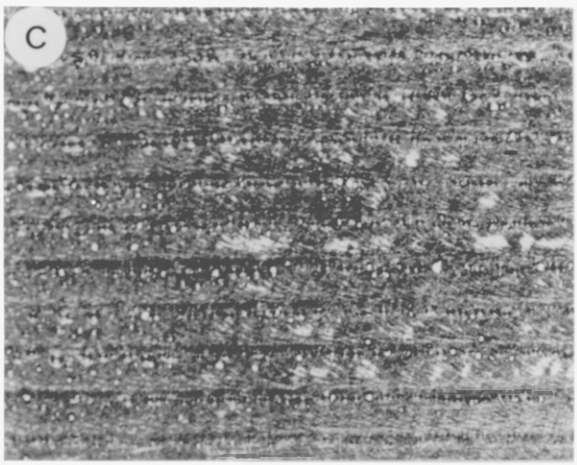
C

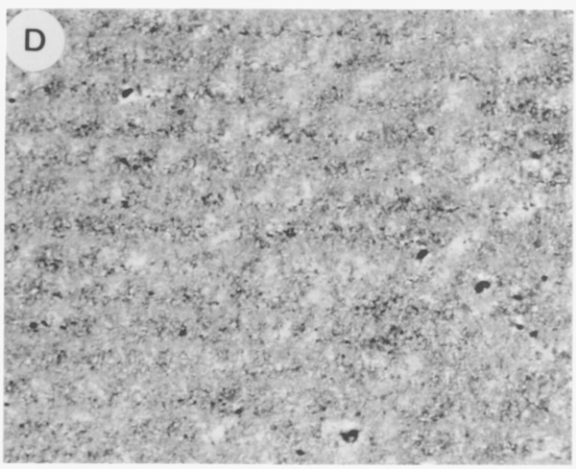
D

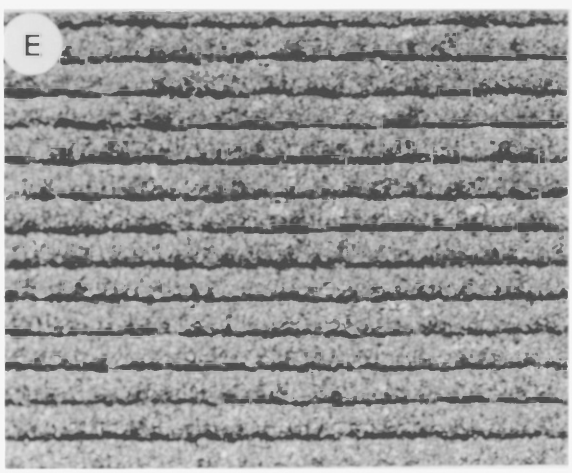
E

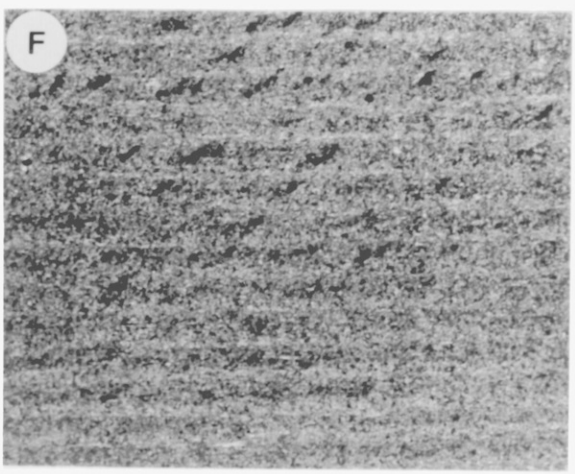
F

be slightly oxidized. However, the extent of oxidation in the case of Alloy 4815 + SiC composite (Fig. 5. 6) clad surface was markedly less than the Alloy 4815 surface.

5.2.2 SiC Injected Clads

Fig. 5.7 shows three clad tracks produced by injecting large SiC particles (250-750 μm) into the mild steel substrate at constant laser power density and traverse speed and different powder feed rates. The proportion of embedded SiC particles increases with the feed rate. Fig. 5.8 shows part of the transverse section of track 3. The SiC particles are partially dissolved with a tendency to crack formation in some undissolved particles. The average height of these tracks was about 1 mm, so that the SiC particle size used was too big for this track dimensions, which led to the formation of large amounts of porosity.

Fig. 5.9 shows a low magnification micrograph of a clad produced using a medium size range (250-450 μm) of SiC particles. Although some SiC particles were also partially dissolved in this series of clads, the extent of internal porosity was much lower than in the other series of clads formed with larger SiC particles (Fig. 5.7). Microcracks were found in the areas surrounding the partially dissolved SiC particles (Fig. 5.10). These microcracks seem to propagate into the matrix regions which were found to be rich in Si and carbon contents (see section 5.3.1) and hence increased brittleness. Fig. 5.11 shows dendritic microstructure of the matrix region consisting of martensite.

5.2.3 Stellite Clads

Fig. 5.12 shows a low magnification transverse section of overlapping clad tracks. The surface of this overlapping clad was not smooth due to a lesser degree of overlapping as compared with the overlapping clads of other series, e.g. stainless steel overlapping clad tracks in Fig. 5.39. The extent of porosity was almost negligible except for a small amount at the clad-substrate interface, particularly in the regions where two tracks were

A. **Fig. 5.7** Macrograph showing plan view of three different single track clads produced by injecting large (250-750 μm) SiC particles into mild steel, Laser power, P = 2 kW, Beam diameter, D = 5 mm, Powder feed rate, F; track 3 = 14 g/min, track 4 (central) = 10 g/min, track 5 = 6 g/min, Substrate traverse speed, S = 6 mm/s, 1.5 X.

B. **Fig. 5.8** Transverse section of track 4 shown in Fig. 5.7, illustrating large embedded SiC particles (1) in the mild steel substrate matrix (2).

C. **Fig. 5.9** Transverse section of a composite clad produced by injecting medium (250-450 μm) SiC into mild steel substrate, P = 2 kW, D = 4 mm, F = 14.1 g/min, S = 6.5 mm/s, (1) = SiC particle, (2) = matrix, (3) = substrate.

D. **Fig. 5.10** A magnified view of Fig. 5.9 showing completely dissolved SiC particle (1) and area rich in Si and carbon contents.

E. **Fig. 5.11** A magnified view of Fig. 5.9 showing the microstructure in the matrix area.

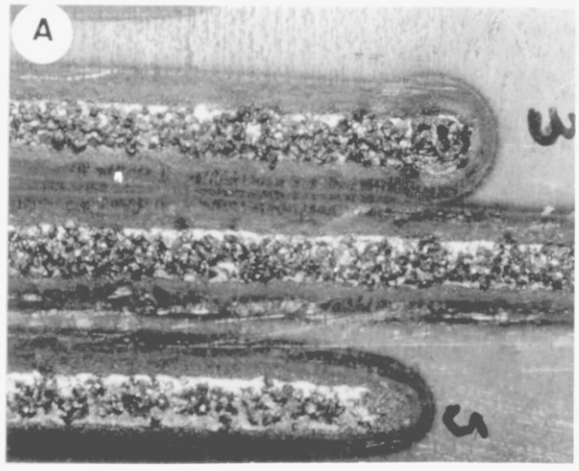
A

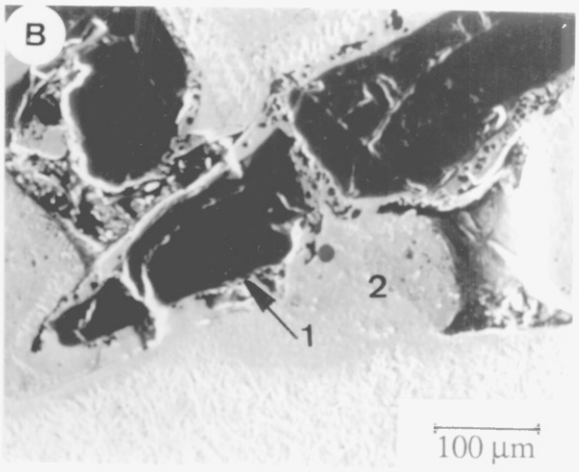
B
1
2
100 µm


C
1
2
3
500 µm

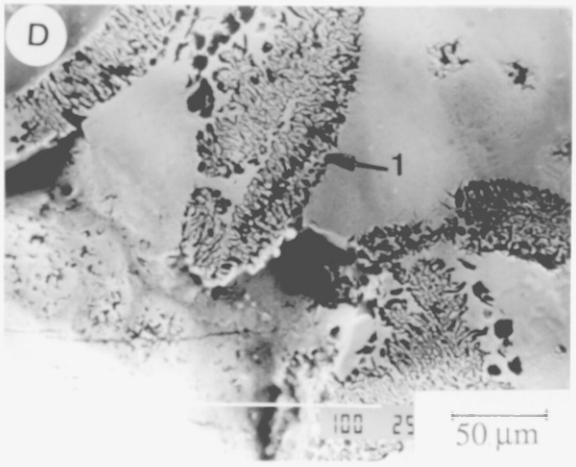
D
1
50 µm

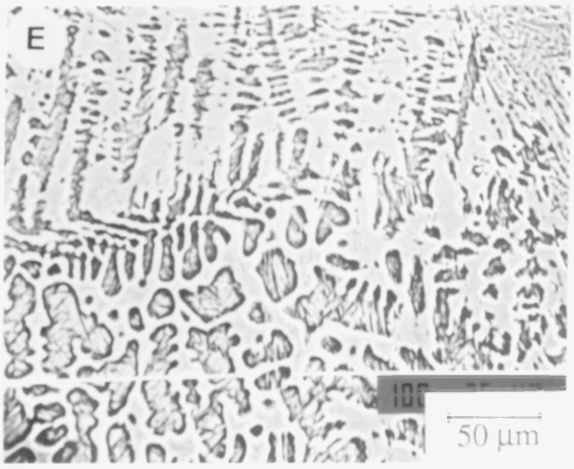
E
50 µm

overlapped. The processing conditions used for producing these clads resulted in a very small area of melting of the substrate (Fig. 5.12) and hence led to a very low dilution of the clad matrix. Although the amount of substrate melting was low, it was sufficient to make a good clad-substrate fusion bonding (Fig. 5.13). Fig. 5.14 shows a micrograph taken from a transverse section of overlapping Stellite clads shown in Fig. 5.12. This micrograph represents a typical solidification structure of Stellite alloy 6, obtained in single tracks also, consisting of primary dendrites, interpreted as Co-rich solid solution of W, Cr, and carbon, with some secondary branching. The secondary dendrite arm spacing was found to be dependent on the cooling rate of the clad matrix. An increase in secondary dendrite arm spacing was obtained with decrease in the substrate traverse speed which resulted in a decreased cooling rate. For example, the mean secondary dendrite arm spacing, in a set of clad tracks formed at constant Stellite feed rate (50 g/min) and laser power density (147 W/mm^2), was found to be increased from ~ 2-3 μm (Fig. 5.15) to ~ 8-10 μm (Fig. 5.16) with decreasing substrate traverse speed from 7.3 mm/s to 2.5 mm/s respectively. Fig. 5.17 shows a TEM micrograph obtained from the thin foil prepared from the overlapping clad tracks. This micrograph shows the typical microstructure of the clad matrix which is expected to consist of primary dendrites of Co-Cr-W-C based solid solution plus interdendritic carbides containing eutectic. Fig. 5.17 is interpreted as showing a dendritic region.

5.2.4 Stellite + SiC

As reported in chapter 4, three particle sizes of SiC were used to produce composites of Stellite + SiC. Fine (50-150 μm) and large (250-750 μm) particle sizes SiC were used to produce both single and overlapping track clads. In the case of clads formed using a mixture of Stellite and fine SiC particles, a large proportion of the SiC particles was dissolved. The remaining small proportion of the fine SiC particles was found to be segregated to the upper regions of the clads (Figs. 5.18-5.20). A small amount of

A. **Fig. 5.12** A transverse section showing overlapping track clad of Stellite, Laser power, P = 1.95 kW, Beam diameter, D = 4 mm, Powder feed rate, F = 22.7 g/min, Substrate traverse speed, S = 4.8 mm/s, Overlapping distance, D = 1.5 mm, (1) = clad, (2) = substrate.

B. **Fig. 5.13** A magnified view of Fig. 5.12 showing clad-substrate interface.

C. **Fig. 5.14** A transverse section of matrix area of overlapping Stellite clad (Fig. 5.12) showing fine dendritic microstructure.

D. **Fig. 5.15** Transverse section of a single track Stellite clad showing finer dendrites as compared with those in Fig. 5.16 due to higher traverse speed, P = 1.85 kW, F = 50 g/min, S = 7.3 mm/s.

E. **Fig. 5.16** Transverse section of a single track Stellite clad showing coarser dendrites as compared with those in Fig. 5.15 due to relatively lower traverse speed, P = 1.85 kW, F = 50 g/min, S = 2.5 mm/s.

F. **Fig. 5.17** TEM of matrix region of overlapping tracks Stellite clad shown in Fig. 5.12.

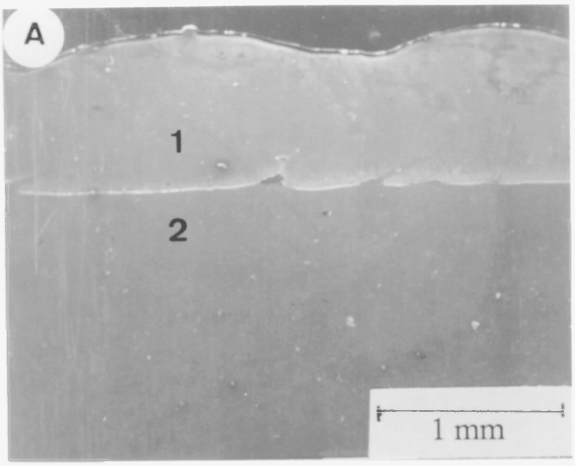
A
1
2
1 mm

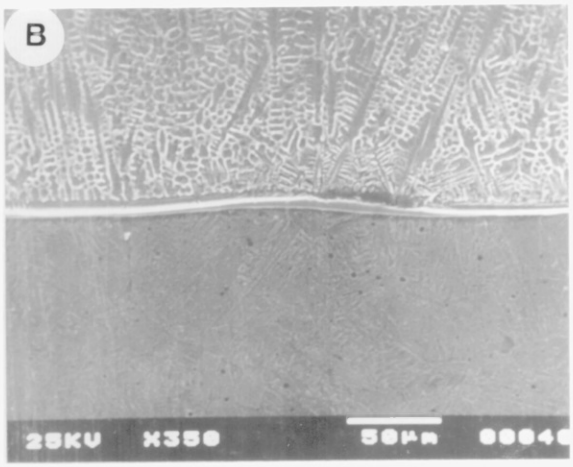
B
25KV X350 50µm

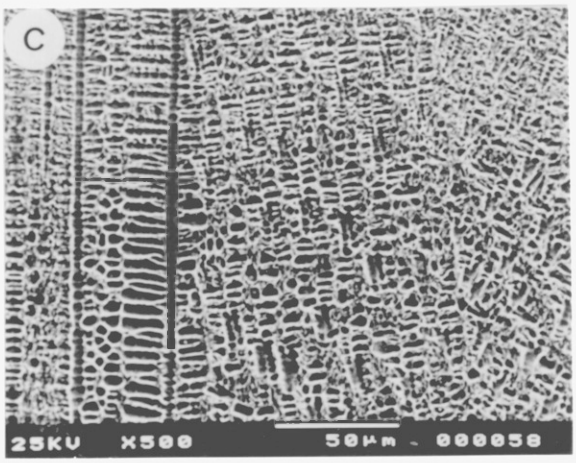
C
25KV X500 50µm

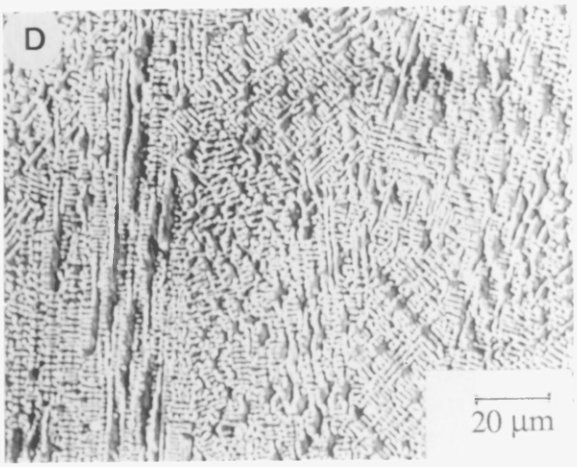
D
20 µm

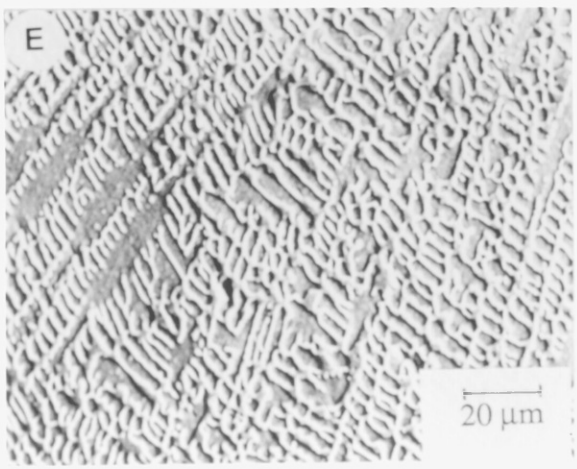
E
20 µm

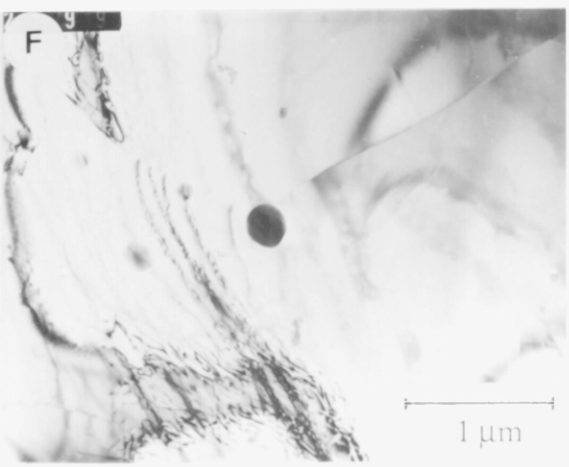
F
1 µm

porosity was found in almost all clads of this series. Some samples also showed a severe extent of microcracks in the matrix regions of the clads (Fig. 5.19), which may be attributed to an increased brittleness of the matrix due to high amounts of carbon from the dissolution of SiC. The area dilution of clads, in this series, was found to be dependent on both total feed rate and wt.% of SiC particles in the cladding powder mixture. For example, at constant Stellite feed rate of 35 g/min, the area dilution of the clad was decreased from 59% (Fig. 5.18) to about 40% (Fig. 5.19) by increasing the total feed rate (Stellite + SiC) from 38.5 g/min to 40.3 g/min respectively. However, at constant SiC feed rate of 7 g/min, a total feed rate of 21.9 g/min showed an area dilution of 59% (Fig. 5.20). Fig. 5.21 shows a micrograph of a transverse section of the clad represented in Fig. 5.19. This micrograph shows a fine dendritic structure, typical of Stellite alloys as also obtained and reported in the previous section for Stellite clads, consisting of carbides of Cr and W and Co-Cr-W-C based solid solution. The carbides formed were interpreted as $M_{23}C_6$ and/or M_7C_3 type carbides, as identified by x-ray diffraction data reported in section 5.4.2. The proportion of these carbides in the composite clads is expected to be larger than that obtained in the case of Stellite alloy, due to the higher amounts of carbon from the dissolution of SiC.

Fig. 5.22 shows a low magnification transverse section of a composite clad produce by blowing a mixture of Stellite and large (250-750 μm) SiC particles. The volume % of SiC particles in the clad matrix was about 50; they were not finely distributed in the matrix but rather floated to the upper surface of the matrix due to their low density (3.2 g/cm^3) as compared with Stellite (8.3 g/cm^3). In this clad the large SiC particles were slightly dissolved in the matrix. However, the high ratio of SiC to clad matrix resulted in the induction of high stresses around the SiC particles. Severe cracks were seen near the SiC particles (Fig. 5.23), which were propagated into the matrix down to the clad-substrate interface, as a result of the high stresses produced in the surrounding areas of SiC particles due to also the difference in their thermal properties with Stellite matrix.

A. **Fig. 5.18** SEM of Stellite + SiC (50-150 μm) clad track. SiC particles were almost completely dissolved in this series of experiments, Laser power, P = 1.85 kW, Beam diameter, D = 4 mm, Powder feed rate, F; Stellite = 35 g/min, SiC = 3.5 g/min, Traverse speed, S = 7 mm/s, % Area dilution = 59, (1) = clad track, (2) substrate.

B. **Fig. 5.19** SEM of Stellite + SiC (50-150 μm) clad track. SiC particles were almost completely dissolved in this series of experiments, P = 1.85 kW, D = 4 mm, F; Stellite = 35 g/min, SiC = 5.3 g/min, S = 7 mm/s, % Area dilution = 40.

C. **Fig. 5.20** SEM of Stellite + SiC (50-150 μm) clad track. SiC particles were almost completely dissolved in this series of experiments, P = 1.85 kW, D = 4 mm, F; Stellite = 14.9 g/min, SiC = 7 g/min, S = 7 mm/s, % Area dilution = 59.

D. **Fig. 5.21** Transverse section of matrix region of Stellite + SiC clad (Fig. 5.19), showing dendritic structure.

E. **Fig. 5.22** Transverse section of a Stellite + SiC (250-750 μm) clad showing large embedded SiC particles in the Stellite matrix, P = 1.92 kW, D = 4 mm, F; Stellite = 35 g/min, SiC = 5 g/min, S = 9 mm/s.
1 = SiC particle, 2 = matrix region, 3 = substrate.

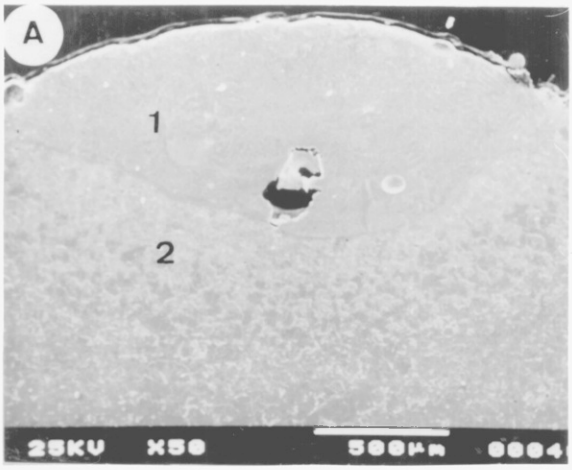
A
1
2
25KV X50

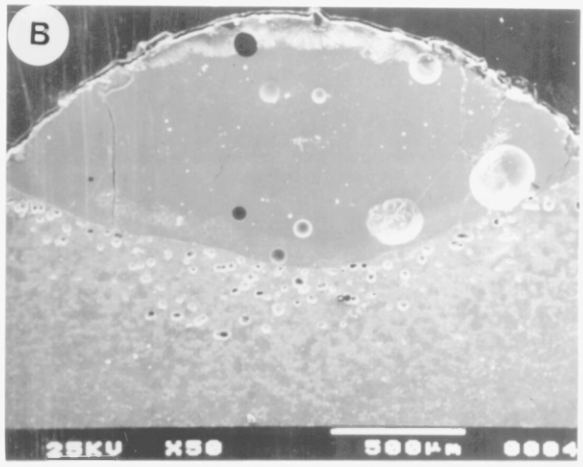
B
25KV X50

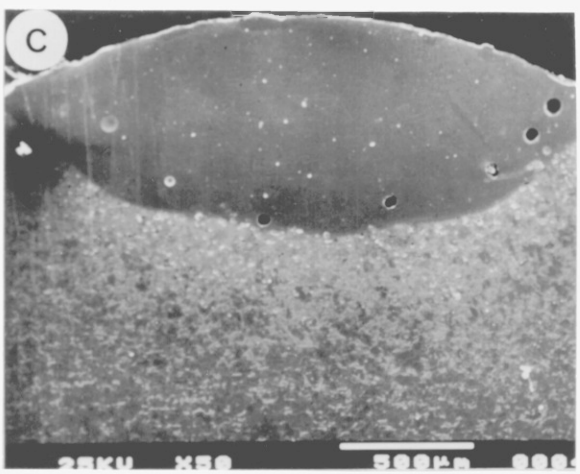
C

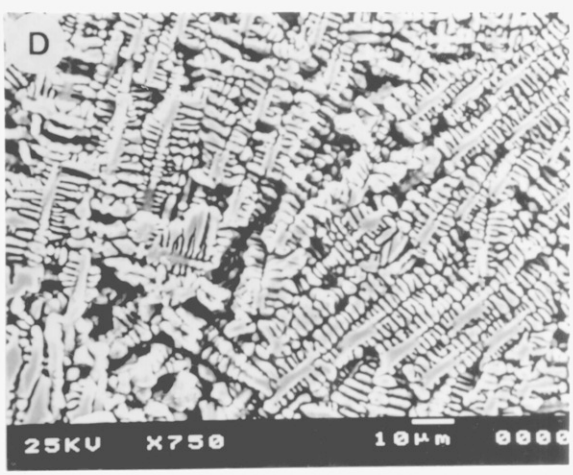
D
25KV X750
10µm

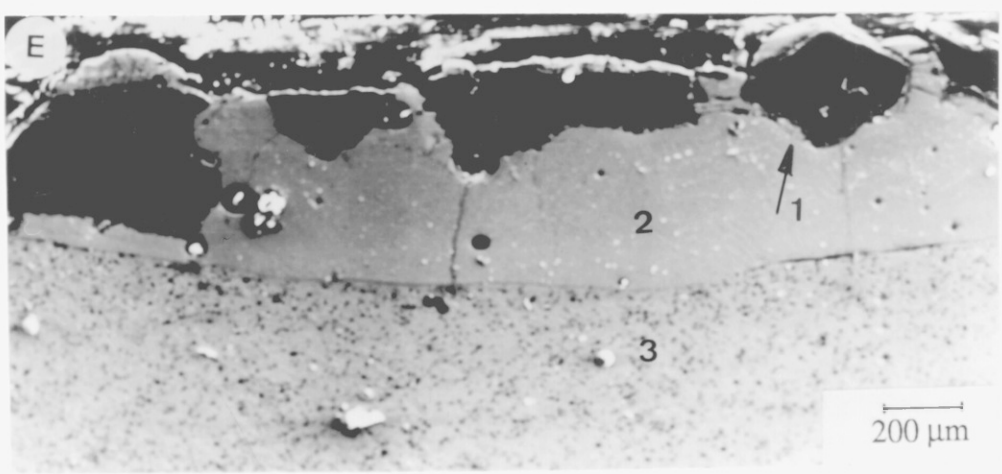
E
1
2
3
200 µm

Fig. 5.24 shows the typical dendritic structure of the matrix area of this clad; the nature of the interdendritic regions has not been determined.

In the series of clads produced with Stellite + SiC (medium particle size, i.e. 250-450 μm), the degree of dissolution of SiC was higher as compared with the previous series with large SiC particles due to the processing conditions used (relatively lower traverse speed). However, the SiC particles were segregated to the upper regions of the clad (Fig. 5.25) as in the other two series. Some SiC particles were found to be completely dissolved and tended to resolidify as fine SiC particles, Fig. 5.26 (as also identified by the x-ray diffraction data). A few large SiC particles appeared to be fractured due possibly to thermal shocks (Fig. 5.27)

Fig. 5.28 shows a low magnification transverse section of overlapping Stellite + 20 wt.% SiC clads. In this series also, the fine SiC particles were dissolved while the rest were segregated to the top surface of the clad. A smooth overlapped clad surface with excellent fusion bonding with the substrate was obtained. Fig. 5.29 shows the dendritic microstructure of the matrix region of the clad similar to that obtained in the other series of Stellite + SiC composites. Fig. 5.30 represents a high voltage TEM micrograph of the same sample showing the regions of duplex structure; this is interpreted as carbide-containing eutectic in the regions between the Co-solid solution dendrites

5.2.5 Alloy 4815 Clads

The overlapping Alloy 4815 clads tracks were about 2.3 mm high with a smooth surface and excellent fusion bonding with the substrate (Fig. 5.31). Since the Alloy 4815 is an iron base alloy containing more than 95% Fe, there was little etching contrast between the clad and the heat affected zone of the mild steel substrate. Hence, the clad-substrate interface appeared on the micrograph (Fig. 5.32) as a very thin dividing line. Fig. 5.33 shows a transverse section of the overlapping clad which is interpreted as fine

A. **Fig. 5.23** A magnified section of Fig. 5.22 showing shrinkage cavity and micro-cracks around a large SiC particle.

B. **Fig. 5.24** SEM of matrix region of clad shown in Figs. 5.22 and 5.23, illustrating dendritic microstructure.

C. **Fig. 5.25** A part of the transverse section of Stellite + SiC (250-450 μm) clad showing SiC particles segregated to the upper regions of matrix, P = 1.9 kW, D = 5 mm, F (Stellite + 20 wt.% SiC) = 10 g/min, S = 5 mm/s, (1) = SiC particle, (2) = partially dissolved SiC particle, (3) = Stellite matrix, (4) = substrate.

D. **Fig. 5.26** A high magnification SEM of matrix region of Stellite + SiC clad shown in Fig. 5.25, illustrating some completely dissolved SiC particles (1).

E. **Fig. 5.27** A magnified section of matrix region of clad shown in Figs. 5.25 and 5.26, illustrating fracture of large SiC particle, (1) = partial dissolution of SiC, (2) = SiC particle, (3) = fractured region of SiC, (4) = matrix region of clad.

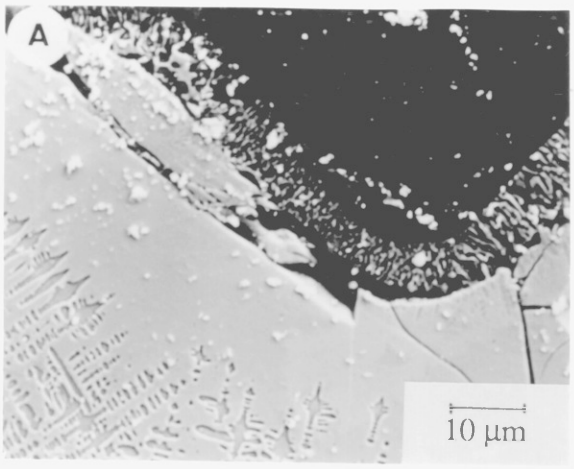
A
10 µm

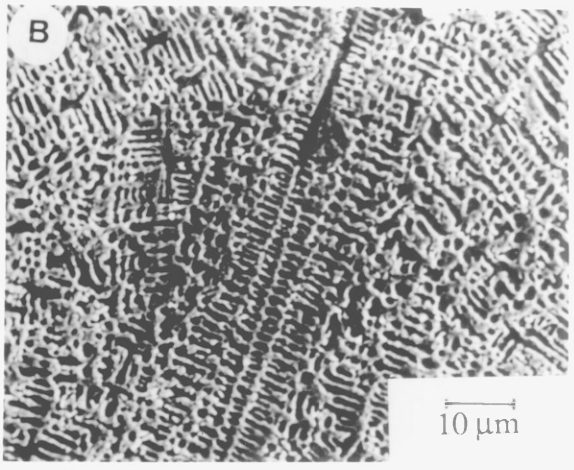
B
10 µm

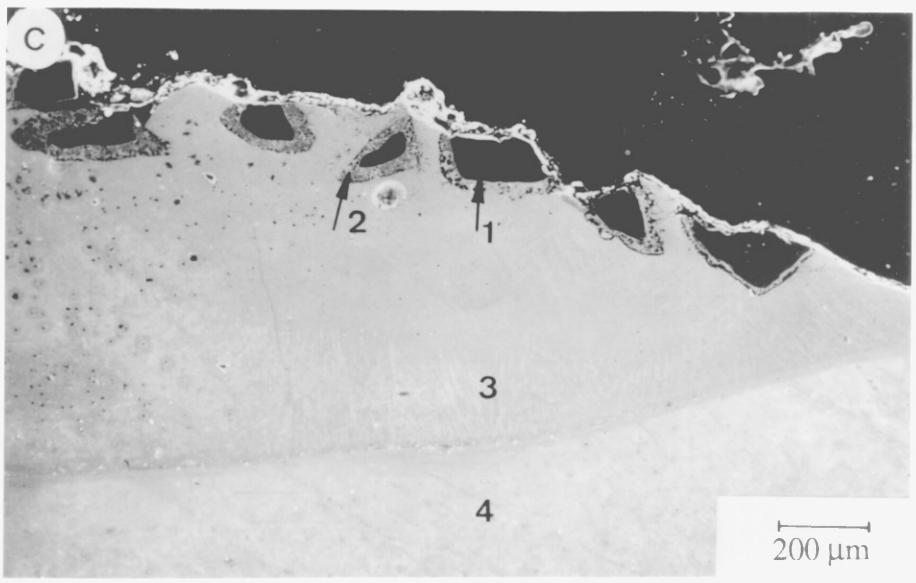
C
2
1
3
4
200 µm

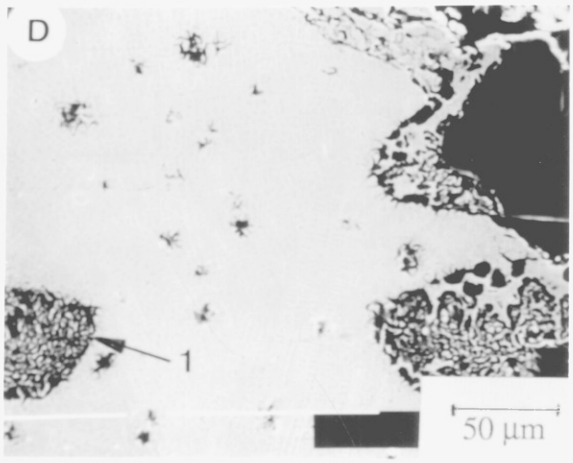
D
1
50 µm

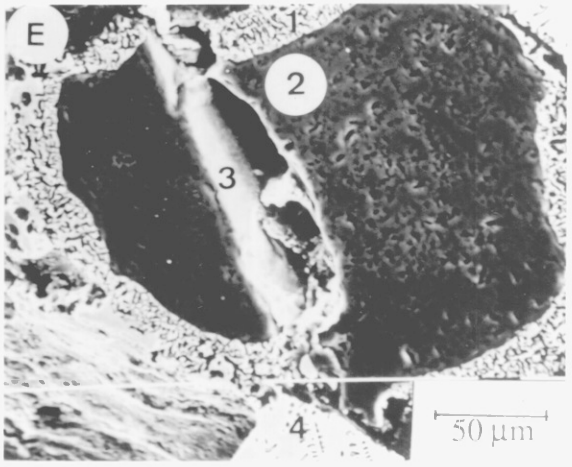
E
1
2
3
4
50 µm

A. **Fig. 5.28** Transverse section of overlapping tracks clad of Stellite + 20 wt.% SiC, Laser power, P = 1.9 kW, Beam diameter, D = 5 mm, Powder feed rate, F = 10 g/min, Traverse speed, S = 4.5 mm/s, Overlapping distance, d = 2 mm.

B. **Fig. 5.29** Transverse section of matrix region of Stellite + SiC clad shown in Fig. 5.28, illustrating fine dendritic microstructure.

C. **Fig. 5.30** A high voltage TEM of Stellite + SiC clad shown in Figs. 5.28 and 5.29 showing eutectic between the regions of Co solid solution.

D. **Fig. 5.31** Transverse section of overlapping tracks of Alloy 4815 clad showing complete mixing of two tracks at overlapping point, P = 1.9, D = 5 mm, F = 13 g/min, S = 2.5 mm/s, d = 2.5 mm.

E. **Fig. 5.32** A high magnification SEM of Alloy 4815 clad shown in Fig. 5.31, illustrating clad-substrate interface, (1) = clad matrix, (2) = clad-substrate interface, (3) = substrate.

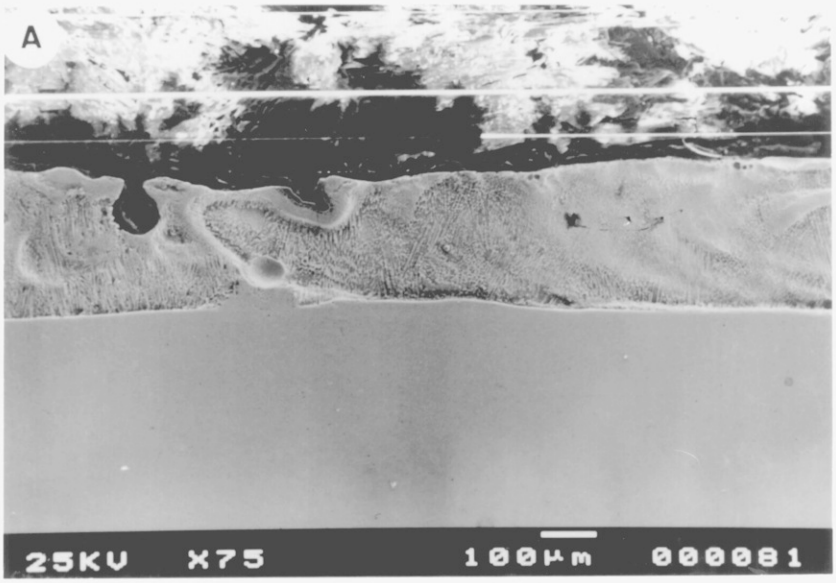
A
25KV X75 100µm 000081

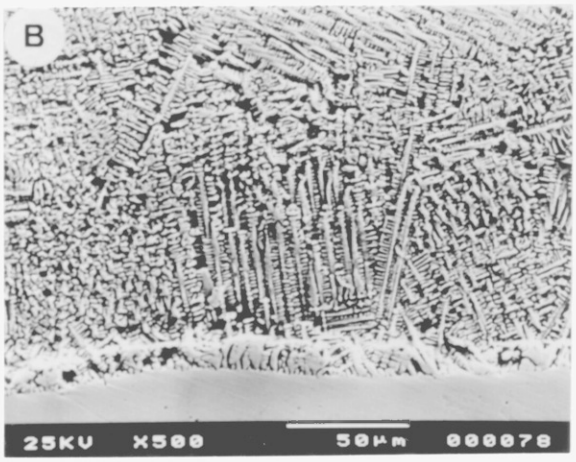
B
25KV X500 50µm 000078


C
1 µm

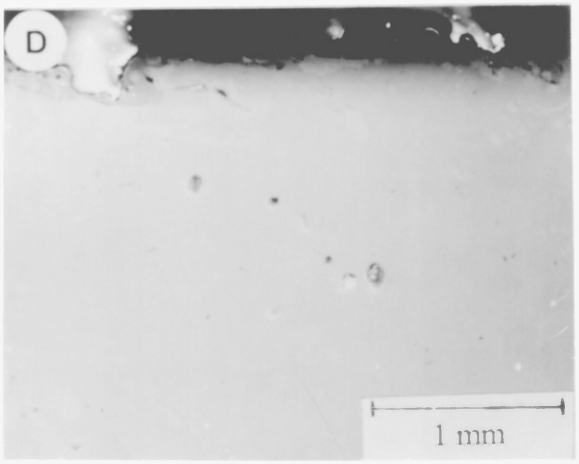
D
1 mm

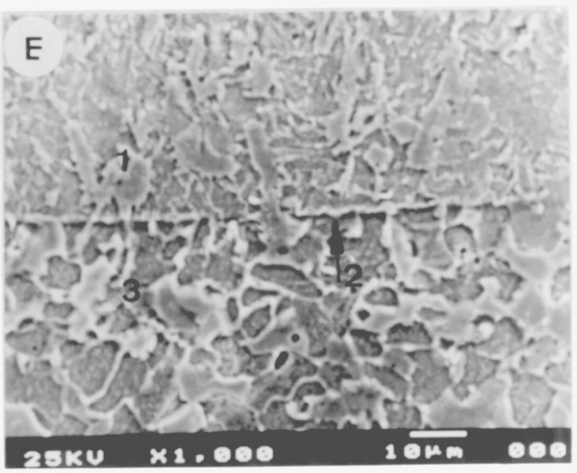
E
1
2
3
25KV X1,000 10µm 000

pearlite + ferrite due to a relatively lower cooling rate resulted from relatively lower traverse speed and also large clad height.

5.2.6 Alloy 4815 + SiC Clads

Fig. 5.34 shows an overlapping track clad. The height of the tracks was about 1 mm. The overlapping was so effective that a very smooth surface was obtained. In this clad too, SiC particles were segregated to the upper regions of the clad and can been seen on the top surface. Large spherical pores were found (Fig. 5.34), the shape suggesting that they resulted from entrapped gas bubbles. Excellent fusion bonding occurred at the interface of the clad-substrate, with the solidification of a smaller planar region (Fig. 5.35). Fig. 5.36 shows a transverse section taken from the starting end of the overlapping track clad. The SiC particles in the overlapping track clads were dissolved to a larger extent due to partial melting of the previously formed track. Martensitic transformation occurred in this clad. A magnified view of Fig. 5.36 is illustrated in Fig. 5.37, which shows a matrix region having a martensitic microstructure with a small amount of porosity. A high voltage TEM micrograph (Fig. 5.38) also showed the evidence of martensite formation in this clad.

5.2.7 Stainless Steel Clads

Fig. 5.39 shows a low magnification micrograph of an overlapping track clad. The height of the overlapping clad is about 2 mm. A smooth clad surface, resulting from adequate overlapping of tracks, was obtained. However, some large unexpected and unusual shaped voids were formed near the clad-substrate interface especially at the regions where tracks overlapped. A good fusion bonding of clad with the substrate was achieved with a relatively wide planar region (Fig. 5.40). A transverse section of this

A. **Fig. 5.33** Transverse section of Alloy 4815 clad shown in Fig. 5.31, illustrating fine pearlite + ferrite microstructure.

B. **Fig. 5.34** Transverse section of overlapping tracks clad of Alloy 4815 + 20 wt.% SiC, P = 1.9 kW, D = 5 mm, F = 10 g/min, S = 4.5 mm/s, d = 2 mm, (1) = overlapping region of two tracks.

C. **Fig. 5.35** A high magnification SEM of Alloy + SiC clad (Fig. 5.34) showing clad-substrate interface.

D. **Fig. 5.36** Transverse section of a part of overlapping Alloy 4815 + SiC clad (Fig. 5.34) showing SiC particles (1) in the upper region of clad.

E. **Fig. 5.37** A magnified section of Fig. 5.36, showing martensite in the matrix region of clad.

F. **Fig. 5.38** TEM of Alloy 4815 + SiC clad (Fig. 5.34) showing martensite in the matrix region of clad.

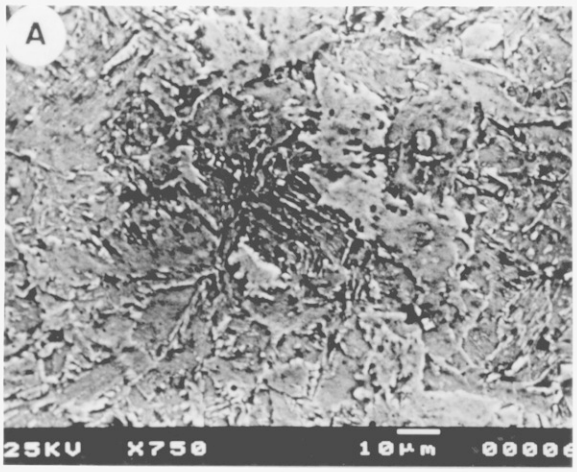
A
25KV X750 10µm

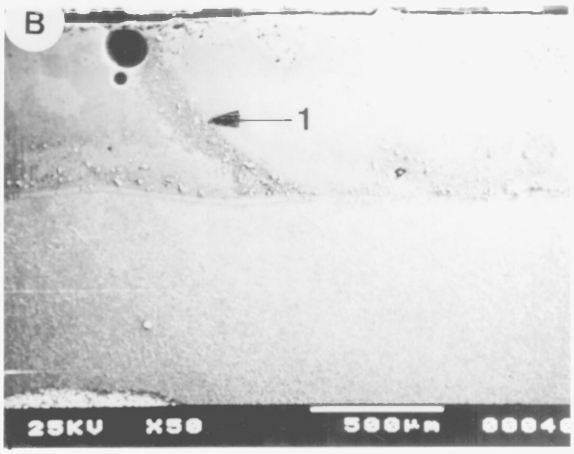
B
1
25KV X50 500µm

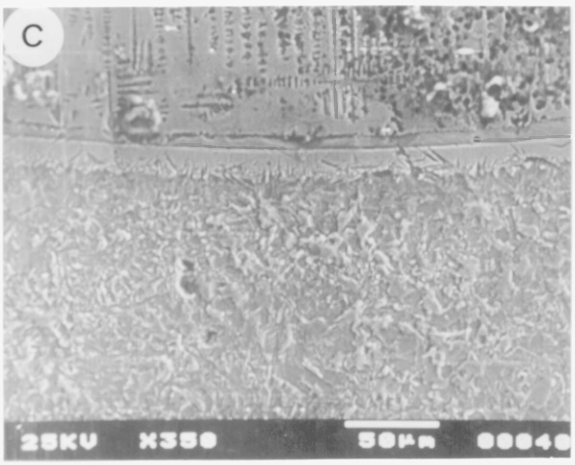
C
25KV X350 50µm


D
1
2
25KV X150 100µm

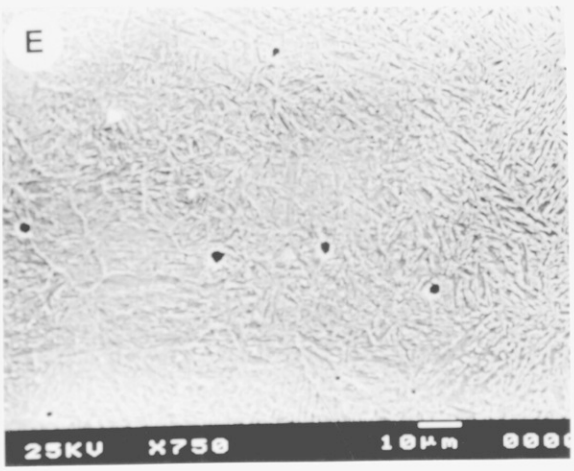
E
25KV X750 10µm

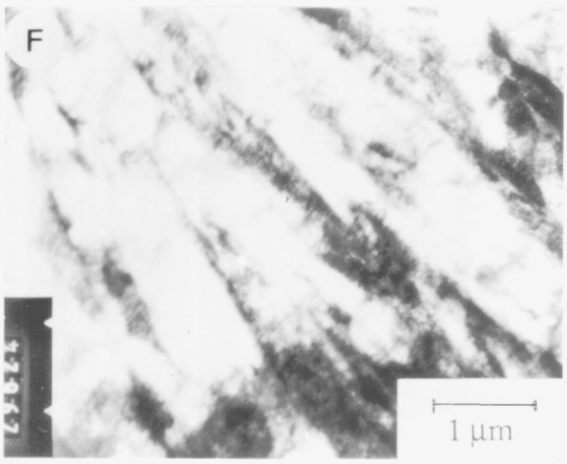
F
1 µm

sample with a dendritic microstructure typical of rapidly solidified austenitic stainless steel is shown in Fig. 5.41.

5.2.8 Stainless Steel + SiC Clads

As in the case of Stellite + SiC composite clads, most of the SiC was dissolved in the stainless steel + SiC clads with some small SiC particles embedded on the top of the clad surface (Fig. 5.42). Almost no porosity was found in the matrix region of the clad. Fusion bonding of clad with the substrate was excellent with a narrow planar region at the clad-substrate solidification front (Fig. 5.43). A homogeneous microstructure throughout the overlapping track clads was achieved. A transverse section of this clad is shown in Fig. 5.44. The microstructure obtained in stainless steel + SiC composite clads was finer (with an average secondary dendrite arm spacing of ~ 5 μm) than the stainless steel clads due to the relatively smaller clad dimensions (1 mm height) and higher traverse speed (4.5 mm/s) in the case of the former as compared with that of the latter (2 mm height and 2.5 mm/s traverse speed).

5.3 COMPOSITIONAL ANALYSES OF VARIOUS CLADS

Compositional analyses of various single and overlapping track clads were carried out using an electron micro probe analyser to determine the compositional homogeneity of the clads and also dilutions resulted from the melting of the substrate. An area of about 10 x 10 μm at various positions of the clads was selected for the analysis. Some typical composition results obtained from the matrix regions of various clads are reported here.

A. **Fig. 5.39** Transverse section of an overlapping tracks clad of stainless steel clad, Laser power, P = 1.9 kW, Beam diameter, D = 5 mm, Powder feed rate, F = 11.2 g/min, Traverse speed, S = 2.5 mm/s, Overlapping distance, d = 2.5 mm, (1) = matrix region of clad, (2) = porosity, (3) = substrate.

B. **Fig. 5.40** A high magnification SEM of stainless steel (Fig. 5.39) showing clad-substrate interface.

C. **Fig. 5.41** Transverse section of matrix region of stainless steel clad (Fig. 5.39) showing fine dendritic structure.

D. **Fig. 5.42** Transverse section of an overlapping track stainless steel + 20 wt.% SiC clad, P = 1.9 kW, D = 5 mm, F = 9 g/min, S = 4.5 mm/s, d = 2 mm.

E. **Fig. 5.43** A high magnification SEM of stainless steel + SiC clad (Fig. 5.42), showing clad-substrate interface.

F. **Fig. 5.44** Transverse section of stainless steel + SiC clad showing fine dendritic microstructure in the matrix region.

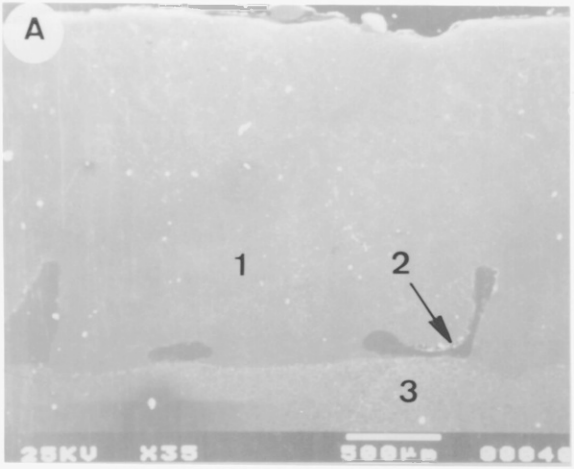
A
1
2
3
25KV X35

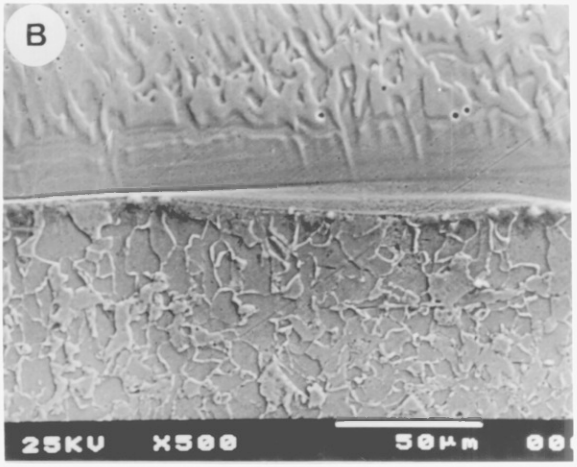
B
25KV X500 50µm

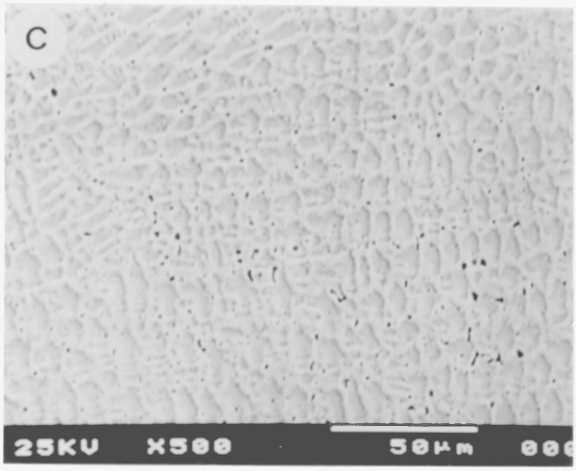
C
25KV X500 50µm

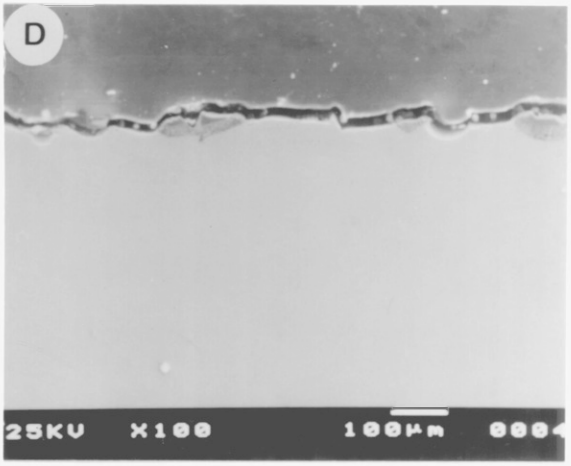
D
25KV X100 100µm

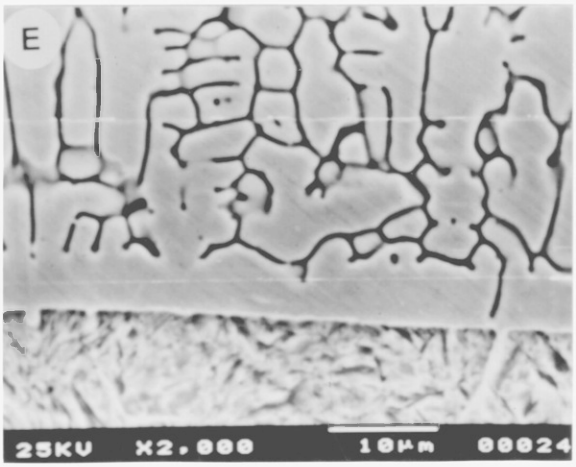
E
25KV X2,000 10µm

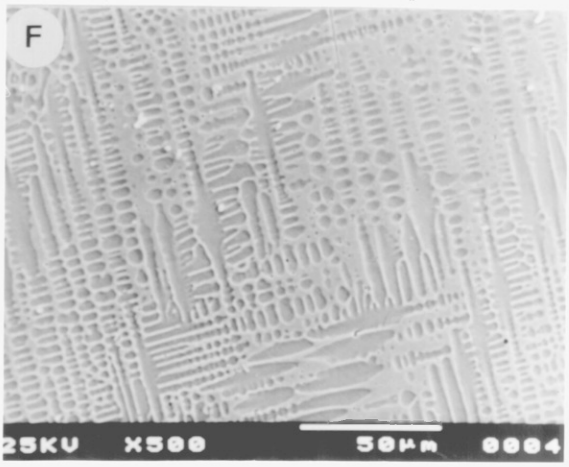
F
25KV X500 50µm

5.3.1 SiC Injected Mild Steel Clads

Table 5.1 shows the chemical composition of the matrix region of a SiC injected mild steel clad. The composition was almost the same (± 5%) throughout the clad except in the regions adjacent to the partially dissolved SiC particles; these regions were higher, as was expected, in the Si content.

Table 5.1

Compositional Analysis of SiC Injected Clads.

Elements	Wt.% in matrix area	Wt.% near partially dissolved SiC
Fe	90.4	84.0
Si	6.8	12.5
Mn	0.5	0.7
Total	97.7*	97.2*

* The balance is assumed to be C dissociated from SiC dissolution, 1.9 and 3.6 wt.% respectively

5.3.2 Stellite Clads

Compositional analyses of a few typical single track Stellite clads formed at constant traverse speed and various powder feed rates are given in Table 5.2. The concentrations of the alloying elements (present in the applied cladding powder) were found to be increased in the clad matrix with increasing powder feed rate. The iron content of the clad matrix was decreased from ~ 10% to 5.8% as the powder feed rate was increased from 23 g/min to 50 g/min. Despite the relatively lower traverse speed (2.5 mm/s) and powder feed rate (12.4 g/min) as compared with the single tracks, the iron content of the overlapping track Stellite clad was about 8.5% (Table 5.3); this is attributed to the fact

Table 5.2

Compositional Analysis of Single Track Stellite Clads

(Traverse speed = 7.5 mm/s, Feed rate; S1 = 23 g/min, S2 = 35 g/min, S3 = 50 g/min)

Elements	Wt.% in the applied powder	Wt.% S1	Wt.% S2	Wt.% S3
Co	60.0	56.1	58.4	60.0
Cr	28.0	27.3	27.6	27.3
W	4.0	3.6	3.6	4.0
Ni	2.0	1.1	1.0	1.6
Fe	~5.0	10.1	7.5	5.8
Total	99*	98.2*	98.1*	98.7*

* About 1.1 wt.% carbon was present in the applied powder.

Table 5.3

Compositional Analyses of Overlapping Track Stellite Clads

(Traverse speed = 2.5 mm/s, Powder feed rate = 12.4 g/min)

Elements	Wt.% in applied powder	Wt.% in clad matrix
Co	60.0	58.6
Cr	28.0	26.0
W	4.0	4.0
Ni	2.0	1.5
Fe	5.0	8.5
Total	99.0*	98.6*

* About 1.1 wt.% carbon was present in the cladding powder.

that in the overlapping, in producing the consecutive clads a part of the preclad track is melted rather than the complete substrate and hence the dilution by the substrate is decreased.

5.3.3 Stellite + SiC Clads

Some typical compositional analyses of the single track clads produced in the series feeding separately Stellite and SiC powders, to achieve composites of various compositions , are reported in Table 5.4. The composition was uniform throughout the matrix region of the clad. The iron content of the clad was found to be dependent on both the total feed rate (Stellite + SiC) and the wt.% of SiC in the cladding powder mixture; a decrease in the iron content of the matrix with increase in the powder feed rate was observed.

The composition of an overlapping track clad of Stellite + 10 wt.% SiC is given in Table 5.5. The matrix region of the clad was homogeneous in composition. However, the area adjacent to partially dissolved SiC particles in the upper regions of the clads was higher in the Si content. The dilution of the matrix region of the overlapping track clad by iron from the substrate was markedly lower (< 20%) than that obtained in the other series of single tracks (> 40%, Table 5.4).

5.3.4 Stainless Steel and its Composite with SiC

The compositional analyses of overlapping track clads of stainless steel and stainless steel + SiC clads are reported in Table 5.6. In both of these clads, the concentrations of various alloying elements were very uniform in all regions of the matrix. However, in the composite clad, marked decrease in the content of the alloying elements (e.g. Cr, Ni, Mo) was found. This decrease was replaced by the increase in the iron from the substrate and Si from partial dissolution of SiC.

5.3.5 Alloy 4815 and its Composite with SiC

Table 5.7 shows the chemical analyses of overlapping track clads of Alloy 4815 and Alloy 4815 + 20 wt.% SiC composite. The composition was almost uniform in all the regions of the matrices of both the alloy and composite clads. However, a slight decrease in the concentrations of the alloying elements (e.g. Ni and Mo) was observed. This decrease was comparatively higher in the case of the composite clad as it gained about 6.5% Si from the partial solution of SiC particles and hence the iron content was also decreased accordingly.

Table 5.4

Compositional Analyses of Single Track Clads of Stellite + SiC

(Power = 1.8 kW, Traverse speed = 7 mm/s, Powder feed rate; S1, Stellite = 35 g/min, SiC = 3.5 g/min, S2, Stellite = 35 g/min, SiC = 4.3 g/min, S3, Stellite = 20.5 g/min, SiC = 7 g/min)

Elements	Wt.% in powder	Wt.% S1	Wt.% S2	Wt.% S3
Co	60.0	25.0	29.3	25.8
Cr	28.0	13.1	14.5	9.1
W	4.0	2.7	2.8	2.0
Ni	2.0	0.7	1.2	1.1
Fe	5.0	51.0	41.7	46.2
Si	-	4.8	6.3	11.2
Total	99.0	97.3*	95.8*	95.4*

* Balance is amount of carbon; 1.1 wt.% in the applied Stellite powder + from the dissociation of SiC, 2.5, 3, and 4.5 wt.% respectively.

Table 5.5

Compositional Analyses of Overlapping Clad Tracks of Stellite + 10 wt.% SiC

(Power = 1.8 kW, Powder feed rate = 36 g/min, Traverse speed = 20 mm/s)

Elements	Wt.% in powder	Wt.% in the centre of the clad matrix	Wt.% near partially dissolved SiC
Co	60.0	49.4	46.2
Cr	28.0	22.9	21.5
W	4.0	3.9	3.4
Ni	2.0	1.1	1.2
Si	-	2.3	3.8
Fe	5.0	19.2	21.6
Total	99.0	98.8*	97.7*

* Balance is carbon, 1.1 wt.% from the powder and rest from the dissociation of SiC, 1.8 and 2.2 wt.% respectively.

Table 5.6

Compositional Analyses of Overlapping Track Clads of Stainless Steel, (Power = 1.9 kW, Powder feed rate = 11.2 g/min, Traverse speed = 2.5 mm/s)and Stainless Steel + 20 wt.% SiC (Power = 1.9 kW, Powder feed rate = 9 g/min, Traverse speed = 4.5 mm/s).

Elements	Wt.% in powder	Wt.% in alloy clad	Wt.% in composite
Cr	20.0	19.6	6.9
Ni	18.0	17.2	4.8
Mo	6.0	5.7	2.0
Si	-	-	5.4
Fe	bal.	57.0	78.7
Total	100	99.5	97.8*

* Balance is carbon dissociated from SiC.

Table 5.7

Compositional Analyses of Overlapping Track Clads of Alloy 4815 (Power = 1.9 kW, Powder feed rate = 13 g/min, Traverse speed = 2.5 mm/s) and Alloy 4815 + 20 wt.% SiC (Power = 1.9 kW, Powder feed rate = 10 g/min, Traverse speed = 4.5 mm/s)

Elements	Wt.% in powder	Wt.% in alloy clad	Wt.% in composite
Ni	3.5	3.1	2.5
Mo	0.3	0.2	0.1
Si	0.27	0.3	6.5
Mn	0.25	0.2	0.3
C	0.15	-	1.9*
Fe	bal.	95.2	89.0
Total	100	99.0	98.3

* Calculated as dissociated from SiC.

5.4 X-RAY DIFFRACTION

X-ray diffraction was used to identify various phases present in the matrix regions of single and overlapping track clads of the various alloy and composite samples. The experimental 'd' values obtained were compared with the standard 'd' values of phases that might form, as also reported in the literature. Since the x-ray diffraction data obtained by using different samples (produced at various feed rates) of a given alloy and composite showed almost the same phases (peaks), and also because a detailed study of x-ray diffraction technique is not the main aim of this thesis, only typical x-ray data from each set of clads is reported here. For this purpose, the x-ray data selected and reported here were obtained from the samples prepared from series of experiments carried out to produce overlapping clads of Stellite, stainless steel, Alloy 4815 and their composites

with 20 wt.% SiC. However, the data reported for SiC injected into mild steel substrate were obtained from a single track clad subjected to x-ray diffraction.

5.4.1 SiC Injected Mild Steel Clads

The x-ray data for SiC injected clads are shown in Table 5.8. The data show the presence of a ferrite/martensite phase in the matrix region with some strong peaks of SiC obtained from embedded SiC particles. Some weak peaks possibly corresponding to cementite were also obtained.

Table 5.8

X-ray diffraction data for SiC injected clad.

d(exp), °A	I/Io (exp)	d(std), °A	I/Io (std)	Suggested phase
3.0254	5	3.024	3	Fe_3C
2.52	70	2.53	100	SiC
2.0833	20	2.09	20	SiC
2.03	100	2.026	100	Ferrite/martensite
1.5406	5	1.546	80	SiC, Fe_3C
1.4336	12	1.4332	20	Ferrite
1.4219	8	1.41	30	SiC
1.1706	20	1.1702	30	Ferrite
1.1683	15	1.162	20	Fe_3C
1.013	8	1.0134	10	Ferrite

5.4.2 Stellite and its Composite with SiC

X-ray data for Stellite and its composite with SiC are reported in Tables 5.9 and 5.10 respectively. The main phases expected in Stellite clad were Co (fcc) and Co (cph) with a small amount of $M_{23}C_6$ and/or M_7C_3 type carbide. Most of the peaks for these phases were found to have clearly similar 'd' values leading to overlapping peaks. However, some strong discrete peaks were also obtained.

In the case of Stellite + SiC sample, the main phases identified were also Co (fcc) and Co (cph) with possible evidence of $M_{23}C_6$ and M_7C_3 type carbides formation. Although most of the peaks for these phases were overlapping like in the case of Stellite alloy, a number of distinct peaks for individual phases were also observed. Some strong peaks of SiC were also obtained which showed the presence of SiC in the matrix region. As the SiC particles were segregated to the upper regions of the clads due to their low density, and also as the 0.25 mm top clad layer was removed to make the sample smooth, the reason for the presence of SiC in the matrix region can be two fold; firstly, the presence of some undissolved fine embedded particles in the matrix from the powder feed and secondly complete dissolution of SiC particles and resolidification as fine particles.

Table 5.9
X-ray data for Stellite clad.

d (exp), °A	I/Io exp	Co (fcc) std values		Co (cph) std values		M_7C_3 std values		$M_{23}C_6$ std values	
		d	I/Io	d	I/Io	d	I/Io	d	I/Io
3.028	15	-	-	-	-	3.039	2	3.077	1
2.062	100	2.0467	100	-	-	2.0489	100	-	-
2.049	60	-	-	2.023	60	2.0256	13	-	-
1.780	100	1.7723	40	1.910	100	1.7883	3	1.8016	22
1.2653	30	1.2532	25	1.252	80	1.2622	3	1.2560	12
1.080	35	1.0688	30	1.083	20	1.1248	2	1.0879	6

5.4.3 Stainless Steel and its Composite with SiC

Tables 5.11 and 5.12 show the x-ray data obtained from the samples of stainless steel and its composite with SiC respectively. The peaks obtained in the stainless steel samples were all distinct and strong corresponding to austenite phase. In the case of stainless steel + SiC composite samples peaks for austenite and Cr_7C_3 were obtained. The formation of Cr_7C_3 was expected due to partial dissolution of SiC and hence enrichment of the matrix in carbon content. However, no peak for SiC was obtained.

5.4.4 Alloy 4815 and its Composite with SiC

X-ray data for Alloy 4815 and Alloy 4815 + SiC composite samples are given in Tables 5.13 and 5.14 respectively. X-ray peaks from Alloy 4815 sample showed the presence of typical phases, i.e. ferrite and cementite. In the case of Alloy 4815 + SiC composite sample, some strong peaks corresponding to SiC were also obtained. The reasons for the presence of SiC in the matrix region were the same as in the case of Stellite + SiC.

Table 5.10

X-ray diffraction data for Stellite + SiC composite sample.

d (exp), °A	I/Io exp	Co std values		SiC std values		M_7C_3 std values		$M_{23}C_6$ std values	
		d	I/Io	d	I/Io	d	I/Io	d	I/Io
3.3607	20	-	-	-	-	-	-	3.214	1
3.0254	10	-	-	-	-	3.039	2	3.077	1
2.6196	8	-	-	2.63	50	-	-	2.666	4
2.5061	100	-	-	2.53	100	-	-	-	-
2.1253	12	2.165	20*	2.17	10	2.1412	6	-	-
2.1111	10	-	-	2.09	20	2.1231	46	-	-
2.0787	65	2.0467	100**	-	-	2.0489	100	2.052	100
2.0214	18	2.023	60*	2.01	30	2.0256	13	-	-
1.9919	100	1.910	100*	-	-	1.9662	1	-	-
1.875	15	-	-	-	-	1.8490	11	1.8840	20
1.8295	10	1.772	40**	-	-	-	-	1.8016	22
1.6626	8	-	-	1.66	10	-	-	1.6857	2
1.5406	30	-	-	1.54	80	-	-	-	-
1.4700	8	-	-	1.497	10	1.4404	5	1.4788	1
1.4143	15	-	-	1.410	30	1.4157	1	-	-
1.3136	20	-	-	1.313	70	1.3281	1	1.3327	2
1.2214	15	1.25	25+	1.229	10	1.2151	3	1.2227	15
1.1983	10	-	-	-	-	1.2107	12	1.1920	2
1.1534	25	1.149	80	1.114	10	1.1694	12	1.1698	4

* Co (cph) ** Co (fcc) + Corresponding to both cph and fcc Co.

Table 5.11

X-ray diffraction data for stainless steel clads

d (exp), °A	I/Io (exp)	d (std), °A	I/Io (std)	Suggested phase
2.08	100	2.08	100	Austenite
1.8024	100	1.80	80	Austenite
1.2726	40	1.270	50	Austenite
1.0874	65	1.083	80	Austenite
1.0398	18	1.037	50	Austenite
0.9047	15	0.900	30	Austenite

Table 5.12

X-ray diffraction data for stainless steel + SiC composite clads

d (exp), °A	I/Io (exp)	d (std), °A	I/Io (std)	Suggested phase
2.298	15	2.296	33	Cr_7C_3
2.08	100	2.08	100	Austenite
2.054	65	2.048	100	Cr_7C_3
2.027	58	2.025	13	Cr_7C_3
1.903	12	1.902	5	Cr_7C_3
1.8058	30	1.80	80	Austenite
1.2755	25	1.27	50	Austenite
1.0893	25	1.083	80	Austenite

Table 5.13
X-ray diffraction data for Alloy 4815 clads

d (exp), °A	I/Io (exp)	d (std), °A	I/Io (std)	Suggested phase
3.0254	15	3.024	4	Cementite
2.5475	35	2.545	4	Cementite
2.023	100	2.026	100	Ferrite
1.5199	20	1.521	2	Cementite
1.4356	18	1.433	20	Ferrite
1.2980	8	1.297	2	Cementite
1.2174	8	1.2162	16	Cementite
1.1753	10	1.1702	30	Ferrite

Table 5.14
X-ray diffraction data for Alloy 4815 + SiC composite clads

d (exp), °A	I/Io (exp)	d (std), °A	I/Io (std)	Suggested phase
2.622	15	2.63	50	SiC
2.508	100	2.51	100	SiC
2.067	12	2.067	67	Cementite
2.023	100	2.024	100	Ferrite
1.4336	15	1.4332	20	Ferrite
1.3265	10	1.329	17	Cementite
1.2882	30	1.291	30	SiC
1.2539	20	1.260	30	SiC
1.1694	30	1.170	30	Ferrite
1.013	10	1.013	10	Ferrite
0.9058	12	0.9056	10	Ferrite
0.8692	25	0.864	20	SiC
0.8374	20	0.837	50	SiC

CHAPTER 6

WEAR STUDIES OF CLAD DEPOSITS

6.1 INTRODUCTION

This chapter is divided into three parts. The first part contains the definitions of some basic terms, various types and mechanisms of wear, and a brief review of literature on wear and wear resistant coatings. The second part is about the procedure adopted for the testing and evaluation of wear. In the third part, the results of wear studies of different alloys and composite deposits from the present investigation are reported.

6.2 LITERATURE SURVEY

6.2.1 Wear and its Types

The term 'wear' is generally defined as a progressive loss or displacement of material from a surface as a result of relative motion between that surface and another (82). The wear can occur between surfaces of either similar or dissimilar nature such as metal-metal, metal-nonmetal or nonmetal-nonmetal. The wear of material is a complex phenomenon which can take place in different forms depending upon the service conditions. The factors which affect the service conditions include type and method of loading, speed of relative motion between wearing surface and grinding medium, temperature, material, presence of lubricant and chemical nature of environment.

Five basic forms of wear have been reported by Lansdown and Price (83) which are fatigue, abrasive, adhesive, erosive and corrosive wear. Wear may take place sometimes due to a combined effect of more than one form.

In abrasive wear, the removal of material takes place by the ploughing or scratching effect of hard particles on the softer surface of the worn part.

In adhesion, wear occurs when two smooth bodies slide over each other so that the fragments are pulled off one surface to adhere to the other. These fragments may later come off the surface to which they adhere and are either transferred back to the original surface or may form loose wear particles.

The form of wear referred to as surface fatigue results when a surface is subjected to repeated cycles of stress produced by repeated sliding, rolling or impacting motions. The stress cycles initiate cracks in the surface which spread with time and form freely moving particles between the contacting surfaces.

Erosion is the term applied to the damage produced by the impingement of sharp particles on a surface. The surfaces resulting from erosion are closely similar to those produced by abrasion except that of high roughness in the case of the former due to the removal of material by striking particles.

Corrosive wear may be defined as the process where the loss of material occurs due to chemical or electrochemical reactions with the environment.

6.2.2 Mechanism of Abrasive Wear

Since the results presented in this chapter are concerned with the abrasive type of wear, it will be appropriate to outline the phenomena involved.

Abrasive or cutting wear takes place whenever hard, foreign particles, such as metal grit, metallic oxides, dust and grit from the environment, are present between the rubbing surfaces. Abrasive wear is one of the most common types encountered in engineering practice and it is always found as the highest single cause of wear in many

machine applications (84). A later industrial survey showed that about 50% of the total wear loss results from the abrasive type of wear (85).

A simple model explaining the abrasive wear mechanism was developed by Rabinowicz (86) which showed the action of an abrasive particle on a surface. The model assumed a rigid conical abrasive particle moving through a softer surface and removing the volume of material swept (Fig. 6. 1).

When a load dW is applied on a small portion (asperity) of a surface of hardness H, it will penetrate the softer surface to an extent given by

$$dW = H \cdot dA \qquad \text{Eq. 6.1}$$

Where dA is projected area of the cone and is equal to $\pi \cdot r^2$. Hence the equation will be of the form

$$dW = H \cdot \pi \cdot r^2 \qquad \text{Eq. 6.2}$$

By the geometry of Fig. 6.1

$$\tan\theta = x/r \text{ or } r = x/\tan\theta \qquad \text{Eq. 6.3}$$

Substituting the value of r from Eq. 6.3 to 6.2

$$dW = H \cdot \pi \cdot x^2/\tan^2\theta \qquad \text{Eq. 6.4}$$

When the cone is moved through a distance dL, it will sweep out a volume dV which is given by

$$dV = dL \cdot r \cdot x \qquad \text{Eq. 6.5}$$

Substituting for r from Eq. 6.3

$$dV = dL \cdot x^2/\tan\theta \qquad \text{Eq. 6.6}$$

From Eq. 6.4

$$x^2 = (dW \tan^2\theta)/\pi \cdot H \qquad \text{Eq. 6.7}$$

Substituting the value of x^2 from Eq. 6.7 into Eq. 6.6

$$dV = (dW \cdot dL \cdot \tan\theta)/\pi \cdot H \qquad \text{Eq. 6.8}$$

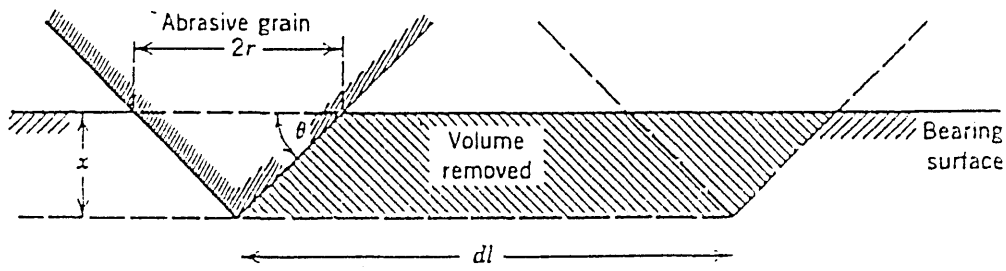

Fig. 6.1 Abrasive wear model (Ref. 86).

If we now add up the contributions of all asperities, we will have

$$V = W \cdot L \cdot \tan\theta/\pi \cdot H \qquad \text{Eq. 6.9}$$

If we take this Eq. 6.9 for a comparative study of various samples subjected to the same wear conditions, then we can simplify this equation as also reported by Monson (25), Johnson (87) and Antony (34).

$$V = (K \cdot W \cdot L)/H \qquad \text{Eq. 6.10}$$

Where,

V = total wear volume (mm^3)

K = wear coefficient

W = total applied load (kg)

L = sliding distance (mm)

H = hardness of abraded material (kg/mm^2)

Two general situations can exist in abrasive wear, namely two-body or three-body wear (83). Two-body abrasive wear occurs when a rough surface, or fixed abrasive particle, slide across a surface to remove material. If the abrading contact is a free grit from an external source or a wear particle which has been generated within the system and is loaded between two surfaces, then the situation is referred to as three-body abrasion.

Misra and Finnie (88) have further classified the three-body abrasive wear as shown in Fig. 6.2. 'Closed' three- body wear occurs when loose abrasive particles are trapped between two sliding or rolling surfaces which are 'closed' to one another (i.e. in intimate contact). 'Open' three-body abrasive wear occurs when the two surfaces are far apart or when only one surface is involved in the wear process. Gouging occurs when rocks or other coarse abrasive particles cut into a surface to remove relatively a large amount of material. If the objective of the process is to crush the abrasive particles, e.g. in ball milling, then the process is termed 'high stress'. If the abrasive particles do not fracture during the wear process, the process is referred to as 'low stress'.

6.2.3 Effect of Materials and Process Parameters on Abrasive Wear

The effect of various experimental conditions and also the properties of material on abrasive wear has been the subject of many studies. Rabinowicz (86) has explained the effect of hardness, abrasive particle size and moisture content of the atmosphere on the abrasive wear rate.

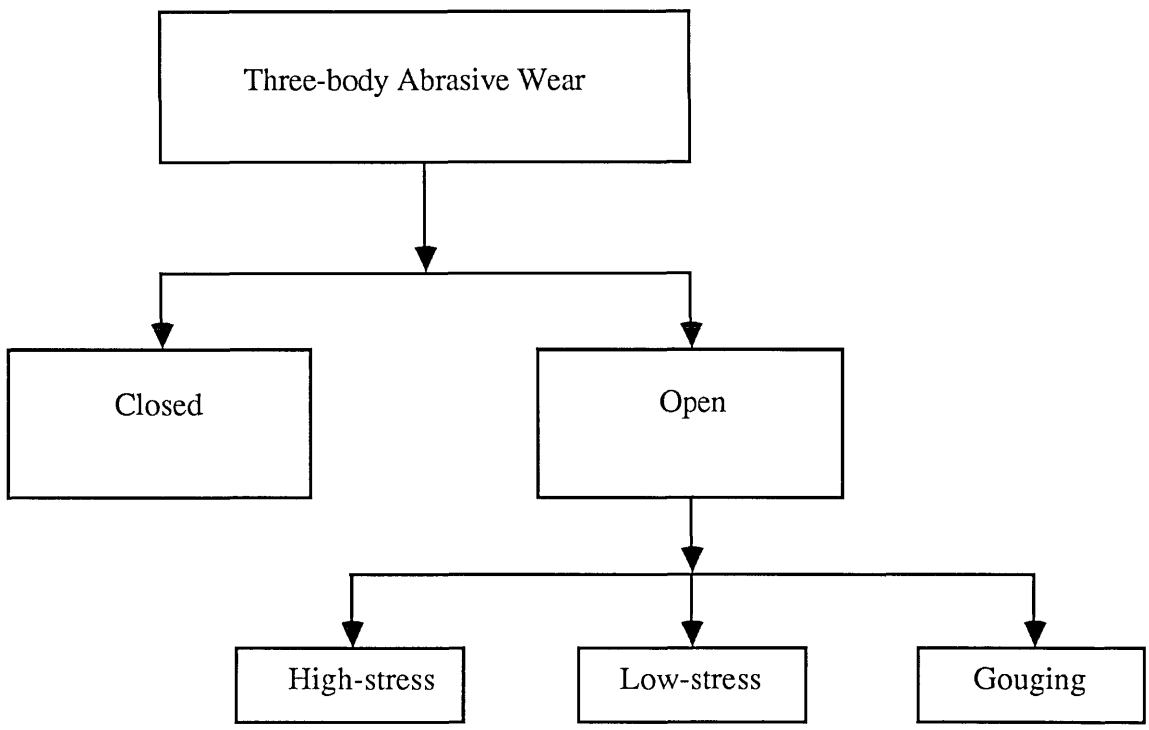

Fig. 6.2 Classification of three-body abrasive wear (from ref. 88)

The abrasive wear equation (Eq. 6.9) derived by Rabinowicz (86) showed that the abrasive wear of a surface using any particular abrading medium is inversely proportional to the hardness of the surface. The abrasive wear increases with increasing abrasive particle size up to a critical value, beyond which the wear becomes independent of

particle size. The wear rates obtained with experiments carried out on M50 steel samples using alumina as abrasive particles, in high humidity were 10-20% higher than those carried out in low humidity, showing an increasing effect of moisture content of the environment.

A later study (89) showed that the relative wear resistance of pure metals was directly proportional to their hardness. The wear resistance of thermally treated (interpreted as annealing to soften) metals was found slightly less dependent on the hardness, whereas despite the considerable increase in hardness, the wear resistance of mechanically treated (work hardened) metals was found unchanged.

Mutton and Watson (90) have reported some effects of hardness of the material on the mechanism of material removal by wear. Their (90) experiments showed that in hard metals, the metal removal was found solely due to a cutting effect rather than ploughing. The grooves formed in harder metals were sharply defined with the formation of chips. In softer materials, along with the formation of chips, there was some evidence of roughness at the edges of the grooves which was considered to be due to the lateral plastic flow of material. They concluded from this study that,

1. If significant plastic flow accompanies penetration of the abrading asperity, as in the case of softer materials, the volume of material removal will be less than that predicted theoretically (Eq. 6.9).
2. If, however, the material is very hard and brittle, relative movement between the asperity and metal may result in cracking and spalling around the wear groove in which case the volume of material removed may be greater than that predicted by Robanowicz (86).

A comparative study of the effect of various microstructures of low alloy steel on two-body and three-body abrasive wear was carried out by Yang and Garrison (91). The study showed that while the three-body wear resistance was higher than the two-body wear resistance, the microstructural trends observed in both cases were closely similar.

For example, retained austenite has been shown to increase both the two-body and three-body wear.

The abrasive wear has been found (92) to be greatly affected by the attacking angle of the abrasive particles. Wear was reported to be increased with increase in attacking angle, reaching a maximum value at 90°. However, it has been reported (93) that there is a critical attacking angle at which maximum wear occurs e.g. 85° for aluminium and 45° for copper.

Abrasive wear studies (94) using ceramic particles such as alumina, zirconia and silicon nitride showed a linear relationship of increasing wear with increasing load applied. At low loads (40 N) the wear resulted from plastic deformation. At higher loads (120 N), the wear was dominated by fracture, resulting in the removal of a greater amount of material.

Extensive work was carried out by Gahr (95) to study the relationship between the microstructure of metal matrices and their abrasive wear. The various design parameters of wear systems which are considered to affect the abrasive wear of structural parts, reported by Gahr, are shown in Fig. 6.3. The parameters of alloy structure which were reported by Gahr (95) to affect wear of alloys are listed in Fig. 6.4. Some of these parameters will be considered later in the discussion section. However, the reader is referred to the original reference (95) for a full understanding of the effect of these parameters on the wear rate.

Avery (96) has divided the abrasive wear test variables into two categories, namely 'opportunity' variables and 'severity' variables. The 'opportunity' variables are those which can easily be controlled in laboratory tests. These variables include running time, travel distance, contact area, abrasive feed and specimen configuration. One or more of these parameters can be adjusted to obtain a desired amount of wear. On the other hand, the 'severity' variables are more complex and are difficult to control. These variables include the size, angularity, hardness, toughness and freedom of motion of abrasive; velocity; impingement angles; the proportion of cutting versus deformation; gross

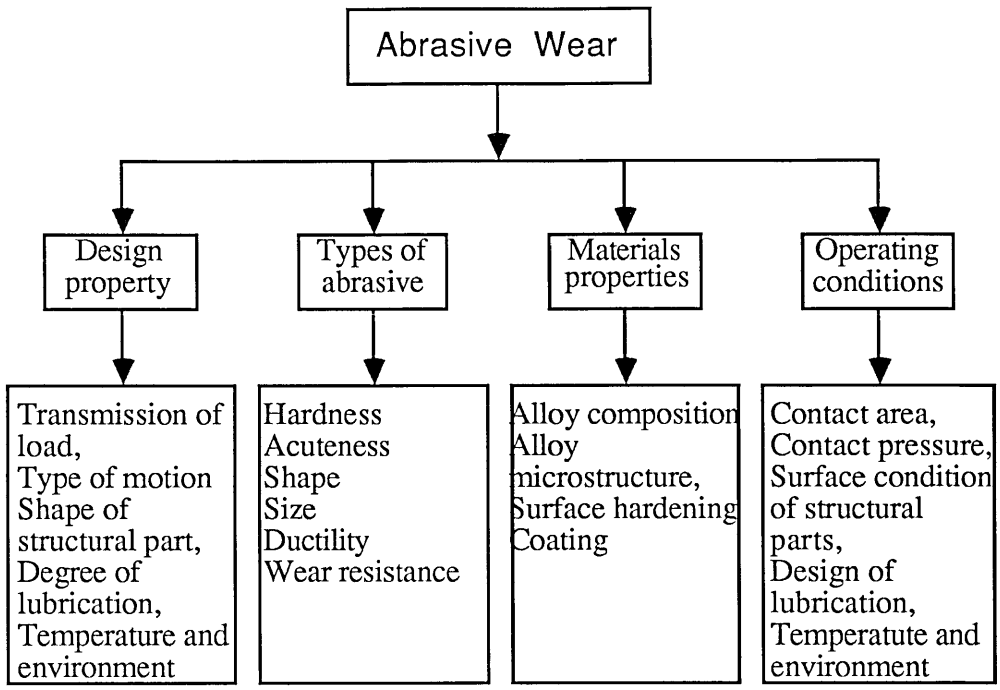

Fig. 6.3 Design parameters of wear system affecting the abrasive wear (Ref. 95)

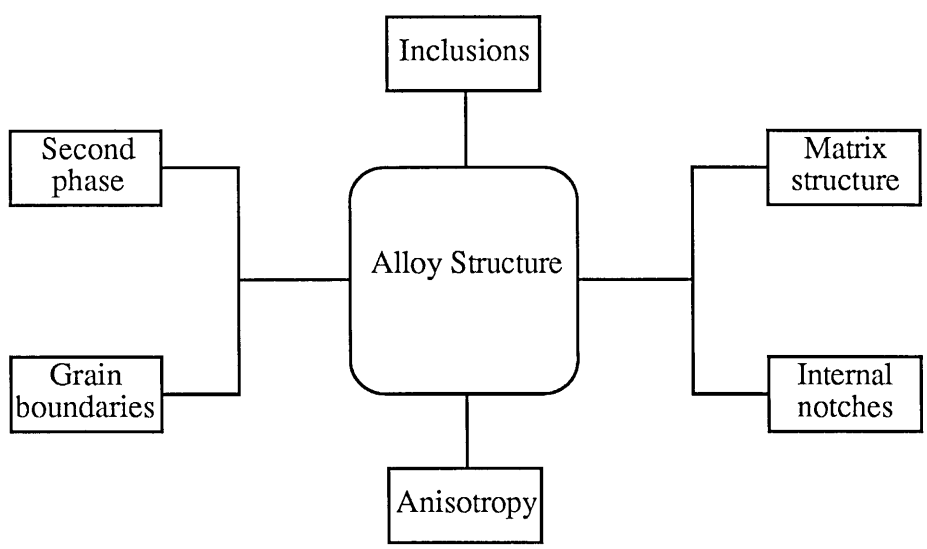

Fig 6.4 Various parameters of alloy structure affecting the abrasive wear (Ref. 95)

loading on the wearing surface; microstresses imposed on the wearing surface. The complexity of these variables is a major factor causing difficulty in the investigation of wear problems in service.

Low speed abrasive tests, of two-body and three-body type, were carried out by Basse (97) on various metals, alloys and cemented carbides to study the effect of their hardness on wear rate. The volumetric wear removal was found to be proportional to the applied loads except at very low loads. A relationship established between hardness and wear resistance showed that relatively soft cemented carbide materials followed the same trend as the conventional metals and alloys. On the other hand, the hard cemented carbides showed a transition hardness level at which the abrasive wear resistance was increased drastically. The transition occurs at a point where the abrasives are no longer hard enough to indent the surface sufficiently to remove the material in plastic deformation as micro-chips. The suggested hardness level of the abrasive for wear testing is reported to be approximately,

$$Ha = 1.2 \times Hm$$

where Ha and Hm are the hardness of abrasive and material to be tested, respectively.

6.2.4 Wear-Resistant Laser Processed Surfaces

With the rapid development of lasers in the last two decades, a number of investigations has been made to improve the wear resistance of surfaces by laser processing. The processes used for producing wear resistant surfaces include laser melting, alloying and cladding using hardfacing alloys. A brief review of the previous work on the subject is reported here.

Gleaser and Fairand (98) have consolidated plasma sprayed TiB_2 coatings on A-6 tool steel, using a 1 kW GTE Sylvenia model 971 CO_2 laser. These coatings showed three different types of structures, depending on the laser processing conditions, namely,

1. TiB_2 completely dissolved in the steel.

2. TiB_2 partially dissolved in the steel.
3. TiB_2 "infused and intact" (i.e. showing good bonding with matrix) with steel matrix.

A comparative study of abrasive wear of the samples with these three structures, along with uncoated A-6 tool steel, was carried out. The results showed that the wear resistance of all the three coated samples was far better than the uncoated sample. Among the coated samples, the sample with completely dissolved TiB_2 particles showed the lowest wear resistance, but it was still three times better than the uncoated sample.

Mordike (99) improved the abrasive wear resistance of titanium alloy substrates by laser injection of TiC particles into the substrate. The wear resistance of the composite layer was about ten times that for untreated Ti-6Al-4V substrate. Both samples showed an increase in the wear loss with increasing applied test load.

Ayers et. al. (100-101) have injected TiC, WC and $(WC)_{75}(VC)_{25}$ particles into various substrates, such as Ti-6Al-4V, 5052 Al, 6061 Al, CP Ti and Inconel X-750 using a 15 kW CO_2 laser at 4-7 kW power levels. The abrasive wear studies of these samples using a dry sand/rubber wheel test (100) showed a substantially better wear resistance of composite surfaces than that for as-received samples. In the second study (101), the wear tests were conducted on a machine with rotating specimen holder and polishing wheel. Two different combinations of wheel and specimen holder rotation rates were used which provided mean polishing velocities of 11 and 23 cm/s. The abrasive used was a diamond paste with two particle sizes of 3 and 30 μm. The tests were carried out on Ti-6Al-4V, 5052 Al and 6061 Al samples injected with WC, TiC and $(WC)_{75}(VC)_{25}$ particles. The results of this study are summarized below,

1. There was no effect of increase in the rotation velocity from 11 to 23 cm/s on the wear resistance of all the samples studied, when tested using 3 μm diamond paste.
2. The wear resistance of aluminium alloys and Ti-6Al-4V was increased by a factor of 30 and 3.8 respectively, when injected with TiC and tested with 3 μm diamond paste.

3. Improvement in wear resistance of WC injected Ti-6Al-4V surfaces was found only when testing was done using 30 μm diamond paste; the wear rates were 4-20 times lower than when 3 μm diamond paste was used. When the testing was done using 3 μm diamond paste, the wear resistance of the composite was equal to, or slightly lower than, that of the alloy.

A comparative wear study of laser processed and plasma sprayed metal + carbide mixture, has been reported by Belmondo and Castagna (102). A mixture of metal + carbide powders (wt.%; 70 Mo, 1.2 Cr, 18.8 Cr-carbide, 5 Ni, 5 Si) was mixed with a binder (Nicrocoat) to make paste for ease in spreading over a cast iron substrate. The substrate was then melted under a laser beam of 15 kW CO_2 laser at a specific energy of 125 J/mm^2. The wear experiments were carried out on a reciprocating motion testing equipment. A series of experiments on sliders coated by laser processing and with the plasma spray technique was carried out by testing against stationary samples of cast iron with a surface roughness of 1.2 μm. The tests were carried out under different normal loads at a relative speed of 1.25 m/s for a total distance of 27 km under insufficient lubrication conditions using paraffin oil. The results (Fig. 6.5) showed that the laser coatings are far superior to plasma sprayed coatings in abrasive wear especially at higher applied pressures (800-1000 N/cm^2). The wear loss, in both type of samples, was found to be increased with the increase in applied load.

Mazumder et. al. (47, 49) have produced surfaces of high wear resistance on AISI 1016 steel substrate by laser cladding with a powder mixture of Cr : Mn : C (10 : 1 : 1) using an AVCO HPL 10 kW CW CO_2 laser. A clad surface containing 40% Cr, 4% Mn and 4% C was produced by feeding powder mixture at a rate of 11.5 g/min and with a laser beam diameter of 3 mm, power 4-6 kW and traverse speed of 8.47-21.17 mm/s.

The wear experiments were carried out on a block-on-cylinder machine. The test conditions are given below,

Grinding disc : AISI 52100 Steel

Load : 222 N

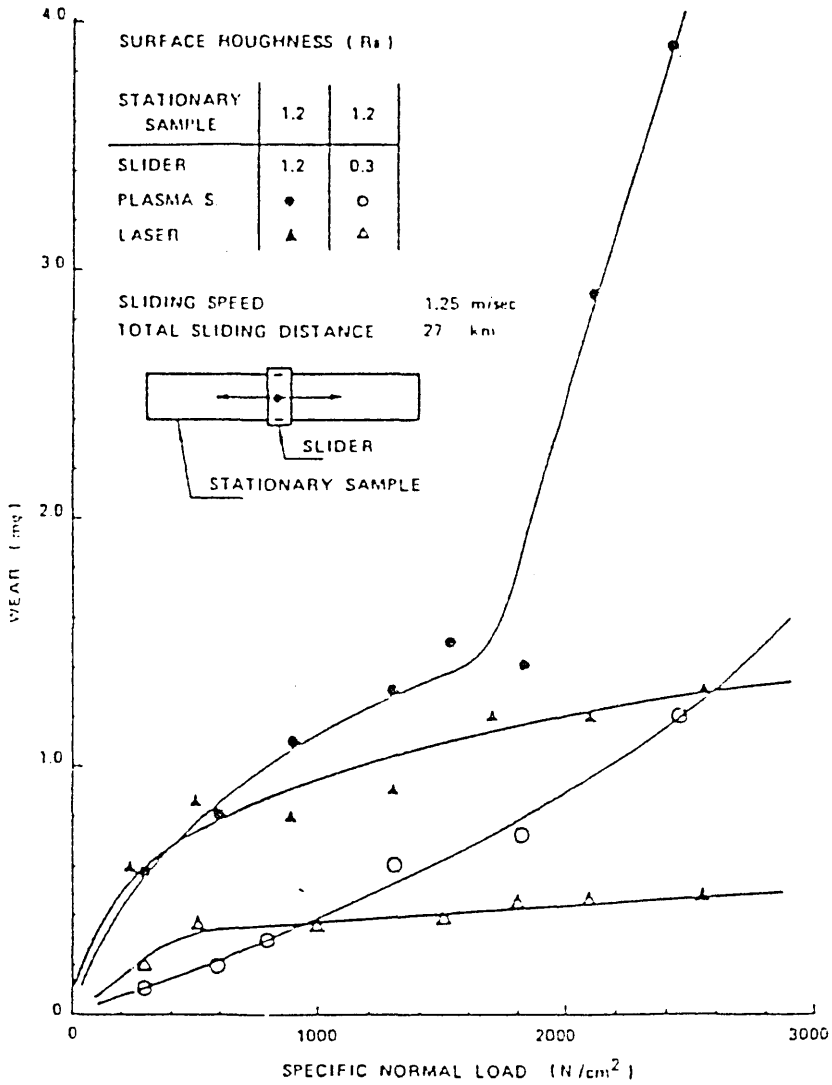

Fig. 6.5 Wear test comparison between plasma spray and laser coating.

Speed : 0.032 m/s

Test duration : 1 hour

The wear and friction data of laser clad samples was plotted as a function of table speed and laser power (Fig. 6.6). For comparison purposes additional data for the substrate material and a Stellite alloy 6 sample are also shown. The wear data indicate that the laser clad samples have superior tribological characteristics as compared with Stellite alloy 6 for the conditions studied. Better wear results were obtained with the laser power at 4 kW as compared with 6 kW. This was attributed to a more rapid solidification rate and also a higher concentration of alloying elements obtained at 4 kW laser power due to a comparatively smaller substrate melting at this power.

The same work (47, 49) was presented subsequently (29) with the addition of some new results. In this work, a set of clads produced at relatively low range of traverse speeds (8-11 mm/s) and three laser powers (4, 5, 6 kW) was subjected to wear tests. The results are shown in Fig. 6.7. The trend observed in this series was almost similar to that obtained in previous work (47, 49).

6.2.5 Wear Resistance of Stellite Surface Layers

Abrasive wear studies on various Stellite alloys surface layers produced by conventional (34, 103) and laser processing (25) have been reported in the literature.

Antony (34) used a dry sand rubber wheel abrasion test equipment to study the effect of hardness and carbide volume fraction on the abrasive wear of various Stellite alloys produced by gas tungsten arc welding (GTAW) and oxyacetylene welding processes. The test conditions used were, 13.6 kg applied load, 385 g/min sand feed rate, 144 m/min sliding velocity and 1412 m total sliding distance. The wear loss of GTAW deposited Stellite alloys was found to be inversely proportional to their hardness. The wear volume loss of oxyacetylene weld deposits of Stellite alloys was 2-3 times lower than those of equivalent GTAW deposits, due to a slight carbon pickup (0.1-0.2%) in the

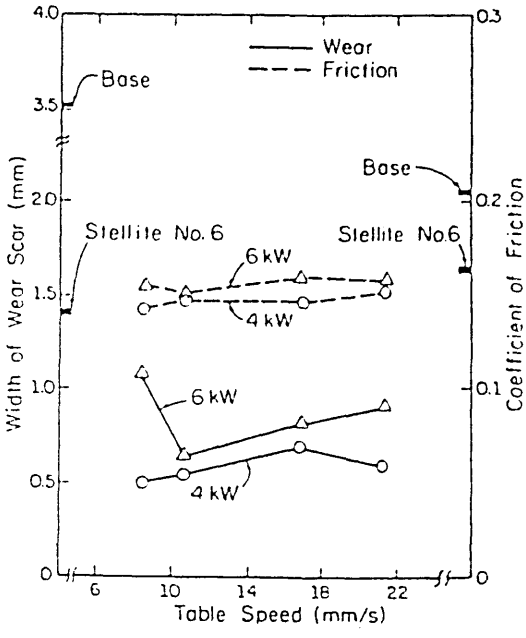

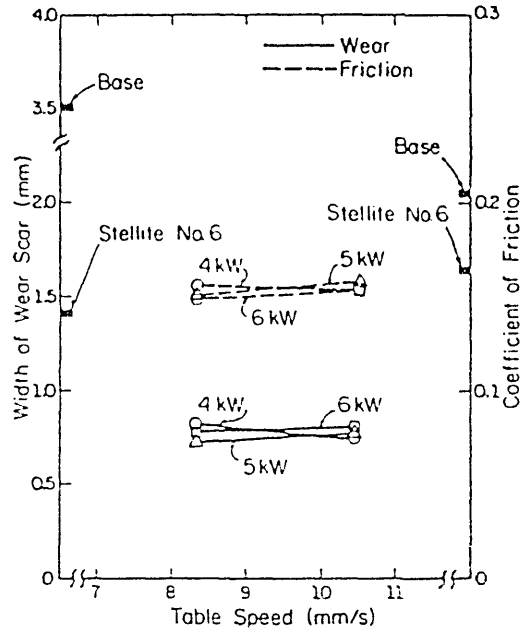

Fig. 6.6 (left) and 6.7 (right) Wear and friction data of various samples as a function of table speed and laser power (Ref. 47 and 49).

case of the former. The wear resistance was also found to be affected by the morphology of the carbides in the deposit matrices produced by the different methods. The general trend observed was an increase in the wear resistance with increase in carbide size.

An extensive abrasive wear study has been carried out by Silence (103) on various cast, wrought and hardfaced Stellite alloys. The wear tests were performed on a dry sand rubber wheel equipment with the following conditions, 13.6 kg load, 144 m/min sliding speed and 10 minutes of total test time. The abrasive tests of cast alloys showed that the samples cast in graphite moulds (faster solidification and finer carbide structure) had 2.5-10 times greater volume loss than the samples of the same alloys cast in sand moulds despite the fact that the former had higher hardness (1-2 Rc). Similarly, the wrought alloy 6K with large carbides showed higher wear resistance than that of smaller carbide containing alloy 6K. Like in the case of the cast and wrought alloys, the abrasive wear resistance of alloys produced by oxyacetylene welding was higher than those produced by TIG welding. The reason for this higher wear resistance in oxyacetylene deposits was two fold, firstly due to the carbon pickup from the acetylene flame and secondly the formation of larger carbides due to longer solidification times. No definite relationship with hardness was found on the wear resistance of all of the alloys studied produced by various methods.

Both these studies on abrasive wear of conventionally deposited Stellite alloys have shown that the wear resistance is increased by increasing the carbide size in the deposit matrix. However, a later study by Monson (25) on the wear of Stellite alloys produced by laser cladding showed that despite the finer carbide distribution in the matrix, the laser processed Stellite alloys had better wear resistance than those deposited by conventional methods. This was attributed to the solid solution hardening of the matrix and formation of fine dendritic microstructure due to the high cooling rates associated with laser processing. The wear set-up used by Monson (25) was a pin-on-disc machine. The testing was performed using a 100 grit SiC paper as abrading medium. The tests were performed for 30 minutes at a sliding speed of 0.25 m/s, load 21.6-140.3 N. The alloys

studied were Stellite alloy 5 and 6 deposited by oxyacetylene, TIG, PTA and fusion welding and also laser cladding. A linear relationship of increase in wear volume loss with applied load was found in all the deposits.

6.2.6 Salient Features of Abrasive Wear Studies

The salient features of the previous studies (86-103) on abrasive wear of various materials are listed below.

1. In general, abrasive wear of a material is inversely proportional to its hardness (86).
2. Wear loss increases with increase in abrasive particle size up to a critical limit and after that it becomes independent of size (86).
3. Wear loss increases with increase in moisture content of the environment (86).
4. Two-body abrasive wear conditions result in a greater wear loss as compared with three-body wear conditions (91).
5. Abrasive wear increases with increasing attacking angle of abrasive particles (92).
6. There is a critical attacking angle of abrasive particles for every material which results in maximum wear loss (93).
7. To obtain reasonable results from a wear testing process, the hardness of the abrasive particles used should be at least 1.2 times the hardness of the material to be tested (97).
8. Wear increases with increase in applied load (99).
9. Laser surface coatings proved to be superior in wear resistance to plasma sprayed and conventionally deposited coatings (25, 102).
10. Wear resistance of a material consisting of carbide particles in a metallic matrix increases with increase in the carbide size (103).

6.3 EXPERIMENTAL PROCEDURE

6.3.1 Wear Testing

Wear studies of different alloy and composite samples were performed using three different types of tests simulating various service conditions. These tests were;

1. Two-body abrasive wear tests of variable composition single track of Stellite + SiC composite clad.
2. Two-body abrasive tests of different alloys and composites.
3. Three-body tests for the samples used in test two.

6.3.1.1 Two-body Qualitative Wear Tests for Variable Composition Samples

The samples were subjected to a simple type of wear test for comparative studies of low and high SiC content in the Stellite - SiC composite. This test provided a qualitative wear analysis of the samples. For these tests, three samples of En 3b mild steel substrate were prepared to 200 x 25 x 5 mm size (Fig. 6.8). Samples were clad on one of the longitudinal edges (surface with 200 x 5 mm dimensions), Fig. 6.9, to obtain single tracks under different processing conditions.

The method adopted for studying the wear behavior of variable composition clad samples was pushing them at a constant linear speed of 0.75 mm/min against a rock cylinder to assess the relative wear. A 'Yama Zaki CNC' turning lath was used for this purpose, consisting of a revolving chuck to hold the rock cylinder and moveable jigs to keep the specimen in position. A schematic diagram of the process is shown in Fig. 6.13. Bath lime-stone and Darleydale sand-stone rock cylinders, the latter being harder than the former, were used as abrasive materials.

6.3.1.2 Two-body Quantitative Abrasive Wear

The samples for this test were prepared in the following sequence;

1. Three samples of 25 x 25 x 10 mm size were cut from each type of overlapping track clads (Figs. 6.10-6.12).
2. About 0.3 mm clad layer was removed from each sample by grinding on a 360 grit size emery paper to make them flat and smooth.
3. Samples were finally ground on a 600 grit size emery paper to obtain the same surface finish.
4. The sharp edges of the samples were made round by grinding on a 600 grit size emery paper to avoid any possible damage to the grinding disc.
5. All the samples were thoroughly washed, cleaned and weighed before subjecting to the wear test.

The abrasive wear tests of overlapping clad samples of various alloys and composites were carried out on a machine which was a modified form of a standard pin-on-disc apparatus to provide more severe wear conditions. The wear testing set-up and a schematic diagram of the machine are shown in Figs. 6.14 and 6.16. This machine consisted of two discs: one acts as grinding medium and is made up of 80 grit size alumina, whereas the other disc is used as sample holder and is smaller in diameter and revolves on the half diameter position of the grinding disc. The sample- holding disc is designed to hold three samples of the same material to be tested. This disc is attached to a hydraulic system for applying variable loads during the test. The tests were carried out in two sets: at constant load and various test time, and for constant time duration with various loads applied in a direction normal to the contact surface. Both the sample grinding and holding discs were made to revolve in the same direction at constant speeds of 150 and 300 rpm respectively. The design of the sample-holding disc provides revolutions in an opposite direction to the grinding disc, hence making the conditions of

A. **Fig. 6.8** A macrograph of samples used for two-body qualitative abrasive wear (series 1), X 0.23.

B. **Fig. 6.9** A plan view of samples shown in Fig. 6.8, illustrating clad surface, X 0.23.

C. **Fig. 6.10** Macrograph showing overlapping tracks clad samples of Alloy 4815 (left) and stainless steel (right) used for preparing the samples for wear tests (series 2 and 3), X 0.5.

D. **Fig. 6.11** Macrograph showing samples of various clads prepared from overlapping track clads (Fig. 6.10) for wear tests (series 2-5), X 1.

E. **Fig. 6.12** Plan view of samples shown in Fig. 6.11, illustrating worn surfaces.

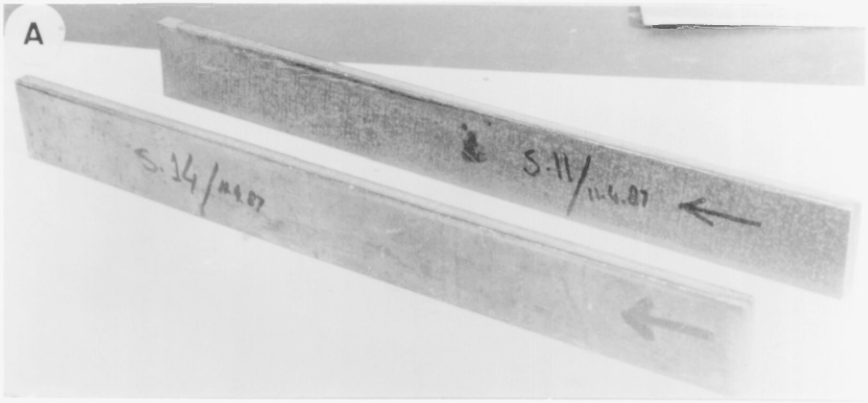
A
S.14/
S.11/

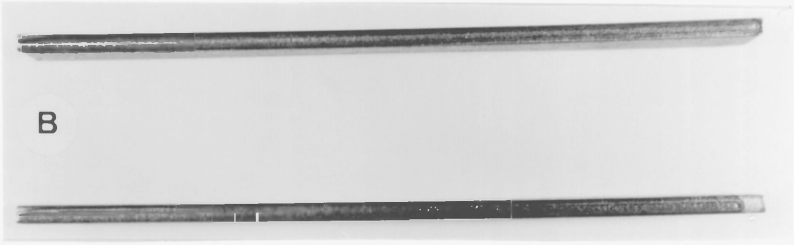
B

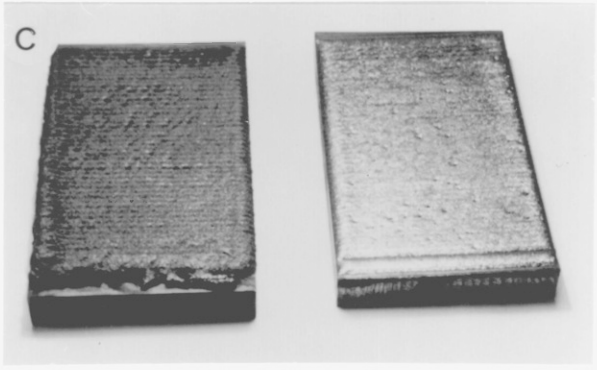
C

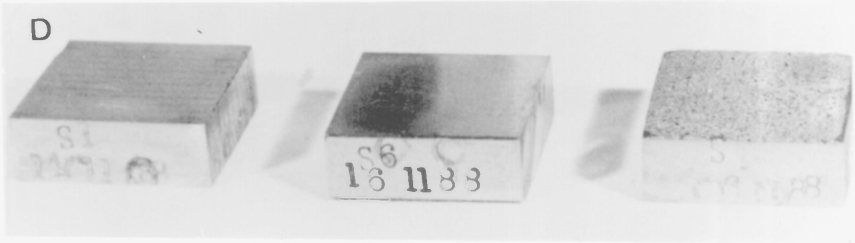
D
S1
S6
16 1183

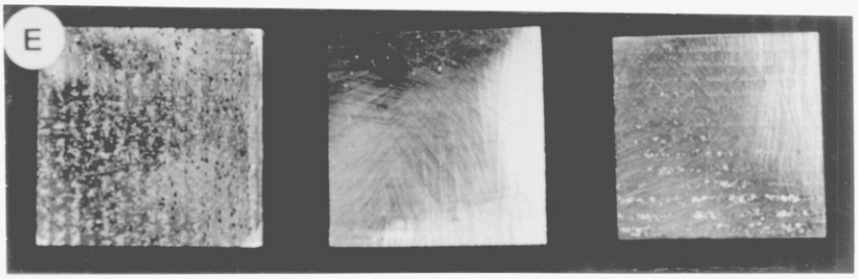
E

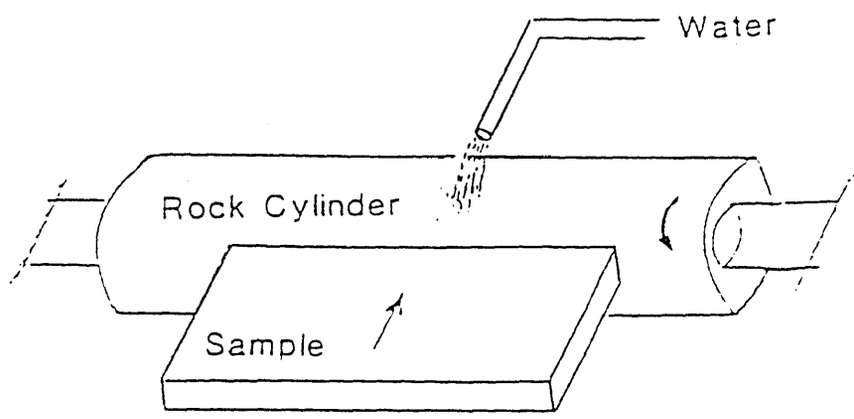

Fig. 6.13 Schematic diagram of two-body qualitative wear testing set-up.

severe abrasive wear on the sample. The contact surface area was flooded with fresh water.

6.3.1.3 Three-body Abrasive Test

The equipment used for this type of wear test was, in fact, a simulation of the service conditions suffered by drilling rigs in the sea water. The same type of samples prepared for the tests mentioned in section 6.3.1.2 were subjected to this type of wear test to find out their feasibility for use as drilling bit material. The process set-up and schematic diagram of the equipment is shown in Figs. 6.15 and 6.17 respectively. The wear testing machine consists of a rubber disc revolving at a constant speed of 52-54 rpm. The revolving rubber disc is enclosed in a container capable of holding 500 ml of water. The container was filled with a sand-water slurry containing 400 ml of water and 80 ml of sand (250-600 μm). The sample was attached to a spring loaded rod designed to provide rotational as well as to and fro motion (at a frequency of 0.6 Hz) to the sample. A 1 kg static weight was applied through the sample holding rod. The sand in the slurry was directed towards the centre of the rubber disc by placing a barrier on the disc. This type of set-up provided three body wear conditions. The test was run for a total time of four hours in one hour intervals for each sample. The samples were weighed after every hour to evaluate wear loss.

6.3.2 Surface Roughness

Comparative studies of worn samples were made by measuring their surface roughness on a 'Talysurf 10' surface texture measuring instrument. A cut-off length of 0.8 mm, with a 2.5 μm radius diamond stylus, was used to generate average surface roughness values (Ra). The average roughness Ra is defined as "the arithmetical average of the departures of the profile above and below the centre line throughout the sampling

A. **Fig. 6.14** Wear testing set-up for two-body abrasive wear.

B. **Fig. 6.14a** A magnified section of Fig. 6.14 showing grinding and specimen holding discs.

C. **Fig. 6.15** Wear testing set-up for three-body abrasive wear.

D. **Fig. 6.16a** A magnified section of Fig. 6.15 showing wear sample and water + silica abrasive slurry container.


A

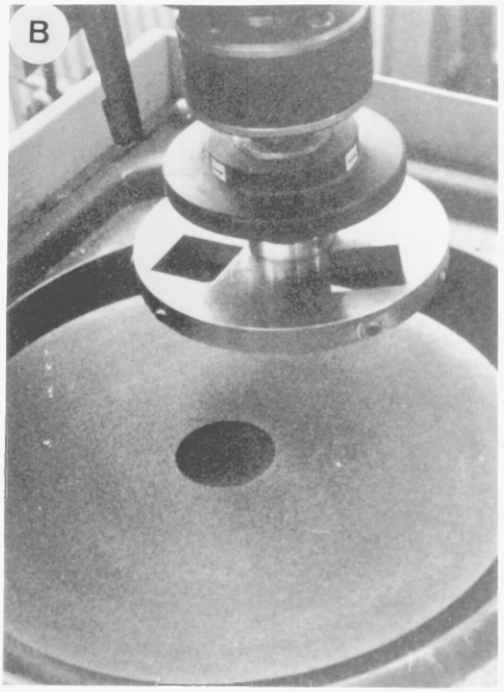
B


C

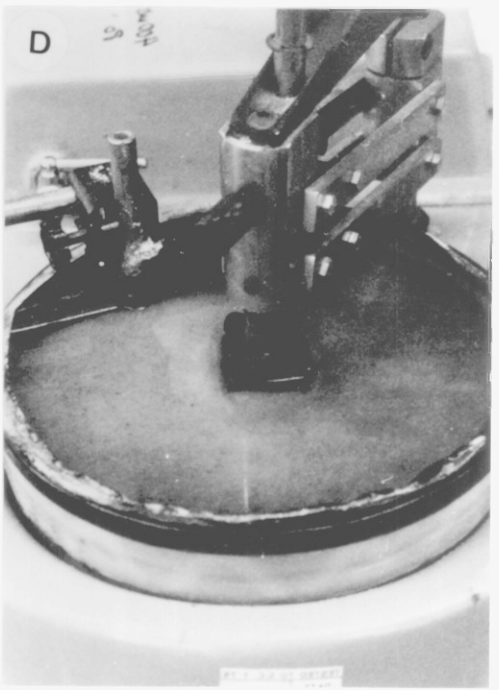
D

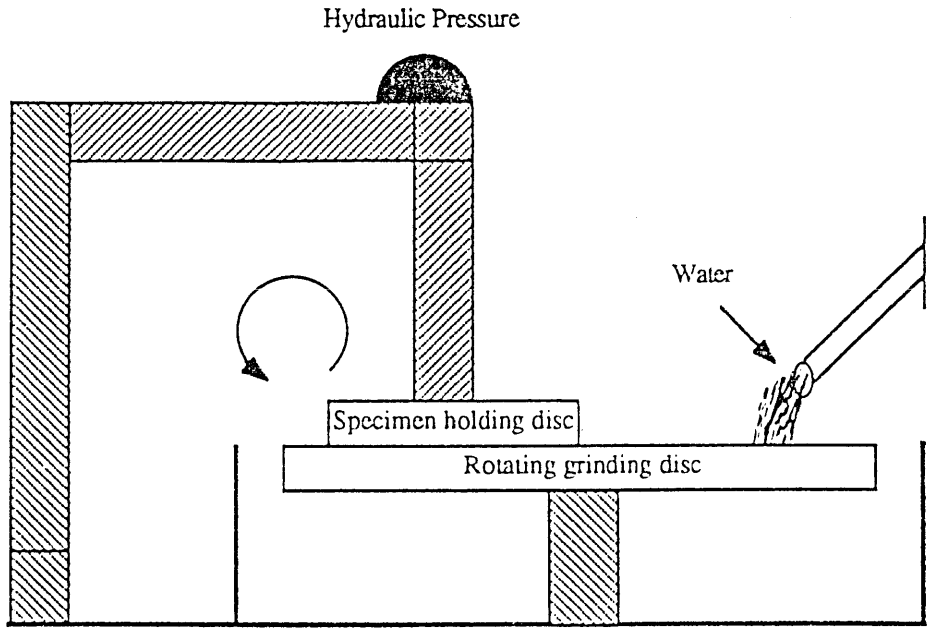

Fig. 6.16 Schematic diagram of two-body abrasive wear testing set-up.

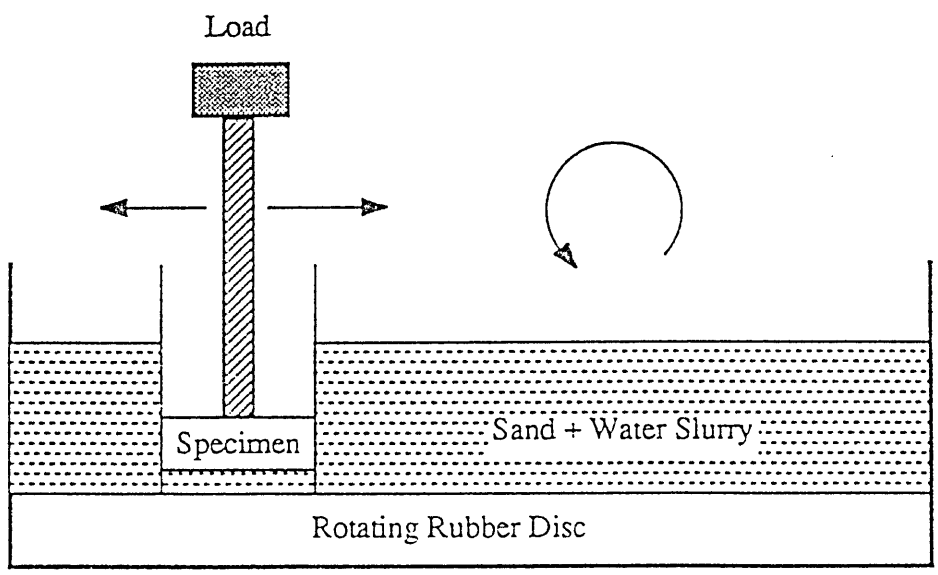

Fig. 6.17 Schematic diagram of three-body abrasive wear testing set-up.

length" as shown in Fig. 6.18 (104). The average roughness of various samples was found to increase with increasing cut-off length (Fig. 6.19): a cut-off length of 0.8 mm was, therefore, selected for the measurement of surface roughness. A mean of the five roughness values measured on the same length was taken as the average roughness value.

6.4. WEAR RESULTS

The results will be presented in the following sequence.

1. Wear tests
2. Microhardness of worn surfaces
3. Surface roughness of worn surfaces
4. Microscopy of worn surfaces

6.4.1 Wear Tests

Two types of abrasive wear, namely two-body and three-body abrasive wear, were studied. The wear experiments were carried out in five series to establish relationships between the wear loss and various processing parameters such as test time, applied load, specimen composition etc. The results of these series will be presented in the following sections.

6.4.1.1 Series One -- Two-body Qualitative Abrasive Wear of Variable Composition Clads

Three single track clad samples were formed at constant Stellite and variable SiC feed rate (i.e. increasing from one end to other end of the sample) to study the effect of SiC proportion in the mixtures on the wear of the clad layers. The processing conditions are given in Table 6.1

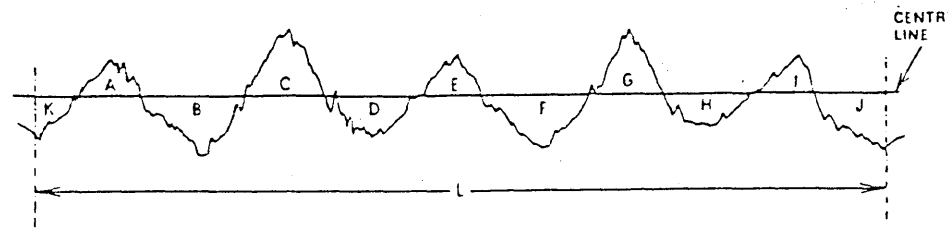

Over a length of surface L, the centre line is a line drawn such that the sum of the areas embraced by the surface profile above the line is equal to the sum of those below the line

Areas A + C + E + G + I = areas B + D + F + H + J + K

Fig. 3 Definition of Centre Line

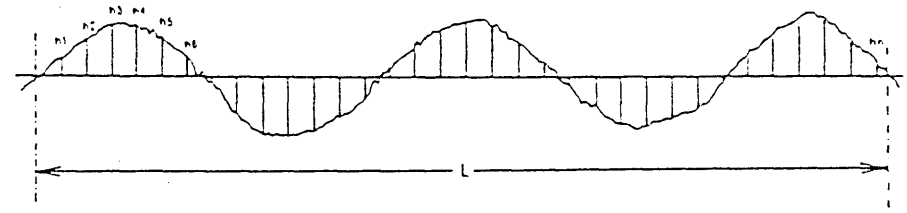

The R_a value of the surface is the average height of the profile above and below the centre line

$$R_a = \frac{h_1 + h_2 + h_3 \ldots h_n}{L} = \frac{1}{L}\int_0^L |h|\,dL$$

Where h is the height of the profile above or below the centre line at points at unit distances apart.
L Units = Sampling length

Fig. 6.18 Definition of roughness (Ref. 156).

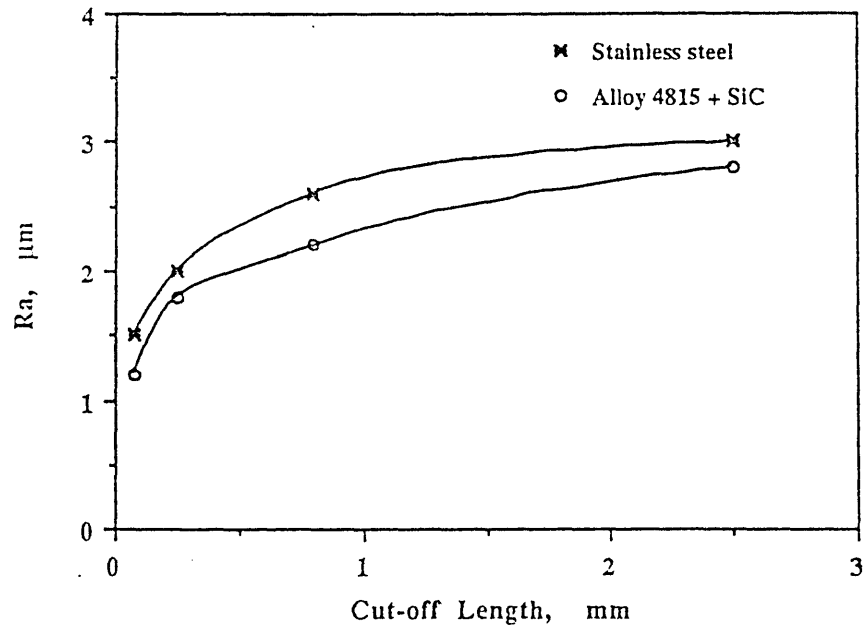

Fig. 6.19 Effect of cut off length on surface roughness (samples from series 2).

Table 6.1

Laser processing conditions for series 1.

Sample Nos.	Laser Power, kW	Traverse speed mm/s	SiC feed rate g/min	Stellite feed rate g/min
1.	1.92	9.0	3.5 - 8.0	35.0
2.	1.92	7.5	3.5 - 8.0	35.0
3.	1.92	7.0	3.5 - 8.0	35.0

The maximum clad dimensions obtained were 4 mm width and 1.5 mm height. The height of the clad layer was found to be increased gradually from one end of the sample to other conforming to the progressive increase in cladding powder feed rate. Samples were subjected to wear tests under the conditions described in section 6.3.1.1. Because of their high wear resistance, samples 2 and 3 were tested by using a relatively harder rock (sand-stone). A qualitative assessment of wear loss was made by measuring the thickness of worn samples at three different points 10 mm apart from each other and corresponding to an increasing proportion of SiC. The results show (Fig. 6.20) that, as expected, the removal of material (i.e. decrease in the thickness of clad layer) was less in the areas where the SiC feed rate was high. The trend observed was an increase in the abrasive wear resistance with the decrease in the traverse speed (Fig. 6.20).

6.4.1.2 Series Two -- Two-body Abrasive Wear (Load varied)

Seven sets of experiments were carried out on samples prepared from overlapping track clads of Alloy 4815, stainless steel, Stellite and their composites with SiC, also the substrate material was tested for comparative studies. The laser processing conditions and clad parameters are reported in Table 4.3.

The samples were subjected to wear testing for a total period of four and three minutes, in intervals of one minute, in the case of alloy and composite clads respectively. The test loads were varied from 50 to 200 N (corresponding to pressures of 28.5 - 103.3 kPa) at increments of 50 N.

Fig. 6.21 shows the wear loss of the substrate, alloy 4815 and Alloy 4815 + SiC composite. The wear loss of Alloy 4815 was less than the substrate at low load, but at higher load ($\geq$ 50 kPa) it followed the same trend as that of the substrate (i.e. increase in wear rate by the same amount with increasing load). The wear resistance of Alloy 4815 + SiC composite was found to be four times that of the Alloy 4815 up to the applied pressure of 77.5 kPa. However, the wear loss of the composite was increased with increasing the pressure from 77.5 to 103.3 kPa. This increase in wear loss was due to the removal of the clad layer and exposure of clad-substrate interface area.

Fig. 6.22 shows the wear behaviour of Stellite and Stellite + SiC composite. As expected, the Stellite clad showed a far better wear resistance than the substrate and a steady increase in the wear loss with increasing applied pressure. Although the Stellite + SiC composite did not show a very high wear resistance, it was still slightly better than the Stellite clad. The wear loss of Stellite + SiC composite rapidly increased with increasing pressure from 77.5 to 103.3 kPa for the same reasons as described in the case of Alloy 4815 + SiC composite.

The wear resistance of stainless steel clad was also found to be far better than the substrate. The wear resistance of stainless steel was slightly improved by the inclusion of SiC particles to form composite (Fig. 6.23). The trend in both stainless steel and its composite with SiC was an increase in the wear rate with increase in the applied load.

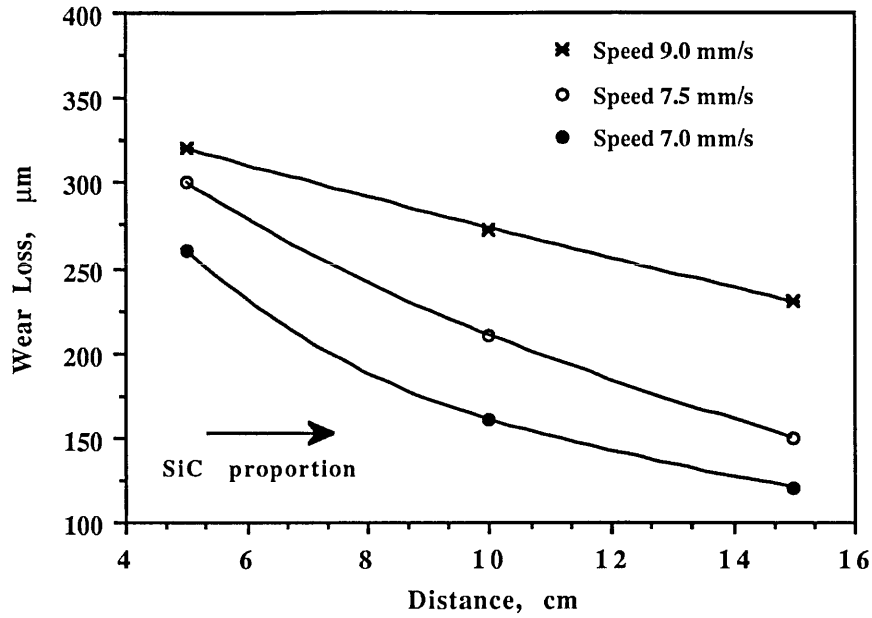

Fig. 6.20 Wear loss at various points along the length of the sample.

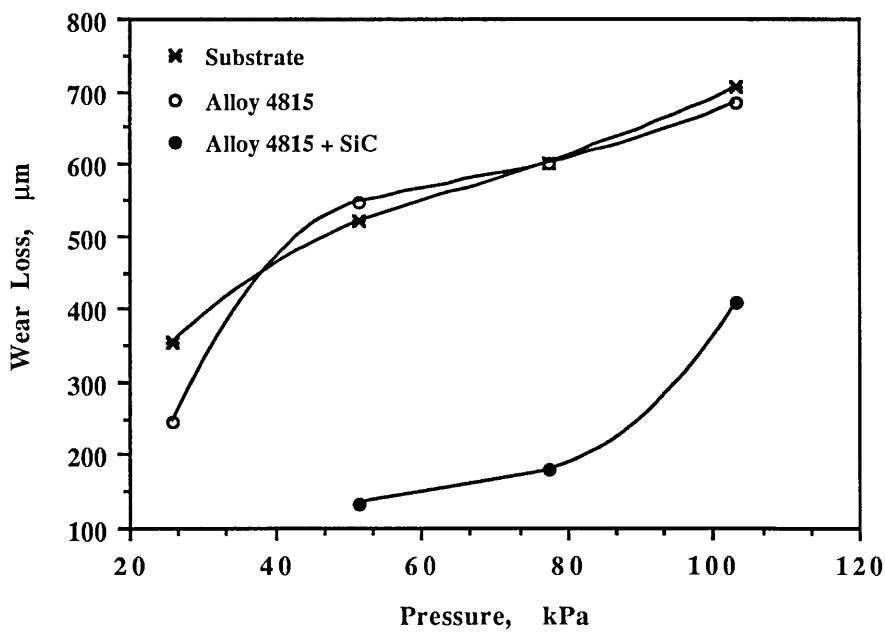

Fig. 6.21 Effect of applied pressure on the wear loss (series 2).

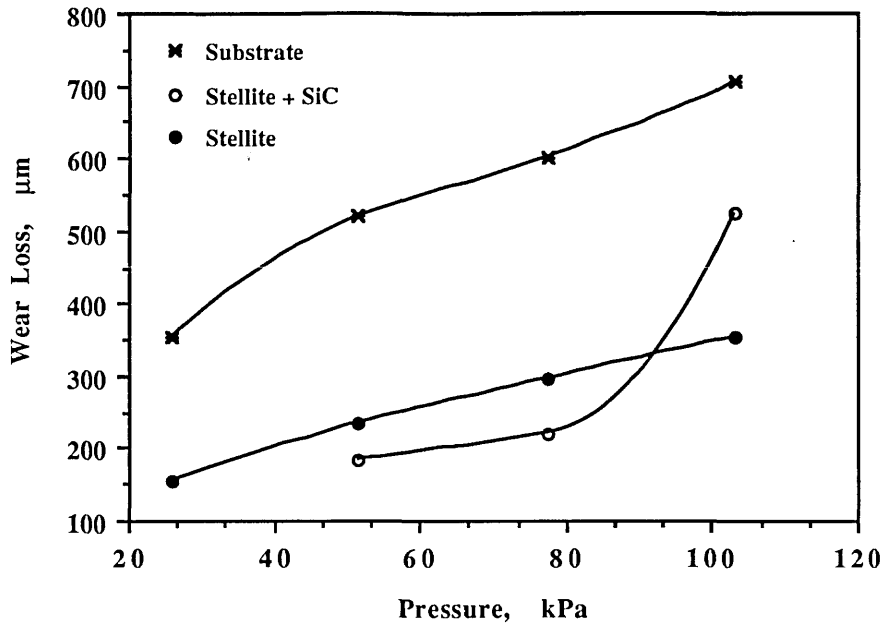

Fig. 6.22 Effect of applied pressure on the wear loss of Stellite and Stellite + SiC clads (series 2).

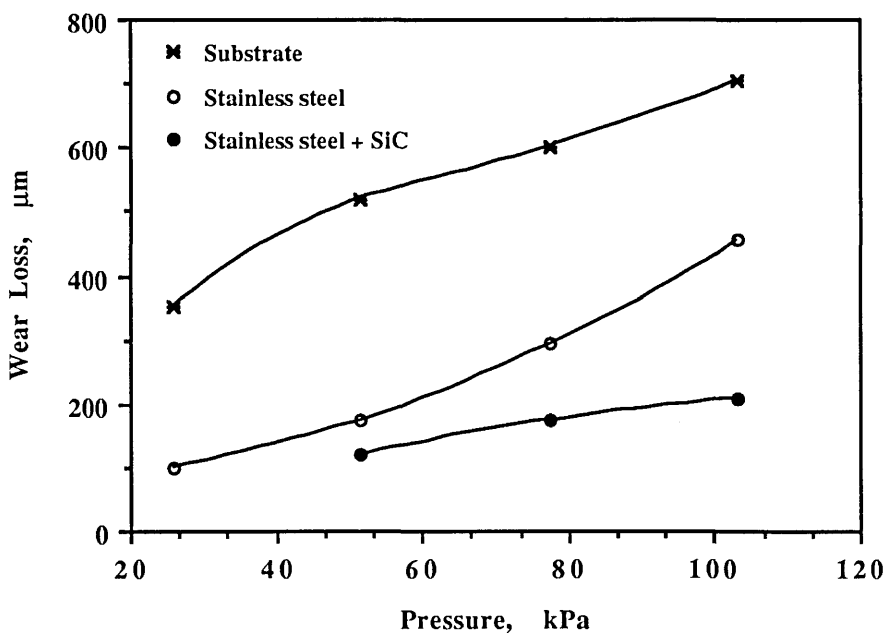

Fig. 6.23 Effect of applied pressure on the wear loss of stainless steel and stainless steel + SiC clads (series 2).

6.4.1.3 Series Three -- Two-body Abrasive Wear (Test time varied)

Five sets of experiments were carried out in this series on samples of substrate, Stellite, Alloy 4815 and composites of Alloy 4815 and Stellite with SiC. The laser processing conditions for producing these clads are reported in Table 4.4.

All samples were subjected to wear testing for a total time period of four minutes in intervals of one minute at a constant load of 200 N (103.3 kPa).

The results showed (Fig. 6.24) a very high wear resistance of Stellite clad as compared with substrate. Stellite + SiC composite showed a slightly better wear resistance than the Stellite clad. The trend observed, in both Stellite and Stellite + SiC composite clads, was an approximately constant increase in the wear loss with increasing test time. However, after 3 minutes, the Stellite + SiC composite showed a decline in the wear resistance. This was attributed to the removal of the complete clad layer in three minutes test time.

Fig. 6.25 shows the wear behaviour of alloy 4815 and alloy 4815 + SiC composite clads. In this test, both alloy 4815 and its composite with SiC, showed an unexpected wear behaviour. The wear loss of alloy 4815 clad was found greater than that of the substrate. The trend was a constant increase in wear loss with increasing time. The composite of alloy 4815 and SiC showed a very high wear resistance with extremely low wear losses. The wear loss was relatively higher after the first minute of test and was decreased during subsequent tests of one minute intervals.

6.4.1.4 Series Four -- Three-body Abrasive Wear (Various alloys and composites)

The same type of samples used for the two-body abrasive tests in section 6.4.1.2 was used for this test under the conditions described in section 6.3.1.3. The wear losses in this series were very low (only a few microns) due to the mild test conditions applied.

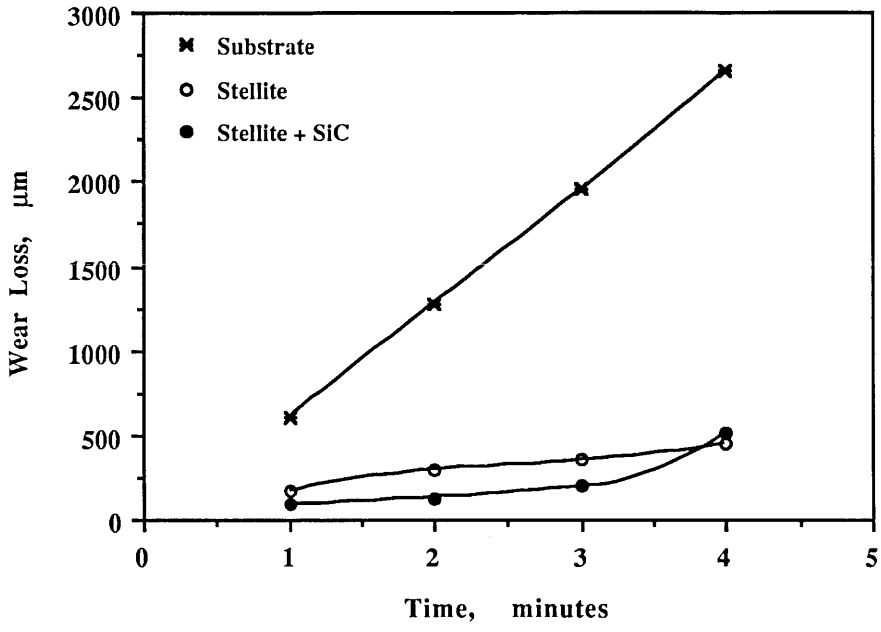

Fig. 6.24 Plot showing wear rate of Stellite and Stellite + SiC clads (series 3).

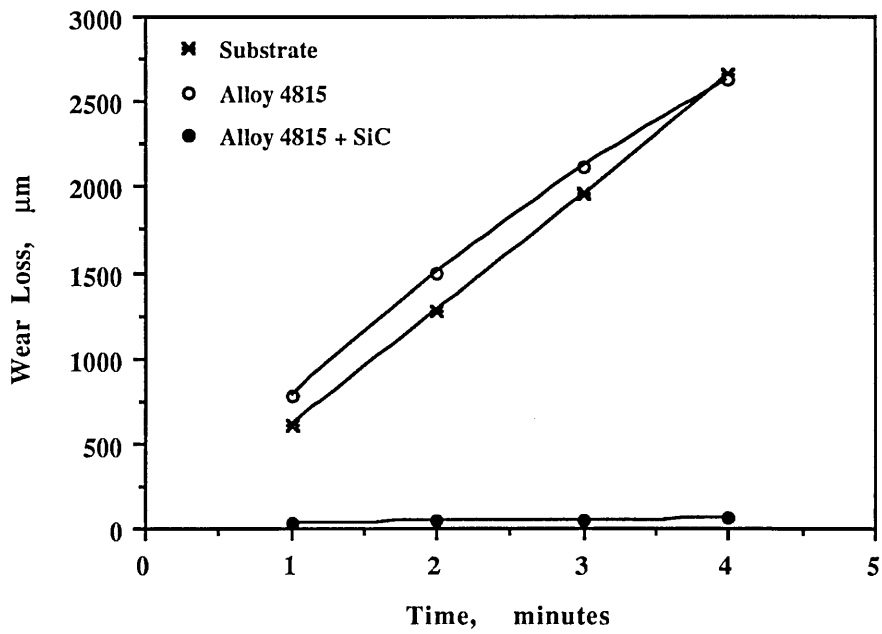

Fig. 6.25 Plot showing wear rate of Alloy 4815 and Alloy 4815 + SiC clads (series 3).

Fig. 6.26 shows the wear data of Alloy 4815 and its composite with SiC. The wear resistance of alloy 4815 was approximately 40% higher than that for the substrate. The improvement in the wear resistance of alloy 4815 resulting from the inclusion of SiC was also very small. The wear loss of both alloy 4815 and alloy 4815 + SiC composite clads was the same at the beginning of the test but it was decreased in the case of the latter during subsequent intervals of test time. The trend, in both cases, was a constant increase in the wear loss with increasing time after the first hour of test.

The Stellite alloy and its composite showed a better wear resistance than alloy 4815 and its composite. The wear resistance of Stellite + SiC composite was about double of that for the Stellite samples (Fig. 6.27). In both cases, the wear loss increased steadily with time.

Fig. 6.28 shows the wear behaviour of stainless steel and its composite. The wear resistance of the mild steel substrate was approximately doubled by cladding with stainless steel. However, the improvement in wear resistance of stainless steel + SiC composite was relatively small as compared with the stainless steel clad. Both alloy and composite clads showed a steady increase in the wear loss with increasing time.

6.4.1.5 Series Five -- Three-body Abrasive Wear (Alloy 4815 + SiC composite)

In this series of experiments, three samples of Alloy 4815 + SiC composite, produced at different feed rates and traverse speeds, were subjected to wear testing. The processing conditions for these alloys are reported in Table 4.5.

The wear behaviour of these three composite clad samples, namely S1, S2, and S3, is compared with that for the substrate and for the Alloy 4815 clad in Figs. 6.29, 6.30 and 6.31 respectively. The improvement in the wear resistance of composite sample S1 was almost negligible (Fig. 6.29) as compared with Alloy 4815 sample. Composite sample S2 showed a slight increase in the wear resistance (Fig. 6.30). Sample S3

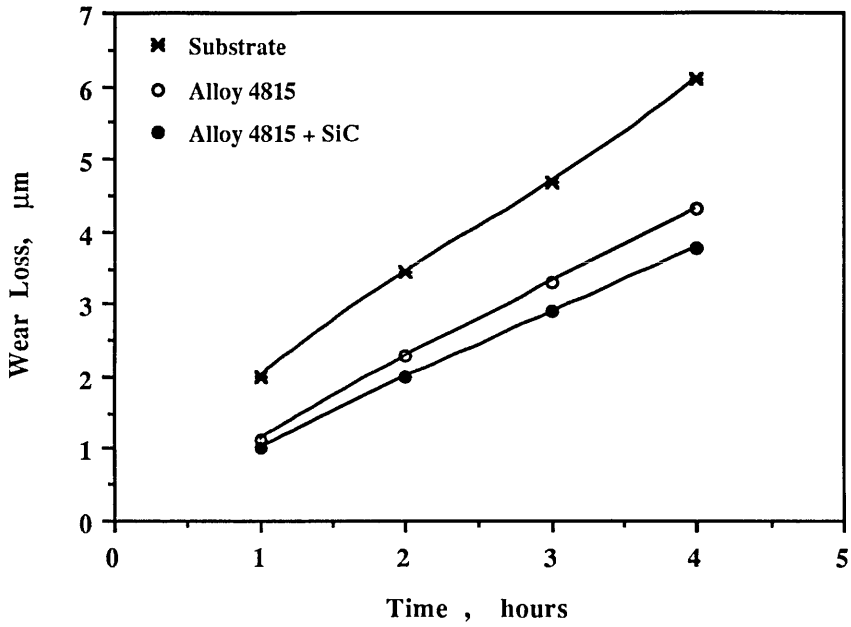

Fig. 6.26 Plot showing wear rate of Alloy 4815 and Alloy 4815 + SiC clads (series 4).

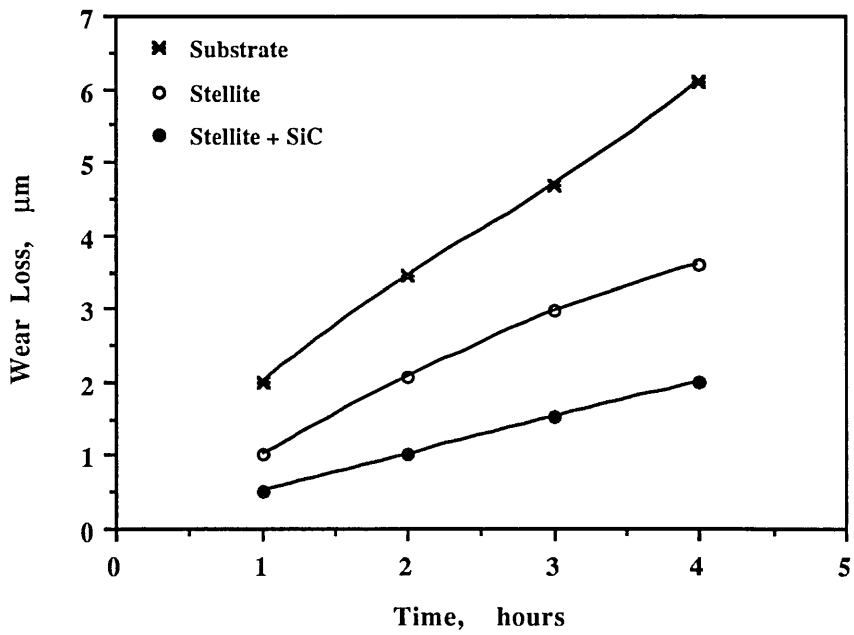

Fig. 6.27 Plot showing wear rate of Stellite and Stellite + SiC clads (series 4).

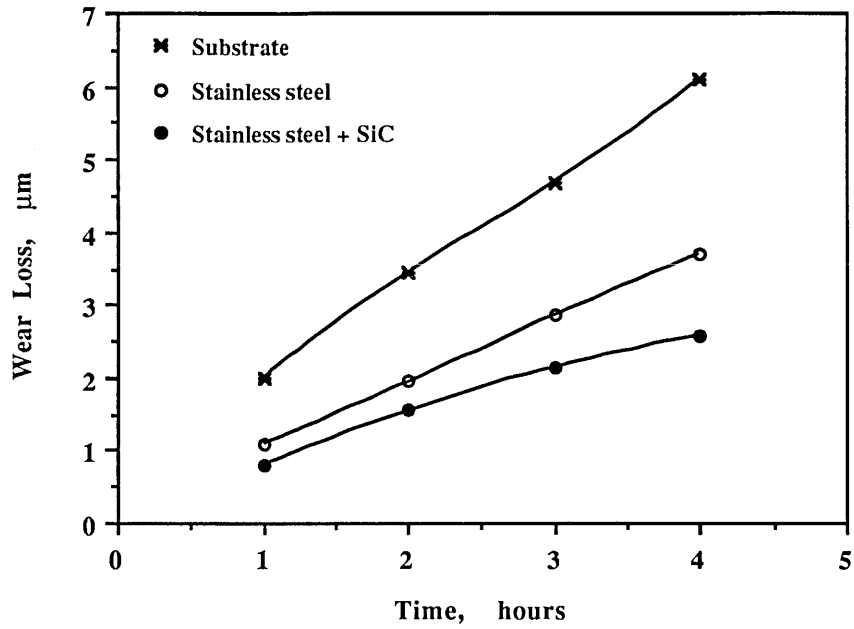

Fig. 6.28 Plot showing wear rate of stainless steel and stainless steel + SiC clads (series 4).

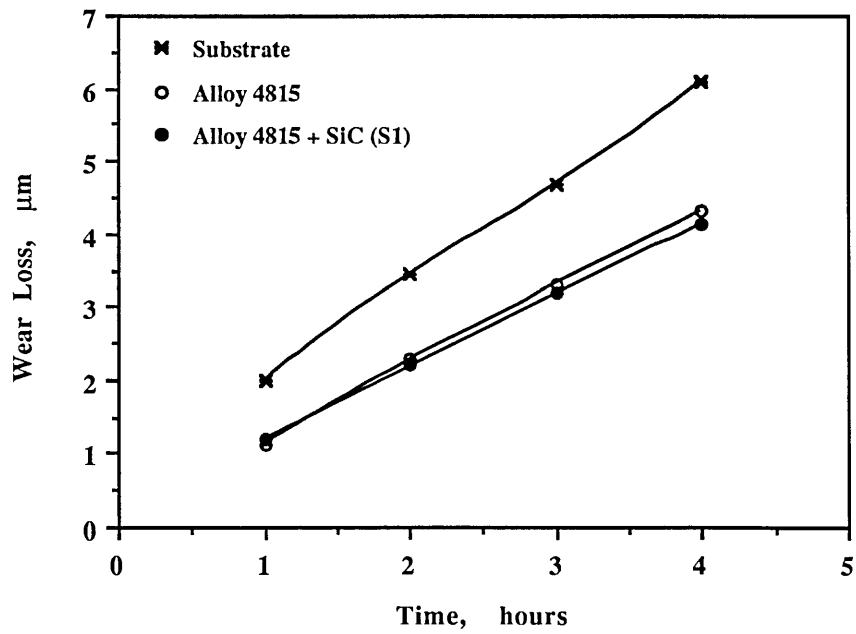

Fig. 6.29 Plot showing wear rate of Alloy 4815 and Alloy 4815 + SiC clads (sample S1, series 5).

showed the highest wear resistance relative to other two samples in this series (Fig. 6.31).

In the set of samples with constant feed rate of 17.5 g/min, a lower traverse speed gave slightly better wear resistance than higher speed (Fig. 6.32). In the other set at constant traverse speed, high feed rate led to slightly better wear resistance than the low feed rate (Fig. 6.33).

6.4.2 Microhardness of Worn Surfaces

The microhardness was measured on the worn surfaces produced by the quantitative two-body abrasive wear tests (series 2 and 3) for comparison with those measured before the test. It was observed that the hardness of the alloy samples and of the substrate, in both series 2 and 3, was substantially increased after the wear tests (Tables 6.2 and 6.3). However, the hardness of the Stellite + SiC and stainless steel + SiC and Alloy 4815 + SiC composite samples of series 2 was markedly decreased due to the removal of the complete clad layer (Table 6.2). In series 3, the hardness of Stellite + SiC composite was decreased, whereas a marked increase in hardness was observed in the case of Alloy 4815 + SiC composite (Table 6.3).

The hardness results of worn surfaces produced by the three-body wear tests (series 4 and 5) are given in Tables 6.4 and 6.5. In series 4, the hardness of the worn surfaces of the alloy samples and of the substrate was increased slightly except that for the Stellite sample which was decreased (Table 6.4). However, the hardness of Stellite + SiC and stainless steel + SiC composites was decreased whereas an increase in the hardness of Alloy 4815 + SiC composite was observed. In series 5, unlike the other series, the hardness of all the composites was markedly increased after the wear test (Table 6.5).

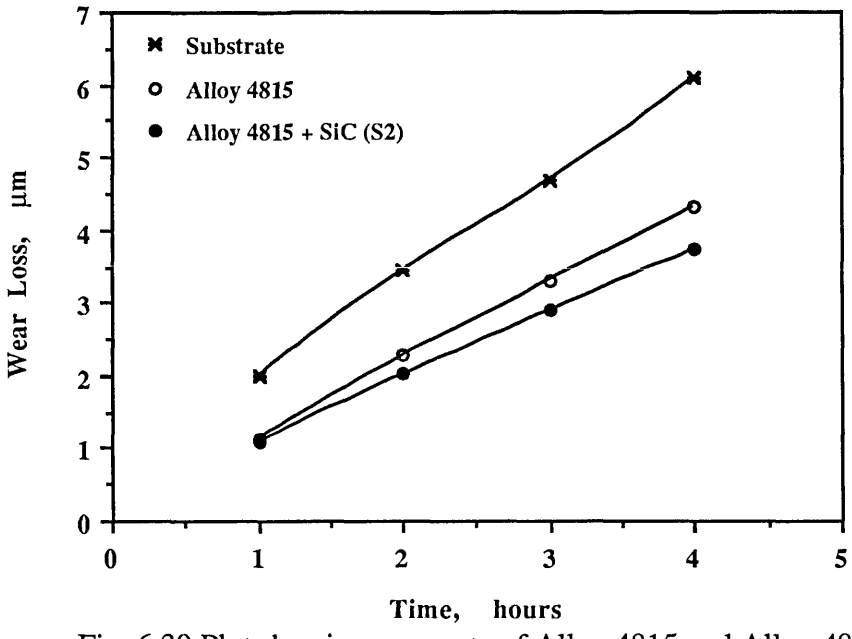

Fig. 6.30 Plot showing wear rate of Alloy 4815 and Alloy 4815 + SiC clads (sample S2, series 5).

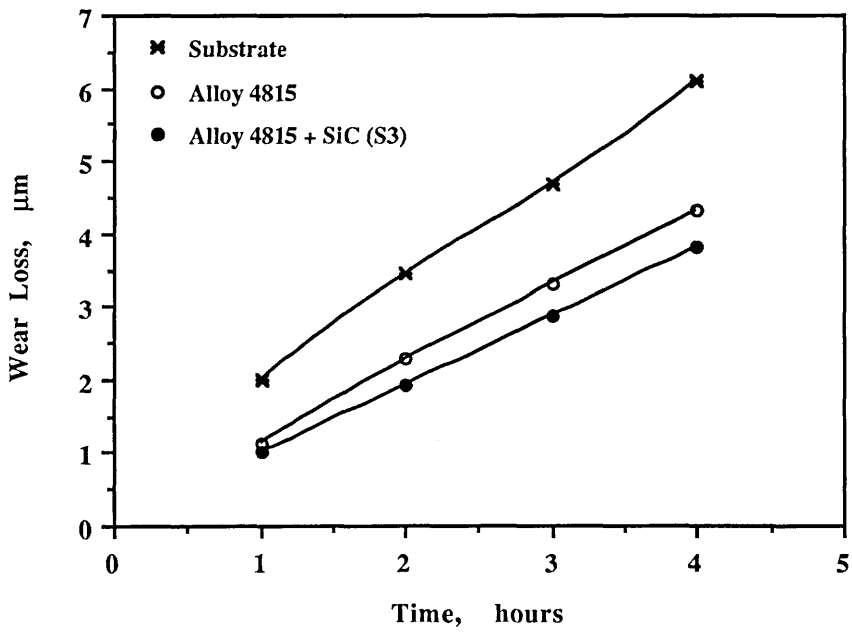

Fig. 6.31 Plot showing wear rate of Alloy 4815 and Alloy 4815 + SiC clads (sample S3, series 5).

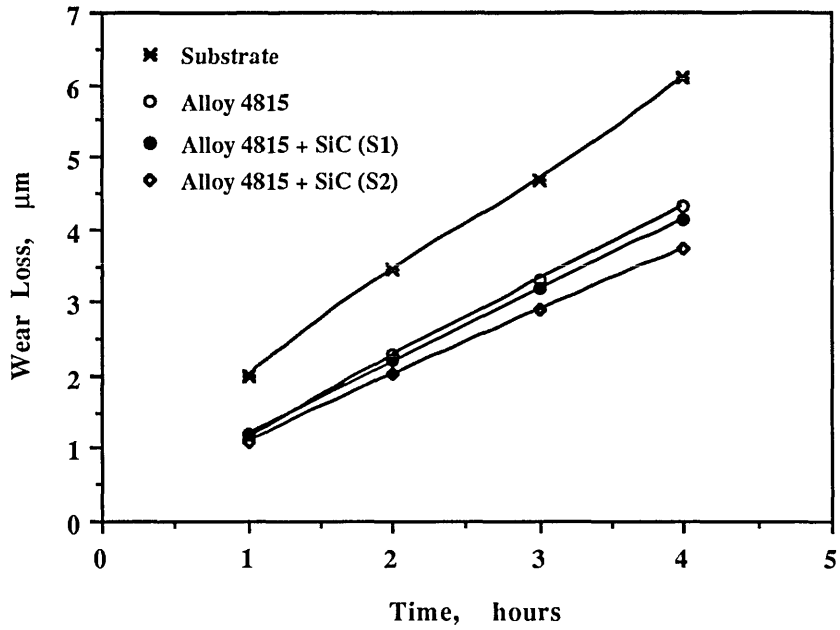

Fig. 6.32 Plot showing comparative wear rate of a set of Alloy 4815 + SiC clads produced at constant feed rate (17.7 g/min) and different speeds, 12.5 (S1) and 5 (S2) mm/s (series 5).

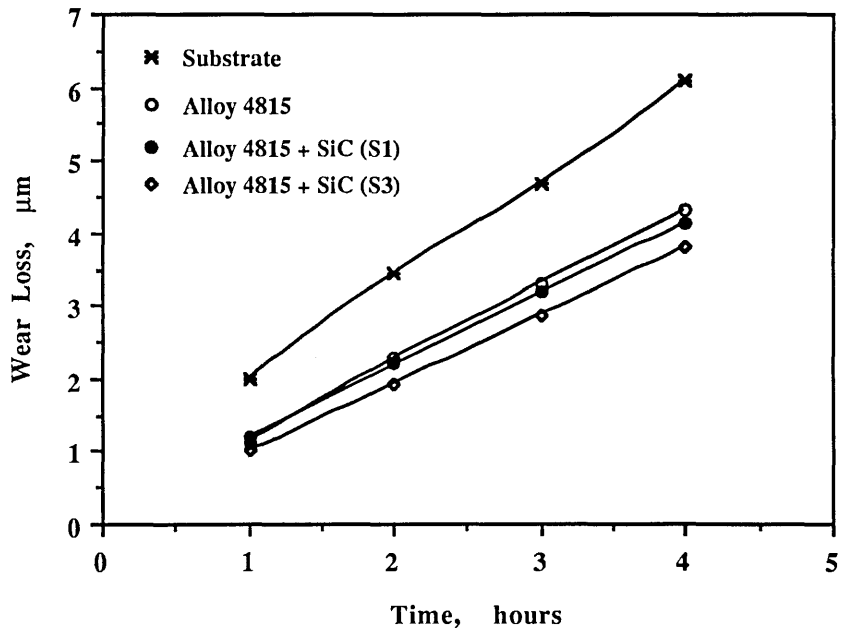

Fig. 6.33 Plot showing comparative wear rate of a set of Alloy 4815 + SiC clads produced at constant speed (12.5 mm/s) and different feed rates, 17.7 (S1) and 21.5 (S3) g/min (series 5).

Table 6.2

Microhardness of samples before and after wear test (series 2).

Nos.	Clad composition	Hardness, Hv before test	Hardness, Hv after test
1.	Substrate	223	348
2.	Stainless steel	241	348
3.	Stellite	618	618
4.	Alloy 4815	165	348
5.	20% SiC + Stellite	823	454*
6.	20% SiC + Stainless steel	966	454
7.	20% SiC + Alloy 4815	890	454*

* Complete clad layer was removed.

Table 6.3

Microhardness of samples before and after wear test (series 3).

Nos.	Clad composition	Hardness, Hv before test	Hardness, Hv after test
1.	Substrate	223	348
2.	Stellite	540	763
3.	Alloy 4815	211	348
4.	10% SiC + Stellite	763	454*
5.	10% SiC + Alloy 4815	710	890

* Complete clad layer was removed.

Table 6.4

Microhardness of samples before and after wear test (series 4).

Nos.	Clad composition	Hardness, Hv before test	Hardness, Hv after test
1.	Substrate	223	275
2.	Stainless steel	241	263
3.	Stellite	618	511
4.	Alloy 4815	165	275
5.	20% SiC + Stellite	823	618
6.	20% SiC + Stainless steel	966	579
7.	20% SiC + Alloy 4815	890	890

Table 6.5

Microhardness of samples before and after wear test (series 5).

Nos.	Clad composition	Hardness, Hv before test	Hardness, Hv after test
1.	Substrate	223	275
2.	S1	406	966
3.	S2	366	763
4.	S3	543	966

6.4.3 Surface Roughness

The surface roughness of all worn surfaces was measured to correlate with the wear loss data obtained. No definite relation in the increase in surface roughness with wear loss was found in any of the series. However, the samples subjected to two-body wear tests showed comparatively rough surfaces (Tables 6.6 and 6.7). In the case of three-body wear, the worn surfaces showed a polished appearance with low surface roughness (Tables 6.8 and 6.9). However, in general with only a few exceptions, the samples with high wear resistance showed a lower surface roughness than those with low wear resistance.

Table 6.6

Surface roughness of worn samples after wear tests (series 2).

Nos.	Clad composition	Ra, minimum μm	Ra, maximum μm	Ra (mean of 5 readings)
1.	Substrate	2.0	2.8	2.48
2.	Stainless steel	2.0	2.8	2.5
3.	Stellite	0.68	1.15	0.84
4.	Alloy 4815	2.3	2.6	2.48
5.	20 wt.% SiC + Stellite	1.2	2.5	1.8
6.	20 wt.% SiC + Stainless steel	0.55	0.72	0.61
7.	20 wt.% SiC + Alloy 4815	2.0	2.6	2.3

Table 6.7

Surface roughness of worn samples after wear tests (series 3).

Nos.	Clad composition	Ra, minimum μm	Ra, maximum μm	Ra (mean of 5 readings)
1.	Substrate	2.0	2.8	2.48
2.	Stellite	2.0	2.8	2.48
3.	Alloy 4815	2.3	4.6	3.38
4.	10 wt.% SiC + Stellite	1.2	1.8	1.56
5.	10 wt.% SiC + Alloy 4815	0.18	0.25	0.20

Table 6.8

Surface roughness of worn samples after wear tests (series 4).

Nos.	Clad composition	Ra, minimum μm	Ra, maximum μm	Ra (mean of 5 readings)
1.	Substrate	1.0	2.2	2.54
2.	Stainless steel	0.07	0.10	0.08
3.	Stellite	0.08	0.40	0.17
4.	Alloy 4815	0.25	0.42	0.35
5.	20 wt.% SiC + Stellite	0.08	0.30	0.15
6.	20 wt.% SiC + Stainless steel	0.06	0.20	0.14
7.	20 wt.% SiC + Alloy 4815	0.50	0.62	0.54

Table 6.9

Surface roughness of worn samples after wear tests (series 5).

Nos.	Clad composition	Ra, minimum μm	Ra, maximum μm	Ra (mean of 5 readings)
1.	Substrate	1.0	2.2	1.54
2.	S1	0.25	0.85	0.59
3.	S2	0.80	2.3	1.76
4.	S3	1.0	1.8	1.46

6.4.4 Microscopy of Worn surfaces

Microscopical studies of worn surfaces, without any preparation, were carried out to understand the mechanism of the removal of material from various samples. Subsurface features were also revealed by high magnification scanning electron microscopy. Since the abrasive material and wear conditions used were the same in a given series of experiments, the wear groove width as it appeared on the micrographs is used to characterise the relative groove depth of various samples. It was found that the increase in width was associated with an increase in depth. The wear mechanisms involved and the behaviour of individual samples in various series subjected to wear testing will be discussed fully in the chapter on discussion , however, the micrographs of worn surfaces are briefly described here emphasizing the typical features observed; specific detailed features will be referred to in the discussion.

6.4.4.1 Micrographs of Worn Surfaces Produced by Two-body Wear Conditions

The geometry of the two-body set-up used indicates that the worn surfaces of a given sample should have multidirectional grooves of uniform depth. The majority of the worn surfaces showed the groove features conforming to the two-body wear conditions applied.

In series two, the alloy clad samples; stainless steel (Figs. 6.34-6.35), Stellite (Figs. 6.36-6.37), Alloy 4815 (Figs. 6.38-6.39); showed relatively deeper grooves than the composite clad samples; Stellite + SiC (Figs. 6.40-6.41), stainless steel + SiC (Figs. 6.42-6.43) and Alloy 4815 + SiC (Figs. 6.44-6.45); indicating the higher wear resistance of the latter. However, the features of the worn surfaces imply that the mechanisms involved were different in the case of alloy and composite samples.

In series three, the features of the worn surfaces were nearly similar to those obtained in series two, except for that of the mild steel substrate sample which showed a less uniform groove structure indicating a severe wear (Figs. 6.46-6.47). The alloy samples in this series; Stellite (Figs. 6.48-6.49) and Alloy 4815 (Figs. 6.50-6.51); showed almost uniform grooves in multidirections. The groove depth in the case of alloy 4815 was very large as compared with the Stellite alloy sample. The Stellite + SiC composite sample showed relatively greater groove depth due to removal of the complete clad layer during wear testing (Figs. 6.52-6.54). However, the Alloy 4815 + SiC composite worn surface showed a very shallow groove depth (Figs. 6.55-6.57). Again as in the case of series two, it seems that the wear mechanisms involved were different in alloy and composite samples.

A. **Fig. 6.34** Worn surface of stainless steel clad sample showing the groove depth and groove features conforming to two-body abrasive wear (series 2).

B. **Fig. 6.35** A magnified section of Fig. 6.34, illustrating the mechanism of material removal.

C. **Fig. 6.36** Worn surface of Stellite clad sample showing the groove depth and groove features conforming to two-body abrasive wear (series 2).

D. **Fig. 6.37** A magnified section of Fig. 6.36, illustrating the mechanism of material removal.

E. **Fig. 6.38** Worn surface of Alloy 4815 clad sample showing the groove depth and groove features conforming to two-body abrasive wear (series 2).

F. **Fig. 6.39** A magnified section of Fig. 6.38, illustrating the mechanism of material removal.

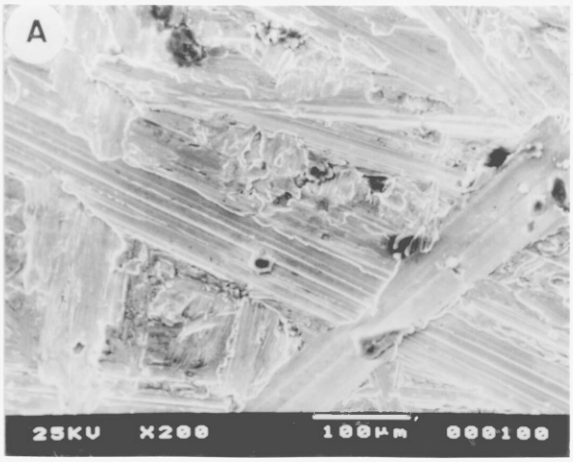
A
25KV X200 100µm 000100

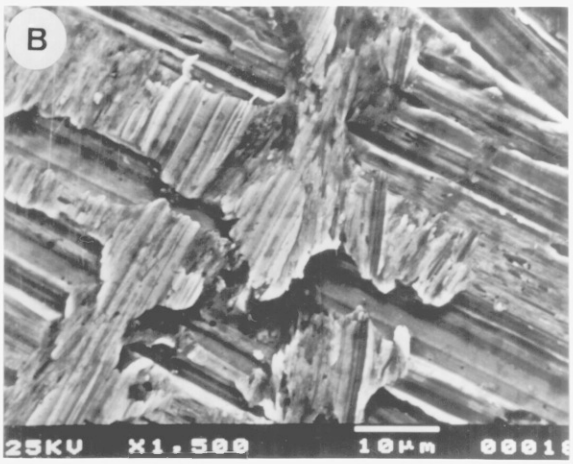
B
25KV X1,500 10µm


C
25KV X100 100µm 0001

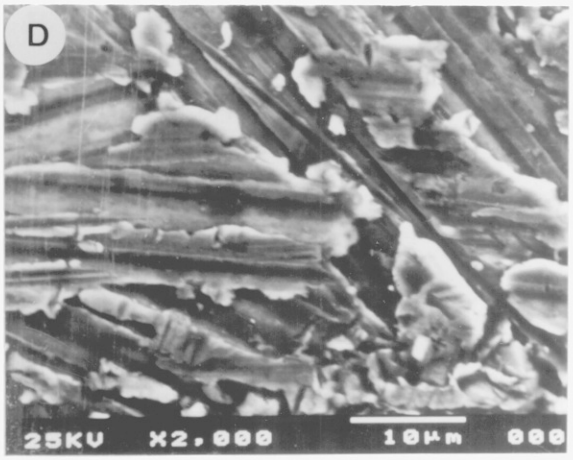
D
25KV X2,000 10µm

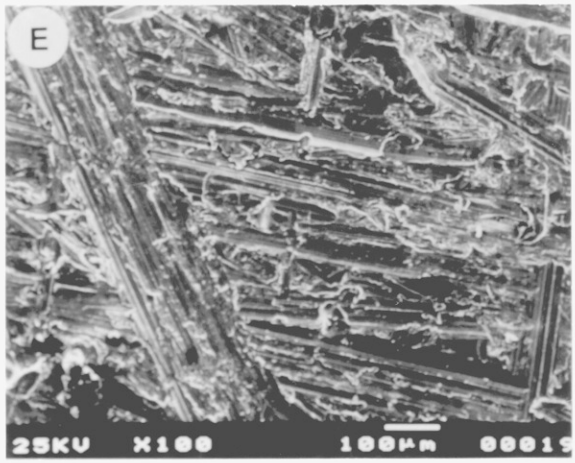
E
25KV X100 100µm

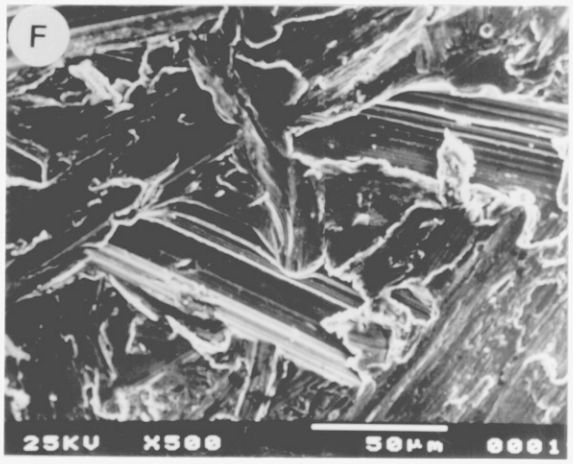
F
25KV X500 50µm 0001

A. **Fig. 6.40** Worn surface of Stellite + SiC clad sample showing the groove depth and groove features conforming to two-body abrasive wear (series 2).

B. **Fig. 6.41** A magnified section of Fig. 6.40, illustrating the mechanism of material removal.

C. **Fig. 6.42** Worn surface of stainless steel + SiC clad sample showing the groove depth and groove features conforming to two-body abrasive wear (series 2).

D. **Fig. 6.43** A magnified section of Fig. 6.42, illustrating the mechanism of material removal.

E. **Fig. 6.44** Worn surface of Alloy 4815 + SiC clad sample showing the groove depth and groove features conforming to two-body abrasive wear (series 2).

F. **Fig. 6.45** A magnified section of Fig. 6.44, illustrating the mechanism of material removal.

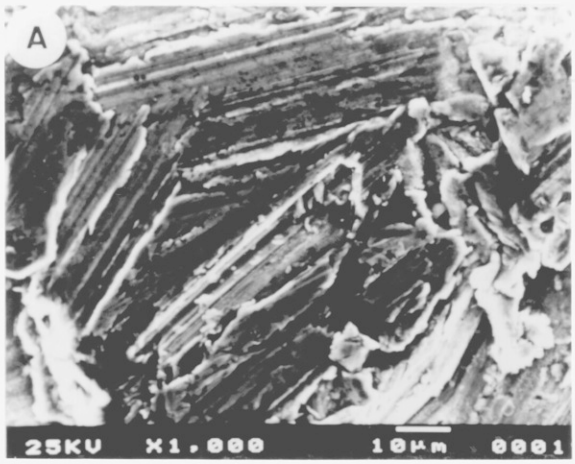
A
25KV X1,000 10µm 0001

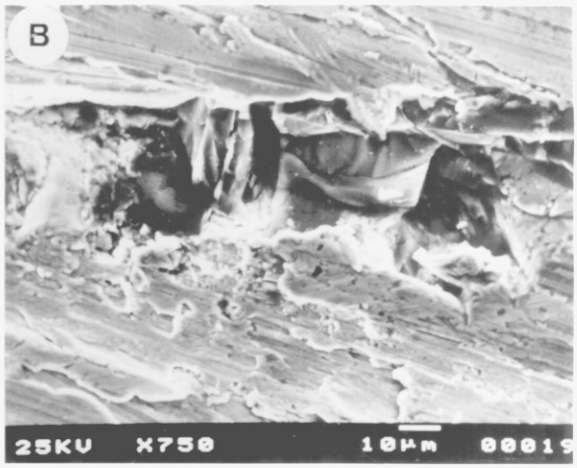
B
25KV X750 10µm 00019

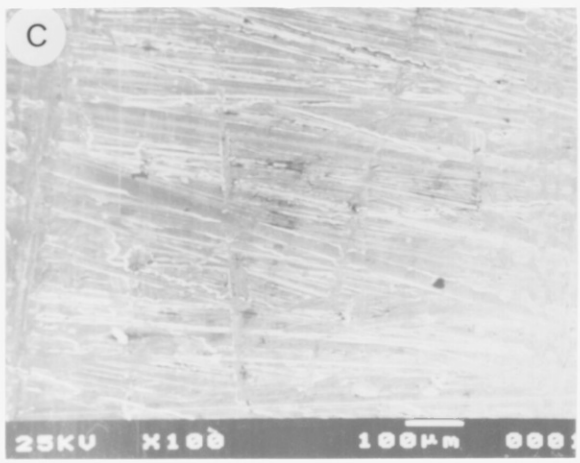
C
25KV X100 100µm

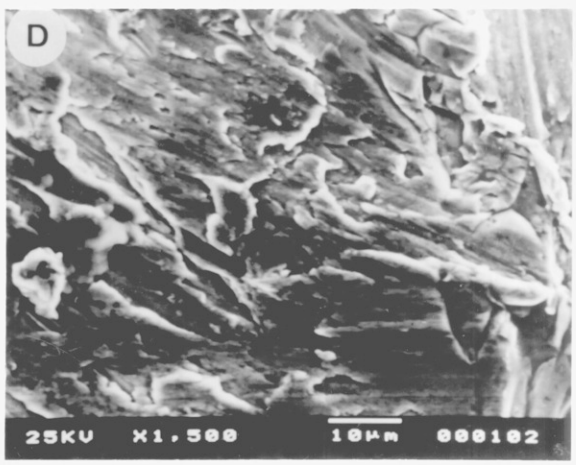
D
25KV X1,500 10µm 000102

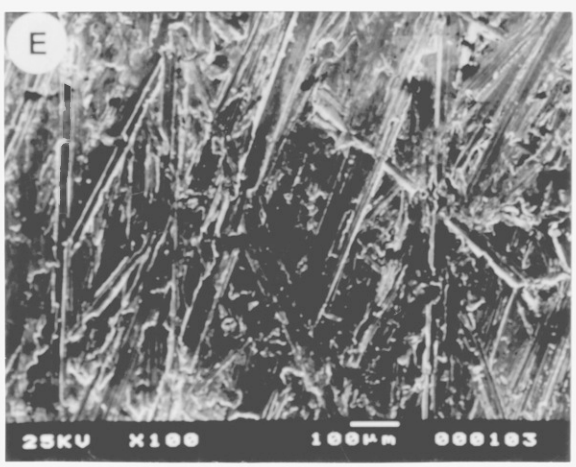
E
25KV X100 100µm 000103

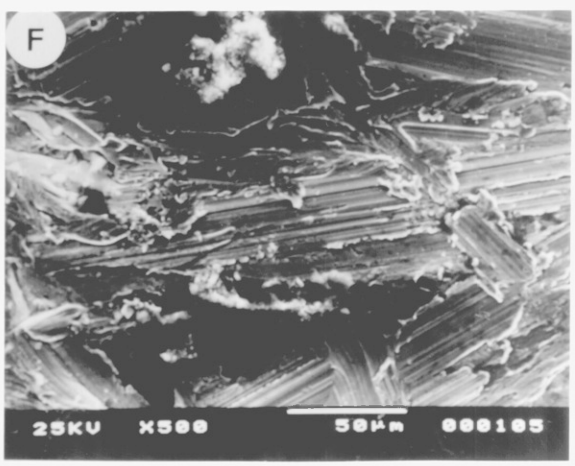
F
25KV X500 50µm 000105

A. **Fig. 6.46** Worn surface of mild steel substrate sample showing the groove depth and groove features conforming to two-body abrasive wear (series 3).

B. **Fig. 6.47** A magnified section of Fig. 6.46, illustrating the mechanism of material removal; a severe wear was observed.

C. **Fig. 6.48** Worn surface of Stellite clad sample showing the groove depth and groove features conforming to two-body abrasive wear (series 3).

D. **Fig. 6.49** A magnified section of Fig. 6.48, illustrating the mechanism of material removal; a subsurface damage was observed.

E. **Fig. 6.50** Worn surface of Alloy 4815 clad sample showing the groove depth and groove features conforming to two-body abrasive wear (series 3).

F. **Fig. 6.51** A magnified section of Fig. 6.50, illustrating the mechanism of material removal; material removal occurred by ploughing of large fragments.

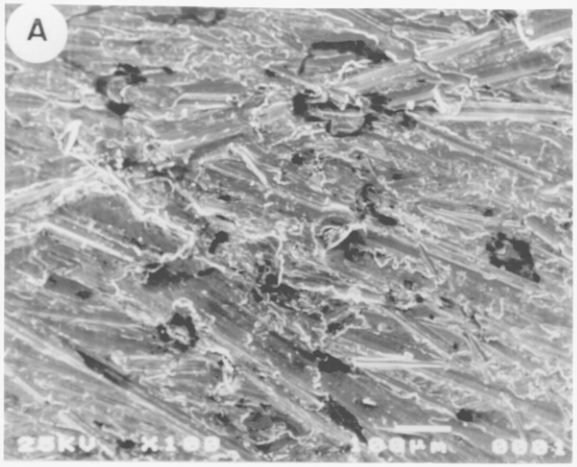
A

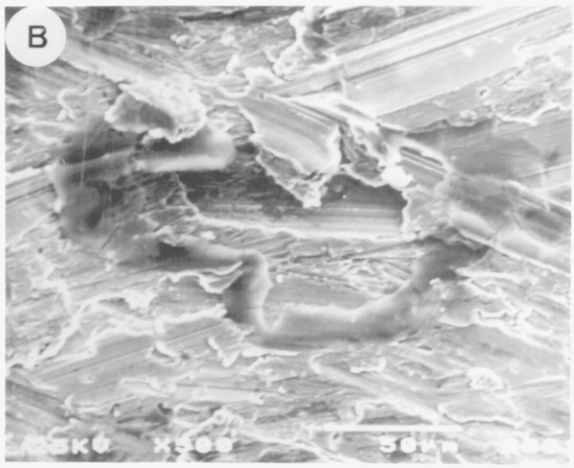
B

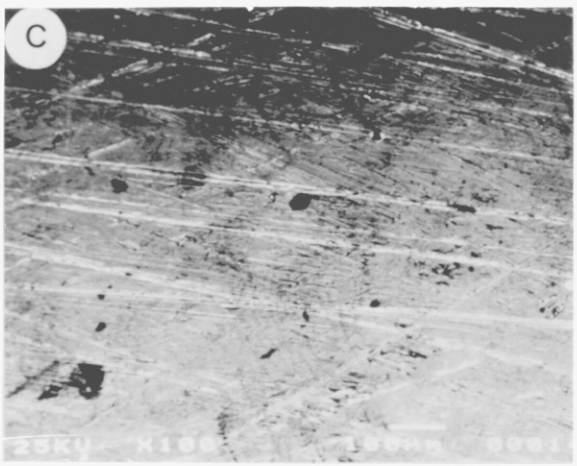
C

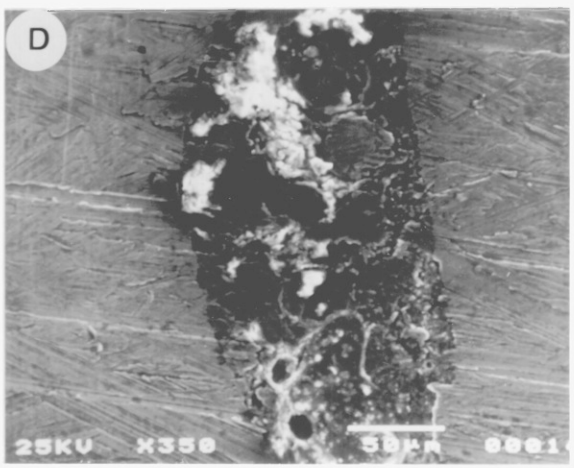
D
25KV X350

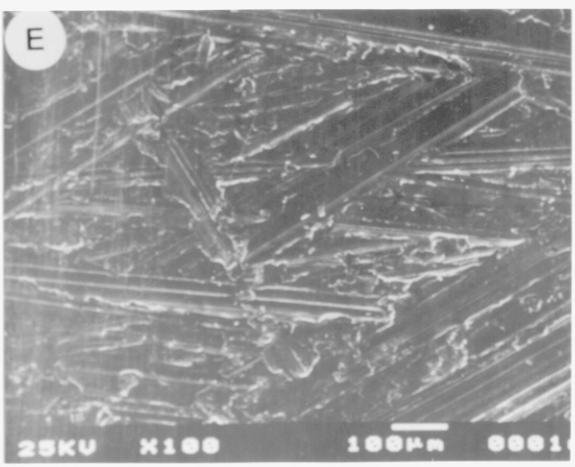
E
25KV X100

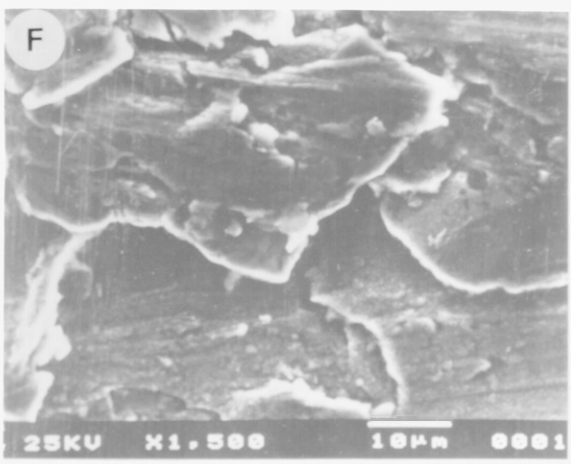
F
25KV X1,500

A. **Fig. 6.52** Worn surface of Stellite + SiC clad sample showing the groove depth and groove features conforming to two-body abrasive wear (series 3); The worn surface resembles to that of a softer Alloy 4815 clad worn surface (Fig. 6.50) due to the removal of complete clad layer at the end of wear test.

B. **Fig. 6.53** A magnified section of Fig. 6.52, illustrating the microcrack.

C. **Fig. 6.54** A magnified section of Fig. 6.52, illustrating the mechanism of material removal; wear occurred due to the cutting action of abrasive particles.

D. **Fig. 6.55** Worn surface of Alloy 4815 + SiC clad sample showing the groove depth and groove features conforming to two-body abrasive wear (series 3); material removal occurred in the form of short and long microchips.

E. **Fig. 6.56** Worn surface of Alloy 4815 + SiC clad (series 3) showing severe wear attack in the surrounding areas of embedded SiC particles.

F. **Fig. 6.57** Worn surface of Alloy 4815 + SiC clad (series 3) showing material removal by flaking off small fragments around a detached SiC particle.

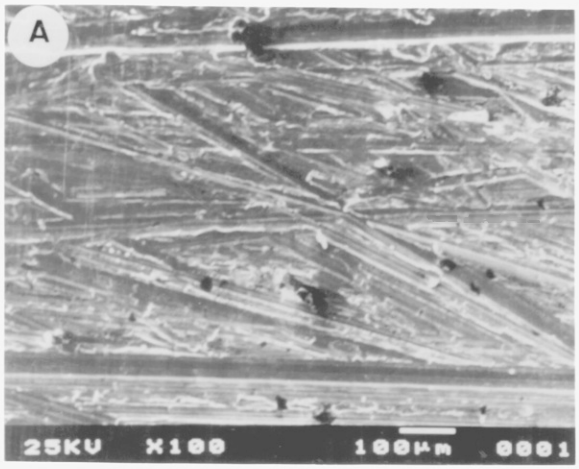
A
25KV X100 100µm 0001

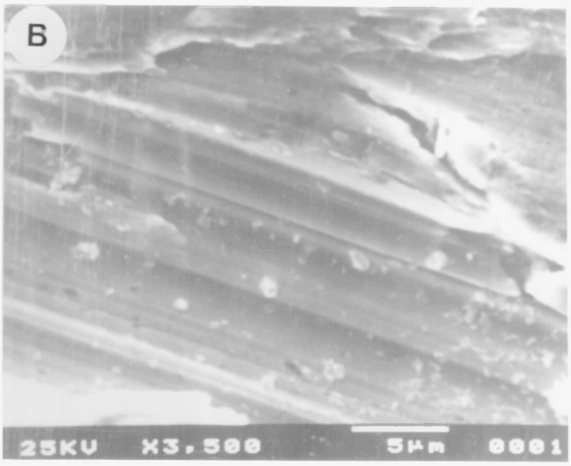
B
25KV X3,500 5µm 0001

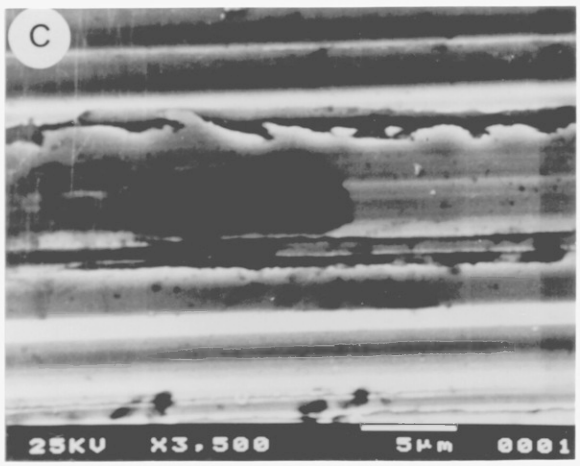
C
25KV X3,500 5µm 0001

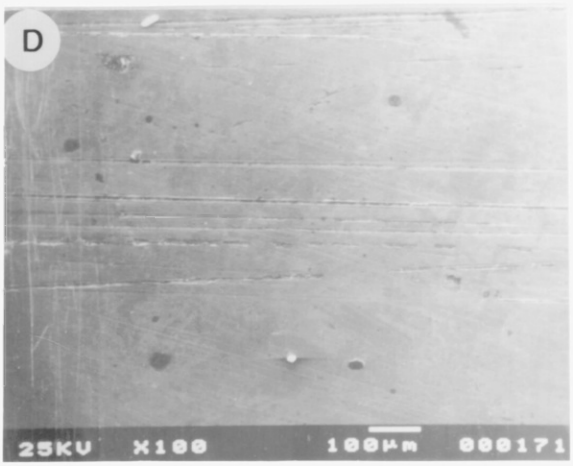
D
25KV X100 100µm 000171

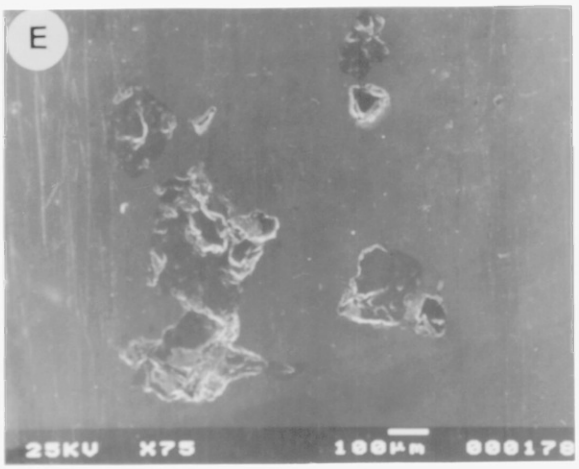
E
25KV X75 100µm 000170

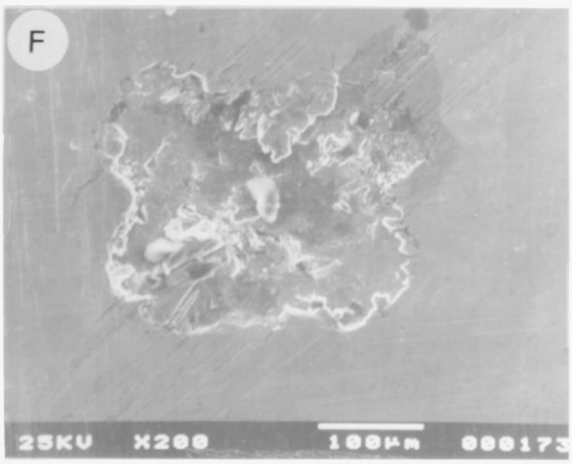
F
25KV X200 100µm 000173

6.4.4.2 Micrographs of Worn Surfaces Produced by Three-body Wear Conditions

The low-stress three-body wear conditions used led to the production of worn surfaces with multidirectional grooves of non-uniform depth. All samples in this set of experiments produced worn surfaces conforming to the three-body wear conditions applied.

In series four, both the alloy samples; stainless steel (Figs. 6.58-6.59), Stellite (Figs. 6.60-6.62), Alloy 4815 (Figs. 6.63-6.65); and the composite samples; Stellite + SiC (Figs. 6.66-6.67), stainless steel + SiC (Figs. 6.68-6.69) and Alloy 4815 + SiC (Figs. 6.70-6.71); showed surfaces with a polished appearance and with shallow and multidirectional grooves. The worn surface of Alloy 4815 + SiC composite sample was polished during the wear test to the extent that in some areas, the dendritic structure was revealed (Fig. 6.70).

Similarly, in series five, the worn surfaces produced were of polished appearance with shallow multidirectional grooves. Since all the three composite samples; S1 (Figs. 6.72-6.75), S2 (Figs. 6.76-6.79), S3 (Figs. 6.80-6.81); in this series showed nearly the same amount of wear, the worn surfaces obtained were also of closely same nature.

A. **Fig. 6.58** Worn surface of a stainless steel clad sample showing the groove depth and groove features conforming to three-body wear (series 4).

B. **Fig. 6.59** Worn surface of a stainless steel clad sample showing the areas of high porosity, severely attacked by the abrasive particles (series 4).

C. **Fig. 6.60** Worn surface of a Stellite clad sample showing the groove depth and groove features conforming to three-body wear (series 4).

D. **Fig. 6.61** A magnified section of worn surface of Stellite clad sample shown in Fig. 6.60, illustrating a subsurface damage due to severe attack of abrasive particles.

E. **Fig. 6.62** A magnified section of worn surface of Stellite clad sample shown in Fig. 6.60, illustrating large extent of pitting caused by localized attack of abrasive particles.

F. **Fig. 6.63** Worn surface of a Alloy 4815 clad sample showing the groove depth and groove features conforming to three-body wear (series 4).

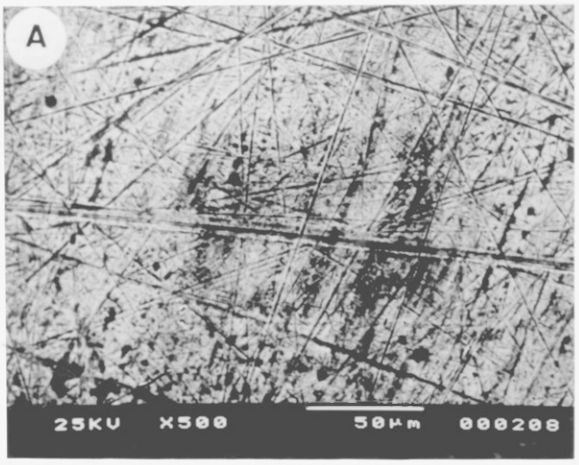
A
25KV X500 50µm 000208

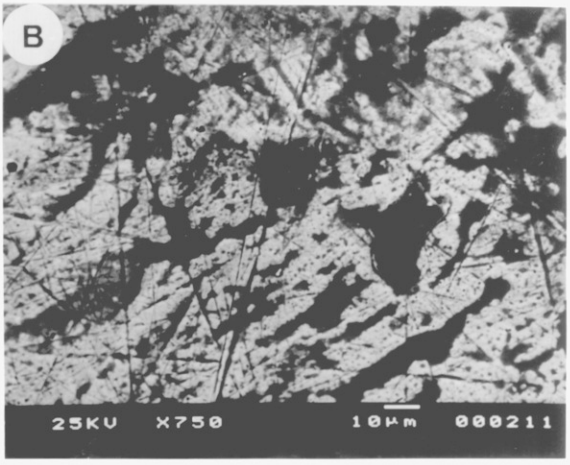
B
25KV X750 10µm 000211

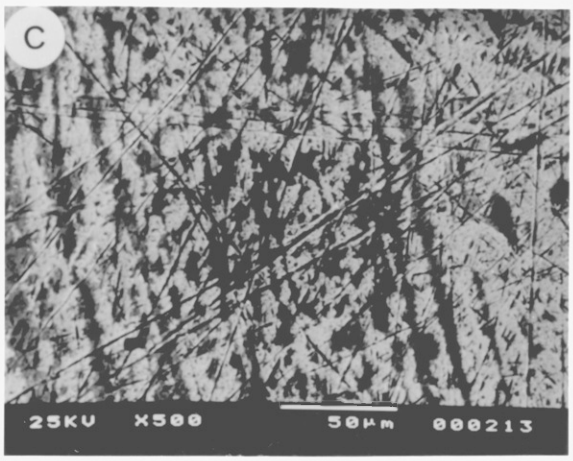
C
25KV X500 50µm 000213

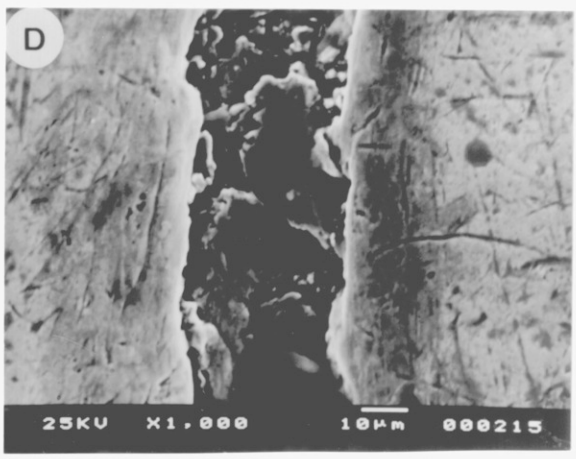
D
25KV X1,000 10µm 000215

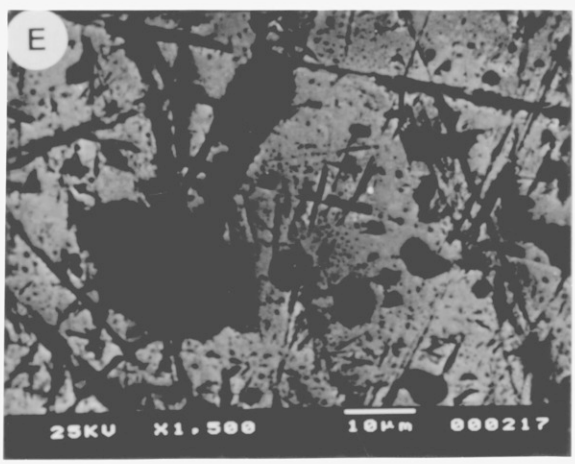
E
25KV X1,500 10µm 000217

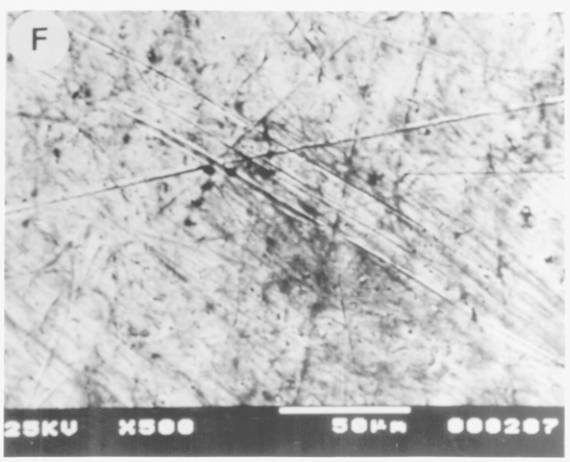
F
25KV X500 50µm 000207

A. **Fig. 6.64** A magnified section of worn surface of Alloy 4815 clad sample shown in Fig. 6.63, illustrating that removal of material occurred by the ploughing action of the abrasive particles.

B. **Fig. 6.65** A magnified section of worn surface of Alloy 4815 clad sample shown in Fig. 6.63, illustrating an unusual zigzag pattern produced by abrasive particle attached to rubber disc.

C. **Fig. 6.66** Worn surface of a Stellite + SiC clad sample showing the groove depth and groove features conforming to three-body wear (series 4).

D. **Fig. 6.67** A magnified section of worn surface of Stellite + SiC clad sample shown in Fig. 6.66, illustrating the presence of microcracks.

E. **Fig. 6.68** Worn surface of stainless steel + SiC clad sample showing large extent of pitting.

F. **Fig. 6.69** Worn surface of a stainless steel + SiC clad sample showing the groove depth and groove features conforming to three-body wear (series 4).

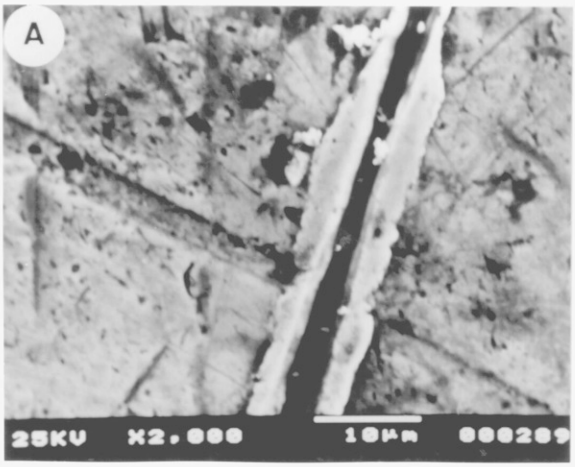
A
25KV X2,000 10µm

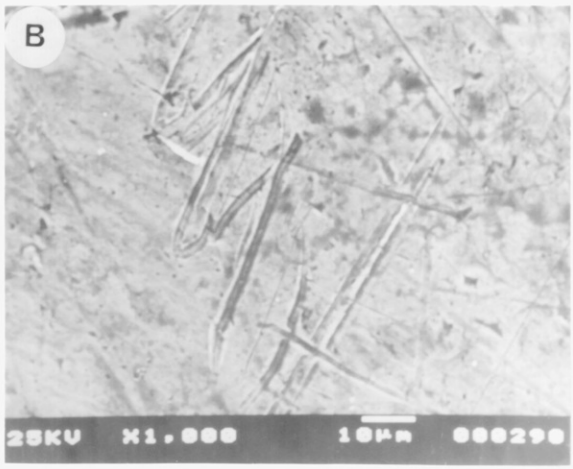
B
25KV X1,000 10µm

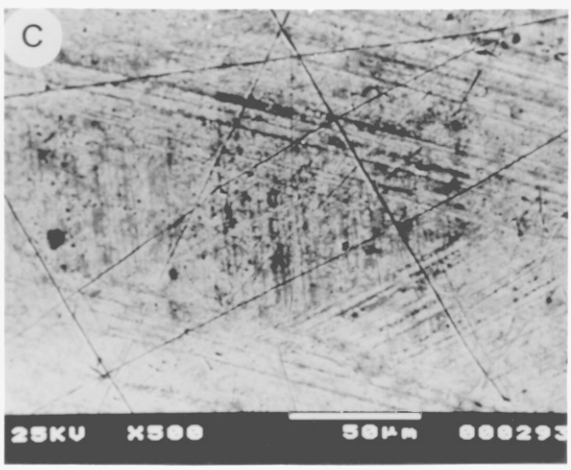
C
25KV X500 50µm

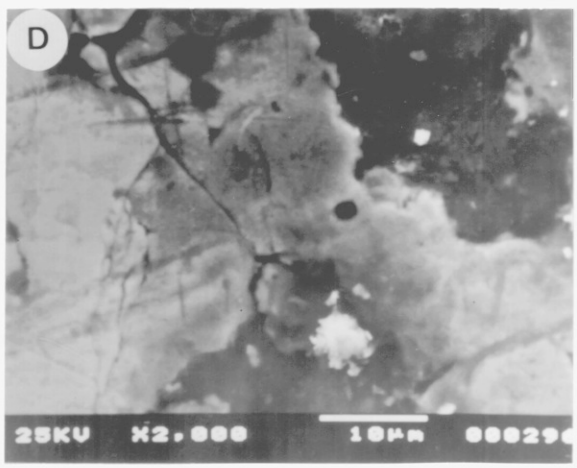
D
25KV X2,000 10µm

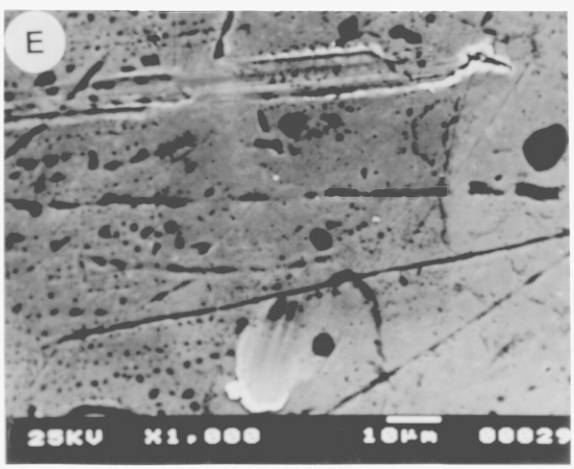
E
25KV X1,000 10µm

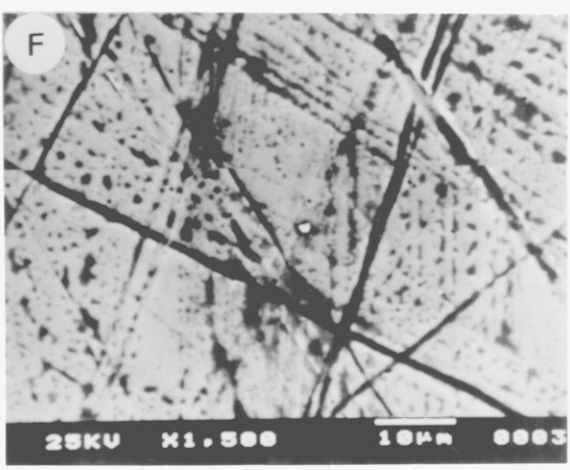
F
25KV X1,500 10µm

A. **Fig. 6.70** Worn surface of Alloy 4815 + SiC clad sample showing microstructure, due to its polished appearance obtained.

B. **Fig. 6.71** A magnified section of Alloy 4815 + SiC clad sample showing area severely attacked by abrasive particles.

C. **Fig. 6.72** Worn surface of Alloy 4815 + SiC clad sample (S1) showing the groove depth and groove features conforming to three-body wear (series 5).

D. **Fig. 6.73** Worn surface of Alloy 4815 + SiC clad sample (S1) showing a disintegrated SiC particle, (1) = clad matrix, (2) = region of partially dissolved SiC, (3) = SiC particle.

E. **Fig. 6.74** Worn surface of Alloy 4815 + SiC clad sample (S1) showing no wear scratch in partially dissolved SiC regions.

F. **Fig. 6.75** Worn surface of Alloy 4815 + SiC clad sample (S1) showing a large microcrack.


A
25KV X500 50µm

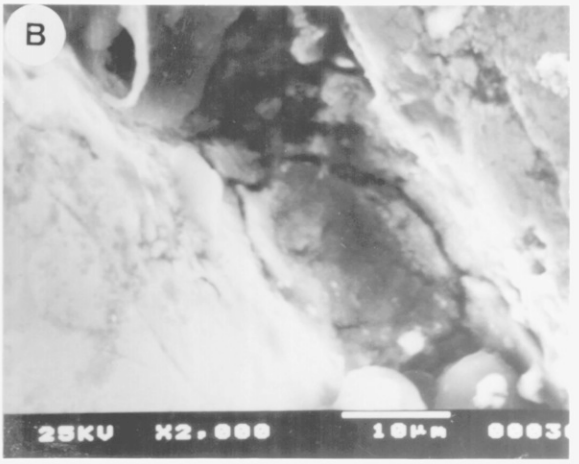
B
25KV X2,000 10µm

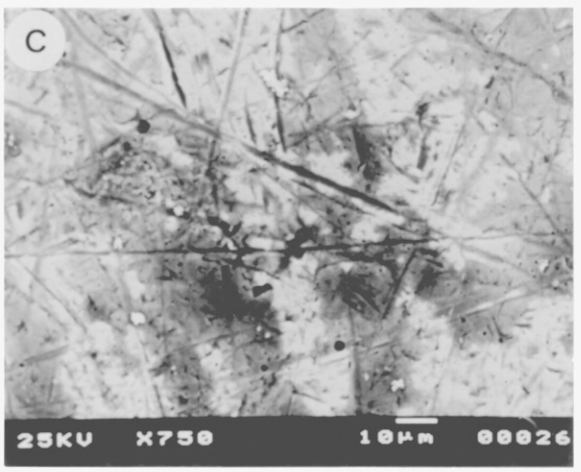
C
25KV X750 10µm 00026

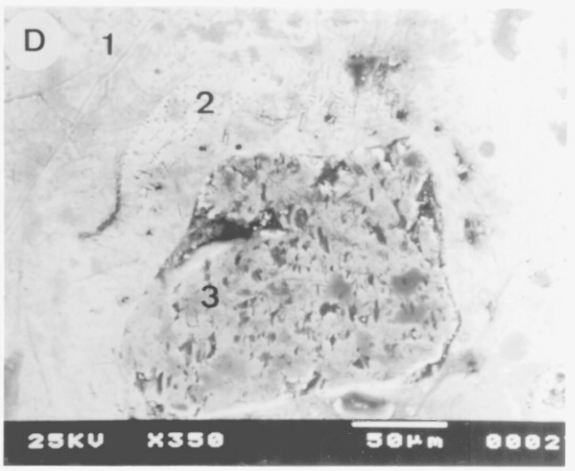
D
1
2
3
25KV X350 50µm

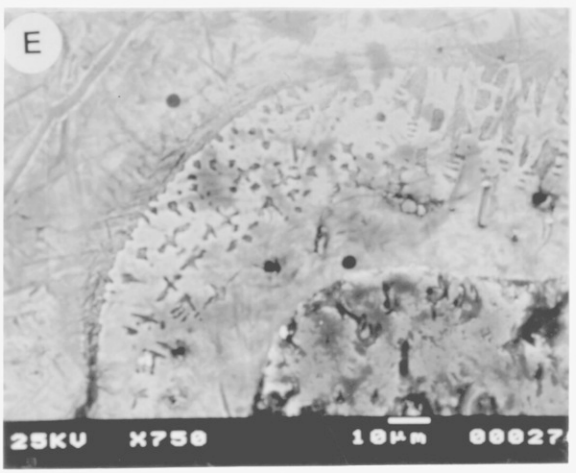
E
25KV X750 10µm

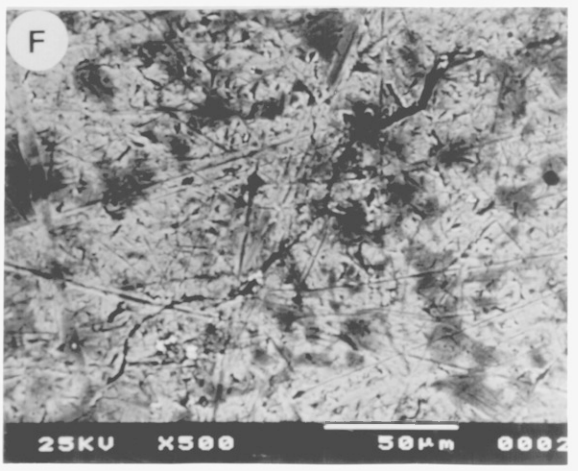
F
25KV X500 50µm

A. **Fig. 6.76** Worn surface of Alloy 4815 + SiC clad sample (S2) showing the groove depth and groove features conforming to three-body wear (series 5).

B. **Fig. 6.77** Worn surface of Alloy 4815 + SiC clad sample (S2) showing severe wear attack by abrasive particles in the areas surrounded by embedded SiC particles, (1) = clad matrix, (2) = SiC particle.

C. **Fig. 6.78** Worn surface of Alloy 4815 + SiC clad sample (S2) showing fracture of SiC particle.

D. **Fig. 6.79** Worn surface of Alloy 4815 + SiC clad sample (S2) showing microstructure in the area exposed by the fragmentation of SiC particle.

E. **Fig. 6.80** Worn surface of Alloy 4815 + SiC clad sample (S3) showing the groove depth and groove features conforming to three-body wear (series 5).

F. **Fig. 6.81** Worn surface of Alloy 4815 + SiC clad sample (S3) showing pitting due to localized attack of abrasive particles.

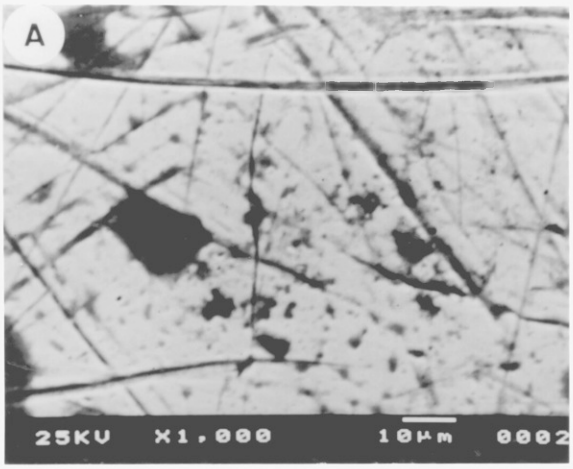
A
25KV X1,000 10µm 0002

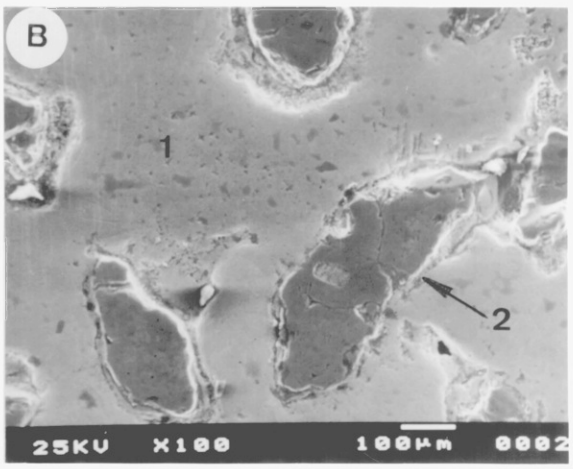
B
1
2
25KV X100 100µm 0002

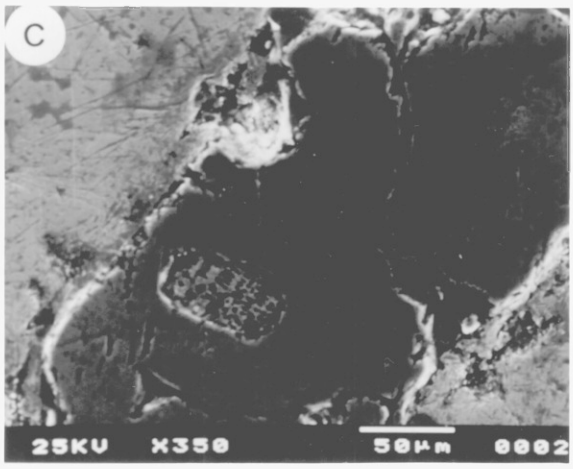
C
25KV X350 50µm 0002

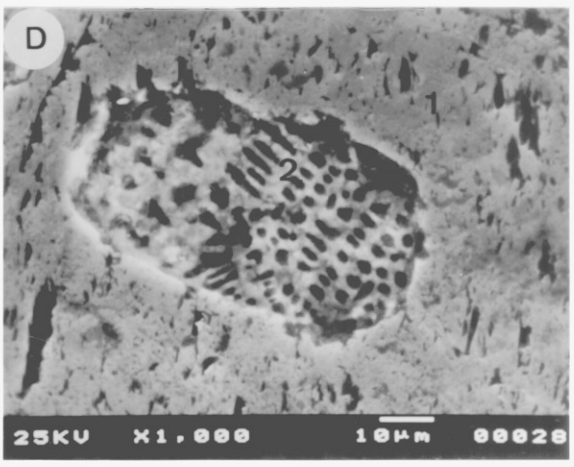
D
1
2
25KV X1,000 10µm 00028

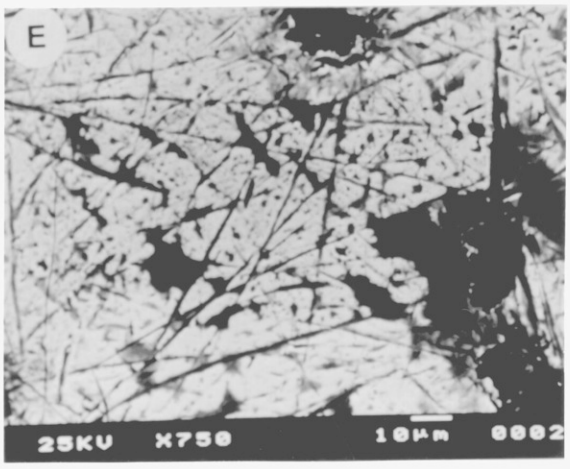
E
25KV X750 10µm 0002

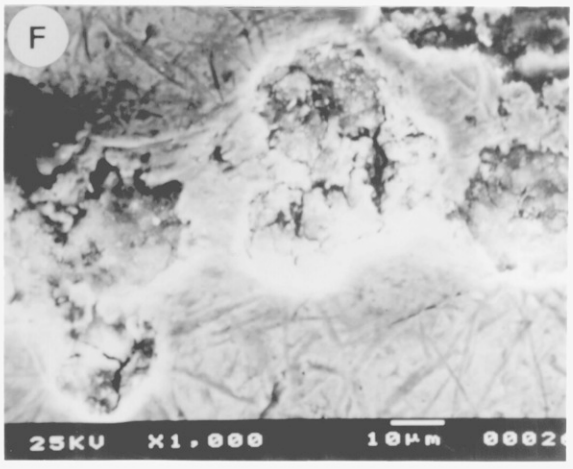
F
25KV X1,000 10µm 0002

CHAPTER 7

ACOUSTIC EMISSION MONITORING OF POWDER FLOW

7.1 INTRODUCTION

The powder flow is an important process parameter in determining the characteristics of the coatings produced by laser cladding, for example, (i) the powder mass flow mainly controls the dilution level of the clad coating and (ii) the mass deposition rate is an inverse function of the particle velocity. An attempt was, therefore, made to determine the effects of various process parameters, related to the powder feed system, on the velocity of the particles emerging from the feed tube. The following parameters were studied,

1. Powder carrier gas flow rate.
2. Feed tube length.
3. Powder particle size.
4. Powder and gas density.
5. Powder feed rate.

An acoustic emission technique was used to obtain these results. Acoustic emission (AE) is a technique based on detecting and analysing the elastic stress waves produced in a material by a dynamic process. Typically the elastic stress waves are detected by a piezo-electric transducer, which is acoustically coupled to the material under investigation, and the resulting voltage analysed by a variety of methods. Several investigations (33, 105-106) have been reported to monitor laser processing by an acoustic emission technique. However, Rawlings and Steen (105) were the first who applied this technique to laser processing when they monitored both transformation hardening and cladding. Powell (33) measured the magnitude of porosity and residual thermal stresses in a clad deposit, during

the cooling process, with the help of acoustic emission. An acoustic emission technique was also applied by Weerasinghe (106) for in-process monitoring of laser beam by receiving the acoustic signals from the transducer attached to the beam reflecting mirrors.

Arrington (107) developed a simple kinetic energy transfer theory for the vertical impact of a mono-disperse powder stream which showed that the acoustic energy (E_{AE}) is a function of the number of collisions per second (n), and the particle mass (m) and impact velocity (v):

$$E_{AE} = nmv^2 \qquad (7.1)$$

E_{AE} is proportional to $V_R^2 = V_T$ where V_R and V_T are the root-mean-square and the true-mean-square voltages respectively. If the transducer is coupled to the substrate, as in the studies by Rawlings and Steen (105), this equation may be applicable. However, it is more convenient when measuring mass flow rates to have the transducer permanently connected to the pipework of the feed system and under these circumstances the energy transfer system will be more complex due to scouring (rolling and sliding) noise in addition to impact noise. Some preliminary work by Arrington with such an arrangement has demonstrated that the frequency spectra is insensitive to powder type, and powder and gas flow rates, and thus does not constrain the choice of working frequency.

7.2 EXPERIMENTAL PROCEDURE

A schematic diagram of the instrumentation is illustrated in Fig. 7.1. A variable screw powder feeder, which produced a uniform flow within 2% irrespective of gas flow, was used to record the powder flow. The pipework of the feed system ended with a section of copper pipe (3 mm internal diameter) which was acoustically insulated from the rest of the system by plastic connectors. The emissions were detected by two piezo-electric sensors with a resonant frequency response of 150 kHz; this high frequency response was

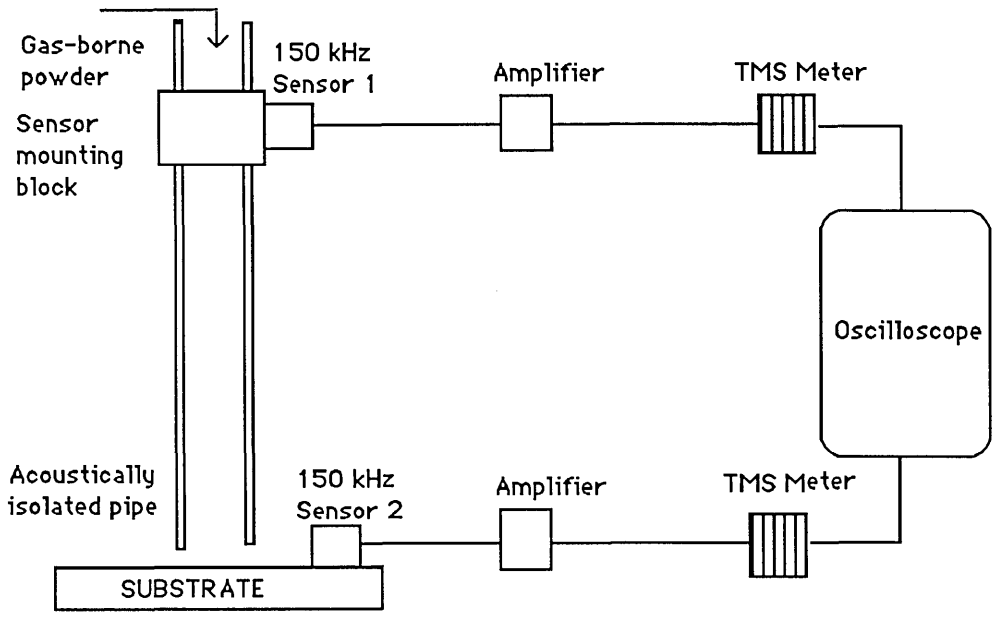

Fig. 7.1 Schematic diagram of acoustic emission monitoring system.

selected so that the low frequency background noise, such as emissions generated by the powder feed motor, would not be picked-up at the gain used of 60 dB. One sensor (S1) was coupled to the copper pipe and the other (S2) to the substrate. The signals from the sensors were recorded using a standard true-mean-square-voltage meter and the V_T's fed to a storage oscilloscope.

The various parameters were studied using a 50 mm long copper feed tube, argon carrier gas (1.7 lit/min) and stainless steel powder unless stated otherwise. The various powders used, either used in the present work or for the comparative study, were stainless steel, Alloy 4815, Stellite alloy 6, aluminium and SiC particles. Since the densities of stainless steel and Alloy 4815 are very close to each other, they both showed similar type of behaviour during the various studies; hence the data for Alloy 4815 was discarded and not plotted in the present results.

7.3 RESULTS AND DISCUSSION

If the feed is started and then stopped the V_T output from both sensors, as recorded by the oscilloscope, was as shown in Fig. 7.2. Point A on the output for S1, which is the sensor coupled to the pipe, corresponds to the entry of the powder into the pipe and point B to the exit of the powder front from the pipe. Similarly, point C on the output from S2, the sensor on the substrate, corresponds to the first powder hitting the substrate and point D to the continuous powder flow. Hence the time T for the powder to flow through the copper pipe of length L is $T_C - T_A$ or $T_B - T_A$ and the particle velocity V_P is therefore given by L/T. The time T_C was more clearly defined than T_B, therefore the former was used to calculate V_P.

First it was necessary to confirm that calculated velocities did not vary significantly with method variables such as the position of S1 on the pipe and S2 on the substrate and length L of the pipe. It was found that the velocities were unaffected by the positions of the

sensors and only slightly dependent on L over an order of magnitude variation in length from a minimum of 16 cm up to a maximum of 160 cm (Fig. 7.3).

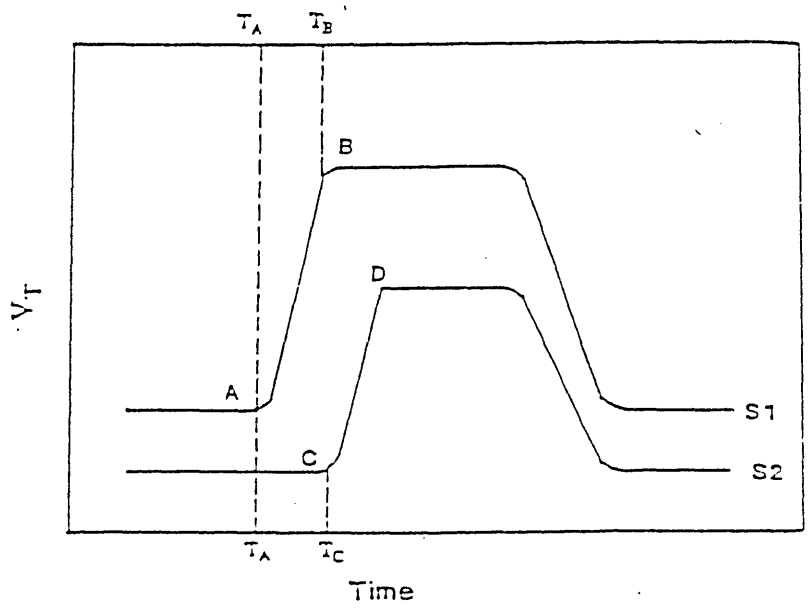

Fig. 7.2 Oscilloscope traces for sensors S1 and S2

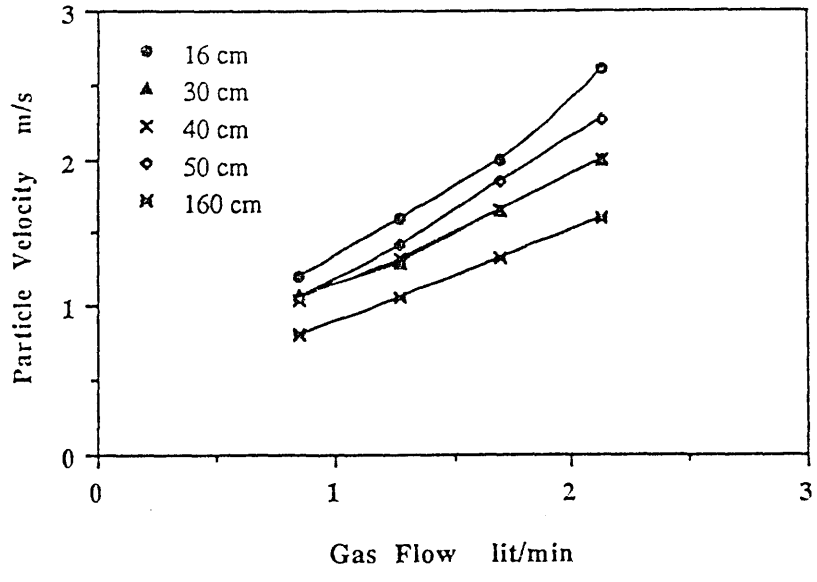

Fig. 7.3 Effect of feed tube length on particle velocity.

Having established the validity of the method it was possible to study the effect of other feed variables, e.g., powder feed rate, carrier gas species, powder density and powder size, on the particle velocity. For a given gas velocity V_g the particle velocity V_P was not particularly sensitive to particle size (d) at small (< 90 μm) sizes but decreased at larger particle sizes (Fig. 7.4). This result is in qualitative agreement with the equation due to Belden and Kassel (108):

$$V_P = V_g - 1.32 \{gd (\rho_P - \rho_g)/\rho_g\}^{1/2} \quad (7.2)$$

which modified for a given material gives:

$$V_P = V_g - Cd^{1/2} \quad (7.3)$$

where C is a constant, and ρ_P and ρ_g are the densities of the powder and gas respectively.

Fig. 7.5 is a plot of particle velocity against density. The particle size of the different powders used to obtain these data varied only slightly and consequently the resulting particle velocities were dominated by the differences in density, and V_P decreased with increasing particle density in accordance with equation (7.2).

The variation in the powder feed rate from 3.6 to 16.6 g/min, at a constant argon gas flow of 1.7 lit/min, showed no significant effect on the particle velocity within the range of feed rates studied (Fig.7.6). To determine the effect of gas density on the particle velocity, two different gases, namely, helium and argon with densities 0.138 and 1.379 respectively, were used as a carrier gases. A plot of particle velocity versus gas flow rate is shown in Fig.7.7. It can be deduced from Fig. 7.7 that to attain a similar particle velocity of, say, 2 m/s, in a powder feed, the amount of gas flow required will be lower if using argon (1.9 lit/min) as carrier gas rather than the helium (4 lit/min). This shows that the carrier gas consumption reduces if the gases of higher densities are used.

The velocity measurements reported here were the results from a fundamental study aimed at demonstrating the potential of AE monitoring. There are two drawbacks to the technique as-described, namely, a sensor is required on the substrate and the powder feed has to be interrupted. Work is in progress on modified techniques which require sensors

only on the pipe-work and which enable velocity to be determined either from rise-times or from monitoring the progress of inherent perturbations in the feed.

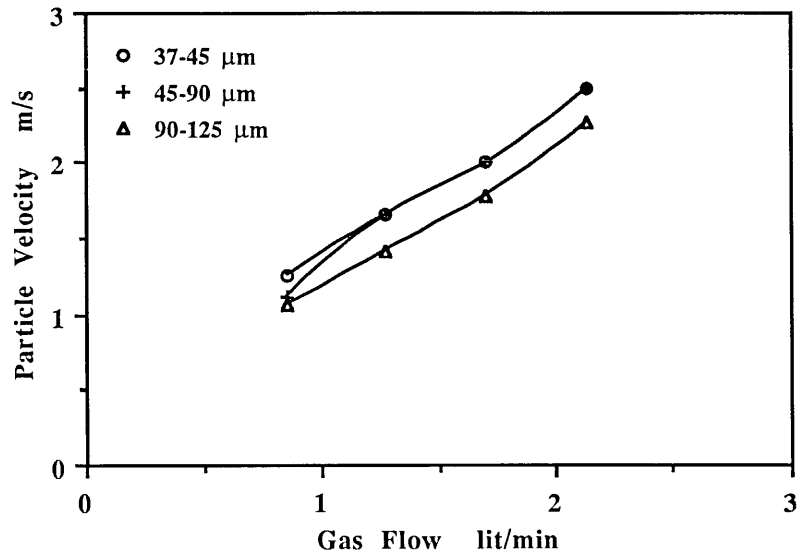

Fig.7.4 Effect of powder particle size on particle velocity.

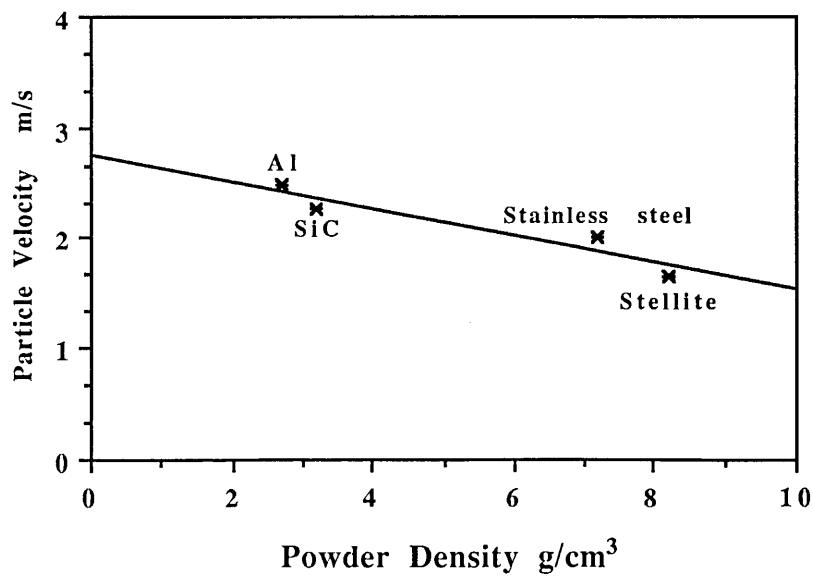

Fig. 7.5 Effect of powder density on particle velocity.

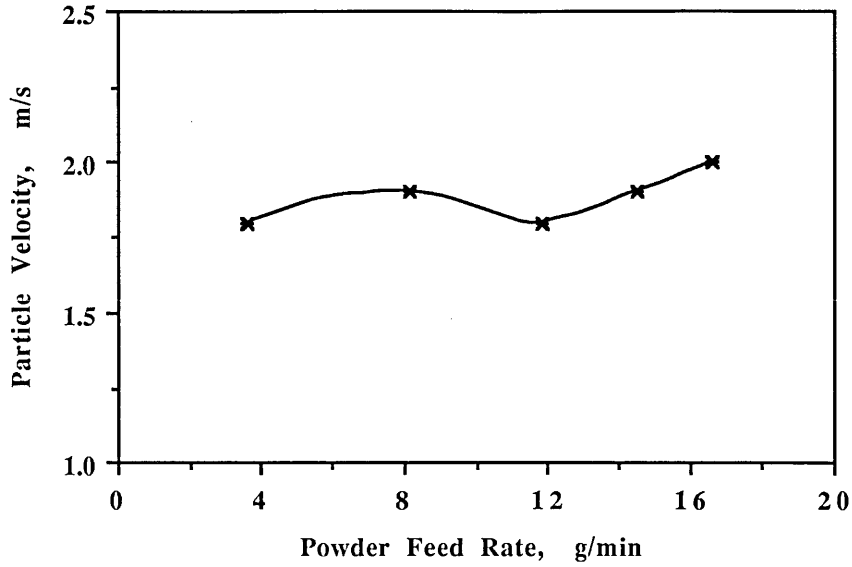

Fig. 7.6 Plot showing relationship between powder feed rate and particle velocity.

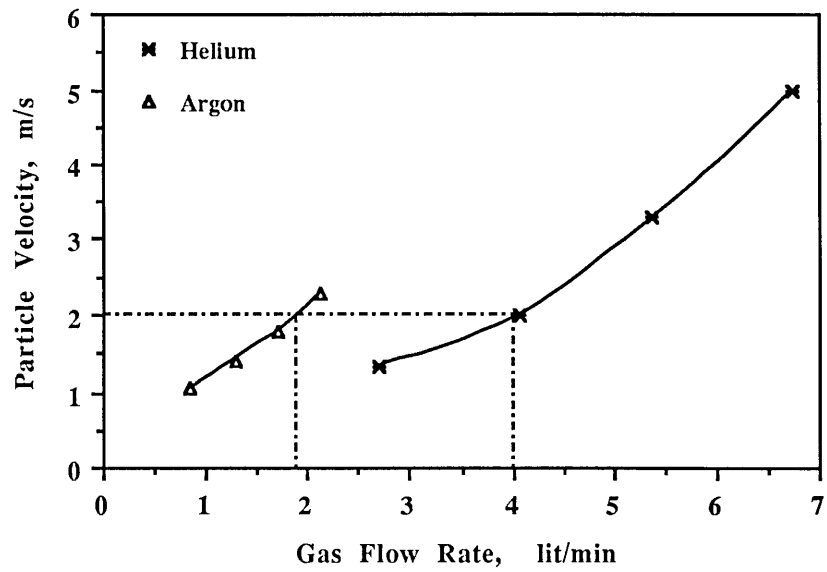

Fig. 7.7 Plot showing effect of gas density on particle velocity.

CHAPTER 8

DISCUSSION

8.1 INTRODUCTION

This chapter is divided into two main parts. The first part deals with the discussion on the process parameters, clad features and structural properties. In the second part the results obtained in the wear studies are discussed.

The first part comprises the effects of various laser processing parameters on the single clad dimensions. Some of the resulting characteristics of the clads, e.g. microstructures and correlation of structure and hardness, dilution, porosity and cracking tendency, will also be discussed. Since the power density was kept constant during a series of experiments, only two variables, namely, powder feed rate and specimen traverse speed, were studied for all the clads. However, for SiC particle injection into mild steel and cladding of separately fed mixtures of Stellite and SiC, two extra variables, i.e. particle velocity and wt.% of SiC in the cladding powder mixture respectively, were also studied.

Since the parametric studies were carried out to produce single clad tracks, the clad dimensions and the related properties discussed in this chapter refer to single tracks only unless stated otherwise. However, the effect of partial overlapping of clads on their properties (e.g. dilution) will be considered. The properties of clads produced under various process conditions and the microstructures obtained will also be related to their solidification morphologies.

8.2. EFFECT OF PROCESS PARAMETERS ON CLAD DIMENSIONS

8.2.1 Effect of Powder Feed Rate

The effect of powder feed rate was studied for four sets of experiments, i.e. SiC injection (Figs. 4.2-4.3), Stellite (Fig. 4.13) and Stellite + SiC (Figs. 4.23-4.26). Two parameters of clad dimensions, namely width and build up (i.e. height of clad above the substrate surface) and also substrate melting were related to the powder feed rate. A derived quantity, i.e. clad thickness (which is equal to the sum of clad build up and substrate melting), is also plotted versus feed rate to represent the total area melted by the laser beam and solidified as clad. The trend observed was similar in all these sets, i.e. an increase in the clad build up and width (decrease in the case of SiC injection) and a decrease in the substrate melting, with increase in the powder feed rate. However the magnitude of the dimensional change was different in each case due to different phenomena (e.g. injection of particles rather than cladding in set 1) and heat balances involved.

In the case of SiC particle injection (Figs. 4.2-4.3), it was intended to produce first the melt pool on the substrate and then inject SiC particles so that they do not come in direct contact with the laser beam before entering the melt pool and becoming the integral part of clad. Any increase in the clad dimensions would, therefore, be a result of increase in the volume of SiC particles injected rather than due to their melting. An increase in the clad build up (from 0.28 to 0.56 mm) was found by increasing the SiC feed rate from 9.0 to 19.2 g/min (Fig. 4.2). The decrease in both the substrate melt depth (Fig. 4.2) and the clad width (Fig. 4.3) show that the increase in the SiC feed rate resulted in widening of the particle spray from the feeding tube hence, some of the SiC particles did come in direct contact with the laser beam reducing the incident laser power on the substrate and consequently decreasing the substrate melting. However, it can be deduced from the small increase in the clad build up, that all the particles which came into

contact with the laser beam did not necessarily enter the melt pool, other wise the clad build up would have been higher than that obtained in the present situation.

In the case of cladding, where both the substrate and applied powder were melted simultaneously, both the clad build up and width were found to be increased with increasing powder feed rate (Figs. 4.13, 4.23-4.26). The magnitude of the change in the clad dimensions with powder feed rate depends on many factors such as specific energy {normally defined as, power/(beam diameter x traverse speed)} and thermal properties of the substrate and the applied powder. At a give specific energy, there is a critical limit for the powder feed rate beyond which the heat available will be insufficient to melt the powder and hence a discontinuous clad will result. In the case of Stellite alloy clads (Fig. 4.13), despite the fairly high feed rates, the specific energy (92.5 J/mm^2) was sufficient to melt the powder and hence an increase in both the clad thickness and width was obtained in the range of powder feed rate studied.

In Stellite + SiC clads, the clad dimensions were affected by varying the powder feed rate and also the wt.% of SiC in the cladding powder mixture. This was, in fact, attributed to the change in heat balance, due to differences in properties of SiC and Stellite e.g. density, thermal conductivity etc., by varying the proportion of SiC in the cladding powder mixture. In both the sets of experiments, i.e at constant SiC and variable Stellite (Fig. 4.23) and constant Stellite and variable SiC (Fig. 4.24) feed rates, clad thicknesses were increased with increasing feed rates. However, in the set with constant Stellite feed rate, no further increase in clad thickness was observed beyond 41 g/min of total feed rate (Stellite + SiC). This shows that in this set of experiments, the specific energy was just enough (66 J/mm^2) to melt 41 g/min of powder. Similarly, the clad width in both the sets was increased with increasing feed rate (Fig. 4.26). However, in the set with constant Stellite feed rate, the clad width was sharply decreased beyond 41 g/min of feed rate for the same reasons as described above.

8.2.2 Effect of Substrate Traverse Speed

In all series of experiments studied, both the clad thickness (Fig. 8.1) and width (Fig. 8.2) were found to be inversely related to the substrate traverse speed. The magnitude of change, however, varied in the different series; e.g. SiC injection (Figs. 4.5-4.9), Stellite (Figs. 4.16-4.17), Stellite + SiC (Figs. 4.20-4.22), stainless steel + SiC (Figs. 4.32-4.33) and Alloy 4815 + SiC (Figs. 4.35-4.37), which was attributed to the differences in the power densities, powder feed rates and also the thermal properties of the various alloys used. At a given powder composition, powder feed rate and power density, the substrate traverse speed can affect the clad dimensions in two different ways, i.e,

1. Increase in the traverse speed will result in a decrease in the laser beam interaction time; hence less powder enters the melt pool (i.e. interaction time x feed rate).
2. Increase in the traverse speed reduces the specific energy and hence there is a reduced melting of both the substrate and the blown powder.

The effect of decrease in the specific energy on decreasing the substrate melt depth was more pronounced in the case of the SiC injection process (Figs. 4.5-4.6) as compared with the composite cladding (Fig. 8.3) because in the former case, most of the heat was utilized in melting the substrate rather than the powder.

Among the composite clads, stainless steel + SiC clads showed greater substrate melt depth due to a higher power density (282.9 W/mm^2) as compared with Stellite + SiC (147.2 W/mm^2) and Alloy 4815 + SiC (192.2 W/mm^2) clads. Accordingly, the change in the clad dimensions with the traverse speed was greater in the case of stainless steel + SiC composite.

The effect of traverse speed on powder intake can be observed by considering Fig. 4.37 where the data are shown for two clad sets produced at 27.5 g/min and 36 g/min feed rates. At a traverse speed of 12.5 mm/s (interaction time = 0.28 s), the clad produced at higher feed rate (36 g/min) showed a slightly greater width. This is

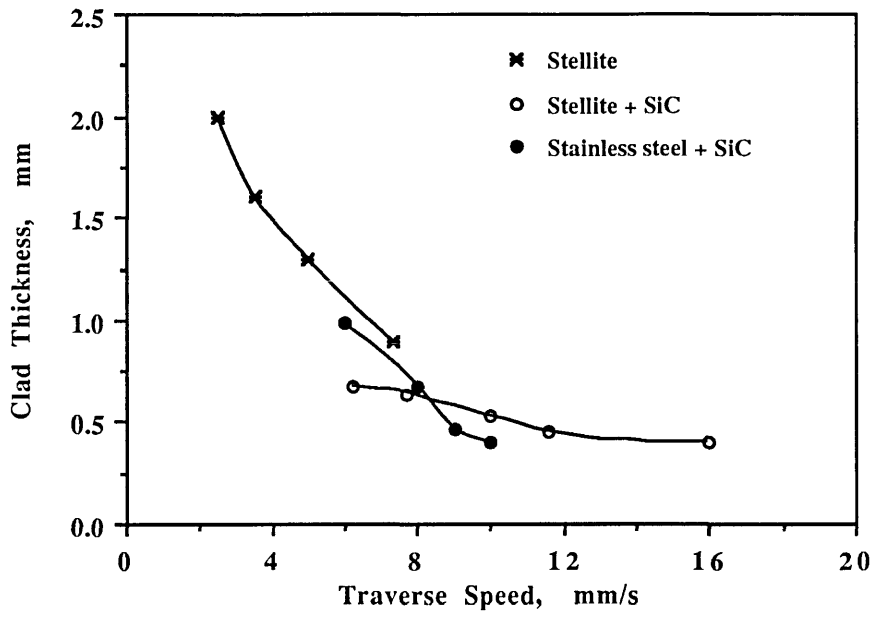

Fig. 8.1 Relationship between the traverse speed and the clad thickness.

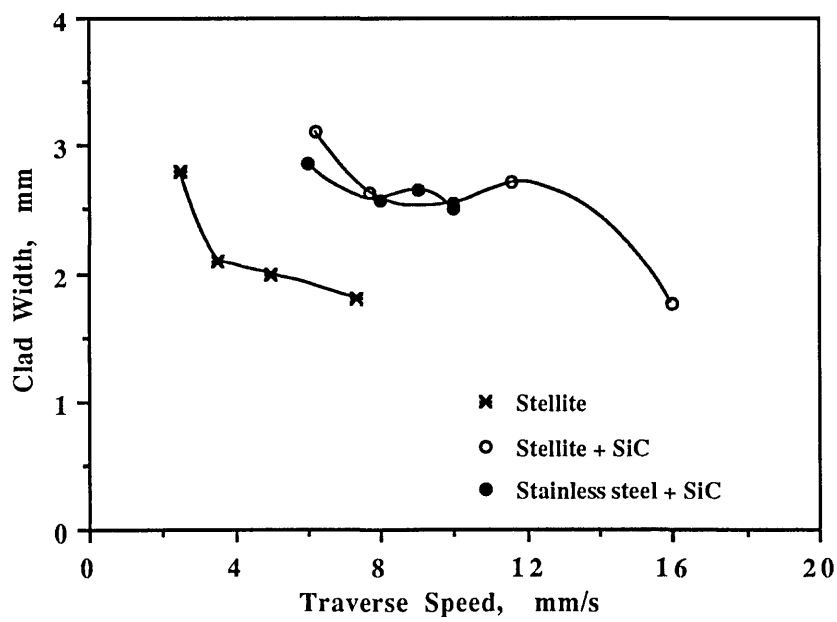

Fig. 8.2 Relationship between the traverse speed and the clad width.

consistent with the greater powder intake, 0.16 g for the higher feed rate as compared with 0.12 g for the lower feed rate. However, the trend was found to be reversed for the thickness of clads and substrate melt depths in these sets. At 12.5 mm/s traverse speed, the clad with higher powder intake (0.16 g) showed relatively lower clad thickness and substrate melt depth (Fig. 4.36) than that (Fig. 4.35) produced at lower powder intake (0.12 g). This shows that the specific energy (42.2 J/mm^2) available was not sufficient to completely melt 0.16 g powder intake. Also, the lower substrate melt depth confirms that the powder intake reached an optimum value for the given specific energy; hence the powder produced a "shadowing" effect on the substrate reducing the amount of heat reaching it.

8.2.3 Effect of Particle Velocity

The effect of particle velocity on the clad dimensions was studied in the set of experiments for producing composite layers by injecting SiC particles into mild steel substrate. In a set of clads produced at two different feed rates of 34 g/min and 59.4 g/min at two different particle velocities of 2.5 m/s and 4 m/s respectively, at a given substrate traverse speed, the clad dimensions (i.e thickness and width) were found to be greater in the case of the former (Figs. 4.7-4.8) despite its lower feed rate as compared with the latter. This was attributed to the higher mass deposition rate at lower particle velocity. These results are in agreement with previous work by Weerasinghe (38). At the higher particle velocities, the particle ejection from the molten pool after striking the substrate increases, resulting in greater powder and heat losses as compared with those at relatively lower particle velocities. The particle velocity has been found (chapter 7) to be dependent on many factors including powder density and carrier gas velocity. It is, therefore, desirable to use a minimum necessary carrier gas velocity to obtain a maximum powder mass deposition. Although the magnitude of the decrease in the clad dimensions with increasing particle velocity may vary, depending upon the material and process

parameters selected, the trend observed of an increase in the clad dimensions with decreasing particle velocity is expected to hold good for most of the materials.

8.3 EFFECT OF PROCESSING PARAMETERS ON CLAD FEATURES

Effects of powder feed rate, powder mixture composition and substrate traverse speed on some of the features of single track clads produced will be discussed. The clad features studied are microstructure, dilution and microhardness.

8.3.1 Effect on Microstructure

It is now well established that the laser cladding process results in high cooling rates of deposits which favour the refinement of the microstructures. The extent of microstructural refinement depends on many factors including laser power density, laser beam interaction time (in other words traverse speed) and melt volume etc. The morphology of solidification depends on the amount and way of heat extraction from the deposit. That is why in almost all the clads, a narrow and featureless region was observed near the clad-substrate interface (Figs. 5.29, 5.35, 5.40, 5.43); this region is usually known as planar region. The solidification front morphologies depend upon G/R ratio, where G is the thermal gradient and R is the solidification rate (109). The planar solidification front will be stable if the following condition is satisfied, i.e.,

$$G/R \geq \frac{M C (1-k)}{K D}$$

Where,

M = Slope of the liquidus.

C = Initial solute concentration.

k = Ratio of solute concentration in the solid to concentration in the liquid.

D = diffusivity of the solute in the liquid.

At a lower value of G/R than the minimum required for stable planar solidification front, the solidification will tend to be cellular or dendritic. At still lower G/R values, constitutional supercooling will result which will favour dendritic growth.

Kear et. al. (110) has reported that the highest values of G/R occurred at the bottom and the sides of the melt zones, where the rates of solidifications were low. The lowest G/R values occur at the top and the centre of the melt zones where the solidification rates are high. The reason for the high G/R values at the bottom and the sides of the melt zones is that at a time when the laser beam has just passed over the melt pool, there will be an instant where the melting is no longer be taking place but the freezing has also not yet started. At this stage the solidification rate R is zero and therefore G/R will be infinite. This situation happens near the clad-substrate interface resulting in a planar region; afterwards the values of G/R are decreased and cellular and dendritic solidification occur.

The product G.R gives the cooling rate of the deposit. The high substrate traverse speeds give rise to higher cooling rates. Hence the clads formed at higher traverse speed (Fig. 5.15) showed relatively lower secondary dendrite arm spacing than those formed at relatively lower traverse speed (Fig. 5.16).

In the SiC injected and Alloy 4815 + SiC blown composites, the high cooling rates produced a martensitic structure (Figs. 5.11, 5.37-5.38). However, in these composites, relatively lower traverse speeds were found more favourable in that more solution of SiC occurred which, in turn, increased the hardness of the matrix. Despite the lower traverse speeds used in these series (6.5 and 4.5 mm/s respectively), the cooling rates observed were high (3.9×10^3 and 2.7×10^3 K/s respectively), estimated as discussed below by G.R, to favour martensite formation.

In Stellite and Stellite + SiC composite clads, the high traverse speeds resulted in fine dendritic structures. The secondary dendrite arm spacing was theoretically calculated by the expression (110-111),

$$\lambda = b \cdot \varepsilon^{-n}$$

Where,

λ = Secondary dendrite arm spacing

b and n = constants

ε = G.R, cooling rate (K/s)

The values for b and n were taken from those given by Meharabian (112) for an alloy closely similar in composition to Stellite alloy 6. To calculate the cooling rate, the assumptions made by Hawkes (113) and Marsden (43) for melt zones were used, Fig. 8.4. The solidification rate R was calculated as R = X/T, where X is the depth of the melt zone and T is the freezing time (or interaction time). The thermal gradient G can be assumed to be equal to the difference between boiling point (assumed to be approached at the top of the melt zone) and the solidus temperature (at the bottom of the melt zone), divided by the depth of the melt zone, X. The cooling rates and corresponding secondary dendrite arm spacings for various Stellite and Stellite + SiC composite clads are given in Table 8.1.

Table 8.1

The calculated and observed values of secondary dendrite arm spacings for various Stellite and Stellite + SiC clads

Clad composition	Figure reference	Cooling rate, K/s, X 10^3	Secondary dendrite arm spacing, λ, μm	
			Calculated	Observed
Stellite	5.15	5.6	3.8	2
Stellite + SiC	5.21	5.2	3.9	2
Stellite	5.14	3.6	4.3	3
Stellite + SiC	5.29	2.7	4.7	1.5
Stellite	5.16	1.9	5.2	4

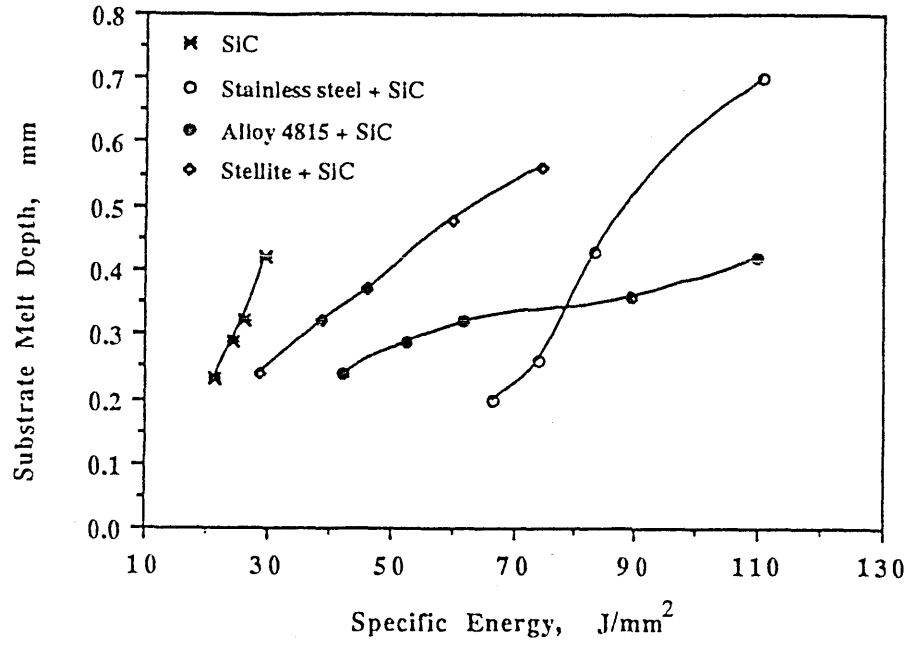

Fig. 8.3 Effect of specific energy on substrtate melt depth.

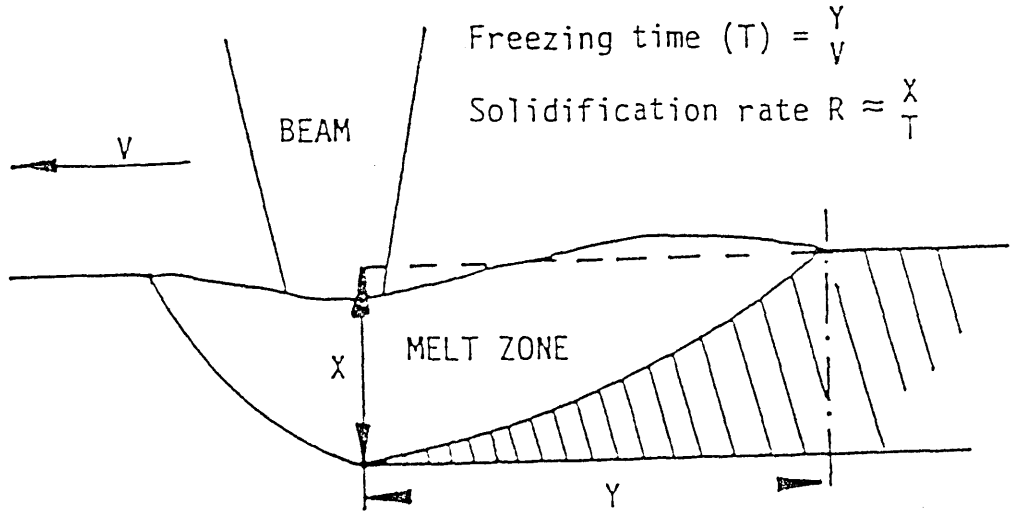

Fig. 8.4 Schematic diagram of laser melt pool (Ref. 113).

By considering the data of Table 8.1, it can be deduced that the calculated and observed secondary dendrite arm spacing values are not in a good agreement which can be attributed to the assumptions made for estimating the cooling rate G.R. However, the trend observed in both the cases was a decrease in the secondary dendrite arm spacing with increase in the cooling rate, except for clad referred to Fig. 5.29 which is unusual..

8.3.2 Effect on Dilution

The present studies have shown that the dilution of the clad surfaces was affected by both the feed rate (Figs. 4.4, 4.14, 4.30, 4.31) and substrate traverse speed (Figs. 4.10, 4.21, 4.34, 4.38). The trends observed were a decrease in the dilution with increase in both the feed rate and the substrate traverse speed. However, when the cladding involves feeding of mixtures of alloy powders and ceramic particles, the situation becomes complex and the trends of dilution results obtained deviate from those obtained in the alloy clads. It is, therefore, appropriate to first consider previous studies (38, 114) of clad dilution to understand its mechanism.

Dilution can be defined as the compositional difference between the clad layer and the applied powder caused by the mixing of melted substrate with the deposit. Bruck (114) has expressed the dilution both in terms of composition and the area measurements of the clad and the melted substrate. The dilution in terms of compositional measurements is given by the expression,

$$\% \text{ Dilution} = \rho_P (\% X_{P+S} - \% X_p)/\{\rho_S (\% X_S - \% X_{P+S}) + \rho_P (\% X_{P+S} - \% X_P)\}$$

where,

ρ_P = density of melted powder

ρ_S = density of the substrate

$\% X_P$ = wt.% of element X in the alloy powder

$\% X_S$ = wt.% of element in substrate

$\%X_{P+S}$ = wt.% of element X in the total overlay

When expressed in terms of area measurements, dilution can be calculated as,

% Dilution = {area of melted substrate/(area of deposit + area of melted substrate)} x 100

This method can be best applied to measure the dilution if there is a distinct difference in the compositions of the substrate and the cladding powder. For example in the present studies, in the case of cladding of mild steel substrate with Stellite alloy, which originally contained about 5 wt.% iron, the clad layers showed the presence of a maximum of 10 wt.% iron when produced at 7.5 mm/s traverse speed and 23 g/min powder feed rate (Table 5.2). The dilution in this clad was measured as about 5% by applying the expression given by the Bruck (114).

If the substrate and the clad layer are closely similar in composition, as in the case of mild steel substrate cladding with Alloy 4815, where the cladding powder itself contained more than 95% iron, the melting of the substrate did not markedly affect the composition of the clad matrix (Table 5.7). In the case of SiC injection or cladding of a mixture of SiC and an alloy, the concept of dilution is made more complex due to the solution of SiC particles; which leads to an important compositional change i.e. enrichment in Si and C contents (Table 5.1).

The compositional analyses of various alloy and composite clads can, therefore, be divided into the following categories.

1. Increase in the iron content of the clad matrix resulted from the mixing with the melted substrate (e.g. Stellite clads).
2. Enrichment of the clad matrix in Si and C contents by partial solution of SiC particles (e.g. SiC injection into mild steel).
3. Slight decrease in the concentration of the alloying elements (e.g. Cr, Ni and Mo in stainless steel and Alloy 4815 clads).
4. Both the enrichment in Si and C contents by partial solution of SiC and dilution by iron from the substrate melting at the same time (e.g. composite clads).

A comparative study of dilution measurements in separately fed Stellite + SiC composite clad has shown reasonable agreement (taking in consideration ± 10% error in calculating area dilution) between the dilution values calculated from composition (Table 5.4) and the area data (Fig. 4.30). The comparative dilution data for a few clads is given in Table 8.2.

Table 8.2

Comparison data of dilution, calculated by compositional (i.e. wt.% of Fe in the clad matrix) and area measurement method, for separately fed Stellite + SiC composite clads, Laser power = 1.85 kW, Traverse speed = 7 mm/s.

Stellite feed rate, g/min	SiC feed rate, g/min	Wt.% Fe in the clad matrix	% Area dilution
35.0	3.5	51	59
35.0	4.3	41.7	47
20.5	7.0	46.2	55

The dilution of both the alloy (Fig. 4.14) and composite (Figs. 4.30-4.31) clads was found to be markedly decreased by increasing the powder feed rate at a given specific energy. At a given specific energy any increase in the powder feed rate leads to a larger amount of energy being required in melting the powder rather than the substrate and hence decreasing the substrate melt depth and thereby decreasing the dilution level. However, for a given specific energy, there is a maximum powder feed rate limit beyond which any increase in the powder feed rate will result in a reduction in melting of both the powder and the substrate. This effect is illustrated by the data in Fig. 4.14 where an increase in the Stellite feed rate beyond 50 g/min produces a little change in dilution. In composite clads, both the total feed rate (Stellite + SiC) and the wt.% of SiC

in the powder mixture also affect the heat balance of powder melting, and some unusual results were obtained (Fig. 4.31).

In SiC injected clads although the carbide particles were not deliberately melted together with the substrate, the area dilution was decreased by increasing the SiC feed rate. The reason for this behaviour was that at higher feed rates, the powder jet stream might have widened leading to direct contacts of some SiC particles with the laser beam, hence reducing the amount of energy reaching the substrate and consequently decreasing the melt depth or area dilution (Fig. 4.4).

At a given power density, an increase in the substrate traverse speed resulted in a reduced dilution in all the clads formed, particle injection (Fig. 4.10) and cladding (Figs. 4.21, 4.34 and 4.38). These results are in agreement with those reported by Bruck (114). These mainly dealt with preplaced powder cladding; but factors controlling dilution are similar for preplaced or continuously fed powder cladding. The dilution increases with increasing specific energy (by decreasing traverse speed at a constant power density) because greater energy delivered per unit area causes greater substrate melting and greater change in clad alloy composition. However, the present results disagreed with those reported by Monson (25) for cladding of mild steel substrate with Stellite, which showed that the traverse speed had little effect on the dilution and that the powder feed rate was the major controlling factor. The results reported by Komvopoulos and Nagarathnam (115) on cladding of AISI 1018 steel substrate with Fe-Cr-C-W alloy also showed that the traverse speed does effect the dilution. However, their (115) observations differ from the present results as the dilution was slightly decreased with increasing specific energy. Monson (25) has derived a heat balance equation to show that the dilution is independent of the substrate traverse speed, but the equation given did not fully support that argument.

A heat balance for zero dilution cladding as reported by Monson (25) is as follows,

(Heat supplied/unit time) - (Heat load/unit time) ≤ 0

where,

Heat supplied = Incident laser power less reflection and powder cloud shadowing effect

Heat load = Heat required to melt the powder and produce melt zone plus conduction, convection and reflection losses.

By neglecting the powder shadowing effect, the equation can be written as,

Heat supplied/unit time, $Q = P(1-R)$ Eq. 8.1

Heat load/unit time, $Q = \phi m (C_P dT + L_f) + Q_2$ Eq. 8.2

Where,

Q = Absorbed laser power (W)

P = Incident laser power (W)

R = Reflectivity

ϕ = Powder catchment efficiency

m = Powder feed rate (g/s)

C_P = Specific heat capacity of cladding material (J/g °C)

dT = Temperature rise to melting point (°C)

L_f = Latent heat of fusion of cladding material (J/g)

Q_2 = Heat losses due to conduction, convection and radiation (W)

Eq. 8.2 can be rewritten as

$\eta Q = \phi m (C_P dT + L_f)$ Eq. 8.3

Where,

$\eta = (Q - Q_2)/Q$ = Melting efficiency

The melting efficiency, η, is a weak function of many variables such as processing speed, powder feed rate, powder particle size and is a strong function of the size of the heat source, i.e f(1/D), where D is beam diameter. Melting efficiency η is also a function of substrate material, level of preheat and geometry. Hence for a given cladding process on a flat plate,

$\eta = \alpha/D$, where α is constant (mm) Eq. 8.4

Combining Eqs. 8.3 and 8.4,

$$Q = m D K \qquad \text{Eq. 8.5}$$

Where, K is constant (J/g . mm)

For zero dilution Eq. 8.1 can be written as,

$$P(1-R) \leq K m D \qquad \text{Eq. 8.6}$$

By considering the heat balance equation (Eq. 8.6) for zero dilution derived by Monson (25), it can be deduced that although the laser beam interaction time is not directly involved in this equation, some of the process parameters taken in account, such as Q, Q_2, R, and powder intake, are indirectly affected by any change in the interaction time or specific energy resulting from any change in the substrate traverse speed.

A decrease in the substrate traverse speed has a two fold effect on the cladding process. Firstly the powder intake into the molten pool will be increased as a result of the increase in the interaction time. Secondly, the applied specific energy will be increased which will lead to an increased heat absorption both by the substrate and the blown powder, the magnitude of which will depend on the thermal properties of the substrate and the powder. At a given powder feed rate and power density, the increase in dilution level with decreasing traverse speed will, therefore, depend on the amount of heat available in excess of that required to melt the powder and the substrate.

In the case of composite cladding, where a mixture of alloy powder and ceramic particles is fed, the dilution situation becomes rather too complex due to differences in the thermal and physical properties of the applied powders together with properties of the substrate. Although the trend observed was a decrease in the dilution with increasing speed, sometimes it slightly deviated which is again due to the thermal imbalance attributed to the presence of SiC particles in the cladding powder mixture (Fig. 4.21). It was observed during the present studies that at a given powder feed rate, there is a range of substrate traverse speeds where the process will produce reasonable clad dimensions and trend to a decreased dilution with increasing speed will hold good. At very low traverse speeds, the powder intake would be so high that the heat available would be insufficient

to melt the substrate and powder at the same time and hence a poor fusion bond with incomplete powder melting will result (Fig. 4.34). Similarly, at very high traverse speed (corresponding to a given powder feed rate) where the powder intake will be low enough to produce good clad buildup, the melting process will dominate the cladding process (Fig. 4.38).

In the composite clads an important factor is the dissolution of carbide particles; which, in turn, affects the composition and properties of the matrix regions of the clads. The amount of the carbide dissolution in a cladding process depends on the properties of the material and the processing parameters. Some of these process and material parameters have been reported by Ayers (46). The most important material parameters are the composition of alloy powder and the carbide particles, and the carbide particle size. The process parameters which can influence the carbide dissolution are the temperature of the melt, the time available for dissolution, the carbide volume fraction and the amount of fluid flow or stirring in the melt. Some of the process and material parameters studied in the present study are discussed here.

The solubility of carbide particles in a metal matrix varies from material to material depending on its chemical affinity and the melting temperature of the substrate material used. For example, no dissolution of TiC is reported in 5052 Al (63) while extensive dissolution of TiC was found in Fe (62) and Ti (63) base alloys. The compositional analyses of the matrix regions of various composites; e.g. SiC injection (Table 5.1), Stellite + SiC (Table 5.4-5.5), stainless steel + SiC (Table 5.6) and Alloy 4815 + SiC (Table 5.7), showed enrichment in Si content resulted from the partial dissolution of SiC particles.

The carbide particle size affects the kinetics of the dissolution because fine particles have a higher ratio of surface area to volume than the coarse particles. When fine SiC particles (50-150 μm) were blown with Stellite alloy powder to produce composite, the clad formed showed almost complete solution of the SiC particles (Figs. 5.18-5.20). A fair dissolution of SiC was observed when medium particle size (250-450 μm) was used

(Figs. 5.9 and 5.25). However, in the case of injection and cladding of large SiC particles (450-750 μm), the clad formed showed a lower dissolution of carbide particles (Figs. 5.8 and 5.22).

High melt temperatures and prolonged melting times increase the particle dissolution rate by increasing the solubility and the rate of diffusion of the powder constituents away from the dissolving particle. The effect of prolonged melting times, resulted from decrease in substrate traverse speed, was found in the case of Alloy 4815 + SiC composites. The composites formed at relatively slower substrate traverse speeds showed higher hardness (Table 6.5) which were attributed to the large amount of SiC dissolution.

8.3.3 Effect on Hardness

The localized heating together with short interaction times are some of the most important advantages of laser processing which give rise to high cooling rates and hence result in the refinement of microstructures. The hardness of laser processed surfaces is higher than those produced by conventional methods. In the present studies both the powder feed rate and substrate traverse speed have been found to affect the cooling rates of the deposits and ultimately their hardness. At constant laser power density, the hardness of various alloy and composite clads was found to be increased by increasing the powder feed rate (Fig. 8.5 corresponding to Figs. 4.15, 4.28-4.29) and the substrate traverse speed (Fig. 8.6 corresponding to Figs. 4.18 and 4.21). However, SiC injected composites were the exceptional case where no definite trend of hardness was obtained by increasing the powder feed rate (Fig. 4.4) and the traverse speed (Fig. 4.11). At a given power density and powder feed rate, any increase in the traverse speed leads to shortening of laser beam interaction time together with a reduced powder intake into the melt pool. Consequently, by increasing the traverse speed, the total melt volume is decreased and hence the cooling rate is increased. However, at a given power

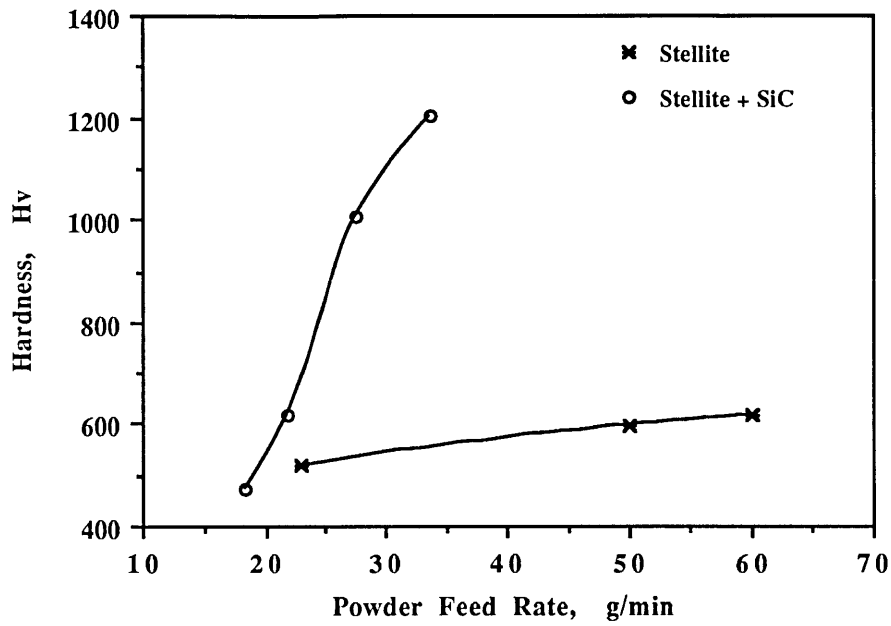

Fig. 8.5 Effect of powder feed rate on the hardness of the clad matrix.

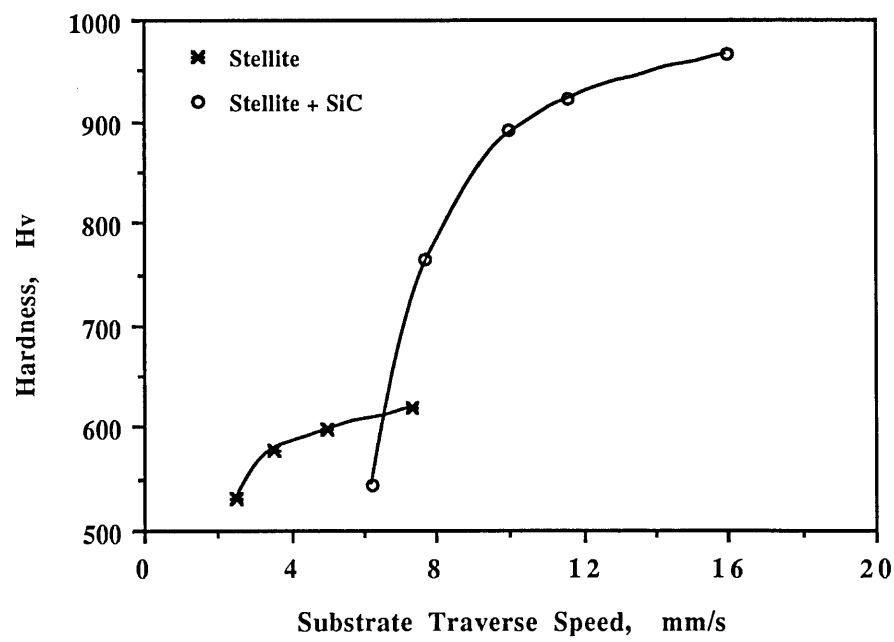

Fig. 8.6 Effect of substrate traverse speed on the hardness of the clad matrix.

density and traverse speed, an increase in the powder feed rate (within certain limits upto which the specific energy is sufficient to melt the powder) will increase the total melt volume and hence result in a decreased cooling rate. Despite relatively lower cooling rate and coarser microstructure, the clads formed at high feed rates showed higher hardness which was attributed to a lower level of dilution from the melted substrate. It can, therefore be deduced that the refinement of microstructure was not the only factor to affect the hardness, several other mechanisms would have been involved in hardening of the clad matrices. In an extensive study (64) of carbide particle injection (TiC and WC) into various substrates, it was reported that the improvement in the hardness of the matrix regions of the various composites was not the result of any single factor. In the present study the following mechanisms are relevant,

1. Solid solution strengthening, (in Stellite and composite clads).
2. Dispersion hardening by fine particles resolidified from carbon enriched melts resulted from the partial dissolution of carbide particles, (composite clads).
3. Transformation hardening of the metal matrix, (steel clads).
4. Matrix hardening through microstructural refinement, (all clads).

Matrix regions of SiC injected composites showed very high hardness (1400 Hv) as compared with that of the substrate (~ 200 Hv). Increase in the feed rate of SiC particles showed some unusual results, i.e. no definite trend on the hardness (Fig. 4.4). The hardness has, however, shown either a little change or a decrease with increasing traverse speed (Fig. 4.11). It can be deduced from these results that the increase in the hardness was mainly due to the dissolution of SiC particles which depends at a larger extent on the melting temperature and interaction time rather than the feed rate; however, there is a minimum feed rate limit below which feed rate could greatly affect the amount of dissolved particles. Since in the injection process, the particles are fed into the leading edge of the melt pool, increase in feed rate (at constant specific energy) will tend to decrease the temperature of the melt pool and hence reduce the dissolution of the particles. Similarly, by increasing the traverse speed, the interaction time will decrease and hence

the dissolution of SiC particles will be decreased. The minimum hardness measured on the sample produced at the highest traverse speed (35 mm/s) was still very high (618 Hv) as compared with the substrate (Fig. 4.11). In a set of clads produced at a relatively low traverse speed (6.5 mm/s) and at various feed rates (Fig. 4.4), the cooling rates obtained were sufficient to produce martensite (Fig. 5.11). The high hardness obtained in the series of SiC injection was, therefore, the combined effect of martensitic transformation and the enrichment of the matrix in carbon by partial solution of SiC particles. Fig. 4.12 supports the latter mechanism (i.e. increase in hardness by solution of SiC), where increase in dilution (increase in melting of substrate due to longer interaction times) leads to an increase in the hardness (which is in contrast to the results obtained in the other series of experiments, i.e. Stellite).

In the composite clads formed by blowing a mixture of Alloy 4815 + SiC, the hardness trends observed were closely similar those obtained in the SiC injection process. In Alloy 4815 + SiC martensite formation was also observed (Fig. 5.37-5.38). It can be deduced that in the processes of either injection of SiC particles into mild steel substrate or cladding of mild steel with a mixture of the iron base Alloy 4815 and SiC, decrease in the traverse speed favours the dissolution of SiC particles and hence results in hardness increase. This effect can be noticed in Figs. 4.38-4.39, where the set of clads formed at relatively lower feed rate (27.5 g/min) and SiC proportion (5 wt.%) but higher power density (192 W/mm^2) showed higher area dilution levels together with closely similar hardness values to those shown by clads produced at relatively higher feed rates (36 g/min) and SiC proportion (10 wt.%) but lower power density (147 W/mm^2).

In Stellite and Stellite + SiC composite clads, the mechanisms were different from those involved in Alloy 4815 + SiC composite. In Stellite clads the hardness was found to be increasing with both the powder feed rate (Fig. 4.15) and substrate traverse speed (Fig. 4.18).

As mentioned earlier, at a given power density and powder feed rate, increase in the traverse speed results in reduced melt volume and increased cooling rate. This fact was

observed when a set of Stellite clads was formed at the same power density (147 W/mm^2) and powder feed rate (50 g/min) with different traverse speeds (7.5 and 2.5 mm/s). The microstructure obtained in the clad produced at higher speed (7.5 mm/s) was more refined with an average secondary dendrite arm spacing of 2 μm (Fig. 5.15), associated with high cooling rate, than that formed at lower speed (2.5 mm/s) and showed relatively coarser microstructure with an average secondary dendrite arm spacing of 8 μm (Fig. 5.16). The hardness was higher in the case of the former as compared with the latter (Fig. 4.18). Although the high feed rates resulted in relatively coarse microstructures corresponding to a larger volume, an increase in the hardness was obtained (Fig. 4.15) which is attributed to the lower dilution of clad by iron from the substrate (Table 5.2). The hardness of the Stellite clads was found to be slightly lower (≤ 50 Hv) towards the substrate-clad interface due to slightly higher dilution from the substrate in these regions.

The hardness of the matrix regions, in a series of Stellite + SiC composites produced at a constant power density of 147 W/mm^2 and 10 g/min feed rate (50 wt.% SiC premixed), increased with increasing substrate traverse speed, which was mainly associated with decrease in the area dilution (Fig. 4.21). However, when the composite clads were formed by separately feeding Stellite powder and SiC particles at various rates, the hardness was affected by the proportion of SiC particles in the cladding powder mixture together with the total feed rate. Clads formed at constant Stellite (35 g/min) and variable SiC (3.5-9.8 g/min) feed rate showed a substantial increase in the hardness with increasing proportions of SiC in the cladding powder mixture upto about 20 wt.% (corresponding to a total feed rate of 44.8 g/min). This increase in hardness was mainly attributed to a larger degree of solution of carbon from SiC in the matrix and hence a larger proportion of carbide forming. Despite the higher total feed rates, the dilution of the matrix was increased by increasing the proportion of SiC, but yet the hardness was also increased.

In the set of clads formed at constant SiC (7 g/min) and variable Stellite (14.9-35 g/min), a maximum hardness value (1390 Hv) was achieved at about 20 wt.% SiC in the

Stellite + SiC powder mixture. However, the hardness was decreased as the proportion of SiC in the cladding powder mixture was increased above about 20 wt.% (Fig. 4.29). This fact was attributed, at least in part, to the progressive increase in dilution of the clad matrix by iron from the substrate (and also a corresponding decrease in carbon content) and hence a possible decrease in the formation of carbides of Cr and W. It can, therefore, be concluded that in both of these sets of clads, i.e. formed at constant Stellite and variable SiC and constant SiC and variable Stellite feed rates, the hardness of the matrix regions of the composites was increased by increasing the total feed rate, i.e Stellite + SiC (Fig. 4.28). Also, the increase in the proportion of SiC in the cladding mixture (Stellite + SiC) led to an increase in the dilution of the matrix by iron from the substrate.

8.4 SOLIDIFICATION OF CLADS IN TERMS OF PHASE DIAGRAMS

8.4.1 Solidification of Stellite and Stellite + SiC Composite Deposits

Despite the fact that Stellite alloys have been in use, as hardfacing materials, for the last more than half a century, there appears to be lack of detailed data available on their constitution. Stellite alloys are generally of a complex constitution based on the Co-Cr-C system but containing small amounts of other alloying elements like W, Ni, Mo, and B. In the present results, the situation is made rather more complex by the partial dissolution of SiC in composite clads, hence enriching the matrix in carbon and silicon contents. However, as an aid to interpreting the solidification structures and also the formation of various phases in Stellite alloys and Stellite + SiC composite deposits, the ternary phase diagram based on the Co-Cr-C system is considered here. Although this phase diagram does not take account of the other important elements present, it can provide important information about the solidification of Stellite alloys.

Figs. 8.7 and 8.8 show the liquidus surface of the cobalt-rich corner and an isothermal section at 800 °C of the Co-Cr-C system as reported by Thompson (116) and Koster (117) respectively. The compositions of matrix regions of a typical overlapping clad of Stellite alloy (Table 5.3) and of Stellite + SiC composite (Table 5.5) are shown, with dotted lines in Figs. 8.7 and 8.8 to represent possible solidification paths.

In the Stellite alloy clads, solidification occurred with the formation of primary dendrites of cobalt-rich solid solution of Co-Cr-W-C surrounded by a eutectic containing M_7C_3 (K_3) and/or $M_{23}C_6$ (K_4) type carbides. A previous study (34) has shown that Stellite alloy structures contain M_7C_3 and M_6C type carbides, where the former is not pure Cr_7C_3 but contains other alloying elements; the composition of M_7C_3 is approximately equal to $(Cr_{.8}Co_{.15}M_{.05})_7C_3$ where M represents other alloying elements. However, M_6C is essentially W_6C. If the W and carbon contents of the alloy are high enough, W_6C type carbide is likely to form. However, the x-ray diffraction data (Table 5.9) did not show the presence of W_6C carbide. In a study on microstructures of laser clad Stellite alloy 6, Jiang et. al. (124) have reported the presence of $M_{23}C_6$ type carbide in the clad matrix. The phase diagrams (Figs. 8.7 and 8.8) suggest that if the carbon content of the matrix is increased, then larger proportions of carbide-containing eutectic will form. This fact was observed in the case of Stellite + SiC clads where the microstructures (Figs. 5.21 5.29) showed a dense network of fine dendrites with larger proportions of interdendritic regions as compared with the Stellite clads (Figs. 5.14 and 5.16).

It can be observed from Fig. 8.8 that a lower chromium to carbon ratio favours the formation of M_7C_3 type carbide while a higher chromium to carbon ratio favours $M_{23}C_6$ type carbide. The chromium to carbon ratios of the present deposits fall in a range where the carbides formed should essentially be M_7C_3 carbide. However, it is difficult to suggest the exact type of carbide from the present results (Tables 5.9 and 5.10) as most of the peaks in x-ray diffraction data for M_7C_3 and $M_{23}C_6$ type carbides coincide with each other. It can, therefore, be concluded that the solidification structure in the Stellite

and Stellite + SiC composite deposits consists of M_7C_3 type carbide in a Co-based solid solution of Co-Cr-W-C.

8.4.2 Solidification of SiC Injected and Alloy 4815 + SiC Composites

The solidification of the matrices of clads formed by SiC injection into mild steel and Alloy 4815 + SiC clads can be interpreted with reference to the Fe-Si-C phase diagram (Fig. 8.9) as assessed by Raghavan (118). The direction of arrow in Fig. 8.9 indicate the possible solidification paths for the compositions (Tables 5.1 and 5.7) of the present alloys. Both the SiC injected and Alloy 4815 + SiC clads contain about 1.9 wt.% (~ 8 at.%) carbon (calculated on the basis of the Si enrichment of the matrix by the solution of SiC) and 6.8 (~ 13 at%) and 6.5 (~12.2 at%) wt.% Si respectively. This phase diagram suggests that in the metastable Fe-Si-C system, matrix regions of the composites solidified as primary dendrites of austenite and a binary eutectic containing γ and τ (a ternary carbide, FeSiC) with possibly some Fe_3C as part of a ternary eutectic.

Although both the clads under discussion contain almost the same amount of Si and C, the solidified microstructures were different. The microstructure of the matrix region of SiC injected clads was interpreted as consisting of primary dendrites of austenite (transformed to ferrite/martensite) surrounded by a network of carbide and possibly regions of martensite also in the interdendritic regions (Fig. 5.11). However, in Alloy 4815 + SiC clad, the microstructure did not show primary dendrites, but appeared to consist of a eutectic of martensite and carbide (Figs. 5.36-5.37). The reason for this could be the presence of Ni (2.5 wt.%) in this clad. As far as the presence of carbides is concerned, the x-ray diffraction data for both the clads, i.e. SiC injection (Table 5.8) and Alloy 4815 + SiC (Table 5.14), showed cementite peaks. However, the presence of the ternary carbide (FeSiC) was not confirmed as most of the peaks for this phase overlap with SiC peaks. It can, therefore, be suggested that the peaks obtained from

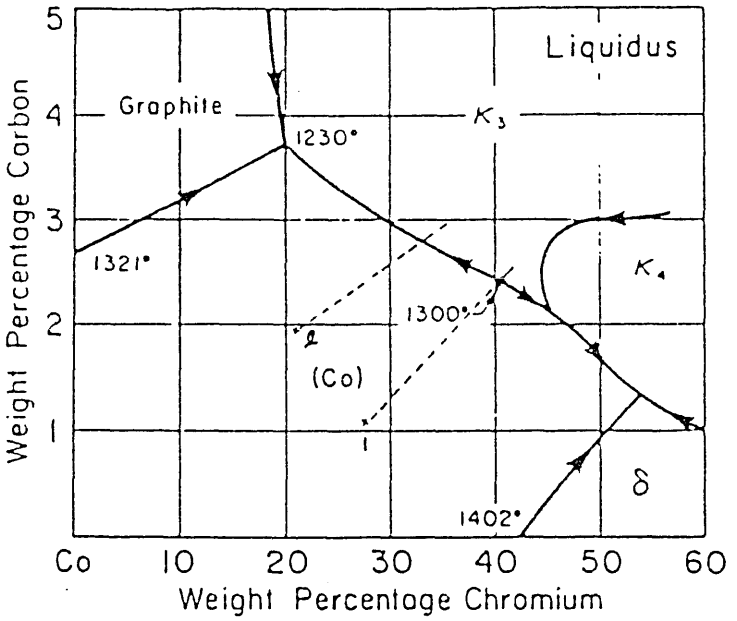

Fig. 8.7 Liquidus projection of Co-rich corner of C-Co-Cr system (Ref. 116), 1 = Stellite, 2 = Stellite + SiC.

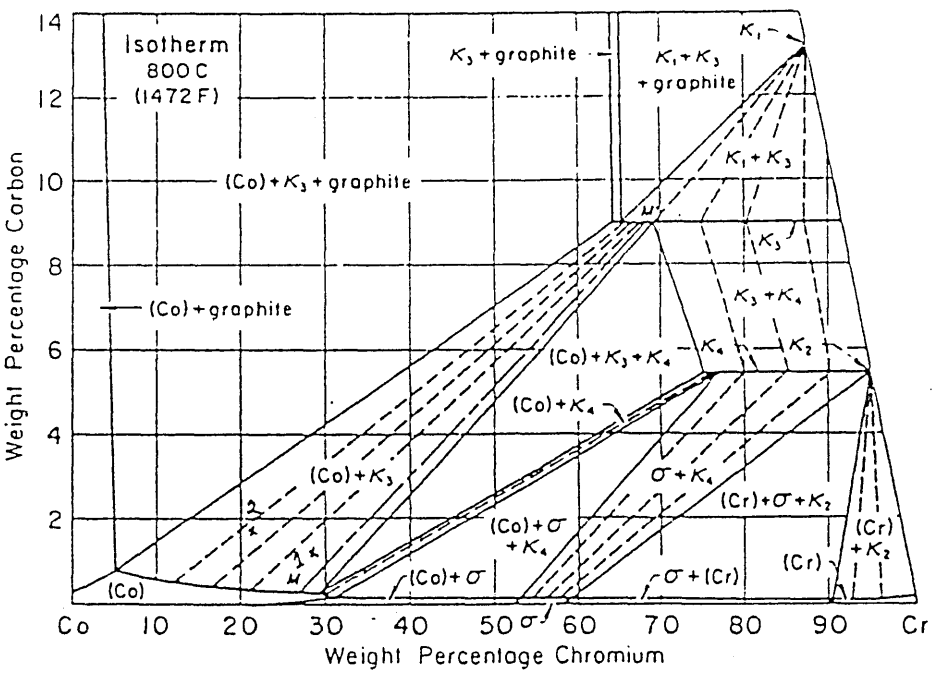

Fig. 8.8 An isothermal section of C-Co-Cr system at 800 °C (Ref. 117), 1 = Stellite, 2 = Stellite + SiC, $K_1 = Cr_3C_2$, $K_2 = Cr_{23}C_6$, $K_3 = (Cr, Co)_7C_3$, $K_4 = (Cr, Co)_{23}C_6$.

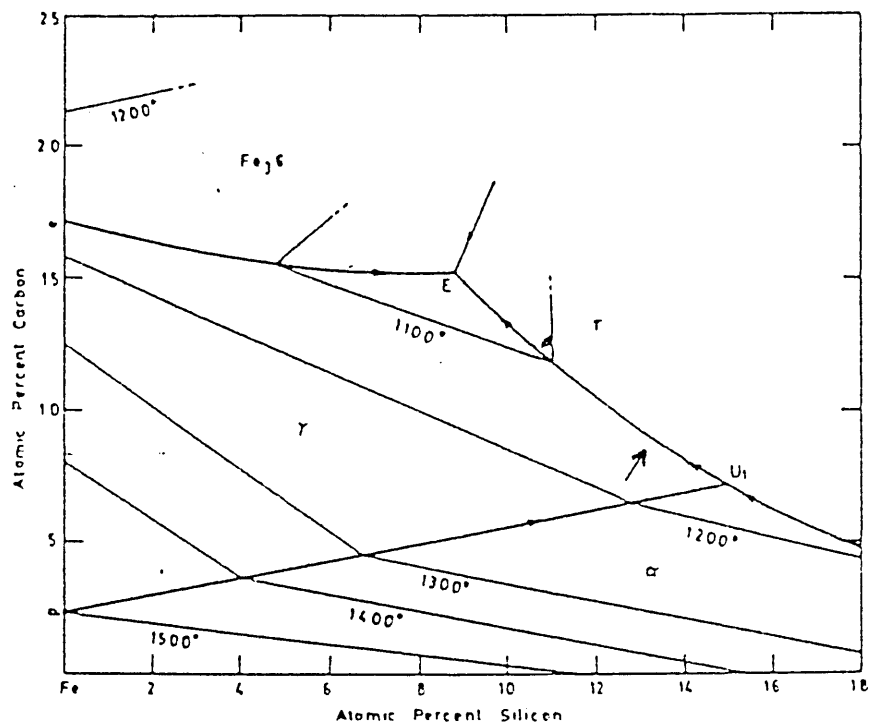

Fig. 8.9 Liquidus projection of surface near iron-rich corner of metastable C-Fe-Si system (Ref. 118), $U_1 = L + \alpha \rightarrow \gamma + \tau$, 1150 °C, $E = L \rightarrow \gamma + \tau + Fe_3C$.

SiC might have resulted from the presence of some undissolved SiC particles in the matrix.

8.5 FORMATION OF POROSITY AND CRACK IN CLAD DEPOSITS

The porosity becomes a problem particularly when the deposit thickness is large (> 1 mm). In the present results, a small amount of porosity and cracking was found in some clads. Depending on their shape and nature, the clad deposit porosity can be classified into the following categories,

1. Macro surface porosity.
2. Micro internal porosity.
   (a) Entrapped gas bubbles.
   (b) Shrinkage porosity.
   (c) Inter run porosity (in overlapping clads).

The first type of porosity, i.e. surface porosity, was found only in the overlapping clads of composites; e.g. Stellite + SiC (Fig. 5.2), stainless steel + SiC (Fig. 5.4) and Alloy 4815 (Fig. 5.6). This type of porosity results from the ejection of SiC particles from the melt pool during cladding. However, the extent of the surface porosity was very small and most of the pores were found in the shallow upper skin of the deposit. Decrease in the particle velocity (by decreasing the carrier gas flow) can reduce the amount of SiC particle ejection from the melt pool and hence the surface porosity.

Microstructural porosity results from various mechanisms during melting and solidification. In some clads, small pores of spherical nature were observed (Figs. 5.9, 5.19-5.20 and 5.34), the shape of which indicates that they existed as bubbles of gas trapped in the melt pool. These gas bubbles can be formed either by the entrapment of powder carrier gas or by the gas generated within the melt pool due to decomposition of any moisture present in the powder or on the substrate. If such porosity occurs extensively, it can be reduced by heating the substrate and powder to remove moisture

and also by decreasing the carrier gas pressure to a minimum necessary required for smooth powder flow.

Solidification or shrinkage cavities may occur at or near the clad-substrate interface if the melting point of the clad layer is significantly higher than the substrate (44). Since, in the present studies, the difference in the melting points of the applied powders (except SiC) and the substrate was not high, no evidence of such type of porosity was found. However, in composite clads, the difference in the thermal properties (e.g. thermal conductivity and thermal expansion) of SiC particles and and alloy powders led to the occurrence of shrinkage cavity effects around the particles (Figs. 5.8, 5.10, 5.22-5.23, 5.25-5.26). This effect was, however, limited to only a small proportion of embedded SiC particles, whereas the majority of the SiC particles showed a good fusion bond with the clad matrix. In the injection process of SiC particles into mild steel substrate, using a large particle size (250-750 μm), some regions of clad showed SiC particles embedded in the form of a cluster. In this region together with matrix-particle shrinkage cavity, porosity was found in the regions between the large particles (Fig. 5.8); this could be the effect of hindrance in the easy flow of liquid.

Another type of porosity, i.e. inter-run porosity, was found to occur where two tracks overlapped and especially in the regions near the clad-substrate interface. This type of porosity was found only in two sets of overlapping track alloy clad deposits, i.e. Stellite (Fig. 5.12) and stainless steel (Fig. 5.39). Weerasinghe (38) has reported the same effects and the extent of its occurrence is influenced by the single track dimension and the extent of overlapping. If the conditions chosen for overlapping the tracks are unfavourable, then the overlapping clad tracks will shield the root of the preceding track from the laser contact and also will impair the liquid flow. Clads formed under such process parameters will result in inter-run porosity. In the present results, the occurrence of this type of porosity is less frequent and on a smaller scale and in only a few set of clads, despite the fact that all overlapping clads were formed under closely similar

processing conditions. This suggests that the porosity results from some randomly occurring defects during cladding; e.g. misfeeding or shadowing effect of powder.

The major cause of crack initiation and propagation in the clad deposit lies in the occurrence of thermal changes encountered during rapid melting and solidification. The cracks are formed when clad matrix is unable to withstand the residual stresses that result from the thermal cycle of rapid surface melting and constrained cooling of solidified melt. Weerasinghe (38) has reported the formation of inter-dendritic cracks in austenitic stainless steel deposits produced at high traverse speed (> 20 mm/s) and high power densities (> 366 W/mm^2). Also at slow traverse speed some microcracks or fissures were observed. The reason for inter-dendritic cracking was reported to be the finer dendrite size obtained at a higher traverse speeds, which, in turn, resulted in a larger inter-dendritic surface area per given volume. However, in the present study, no inter-dendritic cracking was found in the austenitic stainless steel clad deposits. Also no evidence of cracking was found in any of the alloy clad deposits.

However, in composite clad deposits, where the situation of solidification becomes complex due to significant difference in the thermal properties of alloy and carbide particles, the matrix regions often show some cracking. In fact, the injected carbide particles play an important role in determining the nature of thermal stresses induced in the matrices which ultimately result in crack initiation. An interesting point noted in the present results was that, among the composites produced, only Stellite + SiC composite showed micro cracks in the matrix regions. However, in clads produced by injecting SiC into mild steel, some hairline cracks were observed in the regions surrounded by the partially dissolved SiC particles (Fig. 5.10); the rest of the regions of the clad were free from cracking.

In Stellite composites, the partially dissolved SiC particles influence the thermal stresses in three ways; by enriching the matrix in Si and carbon, favouring the formation of $M_{23}C_6$ and M_7C_3 type carbides and resolidification of fine SiC. The microstructure, hardness and brittleness of the matrix region will be changed by the solution of the SiC.

Increase in the proportion of SiC in the matrix will, therefore, affect the nature and magnitude of the thermal stresses produced. It has been reported by Exner (119) that in a Co-WC composite, the thermal stresses produced are of a compressive nature due to three times higher thermal contraction of cobalt as compared with WC. In the present results, two types of cracks are observed; in the first type, the cracks were found in clads formed using fine SiC particles, where SiC particles were almost completely dissolved in the Stellite matrix, hence making the matrix very hard and brittle (Fig. 5.19). These cracks formed perpendicular to the substrate and extended to the clad-substrate interface. The second type of cracks was initiated near large SiC particles and propagated through the matrix to the clad-substrate interface (Figs. 5.22-5.23). It can be deduced that in the first case (Fig. 5.19) the Stellite matrix was very hard and brittle due to high amount of SiC dissolution and could not withstand high thermal stresses which were greater than the fracture toughness of the matrix; this composite was produced at high Stellite + SiC feed rate and contained relatively lower dilution by iron from the substrate. This is in agreement with the observations of Monson et. al. (120) in a study of cladding of mild steel with various alloys (Ni, Co, and iron base). They (120) report that all the deposits with hardness values greater than 450 Hv showed crack when deposited on cold substrate; cracking increased with hardness and was severe for hardness values greater than 750 Hv. In the second case (Figs. 5.22-5.23), the dissolution of SiC in the matrix was very low, but the large SiC particle size comparable with the matrix area resulted in inducing the high stresses in the matrix. In the overlapping tracks cladding, the cracking was eliminated by the self preheating of the substrate in producing subsequent tracks. The reduction in crack formation by preheating the substrate has also been reported by other researchers (32, 121).

Earlier work (61) on TiC and WC injection into Ti-6Al-4V and Inconel 750 substrate showed that individual carbide particles often crack, even when there is insufficient thermally induced stresses to fracture the matrix. This effect was also seen in some clads

produced in the present study, where matrix regions showed very small hairline cracks (Fig. 5.25), some SiC particles were found to be cracked from the centre (Fig. 5.27).

8.6 OVERLAPPING OF CLAD TRACKS

Partially overlapping clad tracks of various alloys and composites were produced to cover a large substrate area to prepare samples for wear tests. Certain features of the overlapping tracks were found to be different from the single tracks produced under the same processing conditions. First, in overlapping, the clad dimensions (i.e thickness and width) obtained were slightly higher than those obtained for single tracks at the same powder feed rate, power density and traverse speed. The reason for this increase was that because all the tracks were produced consecutively, after producing a few tracks, the substrate and deposited clad attain temperature and hence a larger proportion of the energy is spent in melting the powder rather than the substrate which give rise to a slight increase in the clad dimensions.

The clad dilution, by iron from the substrate, was also decreased in the overlapping clads due to the fact that the subsequent overlapping clads were partly diluted by the substrate and partly by the previous clad track rather than completely by the substrate.The same type of effect of overlapping the tracks on the dilution was also observed by Monson (25) and Weerasinghe (38).

The surface finish (i.e smoothness) of the overlapping track clads was found to be dependent on both the extent of overlap and the aspect ratio (width to height ratio). For example, the alloy clads formed by overlapping 52% track showed better surface finish (Fig. 5.39 and Table 4.3) than those produced with 42% overlapping (Fig. 5.12 and Table 4.4). It has been reported by Monson (25) that the single track clad profiles with aspect ratios less than 5 were not suitable for producing overlapping track clads free from porosity and low in dilution. However, the present results disagree with the observations of Monson (25) in this regard. The overlapping clads produced at aspect

ratios even lower than 5 (Table 4.3) showed smooth surface finish (Figs. 5.1-5.6) and also low dilution and porosity. It was found that, in all the overlapping tracks, the side bead angle was more than 120°, which favoured the good overlapping of single tracks. This is in agreement with the observations of Bruck (114), who also reported that side bead angles greater than 120° generally result in good fusion at the overlap zone between the passes. Angles` progressively smaller than 120° increase the chances of trapping impurities as well as lack of fusion at the overlap. It is, therefore, concluded that the overlapping range of 45-55% together with side bead angle greater than 120° are suitable for producing overlapping clad tracks of good quality even if the aspect ratios are less than 5. However, these observations are for the range of process parameters studied in the present result. These overlapping parameters may be changed if the powder feed rate and specific energy ranges are changed.

8.7 DISCUSSION ON WEAR RESULTS

8.7.1 Introduction

The discussion on the wear results will be reported here in three parts. In the first two parts, the effect of various process variables such as applied test pressure and sliding distance and resultant features of worn surfaces e.g. hardness and roughness, under two- and three-body wear conditions respectively, will be discussed. In the third part, some metallurgical aspects, e.g microstructure and composition, of various clads will be related to their wear performance.

8.7.2 Two-body Wear

The first three series of wear tests fall under the conditions of two-body wear. In the first series (single track clad), however, the tests were of a qualitative nature because the

exact load applied was not known and hence the wear rate was not calculated. The samples subjected to wear testing, in this series, were Stellite + SiC composite produced under different laser processing conditions. Discussion for this series will be confined to the effect of various process parameters on the wear. In series two, samples of various clad compositions were subjected to wear tests using various test pressures. In series three, the effect of test time (in other words sliding distance) on wear rate was studied.

8.7.2.1 Effect of Traverse Speed and Feed Rate (series one)

In this series, three Stellite + SiC composite samples produced at different traverse speeds (7.0, 7.5, 9.0 mm/s) and constant Stellite and variable SiC feed rates, were subjected to wear testing using two different materials having different hardnesses, namely sand-stone and lime-stone as abrasive media. The following three conclusions were established on the basis of the results obtained.

1. The samples produced at lower traverse speeds showed higher wear resistance. The effect of traverse speed on clad formed was two fold, i.e. decrease in traverse speed means an increased dilution and/or powder intake. If the powder feed rate is not sufficient, then dilution will be dominant over powder intake and vice versa. Since the powder feed rate was sufficiently high in this series, a decrease in traverse speed resulted in high intake of powder especially SiC particles. That is the reason, the wear rate was lower in the clads formed at relatively lower traverse speeds.
2. The wear rate was lower in the regions with high SiC feed rate which resulted in high SiC particles intake; also high dissolution of SiC particles occurs and hence an increase in the hardness and wear resistance of the matrix region of the clad.
3. The lime-stone abrasive rock cylinder, due to its lower hardness, was found to be abraded by two of the samples, with relatively high wear resistance, rather than

abrading them. This shows that to obtain reasonable wear data, the hardness of the abrasive medium should not be lower than that for the material to be tested.

8.7.2.2 Effect of Applied Pressure on Wear (series two)

The abrasive wear rate of various alloy and composite samples; Alloy 4815 and its composite with SiC (Fig. 6.21), Stellite and its composite with SiC (Fig. 6.22) and stainless steel and its composite with (Fig. 6.23); was found to be increased with increasing applied test load. The wear data for these alloys and composites are shown in a combined form in Fig. 8.10. These results are in agreement with the basic wear equation given by Rabinowicz (86), (Eq. 6.10 section 6.2.2).

$V = K (W L)/H$

Where,

V = Wear volume

K = Wear coefficient

W = applied load

L = Sliding distance

H = Hardness

The shape (inclined towards horizontal) of the curves for all the alloys and composite samples studied (Fig. 8.10), shows that the wear loss increased with increasing applied pressure, the magnitude of increase was, however, not constant with each constant increase in the pressure (50 N). This shows that the wear situation was rather more complex than that assessed by this equation. From Fig. 8.10, it can be deduced that by increasing the applied pressure, the wear will be relatively severe in the initial stages of pressure increment and then tends towards a mild wear stage. Any further increase in the pressure will again change the trend towards the severe stage. There is also a critical point beyond which any increase in the pressure leads to seizure rather than to an increase in wear. The reason for this type of wear behaviour is that by increasing the pressure,

there can be a step wise transition from abrasive to adhesive wear where the tendency of increased wear with load is reversed (83).

From the foregoing discussion we can conclude that there is a certain limit of applied pressures where Eq. 6.10 can be applied to calculate the wear rate. For example, at very low applied pressures where the frictional forces are also very low, the wear rate will also be very low; wear data obtained at that low pressure can not be applied to estimate the wear resistance of the material under normal or moderate wear conditions. Similarly, at very high applied pressures where process reaches a seizure stage, the actual wear resistance (i.e. reciprocal of the wear loss) can not be calculated from the data obtained. That is why, at these two extreme stages of very high and very low applied pressures, Eq. 6.10 will not be applicable.

It is reported by some researchers (89, 122-123) that the wear resistance of pure metals increases with hardness but depends on many other factors for alloys containing more than one phases. However, in the present studies, a direct relationship between the hardness and wear resistance of various alloy and composite clads was found. By considering Fig. 8.10 in conjunction with the hardness data for various clad samples given in Table 6.2, it can be deduced that, except for stainless steel, high hardness values also showed high wear resistance (Fig. 8.11). Stainless steel showed higher wear resistance as compared with Stellite with higher hardness (618 Hv) than stainless steel (241 Hv). These results are again in agreement with the general wear equation (Eq. 6.10) given by Rabinowicz (86) which shows wear loss as inversely related to the hardness.

8.7.2.3 Effect of Sliding Distance on Wear (series three)

It has been shown in section 6.4.1.3 that the wear loss for the various alloys and composites studied, was increased continuously with the testing time. The wear loss data versus testing time for Stellite and its composite with SiC and alloy 4815 and its composite with SiC, are shown in Figs. 6.24 and 6.25 respectively. These data are

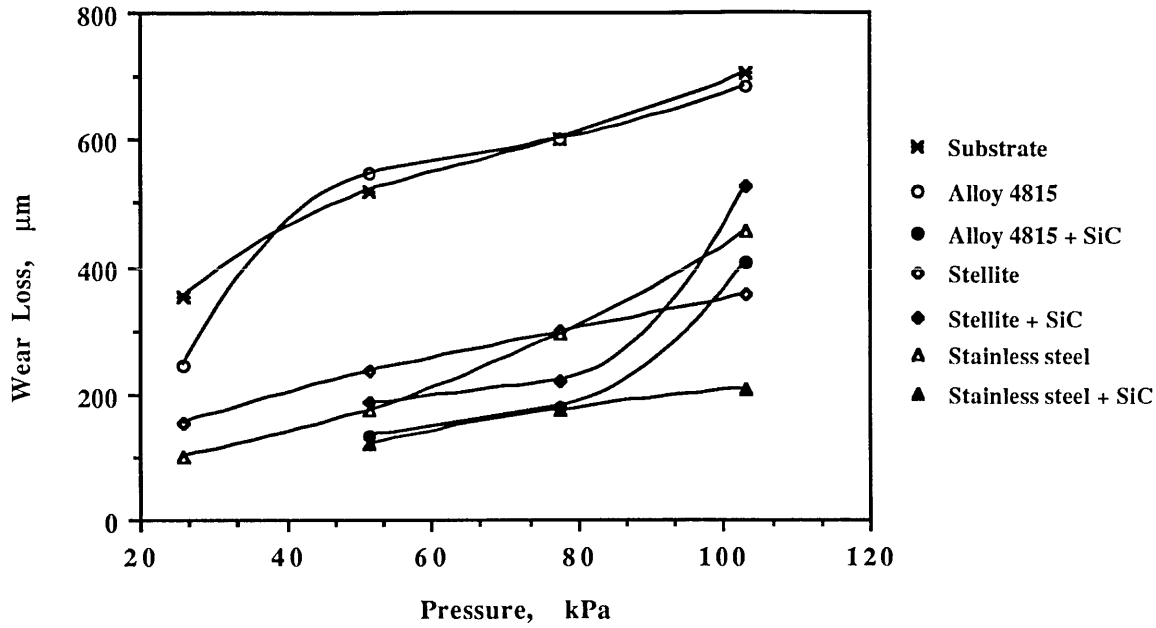

Fig. 8.10 Plot of wear loss versus applied pressure for various alloy and composite clads (series 2).

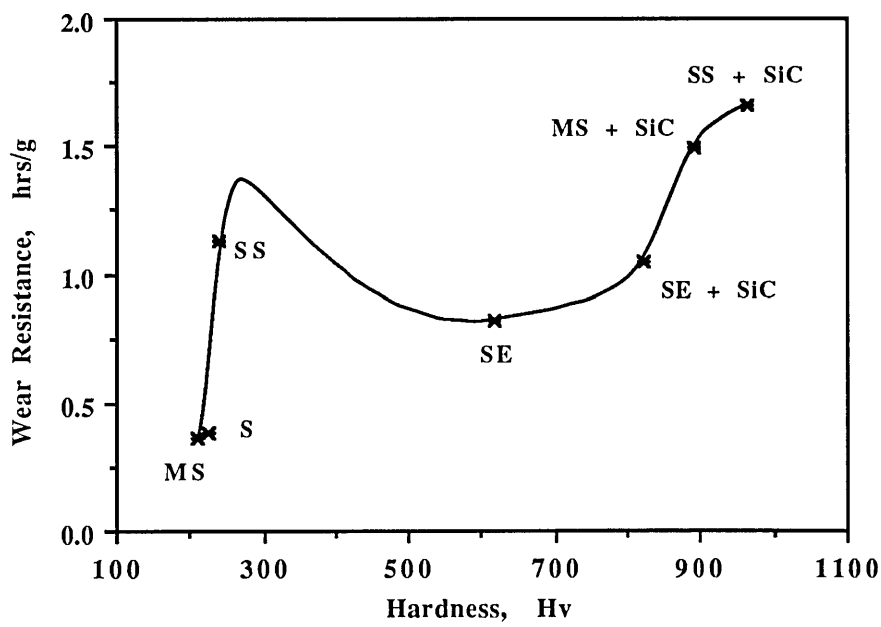

Fig. 8.11 Relationship between hardness and wear resistance of various alloy and composite clads (series 2), S = substrate, MS = Alloy 4815, SS = stainless steel, SE = Stellite.

shown here in a combined form in Fig. 8.12 for the comparison purposes. One common point, for all the clad materials tested, was that the wear rate was slightly higher at the beginning (Table 8.3) of the test and then reached a minimum. The reason for this type of behaviour is that a thin layer of loose particles is formed on the surface during the preparation of the samples (e.g. grinding) for wear testing. This thin layer is removed easily during the test as compared with the surface underneath, resulting in a slightly higher wear rate at the beginning of the test. When this layer is removed, the wear rate comes to a steady state.

Table 8.3

Wear loss data of various samples (series 3) after different intervals of testing time, Pressure applied = 103 kPa.

Material Tested	Wear loss in g after different intervals of one minute testing time			
	1st Min.	2nd Min.	3rd Min.	4th Min.
Mild steel substrate	3.1	3.3	3.4	3.6
Alloy 4815	3.9	3.6	3.1	2.6
Stellite Alloy 6	0.89	0.66	0.30	0.42
Alloy 4815 + 10 wt.% SiC	0.12	0.06	0.03	0.02
Stellite + 10 wt.% SiC	0.40	0.19	0.29	1.44*

* Complete clad layer was removed after 3rd minute of testing time.

Equation 6.10 is again used for discussion, considering first its validity in relation to the variable of sliding distance, i.e.

$$V = K (W L)/H$$

This equation provides a good relationship among different wear processing parameters (e.g. load and sliding distance) and materials properties (e.g. hardness), but it

appears to be oversimplified and to have some shortcomings. For example, according to this equation, for a given material at a constant applied load, wear volume loss is proportional to the sliding distance. The same sliding distance, say 100 m, can be travelled in one minute or ten minutes at the speeds of 100 m/min or 10 m/min respectively. The wear loss, however, will be higher in the case of higher speed as the frictional forces will be higher as compared with those at lower speed. This shows that for the same sliding distance, the wear loss can be higher if the travel speed is high (or in other words if the testing time is short). It is true that this equation considers a constant called the wear coefficient, K, the value of which also be higher in the case of higher speeds resulting in a higher wear loss. However, the wear coefficient, K, does not take into account the relative speed between the test sample and abrasive medium; it also depends on the hardness and particle size of the abrasive medium. From the above discussion it can be concluded that while presenting the wear data calculated by applying this equation (Eq. 6.10), it is also important to mention the speed or test time. Due to the aforestated reasons, wear loss was preferred for plotting against test time rather than sliding distance (Figs. 6.24-6.25 and 8.12).

Considering the present results (Fig. 8.12), it is clear that the wear loss is linearly related to the test time (or in other words sliding distance) which is in agreement with Eq. 6.10. By considering the data (Fig. 8.12) together with the hardness values (Table 6.3), it can be observed that the wear-hardness relationships given by Eq. 6.10, holds good in these results for all the samples except for Alloy 4815 + SiC composite sample. However, despite the lower hardness values as compared with the Stellite + SiC composite, alloy 4815 + SiC showed markedly higher wear resistance than the Stellite + SiC. It shows that although the theoretical expression of increased wear resistance with high hardness holds good in most of the cases, there are certain cases where some other factors, e.g. carbide particle size and phase transformations during the test, are predominant over the initial hardness of the material in determining the wear rate.

8.7.3 Three-body Abrasive Wear

The wear experiments carried out in series four and five fall in the category of three-body wear. The SiO_2 particles in the SiO_2 + water slurry acted as an external grinding medium between two moving surfaces (i.e. the rubber disc and the test specimen). The wear conditions in these tests were mild as compared with those in two-body wear reported in the previous section. The mild wear conditions were attributed partly to the nature of three-body wear and partly to the applied conditions, e.g. low load (1 kg) and lower relative motion between specimen and grinding medium (54 rpm). This is the reason, that, despite the long test time (1 hour) as compared with two-body wear (1 min.), the wear loss was very low in the three-body test. The wear rate, in series four and five, was plotted as a function of test time (Figs. 6.26 and 6.33); however, the data are discussed here in terms of sliding distance to correlate with Eq. 6.10.

8.7.3.1 Effect of Sliding Distance on Wear (series 4 & 5)

Wear data of various alloys and composite samples, tested in series 4 and 5, are shown in Fig. 8.13. Like two-body wear discussed in section 8.7.2.3, the wear loss was found to be directly proportional to the sliding distance. The wear loss for both the alloy and composite samples was upto only a few microns due to the aforementioned reasons. One interesting point to be noticed in three-body wear is that the wear resistance of the composite samples is only slightly better than the alloy samples. This is contradictory to the results obtained in the case of two-body wear where the composite samples showed superior wear resistance. The reason for this type of unusual behaviour could be that due to the comparatively larger amount of porosity in the composite samples, a large amount of material was removed by the preferential localized attack of SiO_2 particles in the high porosity regions and in the surrounding areas of embedded SiC particles. The removal of material in the other regions was found to be less severe.

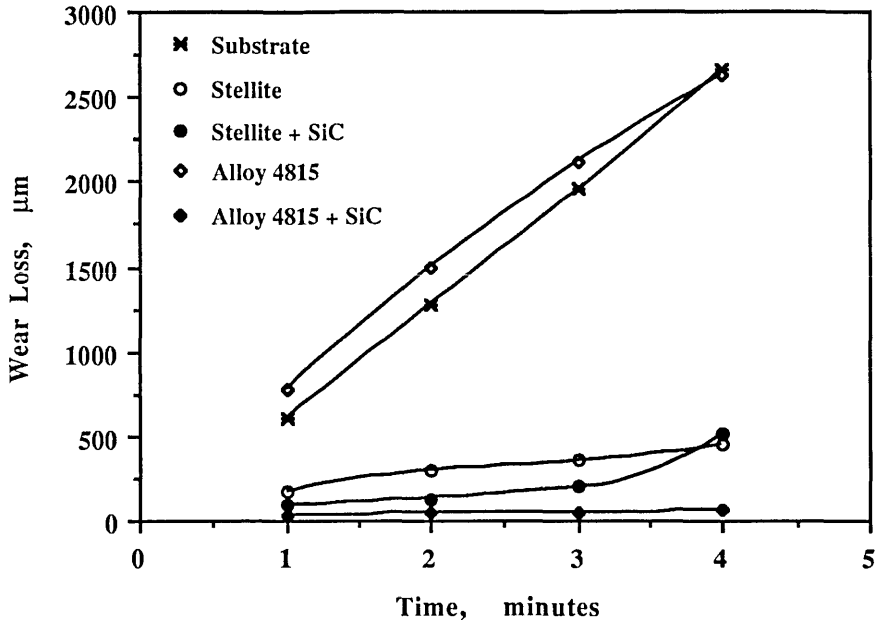

Fig. 8.12 Plot showing wear rate of various alloy and composite clads (series 3).

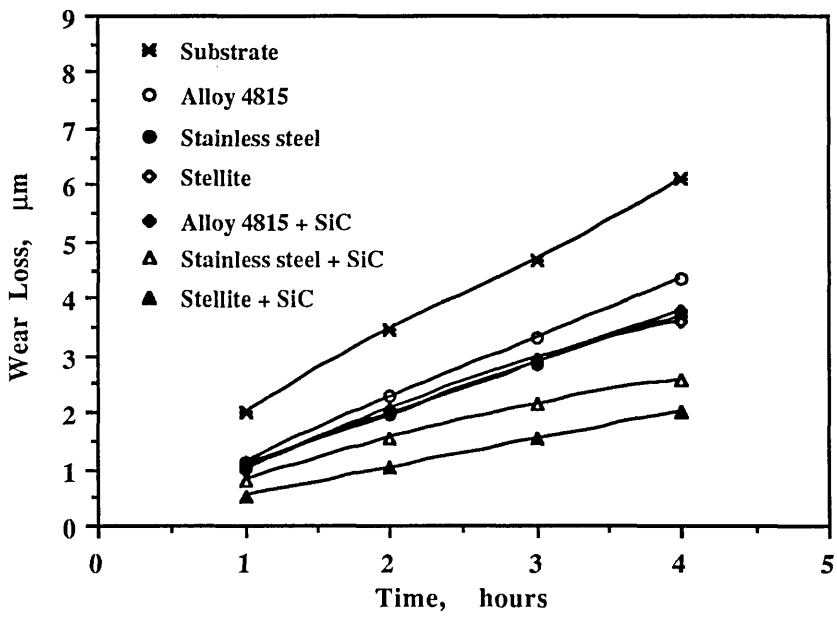

Fig. 8.13 Plot showing wear rate of various alloy and composite clads (series 4, three-body abrasive wear).

These conclusions have been deduced from the size and the shape of grooves on the worn surfaces, as seen in the micrographs, which will be discussed in a later section.

Since the wear loss in terms of decrease in the thickness of sample plotted in Fig. 8.13 was originally calculated from the weight loss obtained in wear experiments, it can be advocated that the actual decrease in the thickness of the sample might be less. Despite the unusual and unexpected behaviour of samples in series 4, the individual samples followed the same trend as suggested by basic wear equation (Eq. 6.10), i.e. the total wear loss increased linearly with time or in other words sliding distance. However, as far as the other part of the wear equation is concerned, i.e. wear decreases (or wear resistance increased) with increasing the hardness (Fig. 8.14), the results showed a contradictory trend. For example, the hardness of the Stellite clad matrix was twice that for the stainless steel sample, but both showed almost the same amount of wear. Similarly in the case of composite samples, stainless steel + SiC and Stellite + SiC had the highest (966 Hv) and the lowest (823 Hv) hardnesses respectively, but the wear loss was higher in the case of the former. Alloy 4815 + SiC composite had higher hardness than the Stellite + SiC, but the wear loss of the former was the highest for the composite materials. This shows that the samples in this series did not follow the wear-hardness relationship given by the wear equation. However, the same materials have been shown to obey this relationship in the case of two-body wear (Fig. 8.11). Although the relationship given in the wear equation governs both two-body and three-body wear, the involvement of another medium, i.e. water with SiO_2, in three-body wear conditions leads to a rather complex situation. The presence of water in the long duration (4 hours) wear testing might have resulted in a transition from abrasive wear to a combined form of corrosion/oxidation and abrasion.

In series five, three samples of Alloy 4815 + 5 wt.% SiC composites produced at various feed rates and traverse speeds showed a slight increase in the wear resistance as compared with Alloy 4815 sample (Figs. 6.29-6.31). The reason for this could be the same as described in the case of the series 4. However, all these samples showed a

linear proportional relationship of wear rate with sliding distance (or test time) as given by the wear equation (Eq. 6.10). The hardness-wear relationship given by the wear equation holds good in this series (Fig. 8.15).

8.7.3.2 Effect of Traverse Speed and Feed Rate on Wear (series 5)

In a set of samples produced at constant feed rate (Alloy 4815 + 5 wt.% SiC) and different speeds, the sample produced with low traverse speed showed a slightly higher wear resistance than that produced at higher traverse speed (Fig. 6.32). This is attributed to the higher hardness of the matrix resulting from increased intake and dissolution of SiC for a given feed rate.

In another set where two samples were produced at constant traverse speed and different feed rates, the sample with higher feed rate showed a higher wear resistance (Fig. 6.33). The reason for this increase in the wear resistance was the same as in the case of the previous set of clads (Fig. 6.32), but this time the controlling factor was feed rate. Increase in feed rate at constant speed means a higher powder intake. These results are also in agreement with the result of Stellite + SiC composite in series one for a two-body wear test (section 8.6.2.1). The only difference is that, in series one, the effect of feed rate and traverse speed was more pronounced for the reason that wear rates were higher than in the present series of three-body wear.

From the foregoing discussion on the effects of laser and wear process parameters on the wear rate under two- and three-body conditions, it can be concluded that the results presented of both type of abrasive wear generally followed the trends given by the basic wear equation. However, there were a few exceptions where the trends deviated; the reason for that was the involvement of some other wear phenomena like corrosion.

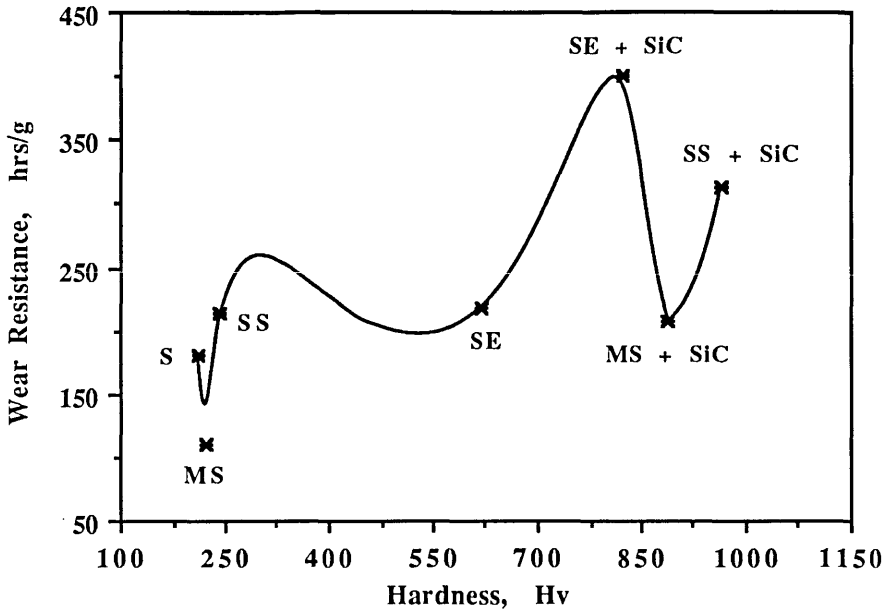

Fig. 8.14 Relationship between the hardness and the wear resistance of various alloy and composite clads (series 4), S = substrate, MS = Alloy 4815, SS = stainless steel, SE = Stellite.

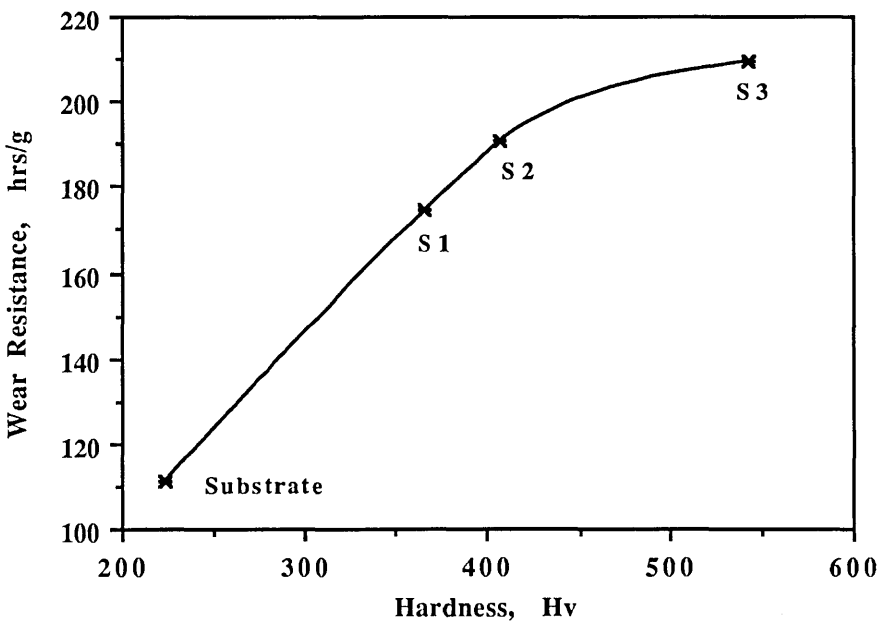

Fig. 8.15 Relationship between the hardness and the wear resistance of various alooy and composite clads (series 5), processing parameters for samples S1-S3 are reported in Table 4.4.

8.8. GENERAL FEATURES OF WORN SURFACES

Some general features of worn surfaces, e.g. hardness, roughness and nature of wear scars formed, of samples from both two- and three-body wear tests, were studied to understand the mechanism of material removal. These results were then related to those reported in the literature to support suggestions about the nature of wear involved.

8.8.1 Hardness of Worn Surfaces (two- and three-body)

Hardness data of worn surfaces for the two-body wear tests are reported in Tables 6.2 and 6.3 and for the three-body wear in Tables 6.4 and 6.5. Considering first the two-body wear tests in series two, the hardnesses of all the alloy samples and also substrate are markedly greater than those measured before the wear test. However, the hardness of the worn surface of composite samples was decreased from that of the original hardnesses of the composites. As far as Stellite + SiC and Alloy 4815 + SiC composites are concerned, the decrease in the hardness is attributed to the removal of the complete clad layer during the wear tests as can be seen in Fig. 8.10 where the sharp decrease in wear resistance of these composites after 80 kPa pressure was due to the same reason. However, in the case of the stainless steel + SiC composite wear data, plotted in Fig. 8.10 showing a consistent increase in the wear rate with pressure, the composite clad layer was not removed during the wear test. However, there was a marked decrease in the hardness of the stainless steel + SiC composite worn surface. The reason for this could be that the hardness measured on the worn surface of stainless steel + SiC composite might not necessarily be the highest hardness value of all the regions of that sample. The hardness values of the worn surfaces listed in Tables 6.2-6.5 are the highest ones among the ten hardness values measured on each sample. A large variation in hardness was found in different areas of the sample. Although the hardness was measured on ten different selected areas on the worn surface, these values can not

certainly represent the highest value of the sample, due to a very large surface area (645 mm^2) as compared with that of the hardness indentation (≤ 40 μm).

In series three of two-body wear tests (Table 6.3), the hardness of all the alloy and composite samples, except for the Stellite + SiC composite, including substrate was markedly increased. The decrease in the hardness of Stellite + SiC composite was due to the same reason as in series two for this composite, i.e. removal of the complete clad layer during the wear testing (Fig. 8.12).

In the case of three-body wear (series 4 and 5), the general trend was the same as in the two-body wear, i.e. the hardnesses of the worn surfaces were higher than those measured on the original samples with the exception of a few samples (Tables 6.4-6.5). In series four, where the same type of samples, as used in series two for two-body wear, were subjected to a three-body wear, a slightly different trend of hardness was obtained. The hardness of the alloy samples, except Stellite, and also substrate sample, was increased. However, the hardness of the composite samples, except Alloy 4815 + SiC, was decreased. The reason for the decrease in the hardness of Stellite + SiC and stainless steel + SiC composite samples cannot entirely be the same as in the case of series two and three, i.e. removal of complete clad layer as the wear loss was only a few microns in this series. However, the second reason described in the case of series two and three, i.e. the hardness values might not be the representative of the highest hardness values of these samples, seems to be more likely to be valid in this series too. Despite the exception of a few samples, it is, however, still a valid statement in the case of three-body wear also that the hardness values of the worn surfaces are greater than those of the original samples. The hardness values for the worn surfaces of series five (Table 6.5), support the claim, where a marked increase in the hardness was obtained after the wear tests.

Now some of the reasons, behind this increase in the hardness of the worn surfaces and how this increase in the hardness can affect the wear rate of the sample, will be discussed. Richardson (122) has carried out thorough study on this subject. He (122) states

"when metallic materials are worn by slow sliding contact with hard abrasive grit, plastic flow occurs, heating is slight, and the material near the wearing surface becomes work hardened". Richardson (122) also claims that work hardening of a material prior to subjection to an abrasive wear test has very little effect on the wear. Results reported by Kruschov (89) also agreed with the observations of Richardson (122). Kruschov (89) has found that the relative wear resistance of pure metals was directly proportional to their hardness. The wear resistance of the thermally treated (i.e annealed or quenched) metals was found slightly less dependent on the hardness, whereas despite the considerable increase in the hardness, the wear resistance of the mechanically (i.e. work hardened) treated metals was found unchanged. This shows that during the abrasive wear tests, the samples undergo work hardening and their hardness reaches a limit which determines the wear resistance of the material. Richardson (122) used various ferrous and non-ferrous alloy samples and subjected them to different types of abrasive tests, namely grinding on 180 and 40 grit corundum, wear in the stony soil and trepanning. The processes have been listed in an increasing order of their severity. The hardness, for all the alloys used, was found the highest when worn by trepanning and the lowest when worn by 180 grit corundum due to the relatively high and the low degree of the surface deformation offered by these processes respectively.

From the above discussion it is concluded that the hardness of the samples subjected to abrasive wear is increased due to the work hardening. The same phenomenon might have occurred during the present studies which resulted in an increase in the hardness of the worn surfaces of almost all the samples with only a few exceptions.

8.8.2 Roughness of Worn Surfaces (two- and three-body wear)

The surface roughness of worn surfaces of two-body (Tables 6.6 and 6.7) and three-body (Tables 6.8 and 6.9) wear series were measured to correlate with other surface features and also to help understand the mechanism of wear involved. From the

discussion in the foregoing sections it can be deduced that the surfaces with relatively high hardness resist to a greater extent to the abrasive particles in a wear test. Also the higher the applied load, the greater will be the penetration of abrasive particles and hence the deeper will be the wear grooves produced. From these conclusions, we can deduce two basic and important facts. Firstly, as the process conditions are comparatively more severe in two-body wear than in three-body wear, the grooves or wear scars produced will be deeper in the case of the former as compared with the latter. Secondly, the wear grooves formed will be less deep in a material of relatively lower hardness. Considering the present results, it can be observed that the present results followed these two basic rules. The surface roughness of the worn surfaces in two-body wear series (Tables 6.6 and 6.7) was markedly higher than the worn surfaces of three-body wear (Tables 6.8 and 6.9). Considering the roughness data of series two of two-body wear (Table 6.6) together with the wear (Fig. 8.10) and hardness (Table 6.6), it can be deduced that except for a few cases, the general trend observed in this series was that the higher the hardness, the higher is the wear resistance and lower is the value of roughness. A similar trend can be observed in series three (Table 6.3, Fig. 8.12 and Table 6.7), series four (Table 6.4, Fig. 8.13 and Table 6.8) and series five (Table 6.5, Figs. 6.32-6.33 and Table 6.9) by studying the combined data of hardness, wear and surface roughness.

8.8.3 Microscopy of Worn Surfaces (Two- and three-body)

Microscopical studies of worn surfaces, without any preparation, were carried out to understand the mechanism of removal of material from various samples. Subsurface features were also revealed by high magnification scanning electron microscopy. Before discussing the micrographs of worn surfaces of various series, it will be helpful to first establish some basic principles which lead to the formation of specific surface features in two- and three-body abrasive wear.

The experimental set-up for two body wear testing, used in the present study, consisted of two revolving discs, one of which was made up of 80 grit size Al_2O_3 and acted as the grinding medium (see section 6.3.1.2 for details). The grinding disc was made of single size (80 grit) fixed abrasive particles. The shape of the grooves formed on the worn surfaces should, therefore, be of a closer size of width, and unidirectional. As the abrasive particles are of the same size, it can be assumed that at a constant applied pressure, a wider groove means a deeper groove too.

On the other hand, in three-body wear set-up, the abrasive particles (SiO_2) used consisted of a range of particle sizes and were free to move. The worn surface produced by this set-up should contain multidirectional wear grooves of different sizes and shapes. As the applied load was very low (1 kg), the width of the grooves must be somewhat finer than those obtained in two-body wear. However, since the abrasive particles are free to move in any direction, local concentrations of wear can arise in low strength areas.

8.8.3.1 Series 2 (two-body abrasive wear)

The micrographs of this series (Figs. 6.34-6.45) show that the wear scars produced conform to the applied two-body wear conditions. However, some micrographs also show a few multidirectional grooves, which might result from the abrasive particles detached from the grinding disc and entrapped between the sample and the grinding disc. It can, therefore, be deduced that the removal of material occurred due to a combine effect of two- and three-body abrasive wear and sometimes an adhesive wear mechanism also.

Figs. 6.34-6.35 show the micrographs of a worn surface of a stainless steel clad sample. The greater depth of the wear grooves (Fig. 6.34, as deduced from the width) shows relatively low hardness of the material as compared with the hard abrasive particles. The nature of the worn surface shows that some adhesive wear also occurred

(Fig. 6.35). Similarly, in the case of Stellite (Figs. 6.36-6.37) and alloy 4815 (Figs. 6.38-6.39) samples, the worn surfaces showed deep wear grooves produced by loose hard abrasive particles (Figs. 6.36 and 6.38). From the appearance of the grooves, it is deduced that the removal of material occurred due to the ploughing action of the abrasive particles. However, the appearance of both the Stellite (Fig. 6.37) and alloy 4815 (Fig. 6.39) worn surfaces also show that during the wear process, fragments of material were detached from these surfaces which resulted in adhesive type of wear.

In the case of the composite clad samples; Stellite + SiC (Figs. 6.40-6.41), stainless steel + SiC (Figs. 6.42-6.43) and Alloy 4815 + SiC (Figs. 6.44-6.45), the depth of the wear grooves was relatively small as compared with the alloy samples, which was consistent with their high hardness. The removal of material in composite samples occurred by the same mechanism as in the case of the alloy samples. However, the sharpness of the grooves (Figs. 6.42 and 6.44) shows that both ploughing and cutting action took place during wear testing. In Stellite + SiC composite samples, some evidence of fragmentation was also found (Fig. 6.40). Fig. 6.41 shows that subsurface damage had occurred due to the deep penetration of the hard particles which could be either Al_2O_3 particles detached from the grinding disc or SiC particles detached from the sample and entrapped between the two moving surfaces. Although the stainless steel + SiC composite showed the highest wear resistance in this series as is evident from Figs. 6.42 and 8.10, in some areas the surface layer was also found to be removed by fragmentation due to severe localized attack of abrasive particles (Fig. 6.43). Micrographs of Alloy 4815 + SiC show that the wear occurred mostly by plastic deformation in ploughing of the material towards the edges of grooves. However, in some areas wear also occurred by the mechanism of fretting forming deep pits (Fig. 6.45).

8.8.3.2 Series 3 (two-body wear)

The micrographs of the mild steel substrate worn surfaces (Figs. 6.46-6.47) show that the samples were severely damaged during the wear tests due to their low wear resistance. The material removal occurred mainly due to deep ploughing mechanism. The shape of the Stellite worn surfaces showed that the wear occurred mainly due to two-body wear process (Fig. 6.48) except for a few shallow multidirectional scratches which resulted from the entrapped abrasive particles. The sharp edges of the grooves show that the wear occurred due to cutting rather than ploughing action. The inter-track regions of overlapping Stellite clads were, however, severely attacked by the abrasive particles causing a subsurface damage (Fig. 6.49). The Alloy 4815 samples showed the lowest wear resistance (Fig. 8.12) in this series and consequently the deepest grooves were produced by the abrasive particles (Fig. 6.50). The material was removed from the surface layer solely by ploughing large fragments to the edges of the wear grooves (Fig. 6.51). Fig. 6.52 shows the worn surface of Stellite + SiC composite sample. Since most of the clad layer was removed at the end of the wear test, the sample shows a worn surface like that of a softer sample (Fig. 6.50). The presence of both rough and sharp grooves shows that the wear took place by both ploughing and cutting action of the abrasive particles. In some areas, the material was removed in the form of long micro-chips resulting in very smooth surface finish of the grooves (Figs. 6.53-6.54). Micrographs of subsurface damage of the worn surfaces showed some evidence of micro-crack initiation and propagation (Fig. 6.53) within the grooves. This may be attributed to the vibrational stresses suffered by the sample during wear testing.

Alloy 4815 + SiC composite showed the highest wear resistance in this series (Fig. 8.12). The worn surfaces obtained showed the features which were produced by a typical two-body wear situation (Fig. 6.55). The removal of material occurred mainly due to the cutting action of the abrasive particles in the form of shallow, long and short micro-chips (Fig. 6.55). The areas most severely attacked by the abrasive particles were

those around the embedded SiC particles (Fig. 6.56). Some evidence of the detachment of embedded SiC particles from the surface was also found, resulting in the removal of the material from the surrounding areas by flaking off small fragments (Fig. 6.57).

8.8.3.3 Series 4 (three-body wear)

The worn surfaces in this series showed multidirectional grooves conforming to three-body wear situation. The grooves dimensions, i.e width and depth, were very small as compared with those obtained in two-body wear series (series 2 and 3) due to the mild process conditions applied in the case of the present series. Figs. 6.58 and 6.59 show the worn surfaces of a stainless steel sample. The material removal, in this case, occurred due to deep scratches produced by the abrasive particles (Fig. 6.58) and also partly due to the severe attack by the abrasive particles at the areas of high porosity by making deep pits (Fig. 6.59). In Stellite samples, although, the groove depth was relatively small (Fig. 6.60) due to the high hardness, some hard abrasive particles were found to be penetrated deeply into the grooves causing subsurface damage (Fig. 6.61). Like stainless steel, Stellite surfaces also showed the presence of a large extent of pitting caused by the localized attack of the SiO_2 abrasive particles (Fig. 6.62). The Alloy 4815 sample showed, as also expected, the lowest wear resistance in this series (Fig. 8.13) and hence the worn surfaces obtained consisted of deep wear scratches (Fig. 6.63). Alloy 4815 was the only sample in this series which showed the removal of material, in some areas, by the ploughing action of the abrasive particles (Fig. 6.64). This was attributed to its low hardness (Table 6.4) as compared with the other samples of this series. It was also found that some of the abrasive particles (SiO_2) which were attached to the revolving rubber disc, caused relatively deeper grooves and also produced some unusual zigzag patterns (Fig. 6.65). These attached particles might have also increased the wear loss which would have been less if they were free.

In the case of composite samples, the extent of pitting was lower as compared with the alloy samples. Stellite + SiC composite showed the highest wear resistance in this series (Fig. 8.13) and consequently the wear grooves produced were relatively shallow (Fig. 6.66). The grooves produced were very sharp due to the high hardness of the sample. It is also evident from Fig. 6.66 that the wear grooves are of various depths; this is probably due to the fact that in three-body wear, since the abrasive particles are free to move, they can attack the sample at different angles. This is also in agreement with the previous studies on this subject (11-12) which reported that the wear rate also depends on the attacking angle of the abrasive particles. That is why some abrasive particles were found to severely attack certain areas causing the initiation of the micro-cracks (Fig. 6.67).

Despite its highest hardness in this series (Table 6.4), the stainless steel + SiC composite samples surfaces showed a large extent of pitting (Fig. 6.68). This may be attributable to the presence of high porosity in this composite sample. Accordingly, the groove depth produced by the abrasive particles in stainless steel composite was also high (Fig. 6.69). However, the groove boundaries were very sharp due to the high hardness of the sample. Although, the Alloy 4815 + SiC composite showed the lowest wear resistance among the composites in this series; the worn surfaces did not show the presence of deep grooves. The worn surfaces obtained gave a polished look revealing the microstructure in the surrounding areas of dissolved SiC particles (Fig. 6.70). The material removal, in this sample, occurred mainly due to the severe attack of abrasive particles in the areas of partially dissolved SiC particles (which showed large amount of porosity), Fig. 6.71. This localized severe attack of abrasive particles, sometimes, led to the removal of material by flaking off the fragments. This was the reason, despite its high hardness (Table 6.4), that the Alloy 4815 + SiC composite sample showed the lowest wear resistance among the composites of this series (Fig. 8.13).

8.8.3.4 Series 5 (three-body wear)

In this series, micrographs showed some interesting features of the worn surfaces. Since the worn surfaces obtained were very smooth with a polished appearance, in some micrographs the microstructures of the samples were revealed without any etching. The features of the worn surfaces were similar to those produced by a typical low-stress three-body abrasive wear situation. Sample S1 showed the lowest wear resistance (Figs. 6.32 and 6.33) in this series and hence the micrographs of worn surfaces showed somewhat deeper scratches produce by the abrasive particles (Fig. 6.72). Disintegration of some embedded SiC particles was observed (Fig. 6.73) which consequently led to an increased wear loss. However, the areas surrounding the partially dissolved SiC particles showed very high wear resistance with no scratch formation (Fig. 6.74). In some areas evidence of relatively wide and deep microcrack propagation was also found (Fig. 6.75).

Sample S2 showed a similar type of worn surface to that of S1 except for the formation of relatively shallower scratches in the case of the former (Fig.6.76) due to its relatively higher wear resistance. Like in the series 3, the areas most severely attacked by the abrasive particles in this series were also those surrounded by the embedded SiC particles (Fig. 6.77). In some embedded particles, the occurrence of cracking and also disintegration of particle, as in the case of sample S1, was found (Fig. 6.78). However, no evidence of subsurface damage in the areas exposed by the fragmentation of SiC particles was seen (Fig. 6.79).

The nature of grooves formed on the surface of the sample S3 also conformed to a typical three-body abrasive wear situation (Fig.6.80). The depth of grooves was relatively smaller as compared with sample S1. Unlike the other two samples in this series, the worn surface of sample S3 showed that the removal of material occurred due to the formation of a large amount of pits (Fig. 6.81). The occurrence of wear by pitting showed severe localized attack of SiO_2 abrasive particles in certain areas. The abrasive particles were also found to attack the areas of relatively higher internal porosity;

subsequently the material was removed by flaking off small fragments and hence producing deep pits (Fig. 6.81).

Considering the wear (Figs. 6.32-6.33), hardness (Table 6.5) and surface roughness (Table 6.9) data together for the composite samples S1, S2 and S3 (Alloy 4815 + SiC) in this series, it can be deduced that despite their high hardness and very low roughness of worn surfaces, the wear resistance was not much better than for Alloy 4815. This unusual behaviour of the composite samples can easily be understood from the above discussion. Although the groove dimensions shown by all micrographs of this series (Figs. 6.72-6.81) were very small, but in almost all samples, the wear occurred mainly by the severe attack of abrasive particles in high porosity areas and also disintegration of the SiC particles. These processes involved in the material's removal led to relatively higher wear losses. This was the reason that the wear resistance of both the Alloy 4815 and Alloy 4815 + SiC composite samples (S1, S2 and S3) was in a very close range.

8.9 SIGNIFICANCE OF WEAR COEFFICIENT IN TWO- AND THREE-BODY ABRASIVE WEAR

To understand the significance of the wear coefficient 'K' in two- and three-body wear situations, the basic wear equation (Eq. 6.10) is considered as,

$$K = (V H)/W L \qquad \text{Eq. 8.7}$$

Equation 8.7 shows that at a given applied load and sliding distance, the wear coefficient 'K' is a function of the product of the wear volume and the hardness of the material. Since during a specific wear test all the parameters, except the wear volume, are constant for a given material, the wear coefficient would be a direct function of the wear volume. The magnitude of 'K' will influence the extent of the wear for a particular material of constant hardness. The value of 'K' depends on the process conditions, e.g. relative speed of the moving bodies, hardness of the abrasive, size of abrasive particles, conditions of lubrication etc. The greater the severity of the process conditions, the

higher will be the value of K and consequently the higher will be the wear rate. For a series of wear experiments carried out on various samples of different hardnesses, the value of 'K' should be constant if the results obtained obey the Eq. 6.10.

The wear results of all the series reported in this chapter satisfied the conditions of Eq. 8.7. The values of wear coefficients for series 2-5 are reported in Tables 8.4-8.7. The values of 'K' for both the two- and three-body wear in various series are almost identical for different materials in an acceptable range. This shows that the wear processes were in stable conditions during the tests. The 'K' values evaluated in the present work are also in agreement with those reported by Rabinowicz (86) and Antony (34).

In series 2 of two-body wear tests (Table 8.4), the wear coefficient values are almost identical for all the alloy and composite samples except for the stainless steel sample which is much lower (3.7×10^{-2}) than the others ($10\text{-}13 \times 10^{-2}$). This lower value of 'K' for stainless steel is attributed to the behaviour of the sample itself rather than any malfunctioning of the process. The reason for low 'K' value for stainless steel is, in fact, that the sample showed a very high wear resistance corresponding to its relatively lower initial hardness.

In series 3 of two-body wear (Table 8.5), a range of 'K' values ($0.9\text{-}7.4 \times 10^{-2}$) was obtained but they were all in an acceptable close range. However, like stainless steel in series 2, the Alloy 4815 + SiC sample in this series showed a low wear coefficient (0.9×10^{-2}) as compared with other samples ($3\text{-}7.4 \times 10^{-2}$). In three-body wear, series 4 and 5, Tables 8.6-8.7, the values of 'K' were very low ($10\text{-}37 \times 10^{-5}$) as compared with those obtained in the case of two-body wear ($0.9\text{-}13.6 \times 10^{-2}$).

The reason for this extremely low 'K' value in three-body wear is two fold. Firstly, the applied conditions, i.e. load, speed, abrasive, were relatively milder than those applied in the two-body wear. Secondly, since the abrasive particles in three-body wear conditions are free to move, it seems that they spend 90% of their time in rolling, thus producing no abrasive wear, and only about 10% of the time sliding and abrading the

surface (86). For these reasons, the coefficient of friction for three-body wear is reported to be only 0.25 as compared with that of 0.6 for two-body abrasion (5).

Table 8.4

Wear coefficients for various materials tested under two-body wear conditions (series 2); Load, W = 10 kg, Sliding distance, L = 71816 mm

Sample tested	Hardness, H, kg/mm^2	Wear volume, V, mm^3	Wear coefficient, K X 10^{-2}
Mild steel substrate	223	335.4	10.4
Stainless steel	241	112.2	3.7
Stellite	618	151.4	13.0
Alloy 4815	211	352.8	10.3
Stainless steel + SiC	966	77.4	10.4
Stellite + SiC	823	119.3	13.6
Alloy 4815 + SiC	890	86.4	10.7

The wear coefficient values in series 5 (Table 8.7) are almost identical whereas in series 4 (Table 8.6) they fall under a close range. The variation in the 'K' values is due to the unusual behaviour of the samples during the wear tests. In series 4 (Table 8.6), the normal 'K' values are within the range 10-25 x 10^{-5}. The values higher than this pertain to composite samples only, e.g. 31 x 10^{-5} and 37.2 x 10^{-5} for stainless steel + SiC and Alloy 4815 + SiC samples respectively. It has been reported in section 8.8.3.3 that wear of composite samples in this series mainly occurred due to the severe localized attack of abrasive particles in the areas of high porosity. The other regions on the worn surfaces showed very shallow wear grooves indicating samples of high wear resistance

corresponding to their hardnesses. However, due to the excessive wear in certain areas, the overall wear loss of the composite samples in series 4 was not as low as was expected from their high hardness. That is why the wear coefficient 'K' values for stainless steel + SiC and the Alloy 4815 + SiC composite samples in this series are very low as compared with the other samples of the same series.

Table 8.5

Wear coefficients for various materials tested under two-body wear conditions (series 3); Load, W = 20 kg, Sliding distance, L = 71816 mm

Sample tested	Hardness, H, kg/mm^2	Wear volume, V, mm^3	Wear coefficient, K X 10^{-2}
Mild steel substrate	223	394.7	6.1
Stellite	540	109.0	4.0
Alloy 4815	211	505.6	7.4
Stellite + SiC	763	57.4	3.0
Alloy 4815 + SiC	710	18.0	0.9

8.10 EFFECT OF MICROSTRUCTURE ON WEAR

Although an indepth study of microstructure and phase transformations has not been carried out in the present work, some general microstructural features of various alloy and composite clads will be related to their wear resistance with reference to the previous work reported in the literature on the subject. Considering the wear results of all series of both two- and three-body wear conditions, the following observations can be deduced,

Table 8.6

Wear coefficients for various materials tested under three-body wear conditions (series 4); Load, W = 1 kg, Sliding distance, L = 1551243 mm

Sample tested	Hardness, H, kg/mm^2	Wear volume, V, mm^3	Wear coefficient, K X 10^{-5}
Mild steel substrate	223	1.3	18.6
Stainless steel	241	0.69	10.7
Stellite	618	0.64	24.4
Alloy 4815	211	0.73	10.0
Stainless steel + SiC	966	0.51	31.0
Stellite + SiC	823	0.33	17.5
Alloy 4815 + SiC	890	0.65	37.2

Table 8.7

Wear coefficients Alloy 4815 + SiC samples tested under three-body wear conditions (series 5); Load, W = 1 kg, Sliding distance, L = 1551243 mm

Sample tested	Hardness, H, kg/mm^2	Wear volume, V, mm^3	Wear coefficient, K X 10^{-5}
Mild steel substrate	223	1.3	18.6
S1	366	0.774	18.2
S2	406	0.709	18.5
S3	543	0.645	22.5

1. The wear resistance of all the alloy samples was improved by the inclusion of SiC particles to produce the composite clads (Figs. 6.20-6.33).
2. Wear resistance of austenitic stainless steel samples was either better than or equal to the Stellite clads (Figs. 8.10 and 8.13).
3. The wear resistance of Alloy 4815 + SiC and stainless steel + SiC composite samples was either better than (Figs. 8.10-8.12) or closely equal to the Stellite + SiC composite sample (Fig. 8.13).

First consider the better performance of austenitic stainless steel than Stellite during wear tests. This was, in fact, not an unusual behaviour of stainless steel as it has already been observed by Mazumder and co-workers that laser clad Fe-Cr-Mn-C alloy samples showed far better wear resistance than the Stellite alloy 6 clad (29, 49). They (29, 49) attributed this higher wear resistance to the presence of M_6C and M_7C_3 type hard carbides in a ferrite matrix. However, in the present work, where a fully austenitic stainless steel structure was obtained, the better performance of stainless steel in wear is attributed to the fine microstructure obtained due to a high cooling rate. It is also possible that martensite is formed as a result of wear deformation during the wear testing; this needs detailed microstructure studies of worn surfaces for confirmation.

As far as the improvement in the wear resistance by the inclusion of SiC particles is concerned, it was a result of the following factors,

1. Partial solution of large SiC particles and resolidification to fine SiC particles.
2. Enrichment of the clad matrix in carbon content by the partial dissolution of SiC particles hence resulting in the formation of M_7C_3 type carbides.
4. The formation of high carbon martensite in Alloy 4815 + SiC clads.

It has been reported in the previous studies (95, 103) that for materials produced by conventional methods, the abrasive wear resistance is promoted by the processing conditions that maximize the carbide particle size. The abrasive wear resistance may also be increased by increasing the proportion of hard constituents particularly for structures with coarse hard phase morphologies (e.g M_7C_3 and $M_{23}C_6$ type carbides in Co matrix).

Since it is a well established fact that the hardness of an alloy is improved by the refinement of the microstructure, it can be, therefore, deduced that in conventionally produced materials, the abrasive wear resistance will be higher for those with even lower hardness. This fact was experimentally shown by Silence (103) where the abrasive wear resistance of a cobalt-base alloy was found to be increased by increasing the carbide particle size, in contrast to the hardness which was decreased.

However, as also reported by Monson (25), these morphologies reported by Gahr (95) and Silence (103) not hold good in the case of laser cladding where both the hardness and wear resistance are improved by the refinement of the microstructures attributed to the high cooling rates associated with laser processing. The reason for high wear resistance in laser clad samples despite a smaller interdendritic carbide size, as reported by Monson (25), is that due to high cooling rates and the hardening effects, a 'trade-off' between carbide size/fraction and deposit hardness exists.

From the above discussion, it can be deduced that since in conventional processes, the hardness of a deposit is usually decreased by increasing the particle size of a harder phase at a constant volume, the hardness based relationships such as that given by Rabinowicz (86) cannot effectively be applied in these cases. However, the equation suggested by Rabinowicz (86) holds good in the case of laser processing, as has been seen in the present results, where the abrasive wear resistance increases with the hardness.

CHAPTER 9

CONCLUSIONS AND SUGGESTIONS FOR FUTURE WORK

9.1 CONCLUSIONS

A 2 kW CW CO_2 laser can be effectively used as a heat source to produce overlapping alloy and composite clad deposits with low dilution from the substrate. A pneumatic powder delivery system is found to be an effective mean of blowing a mixture of alloy and carbide particles into the laser generated melt pool. The abrasive wear resistance of composite clads was found to be at least twice that showed by the respective alloy clads. The increase was attributed to various mechanisms; for example, in the case of Stellite + SiC clads, it was attributed partly to the presence of fine SiC particles and partly to the formation of other carbides ($M_{23}C_6$ and M_7C_3) due to partial solution of SiC. Since the wear results reported in this thesis were obtained by subjecting relatively large size samples (25 x 25 mm) using either severe wear conditions or a simulation of a specific process, they can readily be used as a guideline for selecting the material for use in actual service conditions.

The conclusions made on the basis of results presented in chapters 4 to 7 are summarized in the following sections.

9.1.1 Effect of Process Parameters on Clad Dimensions

1. The clad thickness and width of all the alloy and composite clads produced were increased by increasing the powder feed rate except for the SiC injection process where the clad width was decreased slightly with increasing SiC particle feed rate.

2. The substrate melt depth was decreased by increasing the powder feed rate in all the clads. However, the magnitude of this decrease varied depending on the specific energy applied and the powder feed rate.
3. The general trend observed for the effect of substrate traverse speed on the various aspects of single track clad dimensions, i.e., width, thickness, build up and substrate melt depth, was a decrease with increasing traverse speed.

9.1.2 Clad Dilution

1. Values of clad dilutions, as calculated from compositional difference and from substrate melted area difference (114) showed good agreement.
2. The clad matrix dilution was found to be decreased with increase in the powder feed rate at constant traverse speed and power density.
3. At constant power density and powder feed rate, dilution was decreased with increase in the traverse speed.
4. In the case of Stellite + SiC composite cladding, using various proportions of SiC in the cladding powder mixture, the area dilution of the clad matrix was found to be affected by both the total powder feed rate (Stellite + SiC) and the wt.% of SiC in the cladding mixture.
5. In the SiC particle injection process and also in cladding using composites with mixtures of SiC particles and alloy powders, partial solution of SiC particles occurred. The matrix regions of the clads were, therefore, enriched in silicon and carbon contents.
6. The dilution levels of overlapping track clads were found to be lower than the single track clads produced at the same processing conditions and feed rates. This was attributed to the fact that in overlapping clads, each successive track is produced with partial melting of previous clad track and partial melting of the substrate rather

than the complete melting of the substrate; hence the amount of iron which can enter from the substrate into the clad matrix is decreased.

9.1.3 Microstructure

1. Single track clads formed by the injection of relatively large SiC particles into mild steel substrate showed large amounts of porosity in the regions between the large embedded SiC particles. However, injection of medium particle size (250-450 μm) SiC showed clads with good carbide distribution in the matrix with a low amount of porosity. The matrix regions showed a microstructure containing ferrite/martensite.
2. In Alloy 4815 overlapping clads, the cooling rate was relatively lower, as compared with the Alloy 4815 + SiC composite, due to relatively larger clad thickness (2.5 mm) and lower traverse speed (2.5 mm/s), and hence the solidification structure was fine ferrite and pearlite grains. However, in Alloy 4815 + SiC composite, due to the relatively smaller clad thickness (1 mm) and higher traverse speed (4.5 mm/s), higher cooling rates resulted in the formation of martensite.
3. Both the stainless steel and stainless steel + SiC overlapping clads showed a fine dendritic microstructure typical of a rapidly solidified austenitic stainless steel. However, the secondary dendrite arm spacing in the case of the latter was finer (~ 4 μm) as compared with the former (~ 7.5 μm); this was again attributed to the higher cooling rates in the composites as compared with the alloy clads due to the smaller clad thickness and higher traverse speed (1.3 mm and 4.5 mm/s) in the case of composite as compared with the alloy clads (2 mm and 2.5 mm/s respectively).
4. The matrix regions of Stellite and Stellite + SiC clads showed fine dendritic microstructures, typical of Stellite alloys, consisting of primary dendrites of Co-Cr-W-C based solid solutions and an interdendritic carbide-containing eutectic. The

dendrites were found to grow in different directions which was attributed to the multi-directional heat extraction during the solidification. The high cooling rates associated with laser processing resulted in a refined dendritic structure with an average inter-dendritic secondary arm spacing of 2-10 μm depending upon the cooling rate. At constant other processing parameters, the higher the substrate traverse speed, the higher the cooling rate; hence the clads formed at relatively higher traverse speeds showed finer dendritic structure than those formed at lower traverse speeds. In Stellite + SiC composite clads, due to partial dissolution of SiC and resulting enrichment of matrix in silicon and carbon, an increase in the formation of carbides (e.g. M_7C_3) was expected.

9.1.4 General Features of Clad Layers

1. Low magnification microscopy showed that nearly all the alloy and composite clads were smooth, sound and continuous having a good fusion bond with the substrate metal.
2. In all the composite clads, i.e. Stellite + SiC, stainless steel + SiC and Alloy 4815 + SiC, SiC particles were found to be segregated to the upper regions of the clads. This was a result of the lower density of SiC particles (3.2 g/cm^3) as compared with densities of Stellite alloy 6 (8.3 g/cm^3), stainless steel (7.2 g/cm^3) and Alloy 4815 (7.2 g/cm^3).
3. The overlapping clads formed with aspect ratios (width to height ratio) less than 3 and more than 50% overlapping of track showed smooth clad surfaces. However, overlapping clads formed with aspect ratios less than 3 and also an overlapping of less than 45% showed imperfect overlapping of the single tracks.
4. The overlapping composite clads showed relatively smoother surfaces as compared with the alloy clads; this was associated with the relatively higher aspect ratios and slightly low percentage of overlapping in the case of the former than in the latter.

9.1.5 Microhardness

1. The microhardness of the matrix (the lower part of the clad layer between the clad-substrate interface and the top surface) regions of almost all the alloy and composite clad deposits, was found to be uniform throughout the whole clad area. However, in the case of Stellite + SiC composite clads, a trend was found for slight decrease of microhardness of the matrix regions towards the clad-substrate interface; this was attributed to the slightly higher dilution of those regions by iron from the substrate.
2. The microhardnesses of the matrix regions of composite clads were markedly higher than the alloy clads. This was due to a combination of hardening mechanisms. These include solid solution strengthening, dispersion hardening by the carbides formed during the resolidification of carbon enriched liquid resulting from partial dissolution of SiC, transformation hardening and microstructural refinement.
3. The microhardnesses of the matrix regions of both the Stellite and Stellite + SiC clads were found to be increased by increasing the powder feed rate. This resulted from the lower dilution of clad matrix by iron from the substrate at relatively higher feed rates. However, in the case of Stellite + SiC composite clads produced using variable proportions of SiC in the cladding mixture by keeping Stellite feed rate constant and changing SiC feed rate and vice versa, the hardness of the matrix regions was found to be dependent on both the total feed rate (Stellite + SiC) and the wt.% of SiC in the cladding powder mixture. The clad hardness in both the series of Stellite + SiC clads reached a maximum value (~ 1300-1400 Hv) at about 20 wt.% SiC in the mixture.
4. The microhardnesses of Stellite and Stellite + SiC composite clads were increased with increasing substrate traverse speed at constant power density and powder feed

rate. Increase in the traverse speed has two fold effect on the clads. Firstly it reduces the beam interaction time and hence the substrate melting which, in turn, reduces the dilution of the clad matrix. Secondly, higher traverse speeds results in higher cooling rates and hence increased refinement of microstructures. Both these factors, i.e. lower dilution and refined microstructures, tend to increase hardness.

5. In the case of SiC injection and cladding of Alloy 4815 + SiC composites, the microhardness of the matrix regions was found to be decreased with increasing substrate traverse speed. The reason for this trend which is contrary to that observed in the Stellite + SiC composite, was that at lower traverse speeds and hence higher interaction times, the amount of SiC dissolution was increased and consequently more enrichment of the clad matrix in carbon content, which was a dominating factor in increasing the hardness of these composites.

9.1.6 Cracking and Porosity in Clads

1. Almost all the alloy samples were found to be free from any cracking or porosity. However, composite clads showed a certain amount of both porosity and cracking.
2. The extent of porosity was smaller, only a few volume%. Two types of porosity were observed; one type was of the spherical form and is attributable to the entrapment of the argon carrier gas. The other type of porosity was of irregular shape and occurred at the interface of the SiC particles and the clad matrix due to the difference in their thermal properties (e.g. thermal conductivity and thermal expansion).
3. Another type of porosity was found between the regions of large SiC particles where these irregularly shaped particles made a cluster and hindered the easy flow of molten metal between them.

4. Some hairline cracks were formed in the matrix region of the composite clads. A few SiC particles were also found to be cracked; this seems to be the result of thermal shock occurred due to short interaction times and rapid cooling.

9.1.7 Wear Studies

1. The wear resistance of the composite clads was twice that of the alloy clads studied. This was attributed to fine SiC particles and also other carbides (M_7C_3) formed during resolidification of liquid rich in carbon due to partial dissolution of SiC.
2. The wear resistance of a variable composition Stellite + SiC composite was found to be higher in the regions formed at higher SiC feed rates.
3. The wear testing conditions were found to be reproducible for various alloy and composite samples in different series. The values of wear coefficient 'K' were found to be almost the same for all the composite clads studied in a given series of experiments.
4. The wear loss in the two-body abrasive wear tests was greater than that observed in the three-body wear situation. The reason for this was two fold; firstly in the three-body test, the process conditions applied were less severe than the two-body test. Secondly due to the nature of the three-body test, that is, in three-body wear, the abrasive particles are free to move. Hence the 90% abrasive particles are most of the time in a state of rolling rather than abradding.
5. The wear loss in both the two- and three-body wear tests was found to be increased with increasing applied pressure and sliding distance.
6. Stainless steel + SiC and Alloy 4815 + SiC composites showed better wear resistance than the Stellite + SiC composite in the case of two-body wear, whereas, in the three-body wear, Stellite + SiC composite showed higher wear resistance than the former two composites.

9.1.8 Particle Velocity

1. An increase in the particle velocity showed high powder loss due to higher rate of rebound from the molten pool; hence there was a decreased powder intake into the melt pool and also reduced clad dimensions.
2. The particle velocity was found to be dependent mainly on the carrier gas flow rates; an increase in gas flow rate results in increasing the particle velocity.
3. Particle velocity varies slightly with decreasing particle size at a given powder feed rate and gas flow rate.
4. At a given powder feed and gas flow rate, particle velocity decreases with increasing powder density.
5. Particle velocity was found to be independent of the powder feed rate at a constant gas flow rate and within the range of feed rates studied.
6. The particle velocity was found to be slightly dependent on the feeding tube length; a slight decrease in particle velocity was found when the tube length was increased over an order of magnitude.

9.2 SUGGESTIONS FOR FUTURE WORK

Laser surface cladding can be used effectively to produce hard and wear resistance coatings of various alloys and composites for a range of engineering applications. By exercising a close control over the process parameters the surface finish obtained will be so high that it can be used in service with a little post cladding treatments.

Most of the objectives set for this project have been covered. However, there are still areas which need an indepth further study, and are listed below.

1. A close range of SiC particle sizes, i.e. 100-175 μm, should be studied to produce composites with finely distributed SiC particles in the clad matrix.

2. The alloy and composite samples produced can be tested for another important form of wear, i.e. adhesive wear.
3. Corrosion resistance of stainless steel and Stellite clads and their composites with SiC can be determined.
4. The microstructural features need to be investigated at an extensive scale to establish the microstructure and properties relationships; especially a more detailed TEM analysis of composite clads will be helpful in this regard.
5. A preliminary study was carried out to determine the temperature attained by the SiC particles before entering the melt pool using computer modelling, to help in determining the degree of their solution. The work was given up due to shortage of time. However, it is suggested to carry out this work further to obtain results about the dependence of SiC particle solution on the particle size.

REFERENCES

1. La Rocca, A.V., Developments in laser material processing for the automotive industries, Laser Surface Treatment of Metals, eds., C.W. Draper and P. Mazzoldi, 1986, pp. 521-541.
2. Ayers, J. D., T. R. Tucker and R. J. Schaefer, Wear resistant surfaces by carbide particle injection, Rapid Solidification Processing; Principles and Technologies 2, eds., R. Mehrabian, B.H. Kear and M. Cohen, Claitors's Publishing Division, LA, 1980, pp. 213-223.
3. O'Shea, D.C., W.R. Callen and W.T. Rhodes, An introduction to lasers and their applications, Addison Wesley Pub. Co., 1978, pp. 2-3.
4. Schawlow, A.L and C.H Townes, Infrared and optical masers, Phy. Rev., 112, 6 (Dec. 1958), pp. 1940-1949 (from ref. 2).
5. Duley, W.W., CO_2 Lasers: Effects and Applications, Academic Press, N.Y., 1976, pp. 1-3.
6. Beesley, M.J., Lasers and their applications, Taylor and Francis Ltd., London, 1978, pp. 118-126.
7. Steen, W.M., Laser cladding, alloying and melting, Annual review of laser processing, Industrial Lasers Handbook, 1986, pp. 158-174.
8. Ready, J.F., Material processing-an overview, Proc. of the IEEE, Vol. 70, No. 6, 1982, pp. 533-535.
9. Powell, J., Ph.D thesis, University of London, 1983.
10. Ready, J.F., Effects of High Power Laser Radiation, Academic Press, N.Y., 1971, pp. 68-100.
11. Ready, J.F., Industrial Applications of Lasers, Academic Press, N.Y., 1978.

12. Steen, W.M., Surface engineering with a laser, Metals and Materials, Dec. 1985, pp. 730-736.

13. Ramouse, E., Carburization of steel surfaces by laser treatment, Laser Surface Treatment of Metals, eds., C.W. Draper and P. Mazzoldi, 1986, pp. 475-482.

14. Draper, C.W., Laser surface alloying: The state of art, J. of Metals, June 1982, pp. 24-27.

15. Draper, C.W. and J.M. Poate, Laser surface alloying, International Metals Reviews, 1985, Vol. 30, No. 2, p. 92.

16. Oakley, P.J., Laser heat treatment and surfacing techniques- a review, The Welding Institute Research Bulletin, Jan. 1981, pp. 4-10.

17. Engel, S.L., Heat treating with lasers, American Mechanist, May 1976, pp. 107-111.

18. Chand, T. and J. Mazumder, Estimating effects of processing conditions and variable properties upon pool shape, cooling rates and absorption coefficient in laser welding, J. of Appl. Phys., 56 (7), Oct. 1984, pp. 1981-1986.

19. Seaman, F.D., Laser heat treating: annual review of laser processing, The Industrial Laser Annual Handbook, 1985, pp. 147-150.

20. Roessler, D.M., An introduction to the laser processing of materials: Annual review of laser processing, The Industrial Laser Annual Handbook, 1985, pp. 16-20.

21. Mazumder, J., Laser heat treatment: The state of art, J. of Metals, May 1983, pp. 19-21.

22. Metals Handbook, 9th ed., Vol. 6: Welding, brazing and soldering, ASM, 1983, p. 771.

23. Duley, W.W., Laser processing and analysis of materials, Plenum Press, N.Y., 1983.

24. Belforte, D., High power laser treatment, Lasers in Modern Industry, ed., J.F. Ready, Michigan, 1979.

25. Monson, P.J.E., Ph.D. thesis, University of London, 1988.

26. Nurminen, J.I. and J.E. Smith, Parametric evaluation of laser/clad interaction for hardfacing applications, Lasers in Materials Processing, ed E.A. Metzbower, ASM, Ohio, 1983, pp. 94-106.

27. Matthews, S.J., Laser fusing of hardfacing alloy powders, Lasers in Materials Processing, ed., E.A. Metzbower, ASM, Ohio, 1983, pp. 138-148.

28. Steen, W.M. and C.G.H. Courtney, Hardfacing of nimonic 75 using 2 kW CW CO_2 laser, Metals Technology, June 1980, pp. 232-237.

29. Eiholzer, E., C. Cusano and J. Mazumder, Wear properties of laser alloyed and clad Fe-Cr-Mn-C alloys, Conf. Proc., ICALEO' 84, LIA, Vol. 44, 1984, pp. 159-167.

30. Li, L.J. and J. Muzumder, A study of the mechanism of laser cladding processes, Laser Processing of Materials, eds., K. Mukherjee and J. Muzumder, Proc. Symposium of AIME, CA, March 1984, pp. 35-50.

31. Macintyre, R.M., The use of lasers in Rolls Royace, Laser Surface Treatment of Metals, eds., C.W. Draper and P. Mazzoldi, 1986, pp. 545-549.

32. Weerasinghe, V.M. and W.M. Steen, Laser cladding with pneumatic powder delivery, Lasers in Materials Processing, Conf. Proc., ASM, 1983, pp. 166-174.

33. Powell, J. and W.M. Steen, Vibro laser cladding, Lasers in Metallurgy, eds., K. Mukherjee and J. Muzumder, AIME, USA, 1981, pp. 93-104.

34. Antony, K.C., Wear-resistant cobalt-base alloys, J. of Metals, Feb. 1983, pp. 52-60.

35. Ross, R.B., Metallic Materials: Specification Handbook, John Wiley and Sons Inc., N.Y., 1972, pp. 116-125.

36. Properties of Deloro Stellite alloys, Technical Literature, Published by Deloro Stellite (UK) Ltd., Swindon, England, March 1975.

37. Metzbower, E. A., E. R. Pierpoint and K. Hartman, Hardfacing using a CW laser, Conf. Proc., ICALEO' 86, eds., C.M. Banas and G.L. Whitney, 1986, pp. 177-184.

38. Weerasinghe, V.M., Ph.D. thesis, University of London, 1985.

39. Giordano, L. and E. Ramous, Rapid solidification of surface layers melted by CW laser, Laser Surface Treatment of Metals, eds., C.W. Draper and P. Mazzoldi, 1986, pp. 483-492.

40. Monson, P.J.E. and W.M. Steen, Laser hardfacing/cladding, Conf. Proc., ECLAT' 86, Bad Neuheim, 1986.

41. Liu, C.A., M.J. Humphries and D.W. Mason, Effect of laser processing parameters on the formation and properties of a Stellite hardfacing coating, Thin Solid Films, Vol. 107, 1983, pp. 251-257.

42. Draper, C.W., Laser surface alloying: The state of art, Lasers in Metallurgy, Conf. Proc. AIME, eds., K. Mukherjee and J. Mazumder, Chicago, IL, 1981, pp. 67-91.

43. Marsden, C., Ph.D. thesis, University of London, 1988.

44. Weerasinghe, V.M., W.M. Steen and D.R.F. West, Laser deposited austenitic stainless steel clad layers, Surface Engineering, Vol. 3, No. 2, 1987, pp. 147-153.

45. Takeda, T., W.M. Steen and D.R.F. West, Laser cladding with mixed powder feed, Conf. Proc., ICALEO' 84, LIA, Vol. 44, 1984, pp. 151-158.

46. Takeda, T., W.M. Steen and D.R.F. West, Insitu clad alloy formation by laser cladding, Conf. Proc., LIM 2, Birmingham, March 1985, IFS Pub., Bradford.

47. Mazumder, J. and J. Singh, Laser surface alloying and cladding for corrosion and wear, Laser Surface Treatment of Metals, eds., C.W. Draper and P. Mazzoldi, 1986, pp. 297-307.

48. Singh, J. and J. Mazumder, Microstructure and wear properties of laser clad Fe-Cr-Mn-C alloys, Metall. Trans. A, Vol. 18A, pp. 313-322.

49. Mazumder, J., C. Cusano, A. Ghosh and E. Eiholzer, Laser surface alloying of steel with Cr-Mn-C for enhanced wear properties, Laser Processing of Materials, Symp. Proc., eds., K. Mukherjee and J. Mazumder, AIME, Los Angeles, CA, 1984, pp. 199-210.

50. Liu, C.A. and M.J. Humphries, Effect of process parameters on laser surface modification, Conf. Proc., ICALEO' 83, LIA, Vol. 38, 1983, pp. 108-117.

51. Marsden, C., D.R.F. West and W.M. Steen, Laser surface alloying of stainless steel with carbon, Laser Surface Treatment of Metals, eds., C.W. Draper and P. Mazzoldi, NATO, ASI series, 1986, pp. 461-474.

52. Chand, T., A. Ghosh and J. Mazumder, Surface properties and microstructure of AISI 1016 steel laser alloyed with chromium and nickel, Laser Processing of Materials, Symp. Proc., AIME, eds., K. Mukherjee and J. Mazumder, 1984, pp. 117-130.

53. Rieker, C., D.G. Morris and J. Steffen, Formation of hard microcrystalline layers on stainless steel by laser alloying, Materials Science and Technology, June 1989, Vol. 5, pp. 590-594.

54. Weston, G.M. and D.A. Wright, Laser alloying of low alloy steel with nickel and chromium, Metals Forum, Vol. 13, 1983, pp. 203-210.

55. Oakley, P.J., Laser transformation hardening of a medium carbon steel, Conf. Proc., ICALEO '83, LIA, Vol. 38, 1983, pp. 118-123.

56. Bergmann, H.W., Laser surface melting of iron-base alloys, Laser Surface Treatment of Metals, eds., C.W. Draper and P. Mazzoldi, NATO ASI series, 1986, pp. 351-368.

57. Hawkes, I., A. Walker, W.M. Steen and D.R.F. West, The application of laser surface melting and alloying to alloys based on the Fe-C system, Laser Processing of Materials, Symp. Proc., AIME, eds., K. Mukherjee and J. Mazumder, 1984, pp. 169-182.

58. Walker, A.M., H.M. Flower and D.R.F. West, The laser surface alloying of iron with carbon, J. of Materials Science, Vol. 20, 1985, pp. 989-995.

59. Christodolou, G., A. Walker, W.M. Steen and D.R.F. West, Laser surface melting of some alloy steels, Metals Technology, Vol. 10, 1983, pp. 215-223.

60. Chen, C.H., C.P. Ju and J.M. Rigsbee, Laser surface modification of ductile iron; Part 1 microstructures, Materials Science and Technology, Vol. 4, 1988, pp. 161-172.

61. Scheafer, R.J., T.R. Tucker and J.D. Ayers, Laser surface melting with carbide particle injection, Laser and Electron Beam Processing of Materials, eds., C.A. White and P.S. Peercy, Academic Press, N.Y, 1980, pp. 754-759.

62. Ayers, J.D. and T.R. Tucker, Particulate TiC-hardened steel surfaces by laser melt injection, Thin Solid Films, Vol. 73, 1980, pp 201-207.

63. Ayers, J.D., Particulate composite surfaces by laser processing, Lasers in Metallurgy, Symp. Proc., eds., K. Mukherjee and J. Mazumder, AIME, 1981, pp. 115-125.

64. Montez, C., Manual de Freitas, Dimitris Pantelis and H. Michand, Laser surface alloying of 42CD4 steel with WC powder injection, Paper presented at 2nd International Seminar on Surface Engineering with High Power Energy Beams, IFHT, Lisboa, Sept. 25-27, 1989.

65. Lewis, B.G., D.A. Gilbert and P.R. Strutt, Laser and electron beam melting of iron-base hard materials, Laser and Electron Beam Processing of Materials,

Symp. Proc., eds., C.W. White and P.S. Peercy, Academic Press, N.Y., 1980, pp. 747-753.

66. Ayers, J.D., T.R. Tucker and R.C. Bowers, A reduction in the coefficient of friction for Ti-6Al-4V, Scripta Metallurgica, Vol. 14, 1980, pp. 549-550.

67. Tucker, T.R., A.H. Clauer, I.G. Wright and J.T. Stropki, Laser-processed composite metal cladding for slurry erosion resistance, Thin Solid Films, Vol. 118, 1984, pp. 73-84.

68. Cooper, K.P and J.D. Ayers, The influence of processing parameters on the cracking tendency of laser processed composite surfaces, Focus on Laser Materials Processing, Conf. Proc., ICALEO' 87, LIA, San Diego, CA, 1987, pp. 179-187.

69. Abbas, G., W.M. Steen and D.R.F. West, Laser cladding with SiC particle injection, Conf. Proc., ECLAT' 88, 1988, pp. 68-70.

70. Abbas, G. and D.R.F. West, Laser-processed composite metal cladding, High Power Lasers and Laser Machining Technology, Conf. Proc., ECO 2, eds., M.L. Gaillard and A. Quenzer, SPIE, Vol. 1132, 1989, pp. 232-236.

71. Abbas, G., D.R.F. West and W.M. Steen, Wear studies of variable composition Stellite + SiC laser clad deposits, Surface Engineering with High Energy Beams, Proc. of 2nd International Seminar of IFHT, Lisboa, 1989, pp. 447-453.

72. Abbas, G., D.R.F. West and W.M. Steen, Wear studies of laser produced alloy and composite deposits, Conf. Proc., ICALEO' 89, LIA, Vol. 69, 1989, pp. 116-128.

73. Abboud, J.H. and D.R.F. West, Ceramic-metal composites produced by laser surface treatment (short communication), Materials Science and Technology, Vol. 5, 1989, pp. 725-728.

74. Miyoshi, K. and D.H. Buckley, Tribological properties of SiC in the metal removal process, Wear, Vol. 82, 1982, pp. 197-211.

75. Technical Literature, Electro Minerals Co. (UK) Ltd., Manchester, 1974.

76. Handbook of High Temperature Materials, Plenum Press, N.Y., 1964, pp. 107-110.

77. Murray, J.L., L.H. Bennett and H. Baker, Binary Alloy Phase Diagrams, Vol. 1, ASM, Ohio, 1986, p.590.

78. BOC operator's manual of CO_2 laser.

79. Folkes, J., Ph.D. thesis, University of London, 1986.

80. Operator's Manual, Leitz 'Miniload 2' hardness tester.

81. Powder Diffraction File, Inorganic phases, (JCPDS), International Centre for Diffraction Data, PA, USA, 1989.

82. Metals Handbook, 9th ed., Vol. 8, ASM, Ohio, 1985, pp. 601-608.

83. Lansdown, A.R. and A.L. Price, Materials to Resist Wear; a guide to their selection and use, Pergamon Press, Oxford, 1986.

84. Handbook of Mechanical Wear, eds., C. Lipson and L.V. Colwell, The University of Michigan Press, 1961.

85. Eyre, T.S., Tribology International, April 1978, pp. 91-96.

86. Rabinowicz, E., Friction and Wear of Materials, John Wiley and Sons, N.Y., 1965.

87. Johnson, R.L., A system rationale for the selection or design of tribological surface coatings, Thin Solid Films, Vol. 73, 1980, pp. 235-244.

88. Misra, A. and I. Finnie, A classification of three-body abrasive wear and design of a new tester, Wear of Materials, Conf. Proc., eds., W.A. Glaeser, K.C. Ludema and S.K. Rhee, ASME, N.Y., 1979, pp. 313-318.

89. Khruschov, M.M., Principles of abrasive wear, Wear, Vol. 28, 1974, pp. 69-88.

90. Mutton, P.J. and J.D. Watson, Some effects of microstructure on the abrasive wear resistance of metals, Wear, Vol. 48, 1978, pp. 385-398.

91. Yang, G.H. and W.M. Garrison, A comparison of microstructural effects on two-body and three-body abrasive wear, Wear, Vol. 129, 1989, pp. 93-103.

92. Mashloosh, K.M. and T.S. Eyre, Effect of attack angle in abrasive wear, Metals and Materials, July 1986, pp. 426-430.

93. Sedrik, A.J. and T.O. Mulhearn, Mechanics of cutting and rubbing in simulated abrasive processes, Wear, Vol. 6, 1963, pp. 457-466.

94. Arbabi, H. and T.S. Eyre, Wear behaviour- a preliminary investigation, Metals and Materials, Oct. 1986, pp. 625-629.

95. Gahr, K.H.Z., Relation between abrasive wear rate and the microstructure of metals, Wear of Materials, Conf. Proc., eds., W.A. Glaeser, K.C. Ludema and S.K. Rhee, ASME, N.Y., 1979, pp. 266-274.

96. Avery, H.S., Classification and precision of abrasive tests, Wear of Materials, Conf. Proc., eds., W.A. Glaeser, K.C. Ludema and S.K. Rhee, ASME, N.Y., 1977, pp. 148-157.

97. Basse, J.L., Effect of composition, microstructure and service conditions on the wear of cemented carbides, J. of Metals, Nov. 1983, pp. 35-42.

98. Glaeser, W.A. and B.P. Fairand, Laser surface melting for abrasion resistance, Wear of Materials, Conf. Proc., eds., W.A. Glaeser, K.C. Ludema and S.K. Rhee, ASME, N.Y., 1979, pp. 304-312.

99. Mordike, B.L., Developments in the production of wear-resistant layers, Conf. Proc., LASER-6, IITT- International, Paris, 1990, pp. 9-19.

100. Ayers, J.D., R.J. Scheafer and W.P. Robey, A laser processing technique for improving the wear resistance of metals, J. of Metals, Aug. 1981, pp. 19-23.

101. Ayers, J.D. and R.N. Bolster, Abrasive wear with fine diamond particles of carbide-containing aluminium and titanium alloy surfaces, Wear, Vol. 93, 1984, pp. 193-205.

102. Belmondo, A. and M. Castagna, Wear-resistant coatings by laser processing, Thin Solid Films, Vol. 64, 1979, pp. 249-256.

103. Silence, W.L., Effect of structure on wear resistance of Co-, Fe-, and Ni-base alloys, Wear of Materials, Conf. Proc., eds., W.A. Glaeser, K.C. Ludema and S.K. Rhee, ASME, N.Y., 1977, ASME, N.Y., pp. 77-85.

104. Operator's Handbook, 'Talysurf 10', Rank Taylor Hobson Ltd., Leicester, England.

105. Rawlings, R.D. and W.M. Steen, Acoustic emission monitoring of surface hardening by laser, Optics and Lasers in Engineering, Vol. 2, 1981, pp. 173-188.

106. Weerasinghe, V.M. and W.M. Steen, In-process monitoring of laser processes,

107. Arrington, M., The use of acoustic emission instrumentation to monitor powders flows, NDT International, (14), 1981, pp. 3-7.

108. Belden, D.H. and L.S. Kasel, Ind. Eng. Chem., 41(6), 1949, 1174.

109. Flemmings, M.C., Solidification Processing, McGraw-Hill, London, 1974.

110. Kear, B.H., E.M. Breinan and L.E. Greenwald, Met. Tech., Vol. 6, 1979, p.121.

111. Jones, H., Rapid solidification of metals and alloys, Monograph No. 8, Institute of Metals, London, 1982, pp. 40-43.

112. Meharbian, R., 1978, (from Ref. 111).

113. Walker, A.M., L.M. Lundberg, I. Hawkes, D.R.F.West and W.M. Steen, Ist. Cast. Conf. II, Stockholm, aug. 1984 (from Ref. 43).

114. Bruck, G.J., High power laser beam cladding, J. of Metals, Feb. 1987, pp. 94-106.

115. Komvopoulos, K. and K. Nagarathnam, Processing and characterization of laser-cladded coating materials, J. of Engg. Mat. and Tech., Vol. 112, 1990, pp. 131-143.

116. Thompson, E.R. and F.D. Lamkey, Met. Trans., Vol. 1, 1970, pp. 2799-2806.

117. Koster, W. and F. Sperner, Arch. Eisenhuettenw, Vol. 26, pp. 555-559.

118. Raghavan, V., The carbon-iron-silicon system, J. of Alloy Phase Diagrams, Vol. 2, No. 2, 1986, pp. 97-107.

119. Exner, H.E., Physical and chemical nature of cemented carbides, International Metals Reviews, No. 4, 1979, pp. 149-173.

120. Monson, P.J.E., W.M. Steen and D.R.F. West, Rapid alloy scanning by variable composition laser cladding, Conf. Proc., LAMP' 87, Osaka, 1987, pp. 377-382.

121. Kooper, K.P. and P. Slebodrick, Recent developments in laser melt/particle injection processing, J. of Laser applications, Vol. 1, No. 4, LIA, 1989, pp. 21-29.

122. Richardson, R.C.D., The maximum hardness of strained surfaces and the abrasive wear of metals and alloys, Wear, Vol. 10, 1967, pp. 353-382.

123. Moore, M.A., The relationship between the abrasive wear resistance, hardness and microstructure of ferrite materials, Wear, Vol. 28, 1974, pp. 59-68.

124. Jiang, M., X.P. Jiang, J.G. Huang, X.F. Sun, J.S. Zhang, Y.L. Ge and Z.Q. Hu, Microstructures of laser cladded iron-, nickel- and cobalt-base coatings, Materials Letters, Vol. 7, No. 12, 1989, pp. 453-455.

List of Previous Publications

1.* "Laser cladding with SiC particle injection", G. Abbas, W.M. Steen and D.R.F. West, Conf. Proc., ECLAT' 88, 1988, pp. 68-70.

2.* "Laser-processed composite metal cladding", G. Abbas and D.R.F. West, High Power Lasers and Laser Machining Technology, Conf. Proc., ECO 2, eds., M.L. Gaillard and A. Quenzer, SPIE, Vol. 1132, 1989, pp. 232-236.

3.* "Wear studies of variable composition Stellite + SiC laser clad deposits", G. Abbas, D.R.F. West and W.M. Steen, Surface Engineering with High Energy Beams, Proc. of 2nd International Seminar of IFHT, Lisboa, 1989, pp. 447-453.

4.* "Wear studies of laser produced alloy and composite deposits", G. Abbas, D.R.F. West and W.M. Steen, Conf. Proc., ICALEO' 89, LIA, Vol. 69, 1989, pp. 116-128.

5.** "Acoustic emission monitoring of powder flow for laser cladding", G. Abbas, R.D. Rawlings and V.M. Weeransinghe, Conf. Proc., LASER-6, IITT International, Paris, 1990, pp. 175-180.

6. "Laser surface cladding of Stellite and Stellite + SiC composite deposits for enhanced hardness and wear", G. Abbas and D.R.F. West, Paper accepted for publication in 'Wear'.

* Paper presented by G. Abbas at the conference.

** Paper presented by Dr. R.D. Rawlings at the conference.